



THÈSE DE DOCTORAT

DE L'UNIVERSITÉ PSL

Préparée à MINES ParisTech

Etude de la microstructure induite du PEF, un polymère biosourcé, lors d'étirages uniaxiaux et biaxiaux au-dessus de la transition α

Strain induced microstructure in PEF, a biobased polymer, upon uniaxial and biaxial stretching above the α -relaxation

Soutenue par

Emilie FORESTIER

Le 29 Mars 2021

Ecole doctorale n° 364

Sciences Fondamentales et Appliquées (SFA)

Spécialité

Mécanique Numérique et Matériaux

Composition du jury :

Sylvain, CAILLOL Directeur de recherche, CNRS (ICGM)	<i>Président</i>
Valérie, GAUCHER Professeur, Université de Lille (UMET)	<i>Rapporteur</i>
Isabelle, ROYAUD Professeur, Université de Lorraine (IJL)	<i>Rapporteur</i>
Allisson, SAITER-FOURCIN Professeur, Université de Rouen-Normandie (GPM-EIRCAP)	<i>Examineur</i>
Christelle, COMBEAUD Docteur, MINES ParisTech (CEMEF)	<i>Encadrant</i>
Nathanaël, GUIGO Docteur, Université Côte d'Azur (ICN)	<i>Encadrant</i>
Noëlle, BILLON Professeur, MINES ParisTech (CEMEF)	<i>Directeur de thèse</i>
Nicolas, SBIRRAZZUOLI Professeur, Université Côte d'Azur (ICN)	<i>Directeur de thèse</i>



Strain induced microstructure in PEF, a biobased polymer, upon uniaxial and biaxial stretching above the α -relaxation

Etude de la microstructure induite du PEF, un polymère biosourcé, lors d'étirages uniaxiaux et biaxiaux au-dessus de la transition α

Jury

Sylvain CAILLOL, Président
Directeur de recherche, CNRS (ICGM)

Valérie GAUCHER, Rapporteur
Professeur, Université de Lille (UMET)

Isabelle ROYAUD, Rapporteur
Professeur, Université de Lorraine (IJL)

Allisson SAITER-FOURCIN, Examineur
Professeur, Université de Rouen- Normandie (GPM-EIRCAP)

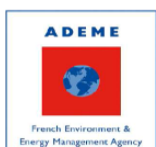
Supervisors

Christelle COMBEAUD, Encadrant
Docteur, MINES ParisTech (CEMEF)

Nathanaël GUIGO, Encadrant
Docteur, Université Côte d'Azur (ICN)

Noëlle BILLON, Directeur de thèse
Professeur, MINES ParisTech (CEMEF)

Nicolas SBIRRAZZUOLI, Directeur de thèse
Professeur, Université Côte d'Azur (ICN)



Glossary

Acronyms	Name
A-annealed	Biaxial test stretched and annealed (slower strain rate)
A-quenched	Biaxial test stretched and quenched (slower strain rate)
A-PEF	Amorphous PEF
A-PET	Amorphous PET
B-annealed	Biaxial test stretched and quenched (faster strain rate)
B-quenched	Biaxial test stretched and quenched (faster strain rate)
DD	D-lactide enantiomer
DIC2D	2D Digital Image Correlation
DIC3D	3D Digital Image Correlation
DMTA	Dynamical Mechanical and Thermal Analysis
D-PEF	Drawn PEF
D-PET	Drawn PET
EG	Ethylene glycol
FDCA	2,5-furandicarboxylic acid
FT-IR	Fourier Transformed Infrared Analysis
GHG	Greenhouse gas emissions

HMF	5-hydroxymethylfurfural
I-PEF	Drawn and interrupted PEF
I-PET	Drawn and interrupted PET
IR	Infrared
ISBM	Injection Stretch Blow Moulding
LD	Meso enantiomer
LL	L-lactide enantiomer
MAF	Mobil amorphous domain
MD	Stretching or machine direction associated to the meridional direction
NDR	Natural Draw Ratio
NREU	Non-renewable energy use
PEF	Poly(ethylene 2,5-furandicarboxylate)
PEN	Poly(ethylene 2,6-naphthalate)
PET	Poly(ethylene terephthalate)
PLA	Poly(lactid acid)
PVC	Polyvinyl chloride
RAF	Rigid amorphous domain
SDG	Sustainable development goal
SIC	Strain Induced Crystallization
SSP	Solid State Process
TA	Terephthalic acid
TC-PEF	Thermally crystallized PEF
TC-PET	Thermally crystallized PET

TD	Transverse direction associated to the equatorial direction
WAXS	Wide Angles X-ray Scattering
WLF	William Landel and Ferry
ZnSe	Zinc selenide

Symbols	Name	Unit
a_T	Shift factor	
c	Celerity of the light	m.s^{-1}
C_1^0	Viscoelastic coefficient	
C_2^0	Viscoelastic coefficient	$^{\circ}\text{C}$
d_{hkl}	Interreticular spacing	\AA
e_0	Initial thickness	mm
E	Absorbed energy	J
E'	Elastic modulus	MPa
E''	Loss modulus	MPa
$F(t)$ or F	Strength	N
h	Planck's constant	J.s
(hkl)	Miller's indices	
I or $I(2\theta)$	Intensity of the 1D scan	Counts
$I(\varphi)$	Intensity of the azimuthal scan	Counts
I_{max}	Maximal intensity	Counts
I_{min}	Minimal intensity	Counts
I_{ratio}	Intensity ratio	
IV	Intrinsic viscosity	dL.g^{-1}
l	Hyperbolic layers	
L_0	Initial length	mm
$L_{diagonal}$	Length on the diagonal	mm

$L(t)$	Current length	mm
M_n	Number average molecular weight	g.mol^{-1}
M_w	Weight average molecular weight	g.mol^{-1}
N_{hkl}	Normal to the diffracting plane	
OE or D	Distance between the sample and the screen	mm
OR	Distance between the diffracted spot and centre of the film	mm
$S(t)$ or S	Section	mm^2
t	Time	s
T	Temperature	$^{\circ}\text{C}$
T_c	Cold crystallization temperature	$^{\circ}\text{C}$
T_{oven}	Temperature of the oven	$^{\circ}\text{C}$
T_{pinch}	Temperature of the pinch	$^{\circ}\text{C}$
T_{ref}	Reference temperature (chosen)	$^{\circ}\text{C}$
$v(t)$	Velocity of the arms	mm.s^{-1}
w_0	Initial width	mm
α	Crystal form obtained for static crystallization performed above 170 $^{\circ}\text{C}$ (PEF)	
α'	Crystal form obtained for static crystallization performed below 170 $^{\circ}\text{C}$ (PEF) and for SIC	
β	Crystal form obtained from solvent crystallization (PEF)	

ΔC_p^0	Heat capacity variation of a fully amorphous sample	$\text{J.g}^{-1}.\text{K}^{-1}$
ΔC_p	Heat capacity variation	$\text{J.g}^{-1}.\text{K}^{-1}$
ΔH_c	Cold crystallization enthalpy	J.g^{-1}
ΔH_m^0	Equilibrium melting enthalpy	J.g^{-1}
ΔH_m	Melting enthalpy	J.g^{-1}
ΔL	Evolution in length	mm
$\Delta V/V_0$	Relative volume variation	
ε_1	Major true strain	
ε_2	Minor true strain	
$\varepsilon_{diagonal}$	True strain on the diagonal	
ε_{xx}^{final}	Final true strain	
ε_{xx} or $\varepsilon_{xx}(t)$	True strain (Hencky's strain) in the longitudinal direction	
ε_{yy} or $\varepsilon_{yy}(t)$	True strain (Hencky's strain) in the third direction (thickness)	
ε_{zz} or $\varepsilon_{zz}(t)$	True strain (Hencky's strain) in the transversal direction	
$\dot{\varepsilon}_0$	Strain rate	s^{-1}
$\dot{\varepsilon}^* a_T^{obtained}$	Equivalent strain rate obtained during the stretching	s^{-1}
θ or 2θ	Angular positions of the diffraction peak with 1D scans	$^\circ$
λ_1 and λ_2	Draw ratio on each direction (biaxial stretching)	
λ or $\lambda(t)$	Draw ratio	

$\lambda_{biaxial}$	Biaxial draw ratio	
$\lambda^{CuK\alpha}$	CuK α radiation	Å
$\bar{\nu}$	Wave number	cm ⁻¹
$\sigma(t)$ or σ	True stress	MPa
$Tan \delta$	Damping factor	
T_{α}	Temperature of the α -relaxation	°C
T_{β}	Temperature of the β -relaxation	°C
φ	Angular position with azimuthal scans	°
χ_c	Crystal ratio	%
χ_{MAF}	MAF ratio	%
χ_{RAF}	RAF ratio	%

General Summary

<u>Introduction and state of the art</u>	1
Table of contents	1
1. Definitions	2
2. Background	2
3. PET and bottles forming	3
4. Biobased plastics	7
5. Comparison of PEF and PET properties	9
6. Project and scientific strategy	11
<u>Chapter 1</u>	15
<i>Description of the materials, techniques and protocols used</i>	15
Table of contents	15
1. Introduction	17
2. Materials	17
3. Differential Scanning Calorimetry (DSC)	18
4. Dynamic Mechanical and Thermal Analysis (DMTA)	19
5. Thermal deformation	19
6. X-ray scattering	20
7. Determination of the Miller's indices	21
8. FT-IR measurements	21
9. Stretching	22
9.1 Arm displacement	22
9.2 Thermal measurement	23
9.3 Optical measurement and relevance of the 2D analysis	25
<u>Chapter 2</u>	29
<i>Uniaxial stretching of PEF and PET</i>	29
Table of contents	29

1.	Introduction.....	32
2.	Experimental protocol.....	32
2.1	Determination of the forming range.....	32
2.2	Static crystallization.....	34
2.3	Master curve building.....	37
2.4	Samples geometry and calculation of the stress.....	40
3.	Definition of the uniaxial stretching conditions.....	42
3.1	Selection of the couples strain rate / temperature.....	42
3.2	Evolution of the strain during the tests.....	44
3.3	Determination of the experimental parameters.....	46
4.	Mechanical behaviour.....	53
5.	Conclusions.....	60
6.	Annexes.....	61
	Chapter 3	67
	<i>Comparison between the crystal induced in static conditions and SIC</i>	67
	Table of contents.....	67
1.	Introduction.....	70
2.	Analysis of the crystalline structure of PEF.....	73
2.1	Crystalline structure induced by the stretching.....	73
2.2	Comparison with the crystal formed by static crystallization.....	79
3.	Conformations involved in PEF and PET.....	82
3.1	Conformational changes due to crystallization occurrence.....	84
3.2	Aromatic =C-H and cycle breathing.....	86
3.3	Transformations in the aliphatic part in PEF and PET.....	88
3.4	Impact on the β -transition.....	91
4.	Conclusions.....	94
	Chapter 4	97
	<i>The formation of a crystal upon stretching in PEF and PET</i>	97
	Table of contents.....	97
1.	Introduction.....	99
2.	Mechanical description.....	100
2.1	Behaviour of PET under loading-unloading tests.....	102
2.2	Behaviour of PEF under loading-unloading tests.....	104
3.	Crystal development scenario.....	106
3.1	PET and PEF thermal behaviour.....	106
3.2	PET and PEF crystal building.....	110

3.2.1	PET crystal formation	111
3.2.2	PEF crystal formation	114
4.	Properties induced by the stretching	118
4.1	PET amorphous phase mobility and rigidity evolution	118
4.2	PEF amorphous phase mobility and rigidity evolution.....	120
4.3	Modification of the local motions by the stretching.....	122
4.4	PET and PEF thermal deformation	124
5.	Conformational analysis.....	126
6.	Conclusions.....	128
7.	Annexes.....	130
Chapter 5	135
	<i>Characterization of the microstructure and of the thermo-mechanical behaviour of the uniaxially stretched PEF and PET samples</i>	135
	Table of contents.....	135
1.	Introduction.....	138
2.	Stretching of PEF up to close strains	141
3.	PET sensitivity to the stretching conditions	146
4.	Comparison with the tests performed up to higher strains.....	152
5.	Conclusions.....	159
6.	Annexes.....	160
Chapter 6	171
	<i>PEF biaxial stretching and associated microstructural development.....</i>	171
	Table of contents.....	171
1.	Introduction.....	174
2.	Biaxial stretching	175
2.1	Protocol	175
2.1.1	Definition of the tests.....	175
2.1.2	Heating protocol.....	177
2.1.3	Strain rate, temperature and equivalent strain rate evolution	179
2.2	True stress/strain curves	180
3.	Microstructural development and properties	182
4.	Microstructural evolution upon biaxial stretching.....	192
5.	Conclusions.....	198
6.	Annexes.....	199
Conclusions and perspectives	203
1.	Conclusions of the work.....	203

2. Perspectives.....	204
3. Environmental impact of PEF	205
<u>References</u>	207

Introduction and state of the art

Table of contents

1. Definitions	2
2. Background.....	2
3. PET and bottles forming	3
4. Biobased plastics	7
5. Comparison of PEF and PET properties	9
6. Project and scientific strategy	11

1. Definitions

Polymers are everywhere around us in our daily life. A polymer is obtained by the replication of molecules, named monomers. These monomers are linked by strong covalent bonds and stabilized by physical interactions [1,2]. For example DNA, plastic bottles, gelatine, suture thread, bumper, cellulose and so many others are, or are made with, polymers. The list is almost endless and illustrates that polymers can be natural or synthetic [3,4].

The structure of a polymer is responsible of all the properties of the polymeric material, and closely related to the temperature. Polymers can be classed into three categories: thermoplastics, thermosets or elastomers. This work focuses only on thermoplastics, or “plastic”, polymers. Thermoplastic polymers soften when the temperature is increased or when a pressure is applied. Then, they can be formed and also recycled.

Several physical transitions can be observed in the thermoplastic polymers. One of these transitions is the glass transition which corresponds to the occurrence of global and cooperative motions of the amorphous chains along the chain skeleton. Below the glass transition the material is rigid and becomes viscoelastic above the glass transition. From a mechanical viewpoint, the glass transition is named α -relaxation and involves the same motions of the chains. Others transitions exist and occur at lower temperatures, in comparison with the glass transition. They are related to more local motions of the chains (no cooperativity is involved). Finally, at high temperatures semi-crystalline polymers may flow and a melting can be observed.

Plastics are now used (and vital) in many fields such as medicine, food packaging, electronic devices, insulating, automobile, clothes and others... But this position has an historical explanation.

2. Background

During the Second World War, some metals become rare (copper, aluminium, steel, zinc) and they were reserved to military needs [5]. Thus, it was necessary to develop other manufacturing

materials: synthetic plastic materials start to be employed. As an example, nylon has replaced the Japanese silk for the parachute.

From this point, and even if plastics exist before, the plastic area begins: synthetic plastics were increasingly produced. It was a real revolution in the households, where plastic starts to be implanted everywhere. For example, from 1957 to 1967 the “house of the future”, which is supposed to exist in 1986, was presented in Disneyland (in California) [6]. This house was sponsored by Monsanto, major producer of plastic in the 40’s, and is fully made of plastic. Inside, it can be found the future objects, in plastic, that will exist in the households (TV screens, microwaves oven, dishwashers). Plastics are not only used on earth but also in the space: in 1969, the American flag planted on the moon is made with nylon [7].

Food packaging has been widely impacted by the plastic revolution! In order to diffuse their products and their brand name, food packaging is of prime interest for companies. As an example, plastic boxes (made with polyethylene and with other plastics) were developed and spread with the housewife network under the brand Tupperware®, in 1946. It is a major implantation of the plastic in the house. The garbage plastic bag (still made with polyethylene) was put on the market on 1950.

The aim of plastic food packaging is not only to have an easily transportable and light weight container, but also a material that can protect the consumable from microbes, light, humidity, gas lost and that will keep the flavour and the aromas [8]. A desired and specific atmosphere around the product can also be kept with packaging. For example, with plastic bottles the re-closable cap is ensured and protects the liquids. Before the essential plastic cap, the crown cork (metal cap with a layer of cork inside) was used on the glass bottles to protect the beverage. But plastic offers a more uniform and tighter seal [9]. Concerning the bottles, polyvinyl chloride (PVC) has been first used, instead of brittle and heavy glass bottles, and then, it has been replaced by the most and still used material in food packaging: polyethylene terephthalate (PET).

3. PET and bottles forming

The success story of PET starts in the 70’s with the need of Pepsi® to pack carbonated drinks [10]. Indeed, the cost of PET is relatively low. PET is obtained from the polycondensation by

an esterification reaction of terephthalic acid (TA) and of ethylene glycol (EG). Most of the time, these reagents come from petroleum resources. Even if ethylene glycol can be biosourced, PET will be only biobased at 30%. As it will be explained further, it is difficult to obtain TA from biobased resources. Figure 1 represents the repeating unit of the molecule of PET.

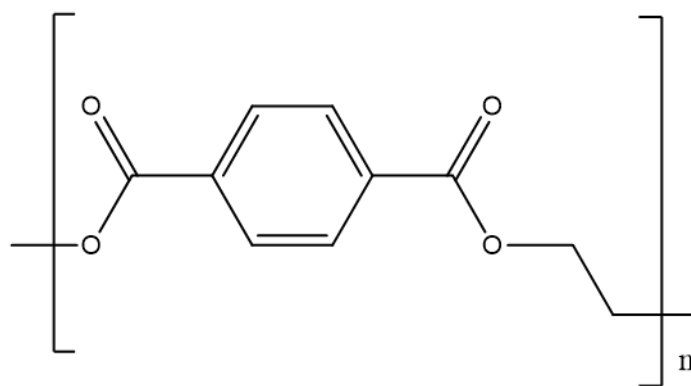


Figure 1. PET repeating unit.

PET is a quenchable polymer. Its crystallization kinetics is slow enough to allow the obtention of an amorphous material, when a rapid quench is applied. But, thanks to the regularity and the symmetry of the chain, PET can form a crystal that will coexist with the amorphous domain. It means that it has the ability to arrange its chains in an ordered and periodic structure. The crystallization takes place in three steps: firstly the nucleation, secondly the crystal growth, and finally the secondary crystallization. The secondary crystallization forms secondary lamellae that will exist between the lamellae induced by the primary crystallization. It forms the radial structure of the spherulites [11,12]. The creation of a crystal improves the mechanical properties, the thermal stability and also the barrier properties of a material, in comparison to its amorphous state.

With a thermal treatment, the static crystallization can occur from the melt (by cooling the material) or from the glassy state (by heating the material). The static crystallization creates some large entities, named spherulites, at the micrometric scale. At a lower scale, around 10 nm, the crystalline lamella exists [2]. Spherulites are responsible for scattering the light and block the light transmission and the resulting material is opaque. The apparition of a crystal upon static crystallization depends on the temperature, and on the heating/cooling rate.

When submitted to a mechanical stress (stretching), the semi-crystalline polymers, such as PET, can crystallize from the rubbery state. The crystallization during the stretching can take place under several mechanical stresses, such as uniaxial and biaxial stretching for example. This

phenomenon is named Strain Induced Crystallization (SIC), and depends on the temperature and on the strain rate. Compared to the static crystallization, SIC is a faster way to crystallize and small crystalline entities are formed. These entities do not scatter the visible light, leading to a transparent material. SIC is then preferred and required in some applications such as bottles forming.

In the industry, bottles are formed using the ISBM process (Injection Stretch Blow Moulding). PET owns an important place in the bottles market. In 2016, around the world, 480 billions of plastic bottles were sold [13]. Sidel company, with the largest installed base of blowing devices in production, is one of the major company involved in PET bottles blowing. During the ISBM process, the microstructure of PET changes, as a result of the SIC occurrence. This process is composed of several steps that are represented in Figure 2 [14]. In the lab, ISBM can be reproduced through uniaxial and biaxial stretching performed at temperatures close and above the glass transition. Years after years, this process has been developed and improved by studies performed on PET. Thus, ISBM process has been mainly optimized for PET.

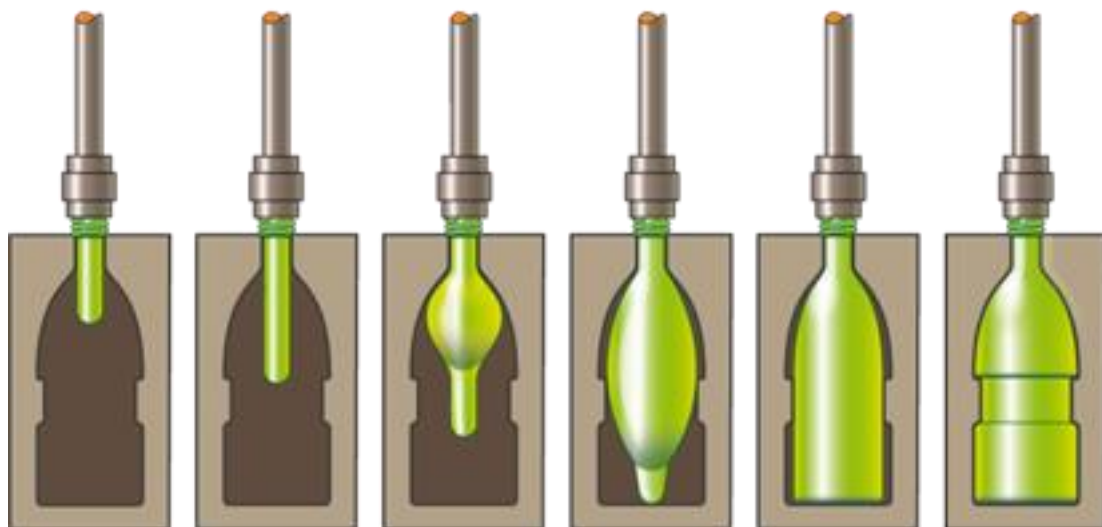


Figure 2. ISBM process [14].

The preform is formed by injection moulding. This step creates the bottle neck. During all the rest of the process, the bottle neck is protected from the heat and from the deformation. The preforms are stored, and then transported towards the blowing devices.

Firstly, the body of the preform is heated, typically using infrared radiations (IR), above the glass transition of the material. By this way, with the increase of the temperature the chains gain mobility, the preform is less rigid and can be deformed. The heart of the process can begin.

A rod stretches longitudinally the hot preform. In the lab, this step is reproduced with uniaxial stretching. Simultaneously, gas is injected in the cavity: a bubble is initiated and aims at increasing the preform volume. In the lab, it is associated to biaxial stretching. Finally, the preform edges reach the mould walls that are thermally regulated. The target of the mould is to freeze the shape of the bottle, and to affix the design of the brand.

Before being commercialized, bottles have to respond to a detailed technical specification.

A “good” bottle must respond to mechanical criteria. To resist at the pallet stacking (in the storehouse or shops), at the users prehensions, in their daily life, and at the internal pressure (due to gas presence), a sufficient stiffness is needed. Thermic criteria are also required. The bottle must be able to be used, while keeping its shape and properties, at several temperatures and pressures. For example, it must be able to be used at the top of a mountain, at the sea-level and also in hot and humid places. Finally, in order to keep the gas in the bottles good barrier properties are desired. The transparency of the materials has also been, and still is, an important criteria for the consumers. However, with the apparition of recycled bottles the transparency criterion can be difficult to ensure as the recycle cycles are applied, causing the transparency to decrease [15].

Despite all PET advantages for bottles blowing, some alternative materials have been scoped these last years. In order to get a material with higher mechanical and barrier properties poly(ethylene 2,6-naphthalate), named PEN, has been widely investigated during the nineties. PEN is the result of the polycondensation reaction between 2,6-dimethylenaphthalene dicarboxylate acid and ethylene glycol, and is commonly compared to PET. Its repeating unit is composed of two naphthalene rings, as it is visible in Figure 3.

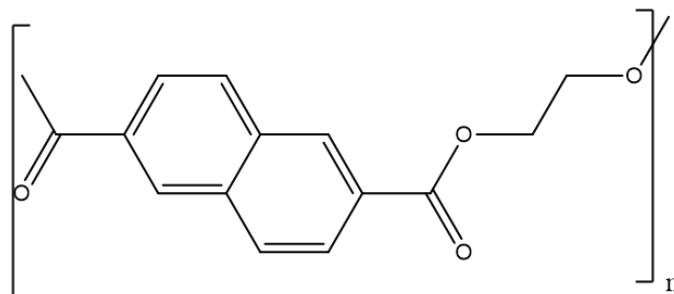


Figure 3. PEN repeating unit.

Because of this peculiar aromatic structure, PEN is known to exhibit higher barrier properties and rigidity compared to PET [16]. As an example, PEN permeability is reduced by 4 for the

dioxygen, by 5 for the carbon dioxide and by 3.5 for the humidity compared to PET [17]. The melting and glass transition temperatures of PEN are also increased in comparison with PET: the glass transition temperature of PEN occurs at 120 °C, while it is around 75 °C for PET. Unfortunately, PEN cost is very high, too high for food packaging [8,16]. Moreover, the stretching temperatures applied to induce SIC are increased by at least 40 °C with PEN [18–21]. Finally, it is more suitable, for economic reasons, to use PET for bottles forming, while PEN is widely used in electronic for circuit boards.

Despite the reduction of the packaging weight and even if food packaging represents a small part of the use of the petroleum resources, the higher part belongs to the transport sector, the actual model reveals the existence of real issues. With the environmental alarming situation, the near future disappearance of petroleum resources, the impact of petroleum resources on the environment, as well as the dependence and conflicts linked to the petroleum business, one of the major challenge of the 21st century is to find other alternatives to petroleum resources to limit, perhaps to stop, the petroleum dependence. The light is now on the biobased materials.

4. Biobased plastics

It is essential to be precise on the vocabulary. Biobased material does not necessary mean biodegradable, compostable or recyclable materials. It only refers to the origin of the resources. Some biobased materials can also be biodegradable, but it is necessary to know the temperature, the time needed and the conditions (natural or in the industry). Up to now, there are no materials that are biodegradable in the sea at 0 °C, for example. It confirms that even if the biobased materials are used instead of the petroleum based materials, the end-life of them must be ensured and still improved (recycling, composting...). The population must be educated and be responsible of its wastes, to reduce the anthropogenic pollution and to protect the biodiversity [22]. Moreover, beside all the polemics, it is evident that plastics must be reduced, specially the one use plastics, but they remain necessary and not replaceable for many applications (such as in the medical, packaging, automobile, sports, aeronautic or building fields). Thus, the interest in biobased plastics is legitimate to offer a green alternative [22].

The world production of plastic has been multiplied by around 20 during the last 50 years: from 15 million of tones in 1964 to 311 million of tones in 2014 [22]. According to the Ellen

MacArthur foundation, this production is going to continue to double in the next 20 years, and to quadruple up to 2050 [22,23]. A global dynamic has been established by the United Nations in order to define sustainable development goals (SDG), up to 2030 [24]. This dynamic aims at increasing the use of technologies and industrial proceeds that are more ecological. It means that they fit with the concept of circular economy, preserve the ecosystems as well as the fossil resources, and reduce the greenhouse gas emissions (GHG) [22,25,26].

The aim of synthesizing biobased plastics is to design materials from the biomass, such as vegetal waste or micro-organisms, similar to the petrosourced ones [22]. It means with equivalent or superior properties compared to the actual petroleum based materials. Another crucial point is to keep the available surface used to produce food: it means that biobased materials must be non-competitive with food production [22]. According to this last point, the biobased materials are classed under several generations [26]. The first generation of feedstock implies the biomass that can be edible (sugarcane, whey, starch, maize); while the second generation of feedstock resources is related to non-edible resources, and are generally issued from the lignocellulosic biomass (residues or side stream products from the agriculture, forest, animal industry and municipal wastes). The last generation, the third one, is focused on feedstocks issued from algae [26,27].

At the beginning of the 21st century, the first biobased material proposed to replace PET in food packaging was PLA, for poly(lactic acid), its repeating unit is represented in Figure 4.

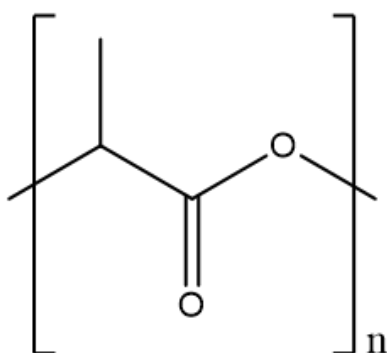


Figure 4. PLA repeating unit.

PLA is obtained from starch and exists under two optically active enantiomers. Depending on the proportion of the two-stereo chemical forms, PLA can be synthesized under three combinations (LL (L-lactide), DD (D-lactide) or LD (meso)) [28]. The most commonly chemical form used for the stretching processes, leading to a semi-crystalline polymer, is a

blend containing a majority of L-lactide (around 93%) and a minority of D-lactide. The ratio between the two determines the molecular architecture and has an influence on the stability, the crystallinity and the mechanical properties of the final material [29]. Even if the intrinsic properties depend on the proportion of each stereoisomer, PLA is known to have lower glass transition temperature (around 10 °C lower) and elastic modulus than PET. Indeed, its chemical formula does not exhibit an aromatic cycle that provides rigidity to the molecule. PLA is also known to have longer chains and a denser entanglement network [30]. The O₂ and CO₂ barrier properties of PLA and PET are similar [29]. Under uniaxial and biaxial stretching, depending on the temperature and the strain rate applied as well as on its initial structure, PLA is able to develop SIC [30–34].

PLA has been found to be insufficient for bottles because of a lack of rigidity. However, this polymer is widely used in other fields such as biomedical, textile, agricultural films and drug delivery system [26]...

So, a new biobased material with properties at least equivalent to those existing in PET is wanted. With this constraint, a biobased polymer, poly(ethylene 2,5-furandicarboxylate) named PEF, is seriously evocated nowadays.

5. Comparison of PEF and PET properties

Indeed, PEF is considered as the PET furan-derived chemical analogue. PEF repeating unit is presented in Figure 5. Amorphous PEF is also a transparent polymer [35]. PEF results from the chemical esterification process of 2,5-furandicarboxylic acid (FDCA) and bio-ethylene glycol [35–39]. Both reagents can be synthesized from biobased resources and lignocellulosic biomass. FDCA is obtained from controlled oxidation of 5-hydroxymethylfurfural (HMF), and HMF is synthesized from the triple oxidation of C₆ sugars, such as fructose or glucose [36,40]. PEF synthesis is relatively direct, and is well advanced as well as mastered by the Dutch company, Avantium Renewable Polymers [37,41]. To synthesize a molecule of PET that is 100% biobased, the terephthalic acid must be synthesized from the biomass too. But, on the contrary to FDCA synthesis, the obtention of TA from carbohydrates is complicated. Indeed, carbohydrates contain at most 6 carbons, while 8 carbons are needed to synthesize terephthalic acid. Thus, an additional step is needed [35,42].

Finally, the furan based molecules are very promising biobased platform molecules that can be obtained from non-food competitive carbohydrates, and thus that belong to the second generation of biobased materials. They are known since several years but, it is only recently that their synthesis has been optimized paving the way for possible industrialization. The development of a new catalytic process allows, by now, a large scale production [43]. The furan molecules are referred to as “sleeping giants” because of their enormous market potential, as it is attested by their presence in the list of the US Department of Energy that gathers the top 10 biobased products with high potential [43,44].

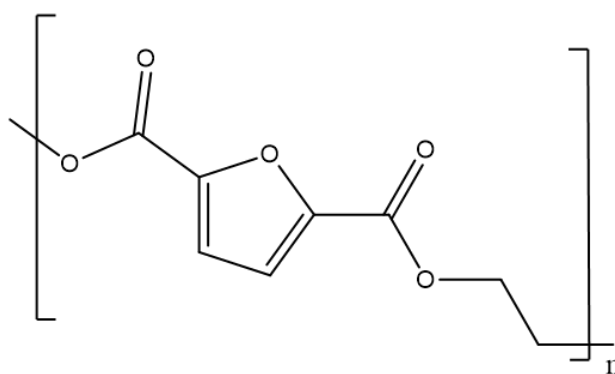


Figure 5. PEF repeating unit.

If Figure 1 and Figure 5 are compared, the existing difference between the PEF and PET repeating units is the presence of a furan ring with an oxygen atom, and its two non-binding electrons, instead of the benzene one. The furan ring is also composed of a smaller cycle with 4 carbons and one oxygen contrary to the 6 carbons found in the benzene ring. The PEF molecule is less linear compared to the PET one: an angle of 130° exists between the carbonyl and the furan ring, while it is of 180° between the phenyl group and the carbonyl. The head to tail distance between the carboxylic groups is also shorter in PEF compared to PET (4.83 \AA vs 5.73 \AA) [45]. The oxygen atom of the furan ring leads to a decrease in the aromaticity and of the orientation along the chain axis. As a result, the covalent strength along the chain is weaker but the polarizability of the polymer is higher. Thus, the dipolar interactions are favoured [36,37].

These structural disparities lead to specific chains motions for PEF in comparison with PET. Firstly, amorphous PEF has a higher rigidity compared to amorphous PET [46,47]. PEF is also known to have excellent barrier properties to gas or liquid, even superior to the PET ones. For amorphous PEF in comparison with amorphous PET, there is a reduction of the permeability by 11 for the dioxygen, by 19 for the carbon dioxide and by 2.8 for the water [48–52]. These

higher barrier properties are attributed to the restricted molecular motions of the furan ring, but also to the non-symmetric PEF chain [16,35,46,53–55]. Secondly, the glass transition temperature occurs at slightly higher temperature for PEF compared to PET (around 10 °C higher) [16,46]. Because of the geometry of the furan ring, the crystallization kinetic is also slower for PEF. The melting behaviour of PEF and PET has been reported to be different. PEF exhibits several melting endotherms, and melts at lower temperature compares to PET [53,55,56]. PET forms larger spherulites in relation to PEF, and the crystal growth rate of PEF is about one order of a magnitude slower than PET, and passes through a maximum at 165 °C [16,37,53,57].

All the previously mentioned works are mainly focused on the study of the amorphous and the static crystallized PEF, but they let supposed that PEF could be a good substitute to PET for packaging products. But to start an industrial campaign of bottles forming, the stretching behaviour of PEF must be deeper explored and put in relation with the stretching behaviour of PET.

6. Project and scientific strategy

This is with the need of a more mechanical approach that this thesis project has arisen. The major aim is to study the behaviour of PEF, during uniaxial and biaxial stretching tests that are close to what can happen in the industry during bottles forming. When this project has been built, in 2017, there was no real existence of works concerning the mechanical behaviour of PEF. Then, few papers have been published, but the stretching conditions were not optimal to induce SIC in PEF and most of the time, the direct comparison with PET was missing [58–62]. In this vein, the will of make a deep complementary mechanical and microstructural work on both polymer is legitim.

Thus, this project is an European wide collaboration between the academic world and the one of the industry, as visible in Figure 6. PEF and PET are studied in the same time and in parallel. By this way the experimental scattering induced by different executor is widely limited.

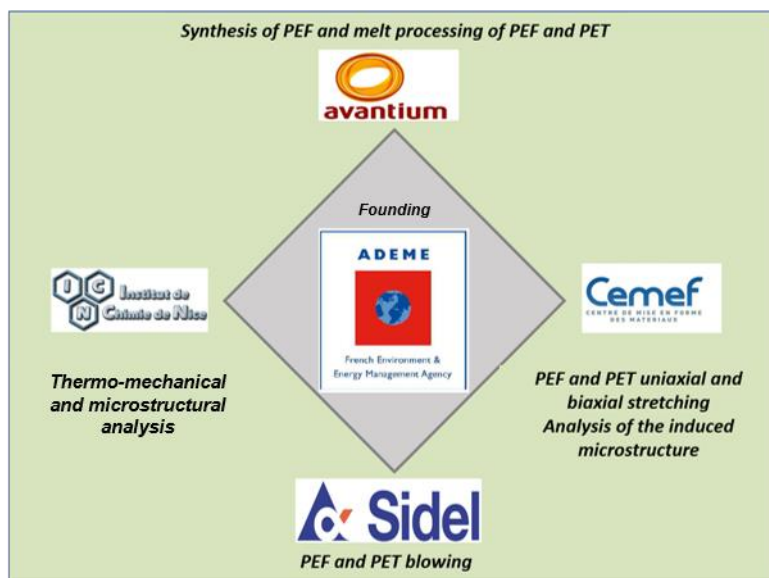


Figure 6. Partners of the scientific project.

Moreover, it is a real meet between the knowledge acquired on PET (CEMEF and Sidel) and on PEF (ICN and Avantium). According to the environmental scope of this research, the French agency of the environment (ADEME) has chosen to fund and to follow this work.

With the previously established level of knowledge, many questions are still looking for answer: is it possible to stretch PEF and to induce a similar microstructure as the one existing in PET when SIC occurs? Can PEF be blown in bottles? Is the induced microstructure stable and does it respond to the requirement specification of bottles? Under stretching, how is modified the PEF microstructure ? And so many others...

To try to respond to that,

Chapter 1 introduces briefly the materials as well as the several techniques and protocol used.

Chapter 2 presents the uniaxial stretching behaviour of PEF and PET. The stretching protocol, as well as the thermo-mechanical behaviour is explained for both materials. Several stretching conditions are used and the mechanical comparison between PEF and PET is established.

Chapter 3 is focused on the PEF crystal characterization, as well as on the study of the conformational changes that occurred during stretching. The comparison with PET and with samples that have been crystallized under static conditions is made. On the other side, **Chapter 4**, aims at understanding the formation of SIC, step by step, for PEF and PET.

Chapter 5 aims at analysing the PEF and PET uniaxially stretched samples that are presented in **Chapter 2**, in order to understand the influence, or not, of the stretching settings on the microstructural development.

Finally, **Chapter 6** describes the biaxial stretching behaviour of PEF. The microstructure, as well as the thermal and mechanical properties of the stretched samples are analysed.

Chapter 1

Description of the materials, techniques and protocols used

Table of contents

1. Introduction.....	17
2. Materials.....	17
3. Differential Scanning Calorimetry (DSC)	18
4. Dynamic Mechanical and Thermal Analysis (DMTA).....	19
5. Thermal deformation	19
6. X-ray scattering.....	20
7. Determination of the Miller's indices.....	21
8. FT-IR measurements.....	21
9. Stretching	22
9.1 Arm displacement	22
9.2 Thermal measurement.....	23
9.3 Optical measurement and relevance of the 2D analysis.....	25

Chapitre 1

Matériels et Méthodes

Ce chapitre décrit, dans un premier temps, les caractéristiques physico-chimiques des deux matériaux utilisés dans cette étude : le PEF et le PET. Les masses molaires ainsi que les viscosités intrinsèques sont données. Les valeurs de polydispersité apparaissent relativement similaires. Le protocole de sélection et de stockage des matériaux est expliqué.

Dans un second temps, les techniques d'analyse sont présentées. Pour caractériser les transitions physico-chimiques des matériaux, des cycles de chauffe, de refroidissement ou des isothermes sont réalisés grâce à une mesure DSC. De ce fait, les phénomènes endothermiques (transition vitreuse, fusion) ou exothermiques (cristallisation, réaction chimique) sont observables. Différentes vitesses de chauffe ou de refroidissement sont appliquées. Le calcul du taux de cristallinité, induit par l'étirage ou par cristallisation statique, ainsi que le modèle à trois phases proposé par Androsch et al. sont détaillés [63]. Ainsi, les quantités de RAF et de MAF de chaque échantillon pourront être connues. Le comportement viscoélastique des matériaux est caractérisé à l'aide d'une mesure DMTA. De ce fait, la dépendance à la fréquence et à la température des différentes transitions est étudiée. La relaxation principale, nommée relaxation α , ainsi que la relaxation secondaire, nommée relaxation β , sont analysées.

Par la suite les méthodes de caractérisation microstructurale telles que la diffraction des rayons X et la spectroscopie infrarouge sont détaillées, et ont pour but de respectivement caractériser la phase cristalline induite par l'étirage, ainsi que de relier les changements conformationnels observés à une phase cristalline ou amorphe, voire à une phase amorphe orientée. L'influence de l'étirage sur le niveau de contrainte des groupes chimiques est également déduite des mesures infrarouges. Le protocole mis en place pour associer les indices de Miller, (hkl), aux familles de plans observées en diffraction des rayons X est expliqué.

Pour finir, la machine d'étirage est présentée et le protocole de mesure thermique mis en place est détaillé. Le temps de préchauffe, de 300 s, des éprouvettes avant étirage est démontré grâce à des mesures isothermes, à l'aide d'un thermocouple, sur un échantillon non étiré et peint. La comparaison entre une analyse par corrélation d'images du champ de déformation en 2D (une caméra) ou en 3D (2 caméras) est menée pour justifier le choix, dans la suite du manuscrit, d'avoir utilisé la corrélation 2D.

1. Introduction

This chapter aims at firstly introducing the materials used in terms of molecular characteristics and then, at explaining the techniques of characterization applied (DSC, DMTA). The methods to analyse the crystal (X-ray scattering) and the conformations (FT-IR) are explained too. Finally, the stretching device is presented.

2. Materials

PEF is synthesized from the direct esterification and melt- solid state polycondensation (SSP) of EG and FDCA, both produced by Avantium Renewable Polymers. PET is an industrial grade (RamaPET N180® from Indorama) classically used for bottle application. Following the state of the art, the intrinsic viscosity of PET was chosen a little lower than the one of PEF [64]. Extruded sheets with a thickness close to 700 μm are provided. Typical molecular weights (M_n , M_w), polydispersities (M_w/M_n) and intrinsic viscosities (IV) after the extrusion are reported in Table 1. The measurements are made by GPC, using PMMA standards.

	M_n (g.mol ⁻¹)	M_w (g.mol ⁻¹)	Polydispersity	IV (dL.g ⁻¹)
PEF	49 000	123 000	2.5	0.94
PET	28 000	64 000	2.3	0.80

Table 1. Materials characteristics after the extrusion.

In order to minimize the thickness variation in the specimens, the samples are tooled in the extrusion direction. The extrusions are performed according to state of the art, after drying to avoid hydrolysis and degradation.

Only one unique extrusion campaign was performed. Then, the materials have been cut into several rectangular sheets and stored under vacuum in aluminium coated bags, in the freezer (-18 °C), to limit water absorption and physical aging. Consequently, the materials are tested dry as processed, without any pre-conditioning. The water content in PEF was estimated on a C30 – Coulometric Karl Fisher Titrator from Mettler Toledo, and is about 1400 ppm.

For the samples crystallized in static conditions, PEF and PET have been crystallized during 2h, in an oven, at respectively 160 °C and 120 °C.

3. Differential Scanning Calorimetry (DSC)

DSC is a thermal analysis technique that allows the characterization of the chemical and physical transitions. DSC method measures the difference of heat flow between two pans during a thermal program. One pan, named “reference”, is empty while the second one contains the sample. Thus, endothermic (glass transition, melting, aging) and exothermic (crystallization, chemical reaction) phenomena are observable.

DSC measurements are performed on a Mettler Toledo DSC 1 equipped with the STAR® software. Aluminium pans of 40 µL are used. The samples weight is of approximately 3 mg in any case, except for some stretched samples for which this weight was difficult to be obtained while ensuring a correct thermal conduction between the pan and the sample. In fact, after biaxial stretching, the samples are really thin and their weight is lower than 1 mg.

From their glassy state the samples have been submitted to isothermal programs of various temperatures (between 90 °C and 180 °C) and durations (between 1800 s and 12000 s), or to a heating scan from 25 °C to 300 °C performed at 1 °C/min, 10 °C/min or 20 °C/min.

A three phases model has been proposed for the semi-crystalline samples [63]. This model is composed of the crystal, close to it there is the presence of a constrained amorphous domain, named RAF (rigid amorphous fraction), and further from the crystal a free amorphous domain, named MAF (mobile amorphous fraction). For an amorphous sample, as no crystallization has occurred, it is supposed that there is the presence of MAF only (100% MAF).

The crystal ratio (χ_c), the rigid (RAF) and the mobile (MAF) amorphous fractions (χ_{RAF} and χ_{MAF}) are calculated according to the following equations (Equations 1 to 3), thanks to DSC measurements.

$$\chi_c = \frac{\Delta H_m - |\Delta H_c|}{\Delta H_m^0} \quad (1)$$

with ΔH_m the melting enthalpy (J.g⁻¹), ΔH_c the cold crystallization enthalpy (J.g⁻¹), and ΔH_m^0 the equilibrium melting enthalpy, taken at 140 J.g⁻¹ for PEF and PET [16,55,60].

$$\chi_{MAF} = \frac{\Delta C_p}{\Delta C_p^0} \quad (2)$$

with ΔC_p ($\text{J}\cdot\text{g}^{-1}\cdot\text{K}^{-1}$) the heat capacity variation at the glass transition, and ΔC_p^0 ($\text{J}\cdot\text{g}^{-1}\cdot\text{K}^{-1}$) the heat capacity variation of a fully amorphous sample.

$$\chi_{RAF} = 1 - \chi_c - \chi_{MAF} \quad (3)$$

4. Dynamic Mechanical and Thermal Analysis (DMTA)

All the DMTA experiments are conducted in tension mode using a Mettler-Toledo[®] DMA 1. Thanks to DMTA analysis, the viscoelastic behaviour of a material as a function of the time, the frequency, or the temperature can be studied. Thus, the elastic modulus (E') and the loss modulus (E'') values can be extracted, as well as the ratio between them, the damping factor ($\tan \delta$). Two transitions have been studied: the main viscoelastic relaxation, T_α , and the sub-glassy transition, T_β . These two temperatures are identified as the maximum of the $\tan \delta$ peak, for a given frequency (generally 1 Hz). The stretched samples are taken off in the middle of the process zone. The dimensions of the samples are $5 \times 4 \times 0.7 \text{ mm}^3$ for amorphous samples, around $5 \times 3 \times 0.3 \text{ mm}^3$ for the uniaxially stretched samples (depending on the total strain imposed) and of $5 \times 10 \times 0.04 \text{ mm}^3$ for the biaxially stretched samples. At the beginning of each test, the samples undergo a preload of 1 N. The temperature scans are performed from $-125 \text{ }^\circ\text{C}$ to $+200 \text{ }^\circ\text{C}$, at a heating rate of $1 \text{ }^\circ\text{C}/\text{min}$, with a displacement amplitude of $5 \text{ }\mu\text{m}$ (i.e. strain of 0.1 %), in the auto-tension mode. The linearity of the behaviour was checked prior to all tests. The temperature scans are carried out with a frequency of 1 Hz.

5. Thermal deformation

The auto tension mode in DMTA is designed to accommodate evolution of the sample length that can result of thermal dilatation or contraction. By measuring this evolution in length (ΔL), it is possible to calculate the thermal deformation, over a temperature scan (Equation 4).

$$Deformation (\%) = \frac{\Delta L}{L_0} * 100 \quad (4)$$

with L_0 the initial sample length.

6. X-ray scattering

To analyse the organized phase, wide-angle X-ray scattering (WAXS) experiments are conducted. WAXS measurement allows to get data concerning the periodicity of the crystal (nature and orientation of the crystalline phase). The process zone of the tensile samples, where the mechanical behaviour is also analysed, is the zone where the microstructural characterizations are performed.

Firstly, in order to address the possible crystalline orientation, 2D Debye-Scherrer patterns using the flat-film camera technique under vacuum at ambient temperature are recorded. To detect a wider range of crystal lattice planes, two sample-screen distances, OE in Figure 7, are chosen (75 mm and 30 mm). The exposure time is kept constant at 45 minutes.

1D scans, $I(2\theta)$, are also carried out at room temperature, in transmission mode (from 5 ° or 10 ° to 50 °), using a diffractometer Philips X'Pert PRO supplied by Panalytical. Azimuthal scans, $I(\varphi)$, for a constant diffraction angle, θ , are conducted on the same device.

In the two cases, the $CuK\alpha$ radiation ($\lambda^{CuK\alpha} = 1.54 \text{ \AA}$) is used. As experiments are performed in transmission, the scan intensities are normalised by the sample thickness.

In the Chapter 5 (and for some samples in the Chapter 6), as many stretching conditions are compared, an intensity ratio is defined (Equation 5) to account for the baseline difference:

$$I_{ratio} = \frac{I - I_{min}}{I_{max} - I_{min}} \quad (5)$$

with I_{ratio} the intensity ratio, I_{min} and I_{max} the minimum and maximum intensities on the given scan.

Some scans (specially for biaxial stretching Chapter 6) are also conducted in reflexion mode from 10 ° to 55 °.

7. Determination of the Miller's indices

As all the angular positions, 2θ , of the diffraction peaks are not yet indexed for PEF, a specific protocol is developed to extract the Miller indices, (hkl) , of the diffracting planes from scattering patterns.

Firstly, the distance between the diffracted spot and the centre of the film, OR , is measured. Then, the angular position of the spot, θ , can be determined. Figure 7 represents the situation. N_{hkl} is the normal to the diffracting plane.

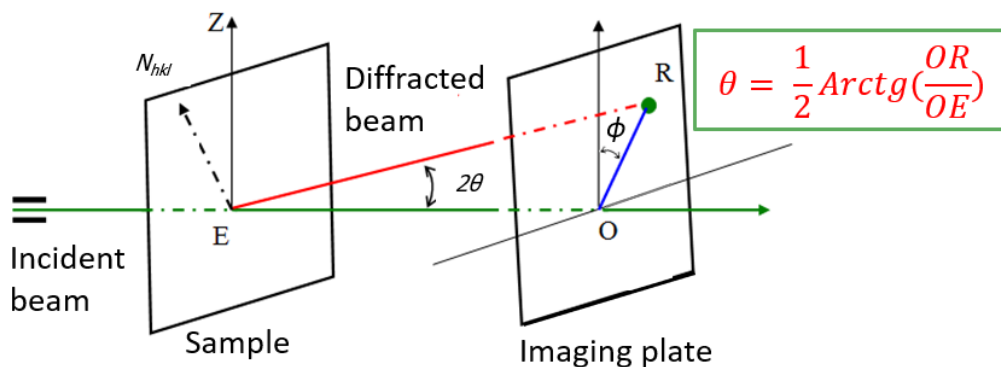


Figure 7. X ray diffracted beam and geometry associated with Bragg's law, in transmission mode [65].

In a second time, an azimuthal scan from 0 to 360° is performed for each angular position (2θ) found, to estimate the angular position ϕ associated to the maximal intensity of this angular position. By this way, all the diffracted spots are referred in terms of (2θ) and (ϕ) angles.

Once the positions of all the dots are identified, and assuming the monoclinic crystalline structure proposed by Mao et al. [58], the diffraction spots can be associated to the crystallographic planes, using the commercial software CaRIne® [65].

8. FT-IR measurements

The microstructure is analysed by Fourier Transform-Infrared Spectroscopy (FT-IR), between 4000 cm^{-1} and 600 cm^{-1} with a Bruker TENSOR 27® spectrophotometer in ATR (absorbance mode), using a diamond crystal. The number of cumulated scans is of 64 and the resolution is of 4 cm^{-1} . In this work, the use of the infrared spectroscopy aims at determining the influence

of the stretching on the conformations of the several constitutive groups, and also at examining if the stretching makes these groups more or less constrained compared to an amorphous sample.

For convenience, the scans are normalized by the maximum of the spectra. In PEF, the band at 1216 cm^{-1} , associated to the ester groups of amorphous sample is used; while in PET the band at 723 cm^{-1} (bending of the benzene ring measured after static crystallisation [66]) is preferred [67].

IR absorption is due to the differences of vibrational energies (E), between the fundamental state and the first excited state, that correspond to the stretching or to the deformation vibrations of the functional groups in the repeating unit. They are associated to specific wave numbers (that are the reciprocal of the wave length), $\bar{\nu}$. Equation 6 shows the link between E and $\bar{\nu}$.

$$E = h c \bar{\nu} \quad (6)$$

where h is the Planck constant and c the light celerity.

9. Stretching

9.1 Arm displacement

The stretching device is composed of four independent motor-driven arms, each of them coupled to a displacement sensor and a 500 N force transducer. For uniaxial stretching, only two arms are involved; while all the arms are used for the biaxial stretching. The arm displacement can be controlled thanks to velocity, position or force regulations.

It has been chosen to control the arms displacement with an exponential velocity. An example of the arms displacement is presented in Figure 8.a. The associated force increase is in Figure 8.b.

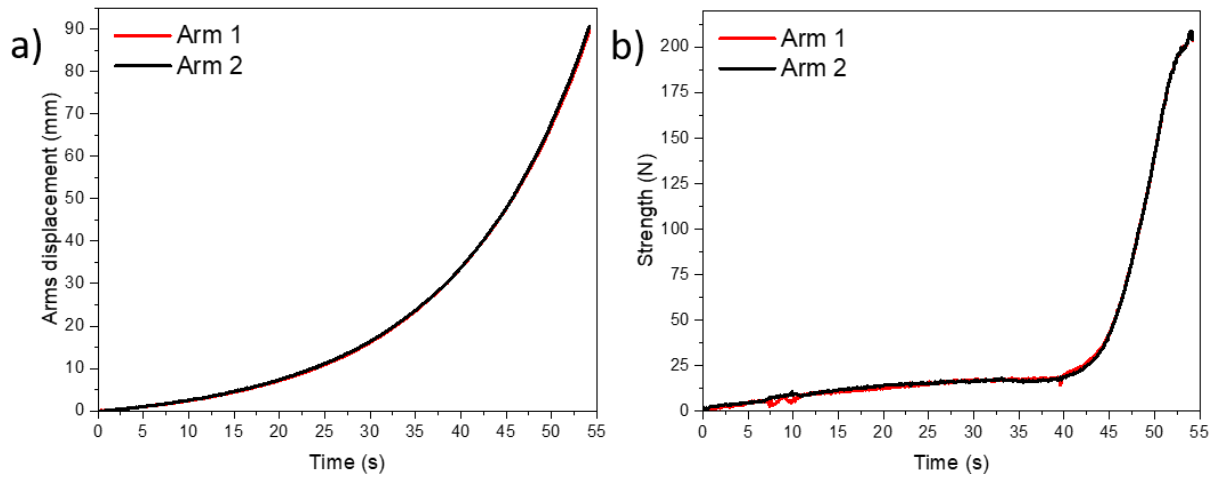


Figure 8. (a) Displacement and (b) force evolution with the time of each arm during an uniaxial stretching test performed with a strain rate of 0.035 s^{-1} and a temperature of $101 \text{ }^{\circ}\text{C}$, for PEF.

These two graphs testify that the strength and the displacement applied by the two arms used for the uniaxial stretching are the same. It is supposed to lead to a relatively uniform stretching of the samples. The displacement of the arms represents perfectly an exponential variation.

9.2 Thermal measurement

The sample can be heated and after the stretching annealed or quenched with several mobile ovens. As presented in Figure 9, a window of zinc selenide (ZnSe), which is partially transparent to infrared radiations, allows to measure the temperature at the surface of the specimen during the tests, with an IR pyrometer. The local optical measurement is performed in the centre of the specimen process zone.

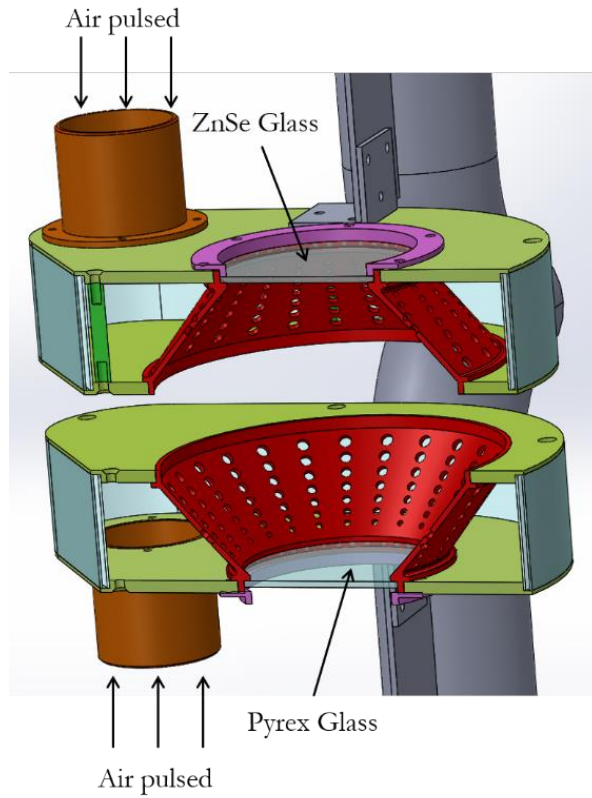


Figure 9. Schematic representation of the oven.

Different isothermal calibration protocols have been imposed, in static conditions, within the forming ranges. They are drawn in Figure 10.a and Figure 10.b, for respectively PEF and PET.

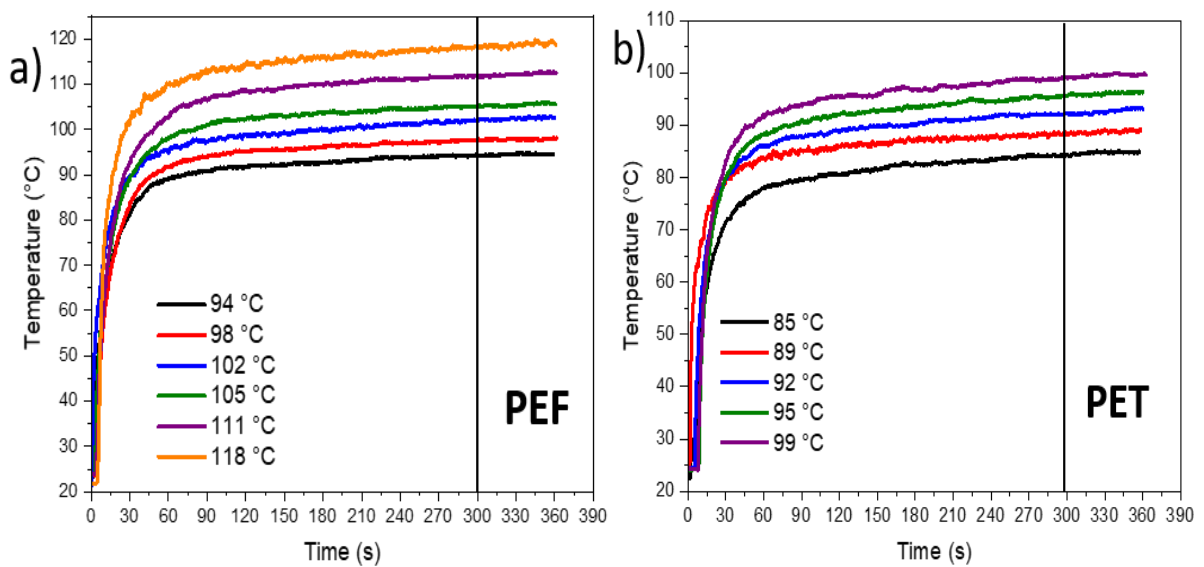


Figure 10. Isotherm curves obtained for (a) PEF and (b) PET painted samples heated during around 360 s.

During these protocols, the temperature is obtained by using a thermocouple welded in the specimen core. To be as close as possible of the stretching tests, the temperature has been recorded on non-stretched samples that have been painted with a speckle. One has to keep in mind that upon stretching, the emissivity of the painting can evolve in an uncontrolled way because of its own stretching. Thus, a slight uncertainty of measurement can exist on the temperature registration, during the stretching. However, on the previous curves, the temperature seems to remain moderately stable from 120 s. To be sure to have a relative homogeneity on the entire material (not only on the surface, but in the core also), it has been chosen to heat the sample during 300 s before the beginning of the test. It is visible, that after 300 s, only an increase of 1 °C is visible on the samples temperatures.

9.3 Optical measurement and relevance of the 2D analysis

The oven is composed of another window of borosilicate glass (Pyrex glass in Figure 9) that allows to perform local measurements of strain fields using DIC2D (2D Digital Image Correlation) on painted speckle. It was shown that adding a painted speckle, of a thickness of around 40 μm , did not impact the force measurement nor the heating, or the cooling rates. The painting is removed before the post-stretching microstructural analysis.

Let's discuss of the relevance of the 2D analysis compared to the 3D analysis.

To address full 3D strain field in tension, one would have to perform measurements on the front and, on the side faces of the sample, for example using two stereo correlation devices [68]. In this study, the thickness is much too low to ensure an accurate measurement on the side face. So, the transverse isotropy is assumed and the analysis of strain field is restrained to the front side. Nevertheless, a comparison between the use of a stereo correlation device (with two cameras and DIC3D) and a single camera device (using DIC2D) has been conducted. In the former case, the out of plane displacements that result from necking, film movements or curvature due to induced anisotropy could be accounted for.

Figure 11 represents the out of plane displacements, measured with DIC3D. Seemingly, these displacements result first from thickening of the film.

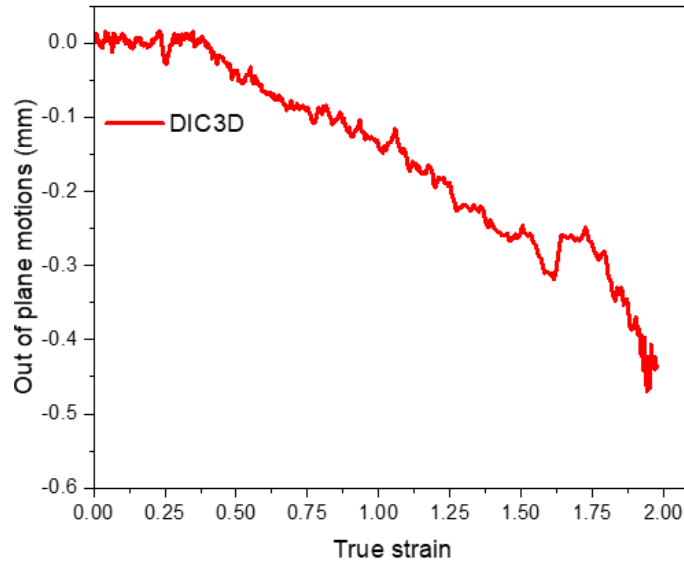


Figure 11. Evolution of the out of plane motions measured with DIC3D.

However, DIC3D is difficult to set up because of ergonomic constraints on the tensile machine. Figures 12.a and 12.b depict the error induced by the simplification of the analysis (DIC2D) compared to stereo correlation (DIC3D).

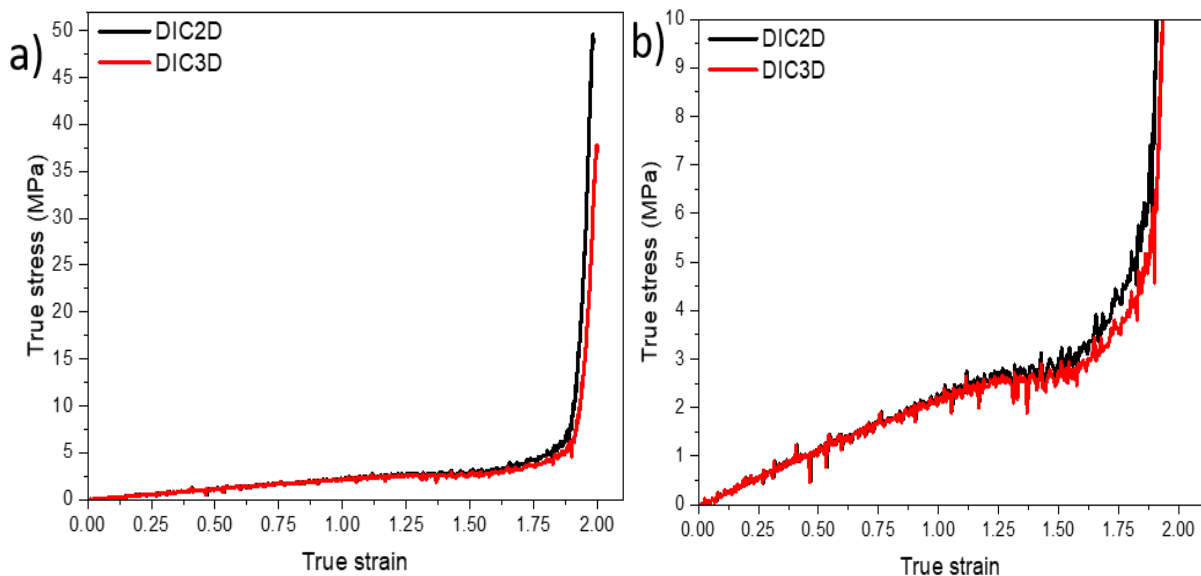


Figure 12. True stress/strain curves of PEF stretched with a strain rate of 0.037 s^{-1} at a temperature of $105 \text{ }^\circ\text{C}$ (a) analyzed with DIC2D and DIC3D; (b) a zoom on the first stages of the deformation is added.

The curves drawn with DIC2D and DIC3D are relatively close. With DIC2D, the stress can be slightly overestimated, specially at the initiation of the strain hardening (Figure 12). At that

moment, the out of plane displacement (Figure 11) decreases more rapidly. Additionally, the main concern of this work is the behaviour prior to crystallization, for which both the two technics are equivalent.

The relative volume variation of the sample can be calculated during the stretching, according to the Equation 7. This calculation informs on the gap from the incompressibility.

$$\frac{\Delta V}{V_0} = \exp\left(\varepsilon_{xx}(t) + \varepsilon_{yy}(t) + \varepsilon_{zz}(t)\right) - 1 \quad (7)$$

with $\Delta V/V_0$ the relative volume variation, ε_{xx} , ε_{yy} , and ε_{zz} the true strains in the three directions.

The comparison of this measurement between DIC2D and DIC3D is represented in Figure 13.

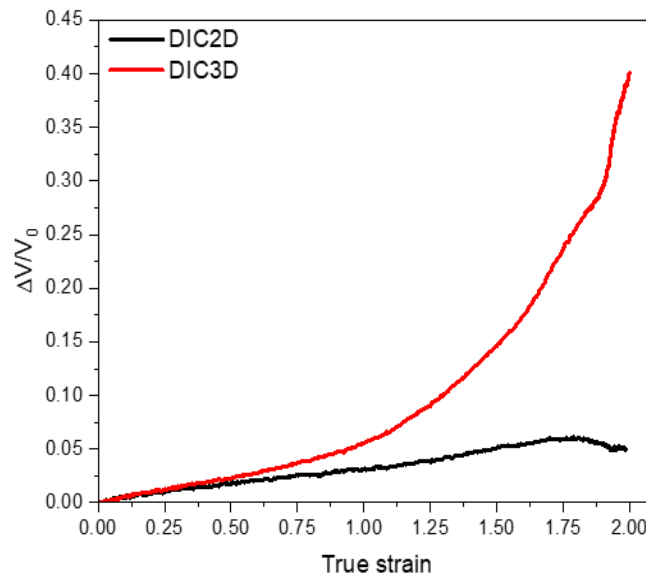


Figure 13. Evolution of the relative volume variation during the stretching.

As the out of planes displacement are not taken into account with DIC2D, the volume change is slightly underestimated (Figure 13).

Nevertheless, as the mechanical curves obtained with DIC2D and DIC3D are relatively close, the use of stereo correlation will be avoided.

Chapter 2

Uniaxial stretching of PEF and PET

Table of contents

1. Introduction.....	32
2. Experimental protocol.....	32
2.1 Determination of the forming range.....	32
2.2 Static crystallization.....	34
2.3 Master curve building.....	37
2.4 Samples geometry and calculation of the stress.....	40
3. Definition of the uniaxial stretching conditions.....	42
3.1 Selection of the couples strain rate / temperature.....	42
3.2 Evolution of the strain during the tests.....	44
3.3 Determination of the experimental parameters.....	46
4. Mechanical behaviour.....	53
5. Conclusions.....	60
6. Annexes.....	61

Chapitre 2

Étirage uniaxial du PEF et du PET

Ce chapitre expose et compare le comportement mécanique du PEF et du PET lors d'étirages uniaxiaux réalisés avec plusieurs couples vitesse/température. Le protocole mis en place avant l'étirage est détaillé. La gamme de formage propre à chacun des matériaux est trouvée et située entre la relaxation α et la cristallisation statique : elle correspond au plateau caoutchoutique. Cette gamme de formage apparaît à plus basse température et est plus étroite pour le PET que pour le PEF. Les mêmes paramètres d'étirage ne peuvent donc pas être appliqués à ces deux matériaux. En DSC, des mesures isothermes, à différentes températures dans cette gamme, sont réalisées pour vérifier l'état amorphe, donc l'absence de cristallisation froide, du matériau avant et pendant l'étirage. On obtient ainsi une estimation du temps nécessaire pour cristalliser statiquement selon la température. Les conditions d'étirage sont choisies en fonction de ces paramètres.

La dépendance à la vitesse et à la température est représentée, pour chaque matériau, grâce à la construction de courbes maîtresses à une température de référence proche de celle de la transition α . La différence de température de transition α entre le PEF et le PET est ainsi prise en compte. Cette courbe permet d'avoir une estimation de l'état physique du matériau avant étirage et donc, de l'étirer avec des couples vitesse/température adéquats. Les matériaux peuvent donc être comparés pour des états physiques similaires. La courbe maîtresse sert de point de départ pour définir la campagne d'étirage.

Sur la courbe maîtresse, différentes localisations le long du plateau caoutchoutique (appelées vitesses de déformations équivalentes) ont été sélectionnées, ainsi que plusieurs couples temps/température. Pour une position donnée sur le plateau caoutchoutique, deux couples temps/température sont choisis : un couple appelé « lent » et un autre appelé « rapide » (vitesse de déformation supérieure d'environ une décade et température plus élevée que pour le test « lent »). Ceci a pour but de tester la validité de l'équivalence temps/température et donc, de pouvoir ensuite transposer les résultats vers l'industrie, qui utilise des vitesses plus rapides et des températures plus élevées. Pour une même position sur le plateau caoutchoutique, peu importe les couples temps/température appliqués, la réponse mécanique est supposée être

identique. Grâce au protocole expérimental mis en place, la vitesse de déformation, la température et la vitesse de déformation équivalente sont suivies durant la totalité de l'essai. Il est donc possible de connaître à tout moment de l'étirage l'état physique du matériau. Il a été observé que l'évolution de la température et de la vitesse de déformation pendant l'essai de traction restait assez faible. Les tests mécaniques peuvent donc être considérés comme relativement bien contrôlés.

La gamme de formage des deux matériaux a été largement explorée. Pour une vitesse de déformation donnée, les deux couples vitesse/température (« lent » et « rapide ») conduisent à la même réponse mécanique. L'équivalence temps/température est donc validée. Les résultats obtenus sont alors transposables à l'industrie. Pour toutes les conditions d'étirage, un important durcissement structural est observé. Ce durcissement semble plus abrupt pour le PEF que pour le PET. L'apparition du NDR est dépendante de la localisation du test sur la courbe maîtresse et augmente avec l'état caoutchoutique du matériau. Les NDRs apparaissent toujours plus tardivement pour le PEF que pour le PET, et ce, également pour des états physiques initiaux proches. Les tests réalisés conduisent également au développement d'une phase cristalline.

Le comportement mécanique du PEF et du PET semble très proche, surtout dans les premières étapes de la déformation. Cela confirme la grande ressemblance entre ces deux matériaux, et surtout la pertinence d'un étirage qui prend en compte leur état physique plutôt qu'un étirage réalisé avec les mêmes paramètres : l'étirage est contrôlé par l'écart à la transition α . La nécessité d'utiliser une courbe maîtresse est indéniablement confirmée. Pour obtenir le même comportement mécanique, jusqu'au NDR, une décade de différence doit exister entre la vitesse de déformation équivalente du PET et celle du PEF.

1. Introduction

The aim of this chapter is to assess of the stretch ability of PEF, in comparison to the PET one. The stretching is ruled to observe the strain hardening apparition, and to develop strain induced crystallization (SIC), in both materials. The strain hardening onset is defined by the natural draw ratio, NDR. PET stretching and SIC have been widely described in the literature [69–82], while works concerning PEF are rarer [58–61]. In these previous works dealing with the SIC of PEF, the mechanical tests were not well-controlled, in terms of mechanical paths, and the induced microstructure had a low definition and perfection.

In PET, SIC is progressively developed [75,77,78,81,83]. It is supposed that, before the crystal apparition, there is the existence of an intermediate phase, named mesophase. This oriented and organized phase acts as a crystal precursor [75,77,84–90]. The stable crystal, with all its symmetries and periodicities, needs a relaxation step to appear, and is formed after the stretching end [91]. The mesophase is formed from the stretching beginning [84,86,87,92]. Thus, the microstructure obtained is directly dependent on the stretching settings, and specially on the post-stretching treatment. In PEF, at this stage, the presence of a mesophase prior to crystallization is evocated [61].

In this work, a more accurate analysis of the mechanical behaviour, based on local measurements (strain, strain rate and temperature) and a better control of actual strain rates, is claimed. To find the relevant stretching conditions, a specific protocol has been developed and applied on PEF and PET. This protocol is firstly detailed. Then, the selection of several mechanical settings is presented, and finally, the mechanical behaviour of both materials is analysed.

2. Experimental protocol

2.1 Determination of the forming range

To perform efficient stretching on PEF and on PET, an original protocol has been established. First of all, the stretching range must be found for each material.

To fit with the industrial protocol, the stretching has to be performed at intermediate temperatures. It means above the α -relaxation temperature, to allow chains mobility, but below the static crystallization occurrence, to only enforce strain induced crystallization. As for PET, PEF static crystallization induces a loss of formability and of transparency of the material, which is not in assessment with the industrial requirements. The forming range corresponds to the rubbery plateau of the materials.

To illustrate the available forming range, a temperature scan in DMTA, from 25 °C to 210 °C at 1 Hz and 1 °C/min, is performed for PEF and PET. It has been completed by a DSC measurement in almost the same conditions (from 30 °C to 250 °C at 1 °C/min). These two scans are presented in Figures 14.a and 14.b.

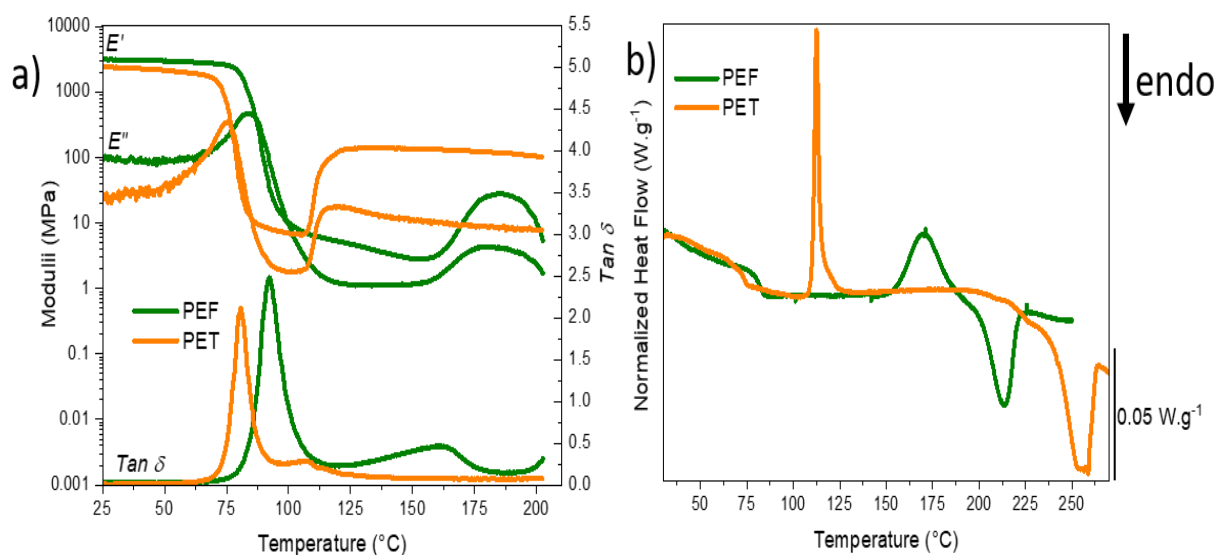


Figure 14. (a) Viscoelastic properties of amorphous PEF and PET, identified by DMTA, from 25 °C to 210 °C at 1 °C/min and with a frequency of 1 Hz; (b) Thermal behaviour of amorphous PEF and PET, measured by DSC, at 1 °C/min from 30 °C to 270 °C.

The low mobility of the chains and the complex interactions induced by the presence of the furan ring, in PEF, lead to a higher α -relaxation temperature (T_a), compared to PET [46,47]. The α -relaxation temperatures (Figure 14.a), taken at the maximum of the $Tan \delta$ peak, are respectively of 80 °C for PET and of 92 °C for PEF. In parallel, the peak of the cold crystallization (Figure 14.b) is detected for a temperature close to 110 °C for PET, and 160 °C for PEF.

The cold crystallization in PEF appears more difficult than in PET. It has to be related with the less stability of the former, as demonstrated by the occurrence of the melting right after the

static crystallization, at a significant lower melting temperature compared to PET. It proves two important differences between PEF and PET that must be considered for the stretching:

- PET forming range appears at lower temperature than PEF one;
- PEF exhibits a wider rubbery plateau compared to PET, and consequently a wider forming range.

It means that to perform efficient stretching in PEF, the same settings as those used in PET cannot be relevant. As it is visible in Figure 14.a, moduli in the rubbery plateaux are close for the two polymers.

2.2 Static crystallization

Before the stretching, the samples are heated during 5 min. Then, the stretching can be performed at slow or rapid strain rates. It is necessary to be sure that the materials will remain amorphous during the entire test. The crystallization temperature at 1 °C/min is not enough to define a forming range. Indeed, an estimate of the time to crystallize as a function of the temperature is needed. It allows to differentiate the sets temperature/maximum duration of test that are relevant or not.

The purpose here is not to design industrial blowing, but to help sorting lab tests. Firstly, the ovens used are not providing an IR heating, but a convection heating for which the efficiency is much lower. Secondly, in the lab, an uniform heating is required, whereas industrial blowing relies on thermal gradients. Thirdly, a stretching test performed with too rapid strain rate could induce a self-heating, which would disturb measurements. Hence, it is chosen to focus on tests performed at slower strain rate. Moreover, in this work, the reach of strains higher than the typical Hencky's strain, of 2.5 in PET, is needed [69,70,91,93]. All those observations contribute to a significant long time at the test temperature that increases the risk of static crystallization occurrence. Then, the key issue is to privilege slow strain rate at lower temperature, in a combination physically equivalent to the industrial conditions.

To assess heating times, the time needed to induce isothermal crystallization at temperatures included in the forming range has been measured by DSC, and is reported in Figures 15.a and 15.b, for respectively PEF and PET. After the isothermal crystallization, samples are quenched (50 °C/min) and then heated (20 °C/min) from 25 °C to 250 °C for PEF and from 25 °C to 270 °C for PET.

For PEF, it can be emphasized that a rapid heating ramp (20 °C/min) seems to not induce any cold crystallisation. On the other hand, PET can cold crystallize in that conditions. Nevertheless, the heating of the samples that have been submitted to isotherms (Figures 16.a and 16.b) allows to estimate whether crystallization has been developed (through the reduction of the cold crystallization enthalpy) or initiated (through the decreasing of the cold crystallization temperature).

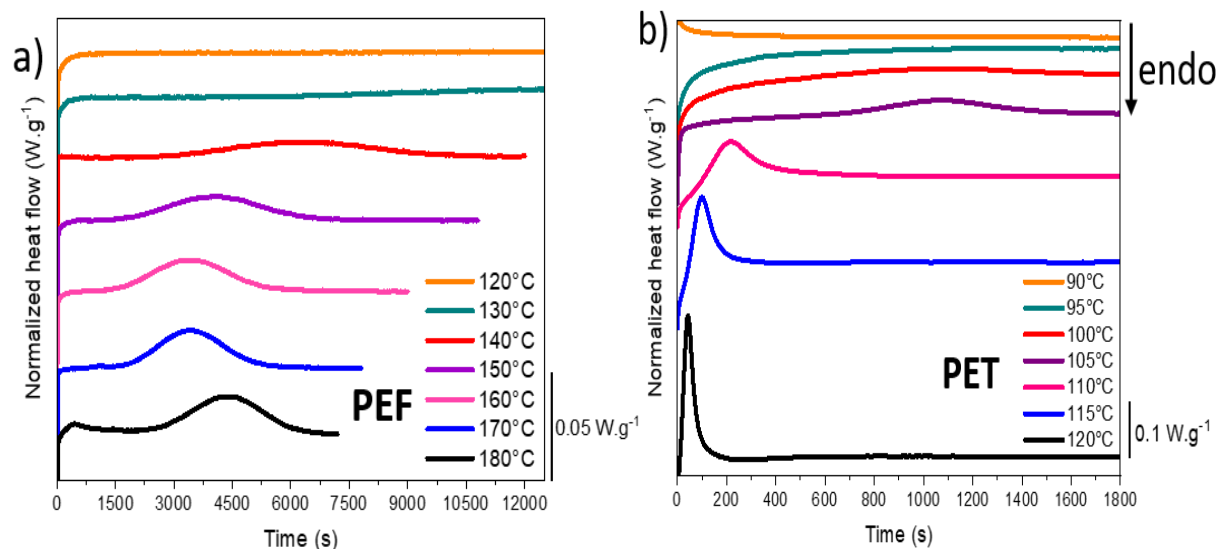


Figure 15. Isothermal scans of (a) PEF and (b) PET for several temperatures included in the stretching range, measured by DSC.

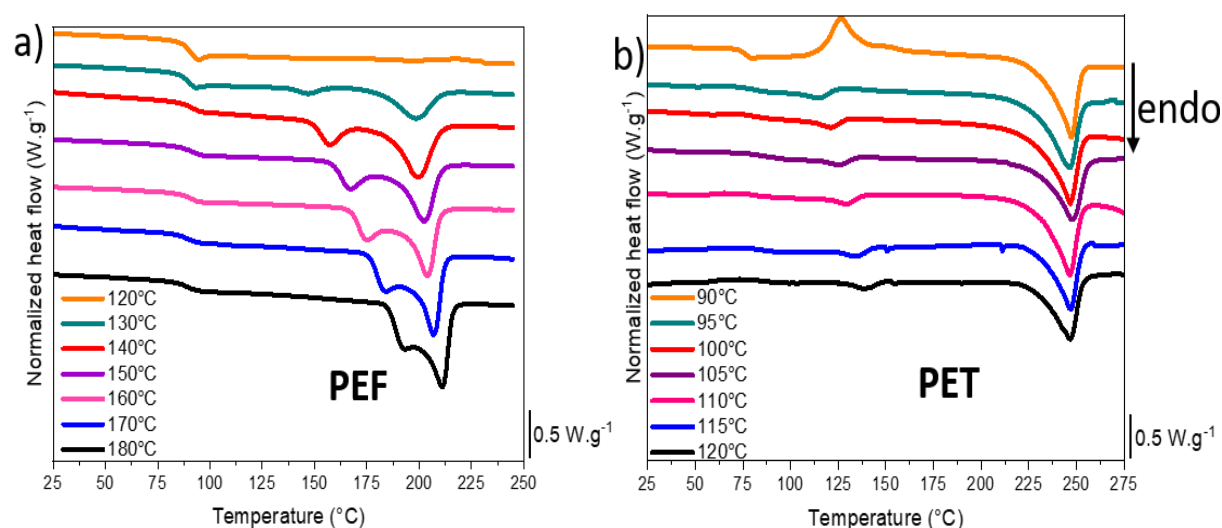


Figure 16. Heating scans, performed at 20 °C/min, of the previous isothermally crystallized samples for (a) PEF, from 25 °C to 250 °C, and (b) PET, from 25 °C from 275 °C, measured by DSC.

Concerning PEF, with this experimental protocol, there is no evidence of the occurrence of crystallisation below 130 °C during the isothermal steps over 12000 s (3 hours). At 130 °C, the crystallization peak is spread but visible. For higher temperatures, the static crystallization onset appears to be higher than 1500 s. It is significantly higher than the time needed for the stretching experiments. Looking at the heating traces afterward gives additional information. Up to the isotherm at 120 °C, the heating does not reveal neither cold crystallisation nor fusion. On the contrary, from 130 °C, the melting occurs which means that seemingly some nucleation can develop during the isotherms. In conclusion, the static crystallisation is negligible in PEF up to 120 °C, whatever the test durations are. From that limit, the crystallization could be firstly initiated during the heating step, and then developed during the tensile test.

PET behaves in a different way.

For the measurement realised at 105 °C, it is visible that the isothermal crystallisation is significant from 800 s. For the higher temperatures, the isothermal crystallisation occurs faster. PET is still amorphous after 1800 s at 90 °C, but semi crystalline after 1800 s at 95 °C (Figure 16.b). This was already pointed out in previous study [94], the static crystallisation of amorphous PET can be neglected up to 90 °C. From 90 °C to 105 °C, one has to be very rigorous in terms of duration of tests, as crystallisation can develop during the tests.

To be complete, the crystal ratios developed during the isotherms are of around 27 % for PEF, and 28 % for PET. It enlightens the fact that the two materials are only different in terms of kinetic. Because of the use of different heating ramps, it is not relevant to compare the glass transition temperature of the fully amorphous sample (heating performed at 1 °C/min, Figure 14.b) and the one of samples that have been crystallized in static conditions (heating performed at 20 °C/min, Figure 16).

Lastly, the melting behaviours are different between PEF and PET. After the isothermal crystallization, PET exhibits one unique melting temperature, while PEF melting appears to be multiple and sensitive to the crystallisation conditions. This trend has already been reported [16,47,53–55].

The stretching ranges, in terms of temperatures, are known for both materials. The strain rates must, by now, be adjusted and must be in adequation with these temperatures. The next part is going to explain how, depending on the material physical state, strain rate/temperature couples can be determined.

2.3 Master curve building

To define the stretching settings composed of couple strain rate/temperature, differences in α -relaxation temperature have to be accounted for. As the aim of this work is to compare the two polymers in an identical physical state, it is decided to not stretch the polymers at the same temperature and strain rate, but at a similar equivalent strain rate at a reference temperature chosen close to the respective glass transition temperature of the materials. As a result, master curves at a reference temperature are built up for PEF and PET. This approach has already been reported relevant for PEF [60], PET [91,95] or other materials [96–99].

The master curves are deduced from isothermal frequency scans, from 1 Hz to 100 Hz. The temperature step is of 5 °C, from 85 °C to 135 °C. Only an horizontal shift is applied. The typical PEF and PET master curves are given in Figure 17.

It has been chosen to realise a master curve, and to identify the associated parameters, at each time one sheet has been extracted from the storage to be used. It enables to account for both the initial variability and the potential aging. Therefore, the master curves correspond always to the given piece of material used.

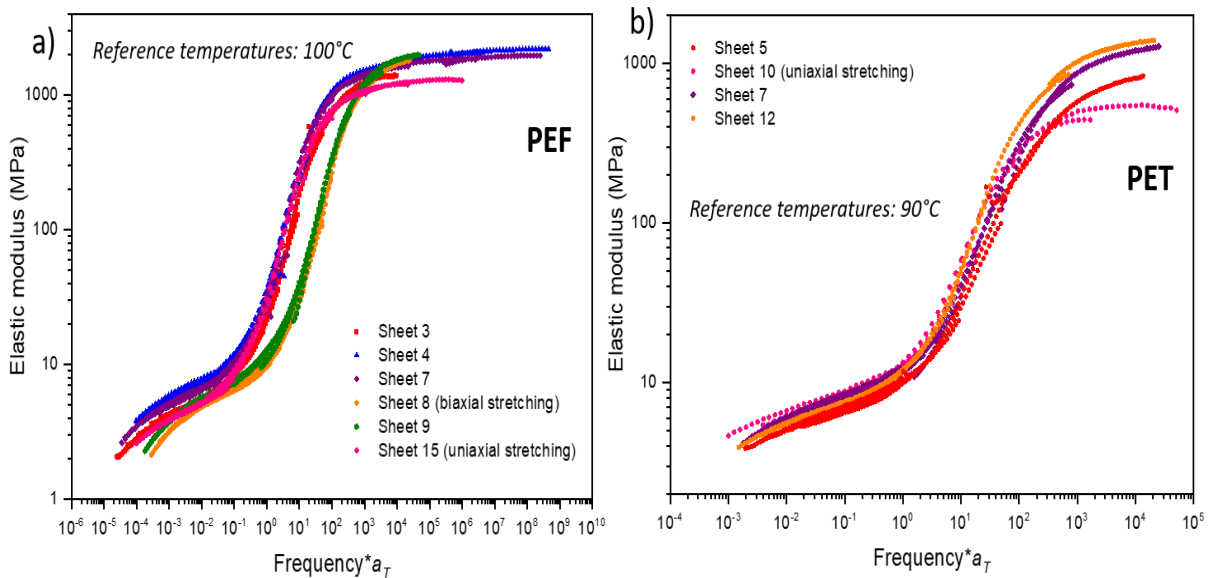


Figure 17. Visualization of the master curves dispersion existing between the several extruded sheets for (a) PEF and (b) PET.

The previous graphs confirm that some disparities can exist between the sheets, with the extrusion and with the time. Despite the storage protocol established, the sheets can change

slightly between the beginning of this thesis and its end (3 years). It is visible, for example, in PEF on the green (sheet 9) and orange (sheet 8) curves. They are related to the sheets opened during the last Ph.D year, contrary to the others that have been used during the first two years. However, thanks to the master curve building these small disparities can be taken into account in the several tests performed.

WLF equation is used to calculate the shift factor values (Equation 8) [100].

$$\log(a_T) = \frac{-C_1^0(T - T_{ref})}{C_2^0 + (T - T_{ref})} \quad (8)$$

with a_T the shift factor, C_1^0 and C_2^0 ($^{\circ}\text{C}$) the viscoelastic coefficients, T the temperature and T_{ref} the reference temperature (in this work $100\text{ }^{\circ}\text{C}$ and $90\text{ }^{\circ}\text{C}$ for respectively PEF and PET).

Figure 18.a shows the master curves used for the uniaxial stretching of PEF and PET (Chapter 2 to 5), and Figure 18.b depicts the evolution of the shift factor for both material depending on the gap from the reference temperature. Figures 18.c and 18.d depict the linear regression that validates the WLF formalism of the PEF and PET master curves used for uniaxial stretching. Table 2 summarizes the scattering of the various sheets used throughout this work.

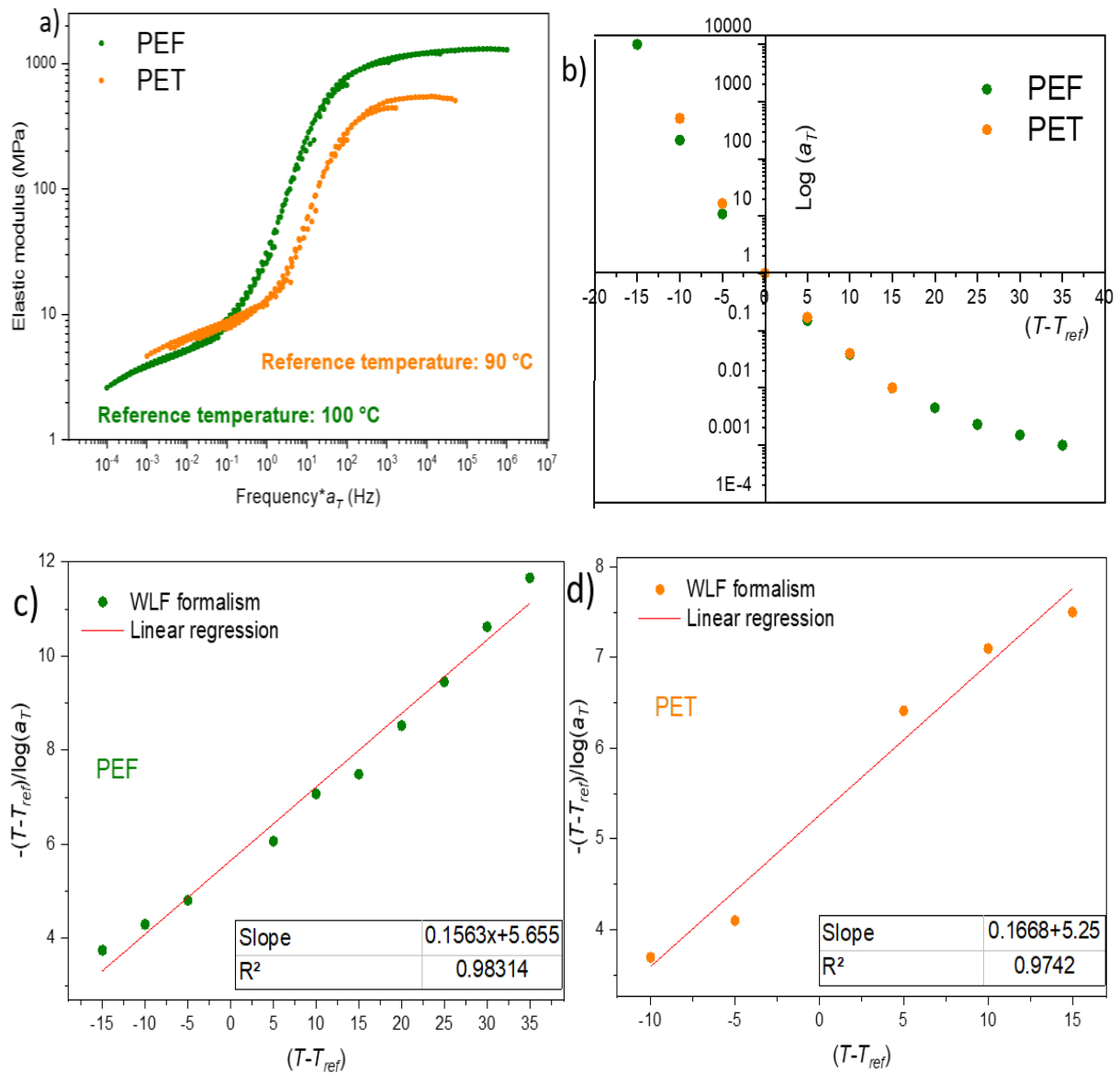


Figure 18. (a) Master curves of PEF and PET at respectively reference temperatures of 100 °C and 90 °C (uniaxial stretching sheets, Chapter 2 to 5), (b) evolution of the shift factor as a function of the gap from the reference temperature, linear regressions of (c) PEF and (d) PET master curves used for uniaxial stretching.

One can observe the closeness of the a_T values, between PEF and PET, once they are expressed as a function of $T - T_{ref}$ (Figure 18.b). The closeness of WLF's parameters is also visible in Table 2. It encourages to think that the materials could be tested in the same physical state.

	Sheets	T_{ref} (°C)	Study	C_1^0	C_2^0 (°C)
PEF	3	100	Calibration of the mechanical and thermal tests	7.27	43.19
	4			6.34	36.13
	7			7.15	40.80
	15		Uniaxial stretching campaign Load/unload tests (Chapters 2 to 5)	6.39	36.18
	9		Comparison between DIC2D and DIC3D (Chapter 1)	6.04	44.20
	8		Biaxial stretching (Chapter 6)	5.76	47.16
PET	5	90	Calibration of the mechanical and thermal tests	6.55	27.56
	10		Uniaxial stretching campaign Load/unload tests (Chapters 2 to 5)	5.99	31.52
	7		Uniaxial calibration test	4.99	27.16
	12		Biaxial calibration test	5.62	30.32

Table 2. Summary of the sheets used, their affected study, the master curve reference temperatures and the viscoelastic coefficients.

2.4 Samples geometry and calculation of the stress

Uni-axial tensile tests have been performed on a lab device designed for film stretching, in controlled temperature conditions (Chapter 1, 9. Stretching). The geometry of the uniaxial samples is represented in Figure 19.

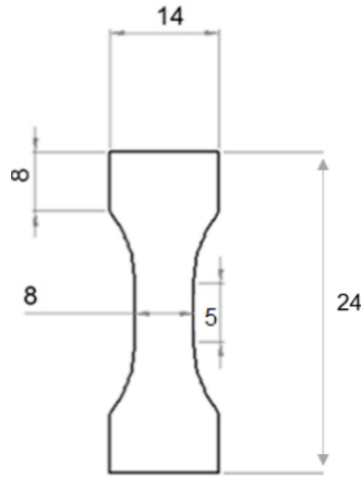


Figure 19. Geometry of the uniaxial tensile specimen (mm). Thickness is 0.70 mm.

To keep the strain rate, $\dot{\epsilon}_0$, as constant as possible in the process zone of the samples, and considering that the specimen length increases, the arms have been controlled in velocity ($v(t)$), with an exponential evolution with time (Equations 9.a and 9.b). Equation 9.c shows the calculation of the draw ratio ($\lambda(t)$).

$$v(t) = \dot{\epsilon}_0 L_0 \exp(\dot{\epsilon}_0 t) \quad (9.a)$$

$$t = \frac{\ln(\lambda(t))}{\dot{\epsilon}_0} = \frac{1}{\dot{\epsilon}_0} \ln\left(\frac{L(t)}{L_0}\right) \quad (9.b)$$

$$\lambda(t) = \left(\frac{L(t)}{L_0}\right) \quad (9.c)$$

where L_0 and $L(t)$ are the initial and current length of the specimen.

After the stretching, the samples are quenched with cold air. The cooling rate is of around -1000 °C/min. DIC2D was used to address local Hencky's strain, on the specimen surface, and in the two directions (transversal, ϵ_{yy} , and longitudinal, ϵ_{xx}). The mechanical tests are analysed in terms of true stress, $\sigma(t)$, calculated using the actual instantaneous section, and true strain as depicted by Equation 11. The transverse isotropy hypothesis is assumed (Equation 10). The true strains are measured in the centre of the process zone, as it is visible in Figure 20. The strain is averaged in the rectangular zone of analysis depicted in Figure 20. As high strains are targeted

in this work, the strain measurement is ensured up to the speckle limit, which can occur slightly before the rupture of the material.

$$\varepsilon_{yy}(t) = \varepsilon_{zz}(t) \quad (10)$$

$$\sigma(t) = \frac{F(t)}{S(t)} = \frac{F(t)}{e_0 * w_0 * \exp(2\varepsilon_{yy}(t))} \quad (11)$$

with respectively w_0 and e_0 the initial width and thickness, $S(t)$ and $F(t)$ the section and the force at time t .

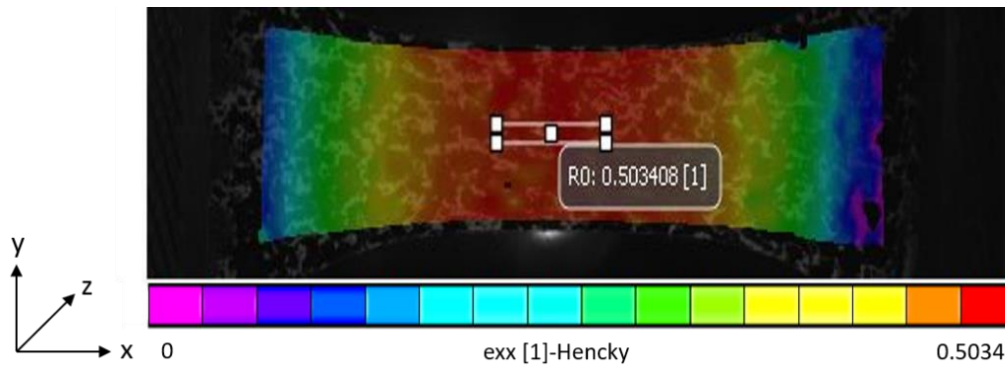


Figure 20. Deformation field during uniaxial tensile test. The rectangular zone represents the zone of analysis.

Considering that the stretching range is perfectly known for PEF and PET, and the equivalent strain rates at the reference temperatures have been defined, the relevant strain rate/temperature couples can be selected.

3. Definition of the uniaxial stretching conditions

3.1 Selection of the couples strain rate / temperature

Based on an analysis within the frame of the time/temperature superposition principle, the stretching is settled in the forming range. Several localizations on the master curves have been selected for PEF and PET.

- Beginning of the rubbery plateau (close to the α -relaxation),
- Middle of the rubbery plateau,
- End of the rubbery plateau.

The stretching conditions chosen for PEF and PET are summarized in Table 3. The duration of the tests is also added.

PEF		PET	
Stretching settings (s ⁻¹ / °C)	Test duration (s)	Stretching settings (s ⁻¹ / °C)	Test duration (s)
Beginning of the rubbery plateau (around 10⁻¹ s⁻¹)			
Slow (0.04 / 98)	81	Slow (0.02 / 87)	144
Rapid (0.40 / 104)	7	Rapid (0.15 / 91)	23
Middle of the rubbery plateau (around 10⁻² s⁻¹)			
Slow (0.07 / 105)	54	Slow (0.05 / 94)	74
Rapid (0.30 / 111)	11	Rapid (0.21 / 99)	16
End of the rubbery plateau (around 10⁻³ s⁻¹)			
Slow (0.03 / 111)	127	Slow (0.02 / 99)	184
Rapid (0.13 / 118)	30	Rapid (0.10 / 105)	35

Table 3. Stretching settings applied on PEF and PET. Associated test duration is reported.

These localizations are represented by the equivalent strain rates at the reference temperature close to T_α (100 °C and 90 °C for respectively PEF and PET). The targeted values are close to $10^{-1} \text{ s}^{-1} / 10^{-2} \text{ s}^{-1} / 10^{-3} \text{ s}^{-1}$, for PEF and PET. Two sets of conditions strain rate/temperature are tested per equivalent strain rate. One set is named “slow” (slower strain rate and lower temperature), while the other condition is named “rapid” (faster strain rate and higher temperature). The two strain rates have generally one decade of difference.

3.2 Evolution of the strain during the tests

Figure 21 depicts the evolution, during the stretching, of the longitudinal strain with the time for PEF and PET. The tests performed with a “slow” strain rate are represented in Figures 21.a and 21.c for respectively PEF and PET; while the tests realised at “rapid” strain rates are depicted in Figures 21.b and 21.d. The duration of each test is visible on the following graphs, in general the tests are longer for PET than for PEF. The derivative of the strain with respect to the time (the slope of the following curves) allows to calculate the strain rate at each moment of the test.

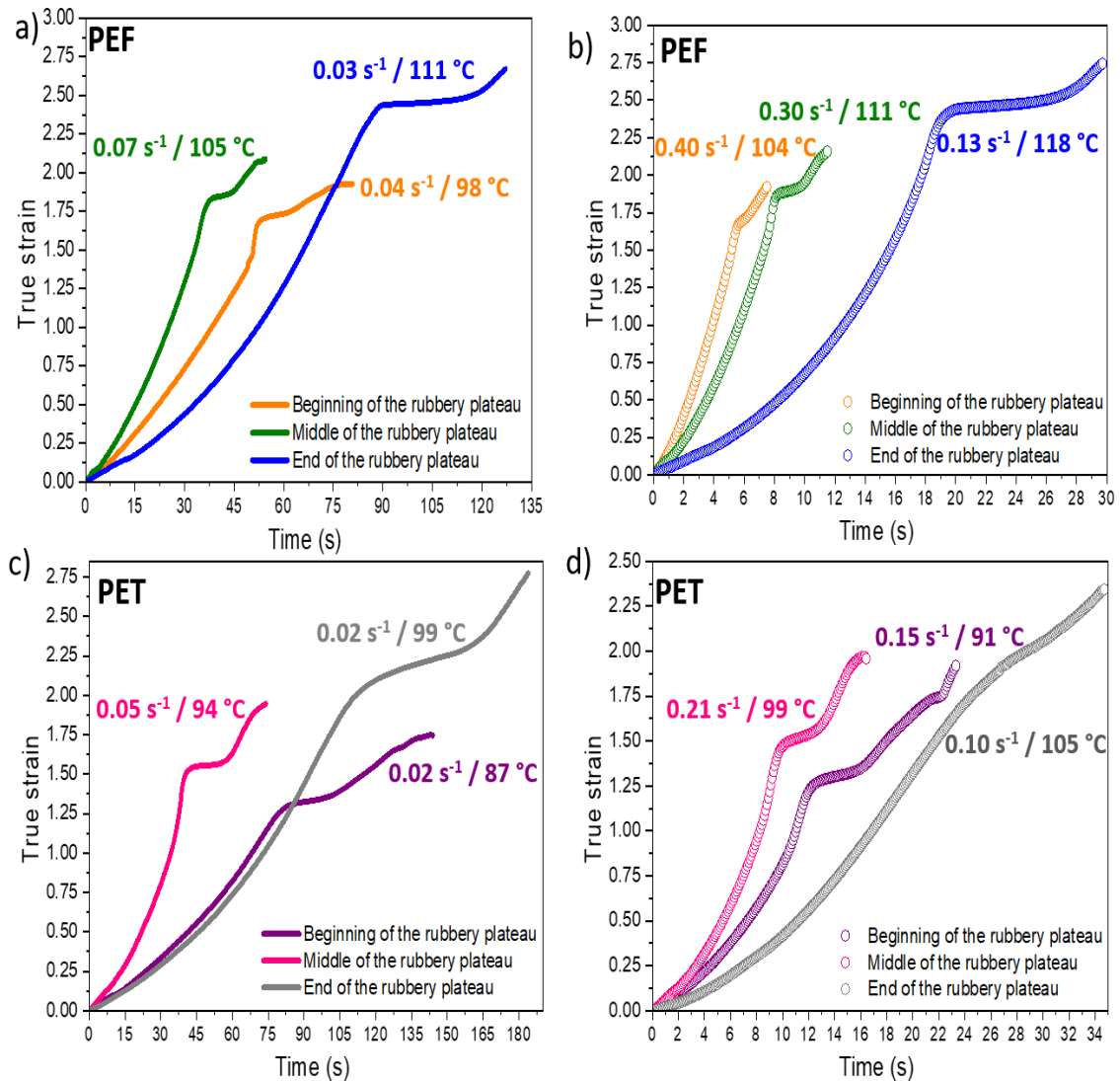


Figure 21. Evolution of the longitudinal strain for stretching performed in PEF with (a) “slow” and (b) “rapid” strain rates, in PET with (c) “slow” and (d) “rapid” strain rates.

An almost linear increase of the strain with the time is visible during the first steps of the test (Figure 21). Thus, the strain rate can be considered as relatively constant. It fits with our expectations, as it testifies that the deformation is well-localized and uniform in all the analysed process zone. When the equivalent strain rate decreases, the linear evolution is slightly lost. It is particularly true for the experiments settled at the end of the rubbery plateau. It means that the deformation is less uniform, and there is more localization within the process zone analysed. After the first increase observed, the strain evolution in the process zone is almost constant: it corresponds to the NDR zone. The deformation moves in other areas closer to the clamps, as soon as the process zone is sufficiently deformed. A slight annealing of the process zone can then occur during the stretching of the areas closer to the clamps. This almost “plateau” lasts a longer time for the experiments settled at the end of the rubbery plateau (blue and grey curves),

compared to the other cases. Finally, the strain increases again up to the end of the stretching, and the process zone is deformed a last time.

Thus, with these first observations, it seems that only the experiments settled at the end of the rubbery plateau (blue and grey curves) have a less uniform deformation, compared to the other settings. Next part will highlight this trend.

3.3 Determination of the experimental parameters

In the following part is examined, for PEF and PET, the progress of the strain rate and of the temperature during “slow” and “rapid” tests. The tests have been performed close to the three expected localization on the master curve: beginning, middle and end of the rubbery plateau.

On the following graphs, the key values that allow to follow the strain rate and the temperature evolution are reported. The dashed line represents the NDR. Firstly, one typical figure is reported to explain one of the typical evolution of strain rate and temperature observed for some tests (Figure 22, test expected at the beginning of the rubbery plateau for PEF). The other graphs, exhibiting the same trend, are represented in annexes:

- Annex 1 (beginning of the rubbery plateau PET);
- Annexes 2 and 3 (middle of the rubbery plateau for respectively PEF and PET)

Then, Figure 23 shows another typical evolution of the strain rate and the temperature (test expected at the end of the rubbery plateau for PEF). The evolution of PET, with the same trend, is in Annex 4.

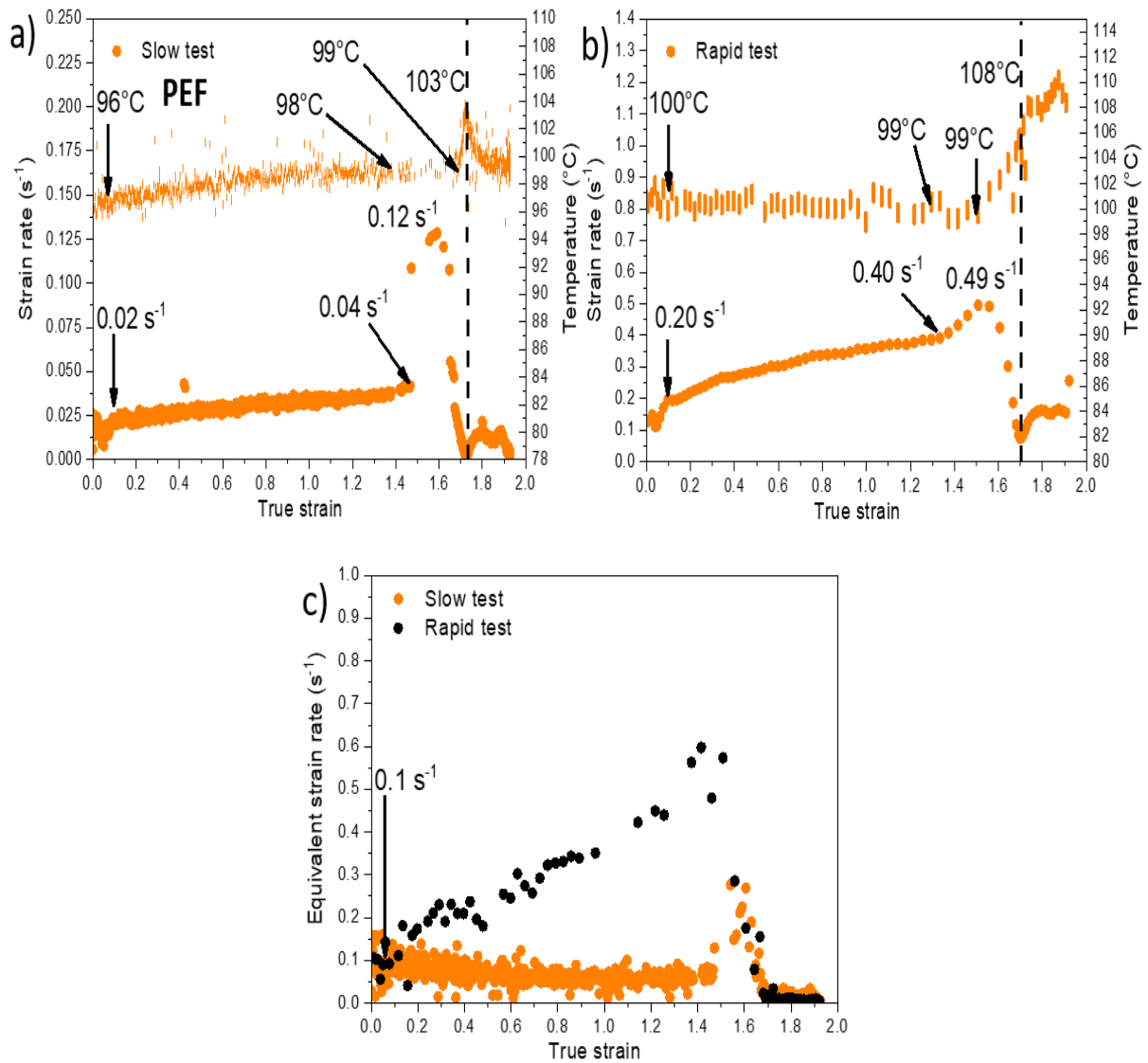


Figure 22. Evolution of the temperature and of the strain rate for (a) "slow" and (b) "rapid" tests; as well as (c) the equivalent strain rate of both experiments realised at the beginning of the rubbery plateau, for PEF.

The local evolution of the strain rate depends on geometrical effects, and on the loading path applied [65]. Firstly, the strain rate is relatively constant. There is the localization of the deformation in the analysed process zone. It corresponds to the almost linear evolution of the strain with the time visible in Figure 21. Then, the "sudden" increase of the strain rate (its beginning is marked by the second black arrow) can be related to the decrease of the section in the process zone. When this zone is sufficiently oriented, the deformation moves towards the other areas closer to the clamps, and the strain rate is equal to almost zero in the process zone. At this moment, the strain hardening occurs. Finally, as the sample still undergoes the

stretching, the process zone is deformed a last time (new increase of the strain rate) just before the end of the test. It corresponds to the last increase of the strain with the time, in Figure 21. During the stretching, the temperature evolves in the same way as the strain rate, but the “sudden” temperature increase occurs, generally, after the “sudden” strain rate increase. For the tests depicted in Figure 22 and in Annexes 1 to 3, the temperature increases slightly and continuously up to the temperature maximum that occurs close to the NDR. For PET “slow” and “rapid” tests an increase of temperature between 4 °C and 7 °C is observed. Concerning PEF, the observed temperature increase is between 7 °C and 11 °C. The higher temperature increase is related to the “rapid” tests, for both materials. As the temperature increases during these tests, it can be supposed that the samples exhibit a viscoelastic behaviour. These increases of temperature might be related to dissipative phenomenon (such as self-heating), to crystallization or maybe to a combination of both.

A difference concerning the temperature evolution after the NDR exists between the “slow” and the “rapid” tests. Indeed, the temperature increases continuously for the “rapid” tests after the NDR, while it remains almost constant for the “slow” tests. The trend is similar for PEF and PET. It can be supposed that this temperature increase during the last steps of the stretching can be due to the occurrence of self-heating.

On the other side, the tests performed and expected at the end of the rubbery plateau exhibit a different temperature evolution, as drawn in Figure 23 and Annex 4.

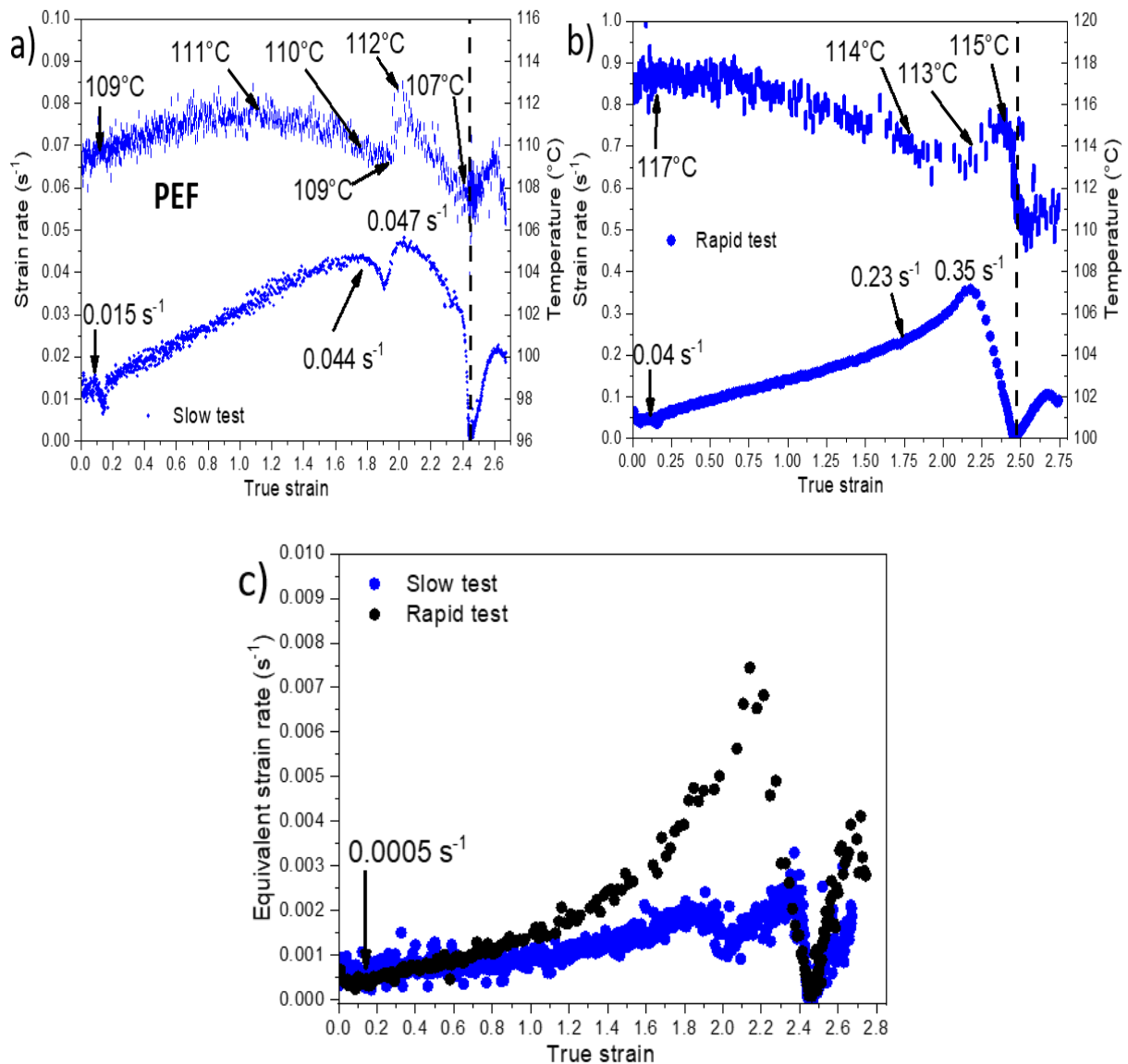


Figure 23. Evolution of the temperature and of the strain rate for (a) “slow” and (b) ”rapid” tests; as well as (c) the equivalent strain rate of both experiments realised at the end of the rubbery plateau, for PEF.

The strain rate evolution is relatively similar to the one of the tests presented previously. But, for these tests, the temperature remains more or less stable, or decreases. The “sudden” peak temperature occurs only for the test depicted in Figure 23, but before that the temperature is not really constant (increasing and decreasing or only decreasing). Moreover, for the test in Figure 23.b, the temperature reached at the peak (at the NDR) is lower compared to the initial temperature. These trends can be the proof of an hyper-elastic behaviour of these samples, rather than a viscoelastic one. The hyper-elastic behaviour seems to be more marked for PET

(Annex 4) than for PEF. After the NDR, the temperature increases that have been previously reported for the “rapid” tests are not observed, or are really low.

Globally, in all the tests (Figures 22 and 23, as well as Annexes 1 to 4), the strain rates and the temperatures evolve slightly. Between the beginning of the test and the NDR, the strain rate is multiplied by around 2 or 3; while the temperature gains around 2 °C or 3 °C for the “slow” and the “rapid” tests. These fluctuations have a low impact on the equivalent strain rates evolution: they remain in the same selected decade. These evolutions are acceptable, as the tests are defined on the rubbery plateau of the materials where the elastic modulus does not significantly change within a decade.

Table 4 and 5 gather the stretching settings obtained experimentally for PEF and PET. In the Figures 24.a and 24.b, the equivalent strain rates are represented by rectangular areas on the PEF and PET master curves. Consequently, the physical state of the materials is estimated for each equivalent strain rates obtained. The range of evolution of the equivalent strain rates is taken between the beginning of the test and before the strain rate “sudden” increase. To simplify afterwards the comparison between the samples, it has been chosen to associate to each test the equivalent strain rate which is the closest of a decade value.

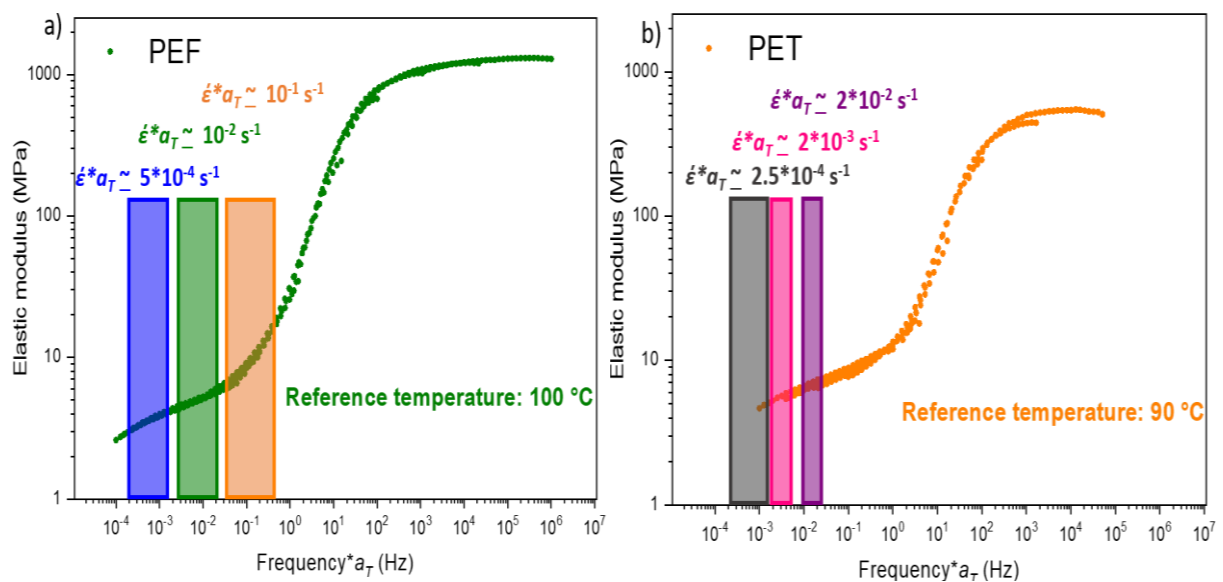


Figure 24. Master curves of (a) PEF and (b) PET with the areas associated to each equivalent strain rate.

	Localization on the master curve	Mechanical settings obtained at the test beginning (s ⁻¹ / °C)	Range of $\dot{\epsilon}^*a_T^{obtained}$ (up to the “sudden” strain rate increase) (s ⁻¹)
PEF	Beginning of the rubbery plateau: Around 10⁻¹ s⁻¹	Slow (0.02 / 96)	0.1 → 0.06
		Rapid (0.20 / 101)	0.1 → 0.43
	Middle of the rubbery plateau Around 10⁻² s⁻¹	Slow (0.035 / 101)	0.018 → 0.021
		Rapid (0.130 / 109)	0.005 → 0.01
	End of the rubbery plateau Around 5*10⁻⁴ s⁻¹	Slow (0.015 / 109)	0.0005 → 0.0019
		Rapid (0.040 / 117)	0.0005 → 0.0028

Table 4. Stretching settings obtained for PEF during uniaxial tensile tests for various localization on the master curves.

	Localization on the master curve	Mechanical settings obtained at the test beginning (s ⁻¹ / °C)	Range of $\dot{\epsilon}^*a_T^{obtained}$ (up to the “sudden” strain rate increase) (s ⁻¹)
PET	Middle of the rubbery plateau Around 2*10⁻² s⁻¹	Slow (0.01 / 87)	0.02 → 0.04
		Rapid (0.06 / 92)	0.02 → 0.03
	End of the rubbery plateau Around 2*10⁻³ s⁻¹	Slow (0.02 / 95)	0.002 → 0.005
		Rapid (0.07 / 101)	0.002 → 0.005
	Right before the cold crystallization Around 2.5*10⁻⁴ s⁻¹	Slow (0.009 / 101)	0.0005 → 0.0019
		Rapid (0.030 / 106)	0.0005 → 0.0028

Table 5. Stretching settings obtained for PET during uniaxial tensile tests for various localization on the master curves.

To conclude on this part, the local measurements allow to precisely know the variation existing between the settings and the real values obtained. It has been concluded that the strain rates and the temperatures changes are relatively low and remain acceptable. Moreover, in most of the case, “slow” and “rapid” tests evolve similarly in PEF and PET.

Regarding the results, PEF has been stretched at the three expected localization on the master curve (beginning, middle and end of the rubbery plateau). Concerning PET, no conditions fit with a stretching at the beginning of the rubbery plateau (equivalent strain rate of 10 s⁻¹ defined at the reference temperature of 90 °C). The final localizations are the middle of the rubbery

plateau, the end of it, and right before the cold crystallization. The analysis of this last condition has to be done carefully, as the temperature of the “rapid” test belongs to a really sensitive range. The next part is focused on the stress/strain curves obtained, and on the comparison between PEF and PET mechanical behaviour.

4. Mechanical behaviour

Figure 25.a represents together the mechanical responses obtained for PEF and PET. For a better reading of the initial steps of the stretching, a zoom is shown in Figure 25.b. For the same reason, curves are redrawn in Figure 26, material by material. Table 6 gathers the NDRs of each experiment, as well as the Hencky’s strain at the NDR, for PEF and PET. As the NDR apparition is relatively abrupted, the value has been determined directly on the curve at the break in slope. Figure 27 depicts an example of the strain field evolution during a stretching test for PEF ($0.035 \text{ s}^{-1} / 101 \text{ }^\circ\text{C}$), which corresponds to a stretching localized in the middle of the rubbery plateau. Table 7 reveals the microstructural changes induced by the stretching in PEF and PET, for one representative condition (the same patterns have been found for the others conditions and are detailed in the Chapter 5).

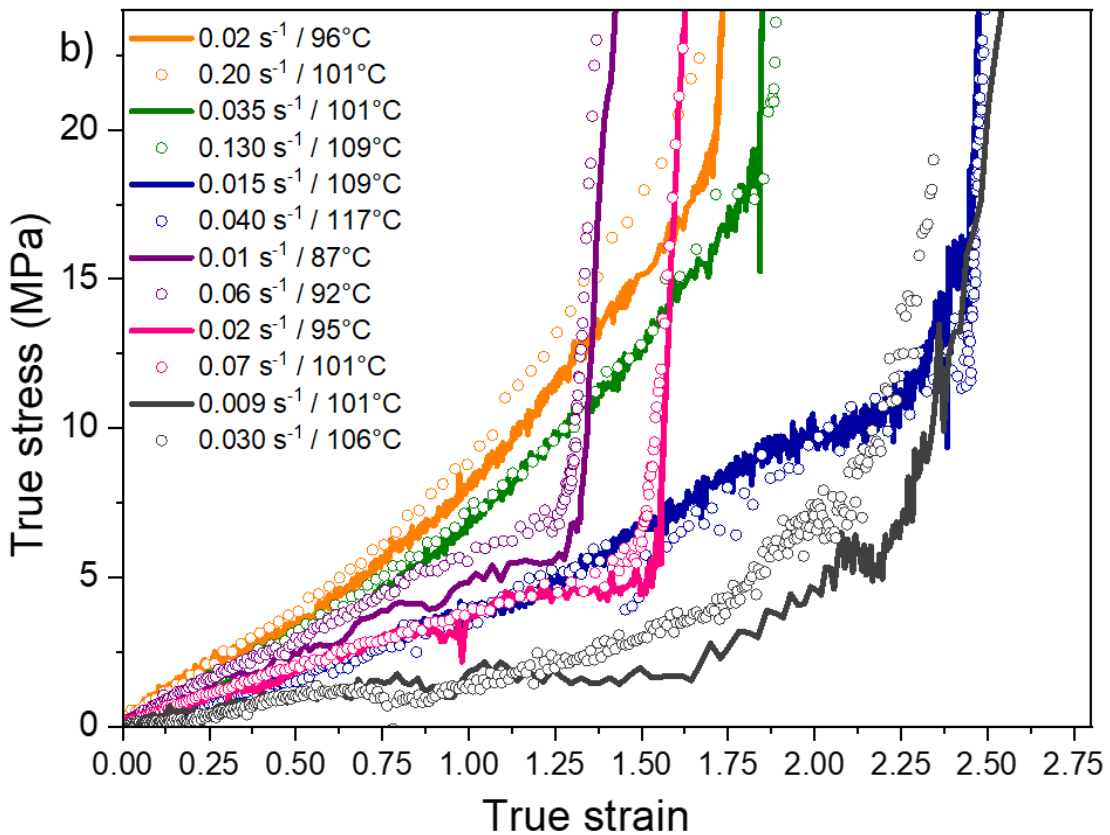
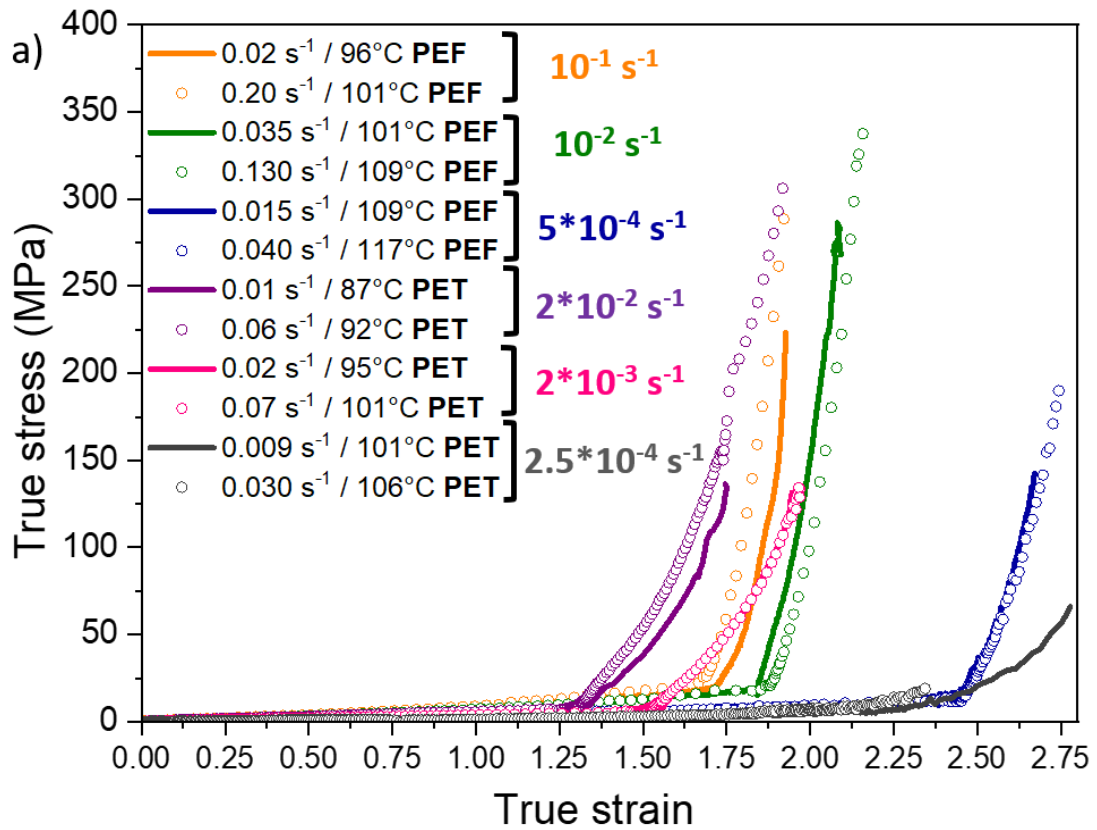


Figure 25. (a) True stress/strain curves of uniaxially stretched PEF and PET. Each colour is associated to an equivalent strain rates, within an equivalent strain rates lines are for “slow” tests while dots belong to “rapid” tests; (b) a zoom is made on the first deformation stages.

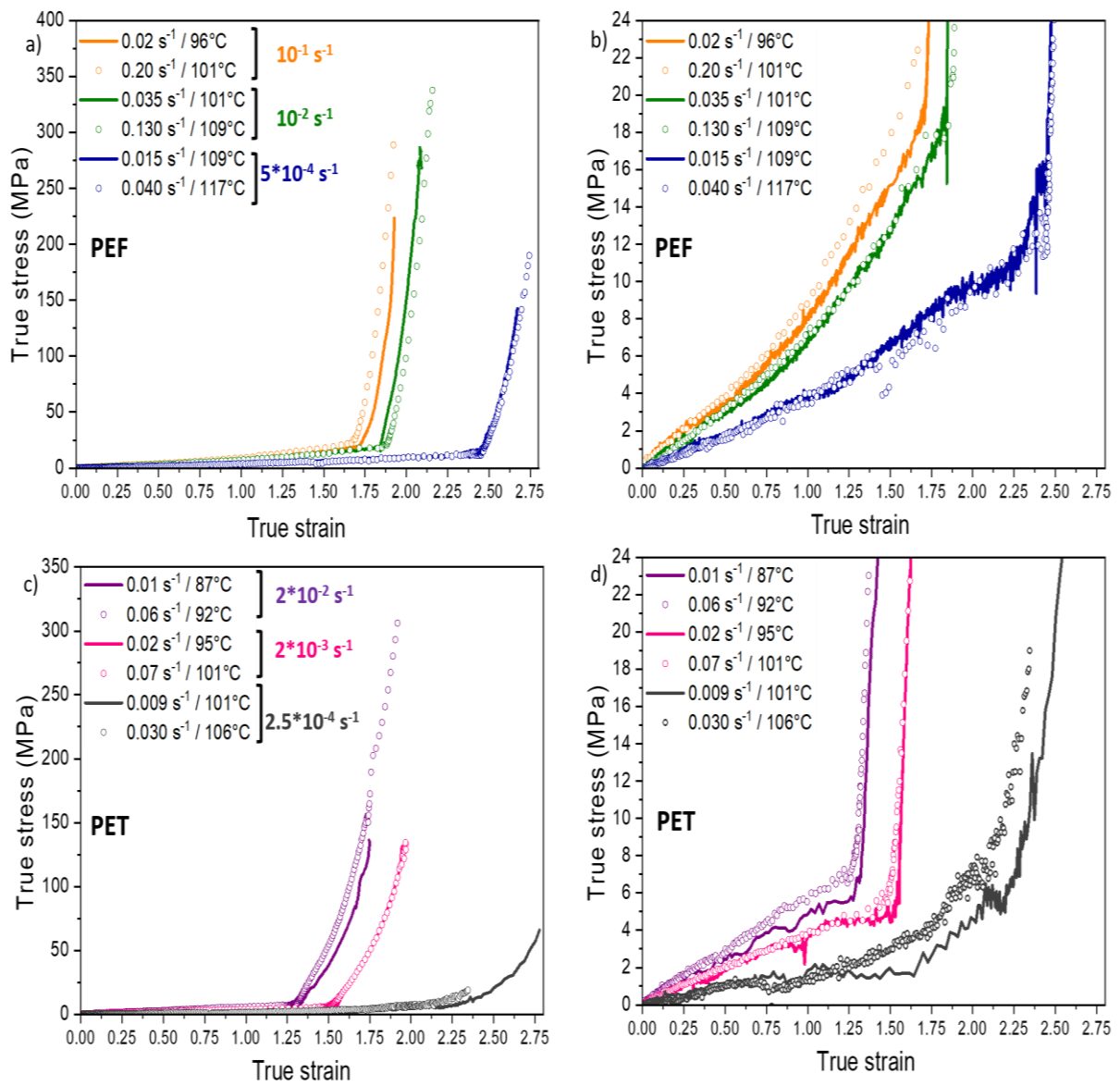


Figure 26. True stress/strain curves for (a) and (b) PEF, (c) and (d) PET.

PEF						
$\dot{\epsilon}^*a_T$	10^{-1} s^{-1}		10^{-2} s^{-1}		$5 \cdot 10^{-4} \text{ s}^{-1}$	
Settings ($\text{s}^{-1} / ^\circ\text{C}$)	0.02 / 96	0.20 / 101	0.035 / 101	0.13 / 109	0.015 / 109	0.04 / 117
Hencky's strain at NDR	1.69	1.68	1.83	1.87	2.39	2.40
NDR (λ)	5.41	5.36	6.29	6.48	11.02	11.13
PET						
$\dot{\epsilon}^*a_T$	$2 \cdot 10^{-2} \text{ s}^{-1}$		$2 \cdot 10^{-3} \text{ s}^{-1}$		$2.5 \cdot 10^{-4} \text{ s}^{-1}$	
Settings ($\text{s}^{-1} / ^\circ\text{C}$)	0.01 / 87	0.06 / 92	0.02 / 95	0.07 / 101	0.009 / 101	0.030 / 106
Hencky strain at NDR	1.27	1.25	1.53	1.47	2.19	2.05
NDR (λ)	3.56	3.49	4.61	4.34	8.93	7.76

Table 6. NDR evolution with the equivalent strain rates for PEF and PET.

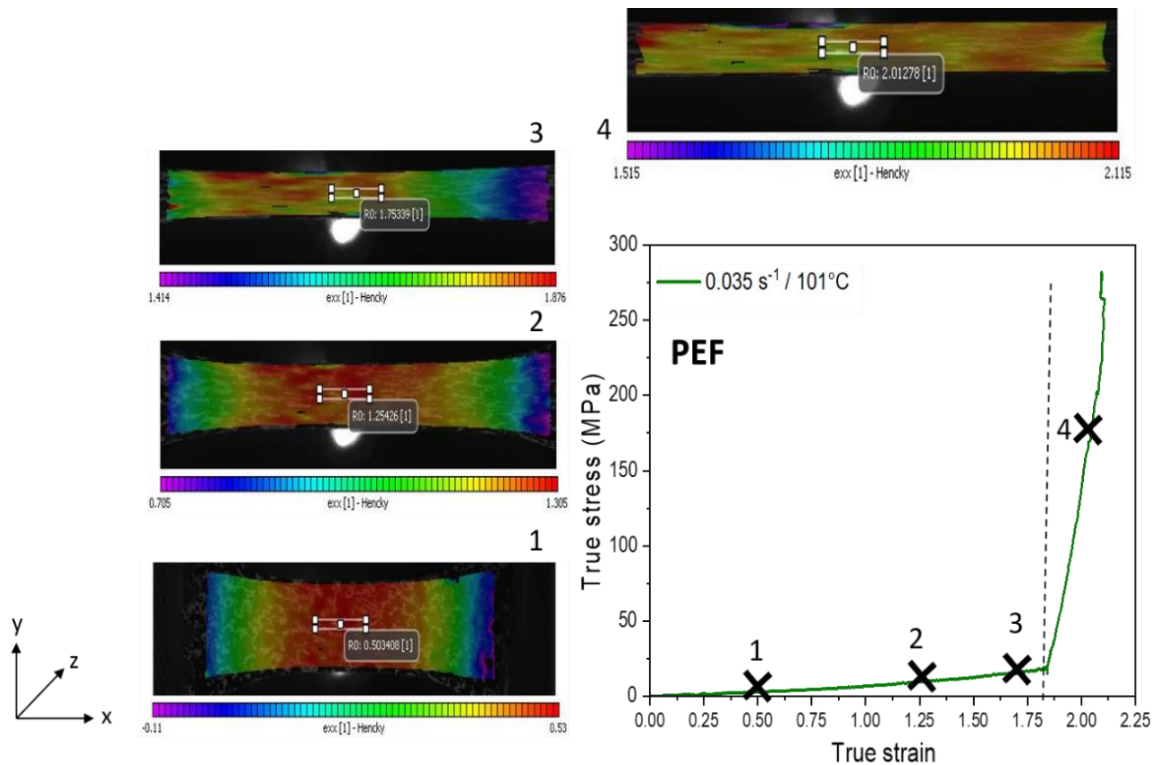


Figure 27. True stress/strain curve of PEF stretched at 105 °C, with a strain rate of 0.035 s⁻¹ and associated deformation fields obtained for different strain stages [65].

The stretching protocol established leads to six mechanical tests, for each material, which exhibit an impressive strain hardening up to the rupture (Figure 25). The progressive increase of the stress is due to the extension of the chains. The reaching of high draw ratios is definitely visible. The NDR apparition is dependent on the equivalent strain rate: its occurrence takes place at higher strains when the rubbery state of the material is more “pronounced”. Moreover, the NDR appears always at higher strains for PEF compared to PET, even for close localizations on their rubbery plateaux. Furthermore, the strain hardening development seems sharper in PEF compared to PET. The results obtained are in good agreement with the previous works in PET [77,91,95]. It confirms the interest of using a master curve to estimate the physical state of the material before its stretching, and then to apply the adequate couple strain rate/temperature. The definition of the PEF stretching settings from the reading of the master curve is more efficient than the choices existing in the literature [58,59,61]. In these previous works, PEF was not able to reach high level of deformations, nor to develop high level of strain hardening (the levels were lower than 10 MPa in these works), and then the induced microstructure was not a well-defined one. It is probably due to the use of a too low temperature and strain rate.

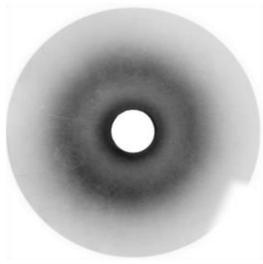
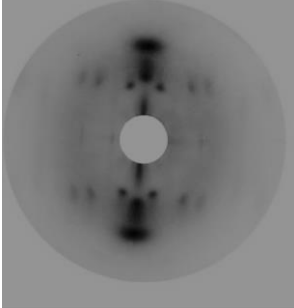
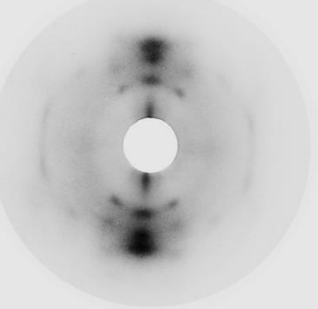
	Initial material	Stretched (10^{-2} s^{-1}) “slow”
PEF		
	Initial material	Stretched ($2 \cdot 10^{-3} \text{ s}^{-1}$) “slow”
PET		

Table 7. Debye-Scherrer patterns (for only one test) of amorphous and stretched PEF and PET.

In this work, the creation of SIC is observable on the Debye-Scherrer pictures for PEF and PET (Table 7). Initially, the materials are amorphous and after the stretching, the observation of intense spots is possible on the pattern. The spots represent the diffraction of the families of planes. It reveals the periodicity of the structure, and thus the presence of SIC.

The local measurement is also responsible of the differences in the NDR values reported in this study, compared to the previous ones concerning PEF [58–61] or concerning PET, for which usual NDRs are around 2-3 [69,70,91,93]. Regarding Figure 27, it is confirmed that the localization of the deformation is well concentrated in the process zone during the stretching. The stretching protocol has been established in this way, and this result is of prime interest as the process zone is the area in which strain rate and temperature are measured, and also where the microstructure is examined thereafter.

For each equivalent strain rate tested, the stress-strain curves associated to two different couples (strain rate, temperature) are superimposed. It confirms that the slight disparities concerning the evolution of the strain rates, temperatures and equivalent strain rates observed in the

previous section are negligible. The time/temperature principle is validated for all the conditions. It is of real interest as it allows the transposition of the results to the industry, that uses faster strain rates and higher temperatures. For the PET samples stretched with an equivalent strain rate equal to $2.5 \cdot 10^{-4} \text{ s}^{-1}$ (grey curves), some differences exist concerning the strain hardening onset between the two tests. For the stretching performed at $106 \text{ }^\circ\text{C}$ (higher temperature), it is possible that some nucleation has occurred during the pre-heating step and the test itself. In total, this sample has been heated above its α -relaxation during around 335 s. Nevertheless, the isothermal tests performed in DSC close to this temperature (2.2 Static crystallization) have reported no crystallization. However, according to the mechanical behaviour of this sample (early apparition of the NDR), this option has to be kept in mind.

In the scale visible in Figure 25.b, the behaviour of PEF and PET appears really close during the first steps of the tests (except for PET stretched with an equivalent strain rate of $2.5 \cdot 10^{-4} \text{ s}^{-1}$). Up to around a strain of 1.3, PEF test performed at the beginning of the rubbery plateau (10^{-1} s^{-1} , orange curves) exhibits the stiffer behaviour. The less rigid tests are those of PET which are localized right before the static crystallization ($2.5 \cdot 10^{-4} \text{ s}^{-1}$, grey curves). Between them, the other tests are close. A superimposition is even noticeable between PEF stretched at an equivalent strain rate of $5 \cdot 10^{-4} \text{ s}^{-1}$ (blue curves), and PET stretched at an equivalent strain rate of $2 \cdot 10^{-3} \text{ s}^{-1}$ (pink curves).

These observations confirm that it is the gap from the α -relaxation that determines the mechanical behaviour. Indeed to have the same localization on the PEF and PET rubbery plateaux, and to obtain a similar response during the first stages of the stretching, around one decade of difference has to be applied on the equivalent strain rates defined at the reference temperature close to T_α . It explains the superimposition of the tests performed at equivalent strain rates of respectively $5 \cdot 10^{-4} \text{ s}^{-1}$ and $2 \cdot 10^{-3} \text{ s}^{-1}$ for PEF and PET.

To conclude this part, the use of the described protocol leads to control tests. It is observed that PEF and PET stretched with the relevant settings are similar in terms of mechanical behaviours.

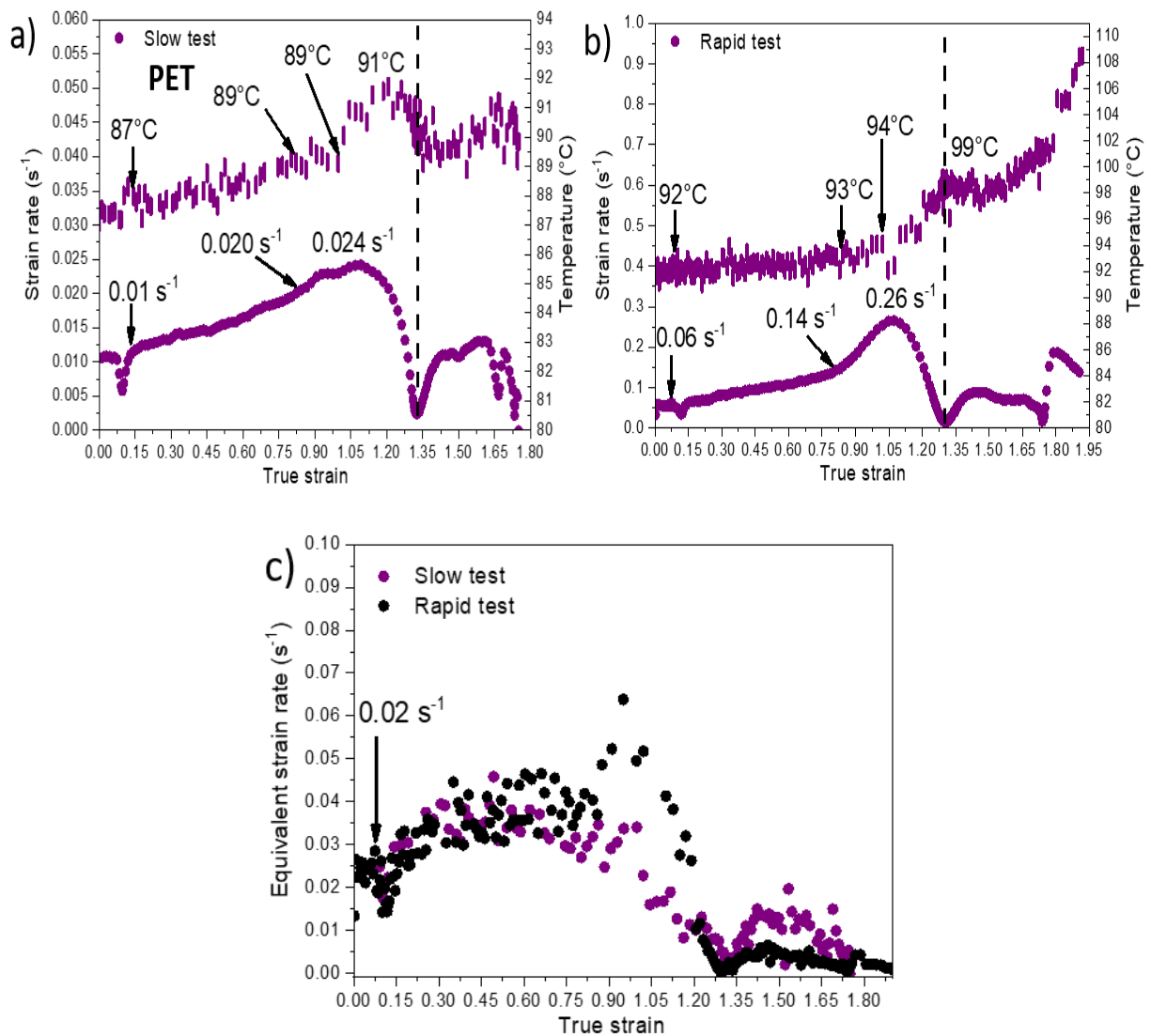
5. Conclusions

PEF and PET are able to be stretched efficiently along their forming range: an impressive strain hardening has been noticed and SIC has been developed for all the samples.

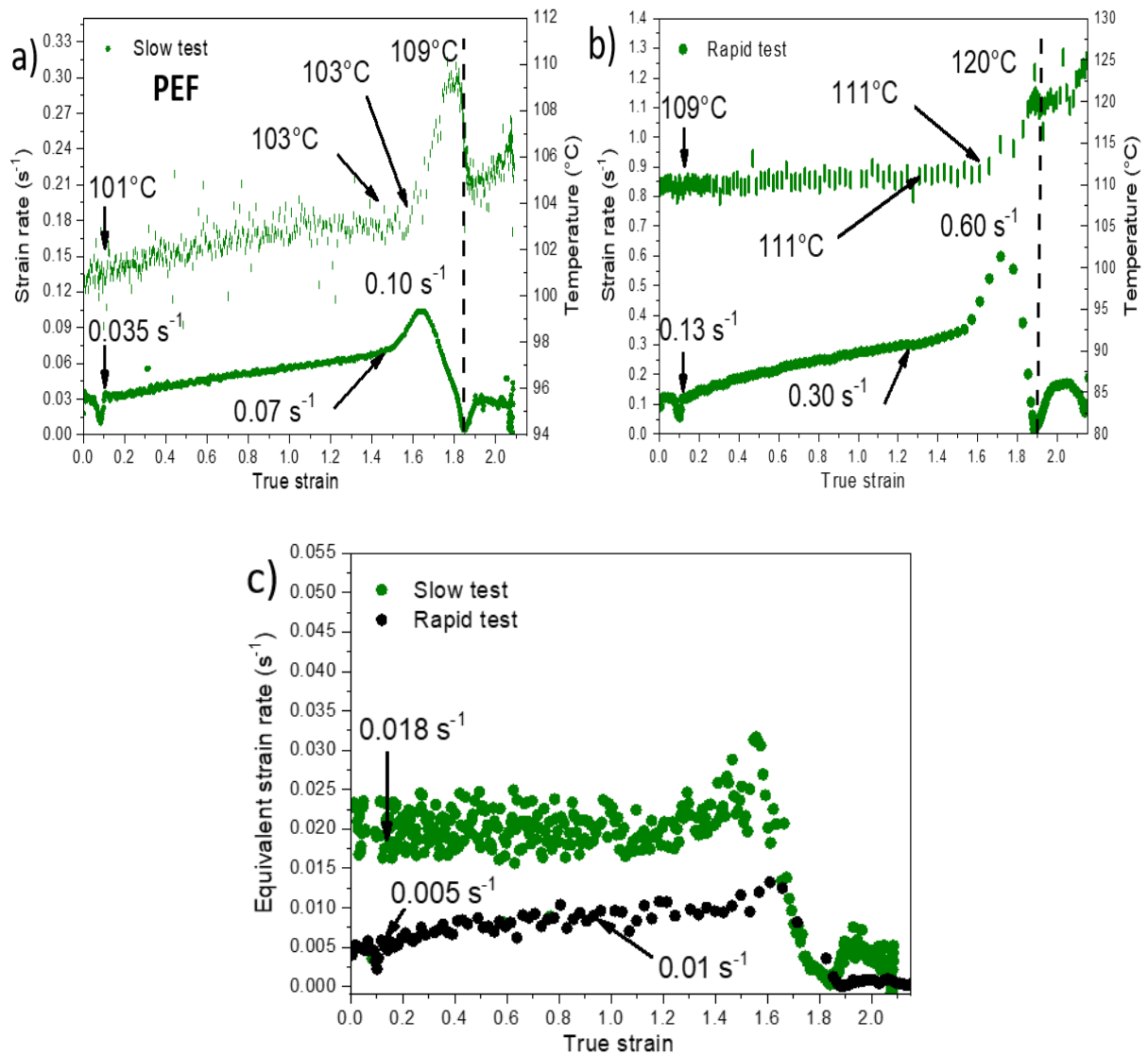
As the stretching settings have been defined according to the master curve reading, an efficient screening of the mechanical behaviours of the materials on their rubbery plateau has been possible. For each equivalent strain rates, the physical state of the material is known and relevant couples strain rate/temperature have been selected. The time/temperature principle has been validated for all the stretching conditions. It is of prime interest to allow the transposition of these results towards the industry. It has been observed that the NDR apparition is directly dependent on the equivalent strain rate applied. Moreover, during the first steps of the test, all the curves are really close, and almost superimposed. It testifies of the high similarity existing between PEF and PET. Then, the same industrial machines can be used.

Henceforth, more details concerning SIC in comparison with the crystal obtained in static crystallization are needed. The next chapter is going to analyse the microstructure induced by the stretching for one mechanical conditions in PEF and PET, respectively 10^{-2} s^{-1} and $2 \cdot 10^{-3} \text{ s}^{-1}$.

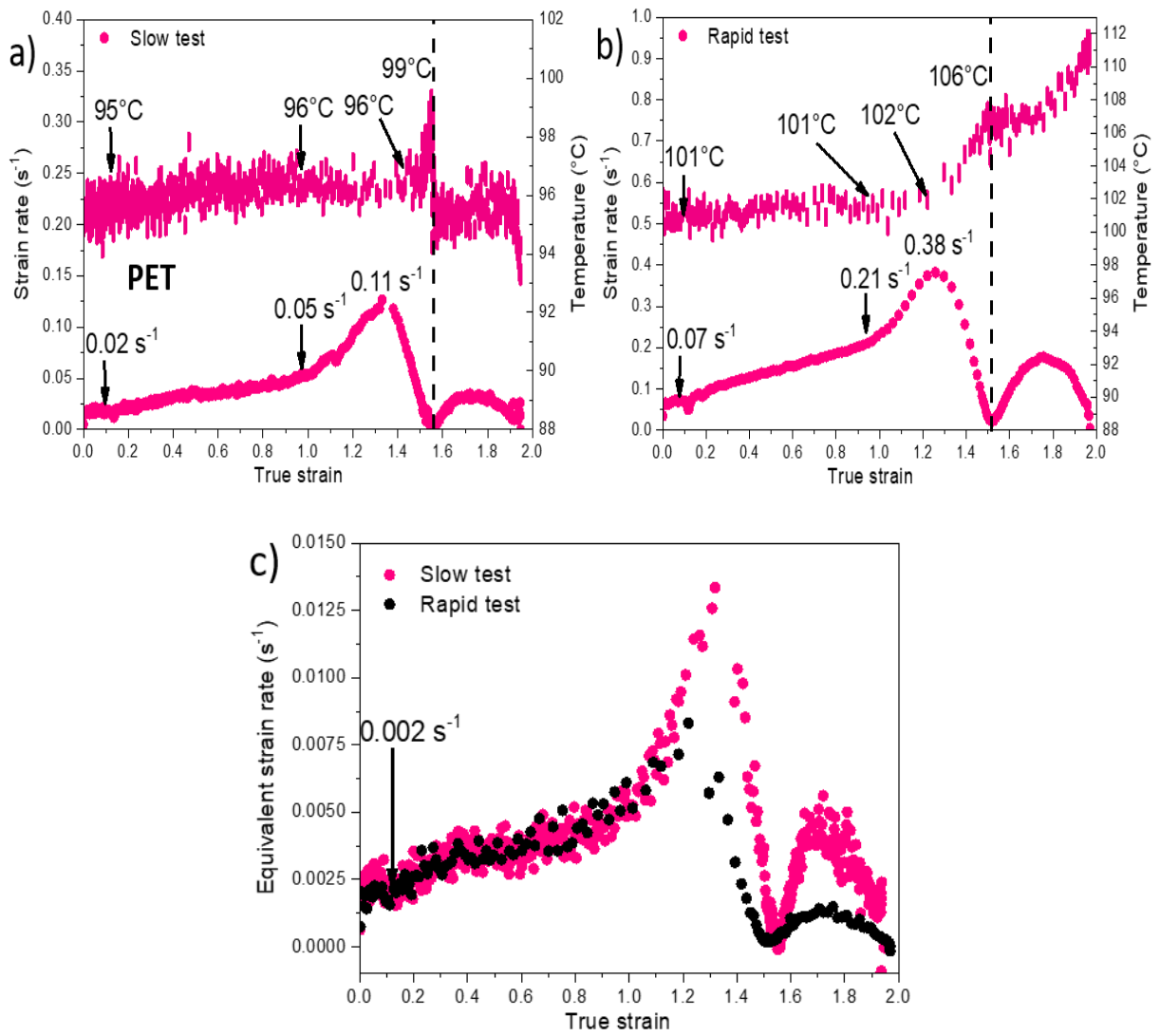
6. Annexes



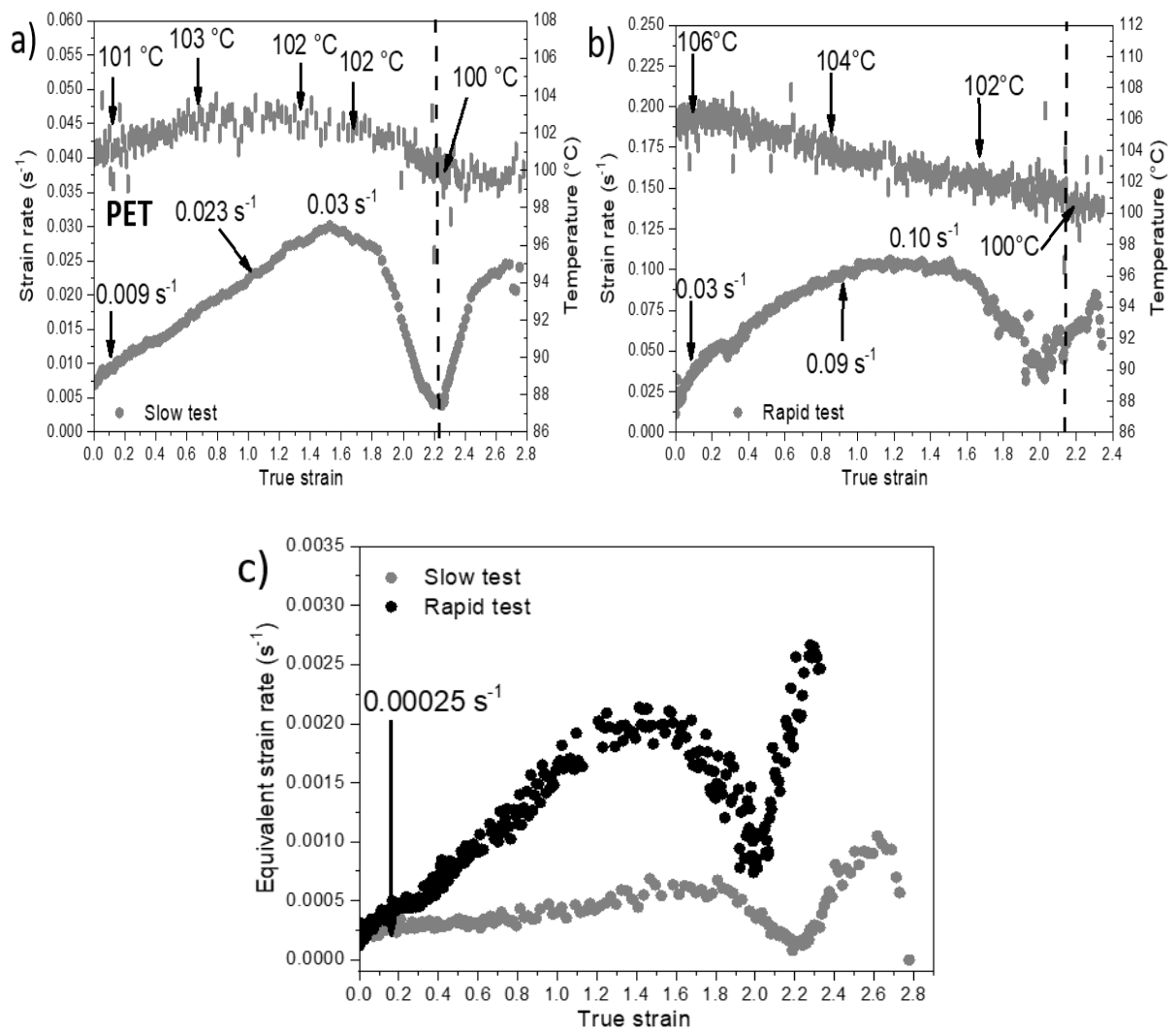
Annex 1. Evolution of the temperature and the strain rate for (a) "slow" and (b) "rapid" tests; as well as (c) the equivalent strain rate of both experiments realised at the beginning of the rubbery plateau (PET).



Annex 2. Evolution of the temperature and the strain rate for (a) "slow" and (b) "rapid" tests; as well as (c) the equivalent strain rate of both experiments realised at the middle of the rubbery plateau (PEF).



Annex 3. Evolution of the temperature and the strain rate for (a) "slow" and (b) "rapid" tests; as well as (c) the equivalent strain rate of both experiments realised at the middle of the rubbery plateau (PET).



Annex 4. Evolution of the temperature and the strain rate for (a) "slow" and (b) "rapid" tests; as well as (c) the equivalent strain rate of both experiments realised at the end of the rubbery plateau (PET).

Chapter 3

Comparison between the crystal induced in static conditions and SIC

Table of contents

1. Introduction.....	70
2. Analysis of the crystalline structure of PEF	73
2.1 Crystalline structure induced by the stretching	73
2.2 Comparison with the crystal formed by static crystallization	79
3. Conformations involved in PEF and PET.....	82
3.1 Conformational changes due to crystallization occurrence.....	84
3.2 Aromatic =C-H and cycle breathing.....	86
3.3 Transformations in the aliphatic part in PEF and PET	88
3.4 Impact on the β -transition	91
4. Conclusions.....	94

Chapitre 3

Comparaison entre le cristal induit sous étirage et celui formé lors de la cristallisation statique

La structure cristalline du PET est bien définie et connue à partir de l'étude de Daubeny et al. datant de 1954 [11]. Ce n'est pas le cas de celle du PEF. Pour définir la structure cristalline du PEF, tout d'abord un système triclinique a été proposé par Kazaryan et al. en 1968 [101]. Récemment cette structure a été revisitée par Mao et al. [58], et un système monoclinique composé de deux unités constitutives (à la place d'une seule dans le système triclinique) serait plus approprié pour permettre l'empilement des chaînes.

Le PEF a également été proposé plusieurs fois comme étant un matériau polymorphe. Ce chapitre a ainsi pour but de fournir plus de détails concernant la structure cristalline du PEF étiré, et de comparer cette structure avec celle d'un PEF cristallisé statiquement à partir de l'état solide à 160 °C pendant 2 heures. Une des conditions d'étirage présentées précédemment a été utilisée dans ce chapitre. A partir d'une analyse Debye-Scherrer et d'un protocole mis en place, les familles de plans du PEF ont pu être indexées et comparées avec celles du PEF cristallisé statiquement. La même structure cristalline a été trouvée. De plus, l'indexation réalisée dans le cadre de ce travail est en accord avec la proposition de Mao et al. [58,59]. Le protocole d'étirage expliqué au précédent chapitre permet ainsi d'obtenir une microstructure qui semble mieux définie que celles exposées dans les travaux antérieurs portant sur le PEF étiré uniaxialement [31,58,59]. Cette observation confirme l'efficacité du protocole d'étirage mis en place et la possibilité du PEF de former une structure cristalline bien définie si le couple vitesse/température utilisé est en accord avec l'état physique du matériau.

Pour parfaire la comparaison entre la microstructure obtenue sous étirage et celle obtenue statiquement, une analyse portant sur les changements conformationnels a été conduite sur le PEF et le PET à partir du travail de Araujo et al. [102]. Il en ressort que les mêmes changements conformationnels prennent place pour une cristallisation statique et une cristallisation sous étirage. Dans le cas du PET, la phase amorphe est composée d'une majorité de groupements éthylènes glycols en conformation *gauche*, tandis que dans la phase cristalline les éthylènes glycols sont en conformation *trans*. Pour le PEF, il est confirmé qu'il existe dans la phase

amorphe une majorité d'éthylènes glycols en conformation *gauche* et de cycles furaniques en conformation *anti* ; dans le cristal, des éthylènes glycols en conformation *trans* et des cycles furaniques en conformation *syn* sont observés. Les différents groupes caractéristiques sont cependant plus contraints lors d'une cristallisation sous étirage, que lors d'une cristallisation statique. Ceci est probablement dû à une cristallisation sous une forme étirée. Le même constat se révèle pour le PET. Il semble également que l'étirage conduit à un environnement chimique plus homogène que celui existant lors d'une cristallisation statique pour le PEF. Grâce à l'analyse d'essais interrompus, il apparaît clairement que la partie aliphatique de la chaîne est la première à être influencée par l'étirage pour le PEF.

L'analyse de la transition β par DMTA fournit des informations complémentaires concernant la mobilité des groupements carbonyles. Il semble que pour le PET, la cristallisation ne modifie pas réellement le mouvement des carbonyles dans la phase amorphe. En revanche, le PEF a une température de transition β qui apparaît diminuée d'environ 10 °C entre un échantillon semi-cristallin et un échantillon amorphe. Le pic de cette transition peut être décomposé en deux parties : le côté gauche (basse température) est à relier avec les carbonyles en conformation *anti* (moins énergétiques), tandis que le côté droit (plus haute température) est lié aux carbonyles en conformation *syn* (plus énergétiques). Lors de la cristallisation, une partie des carbonyles prend la conformation *syn*. De ce fait, la partie amorphe des échantillons semi-cristallins est constituée principalement de carbonyles en conformation *anti*. Il ne reste donc observable, en DMTA, que le côté gauche du pic de cette transition. Ceci explique l'apparente diminution de température pour les échantillons semi-cristallins.

1. Introduction

This chapter is based on two papers published in respectively *Polymer* and *Macromolecules* journals, and aims at comparing the SIC with the crystal obtained from the static crystallization, for PEF and PET [65,67].

The crystal structure of PEF was first proposed by Kazaryan et al., in 1968 [101]. A triclinic system was suggested. This structure has been recently revisited by Mao et al., in a monoclinic system composed of two repeat units, instead of one, along the *c*-axis [58]. This could be more appropriate to optimize the chain packing. Concerning PET, the crystal structure proposed by Daubeny et al. is unique, and is a triclinic one [11]. Only one repeat unit is necessary [11]. The unit cell parameters of PEF, triclinic and monoclinic, and of PET, triclinic, are reported on Table 8.

Material	System	<i>a</i> (Å)	<i>b</i> (Å)	<i>c</i> (Å)	α (°)	β (°)	γ (°)
PEF	triclinic [101]	5.75	5.35	20.10	133.3	90	112
	monoclinic [58]	5.78	6.78	20.296	90	90	103.3
PET	triclinic [11]	4.56	5.94	10.75	98.5	118	112

Table 8. PEF and PET crystal structure and unit cell parameters.

In PET, based on a conformational analysis, it is reported that the amorphous phase is composed of a majority of ethylene glycols (EG) in *gauche* conformation; while in the crystal there is the existence of EG in *trans* conformation [72,76,103–110]. Recently, Araujo et al. [102] have suggested that, for PEF, the crystal needs EG in *trans* conformations, as in PET. Additionally, in the crystal, the furan cycles must be in *syn* conformations. The *trans* conformation is related to the extended chain. In conclusion, in PEF, there is a majority of *anti*^{FDCA}*gauche*^{EG} conformations in the amorphous phase, while in the crystal only *syn*^{FDCA}*trans*^{EG} can exist [102]. This additional conformational change results from the furan ring presence in PEF, which has a lower symmetry compared to the benzene ring of PET [46]. The need of two repeating units in the crystal, and the complexity of combining two changes in conformations could be a clue to explain the slow crystallization kinetic of PEF [53,55,57]. Figure 28 represents the conformations mentioned previously.

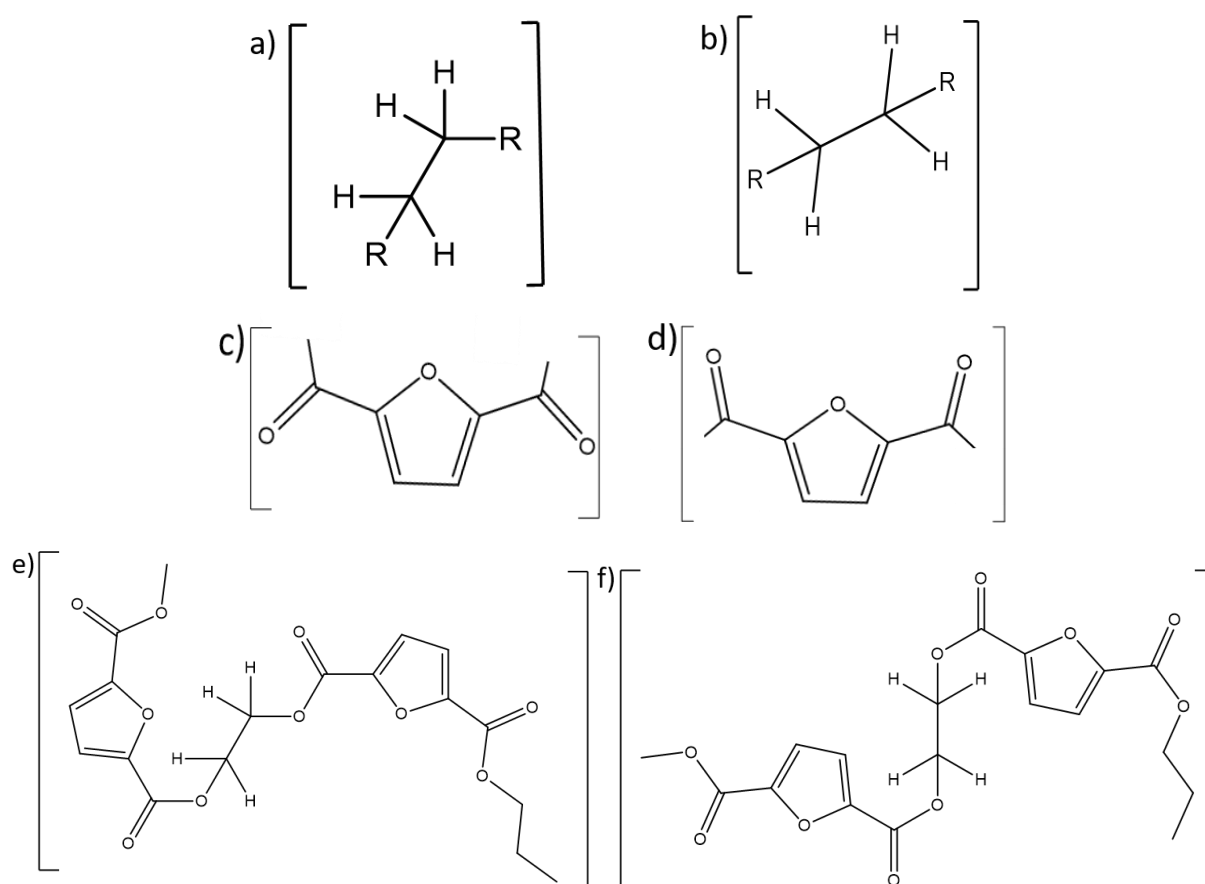


Figure 28. Ethylene glycol in (a) *gauche* (b) *trans* conformations, furan in (c) *anti* (d) *syn* conformations, (e) *anti*^{FDCA}*gauche*^{EG} (f) *syn*^{FDCA}*trans*^{EG} [67].

To build a crystal, either in static or dynamic conditions, the chains must change their initial conformations and be in the conformations that can exist in the crystal. But, the crystal is formed only if these conformations are stabilized by the interactions, such as hydrogen bonding, of the neighbouring chains. During the static crystallization, these conformational changes occur with the thermal energy given to the system; while for SIC, their occurrence is due to the mechanical energy brought by the stretching. During the stretching, the chains are extended, and oriented in the stretching direction. Thus, the conformational changes can occur rapidly, and without being at such high temperature than in static crystallization. Finally, the chains can organize themselves in the space and, if they are stabilized by the interactions, the crystal is formed.

The crystal structure of PET is well accepted, and the diffraction pattern well indexed [111,112]. The same crystal structure is reported for SIC or upon static crystallization. As PEF is a relative new material, the degree of certainness concerning its crystalline system and its unicity is not equivalent. Some existing results suggest a possible crystalline polymorphism for

PEF [55,56,113]. It means that the crystal structure can depend on the crystallization conditions, such as temperature, pressure, way of crystallization (solvent or strain induced crystallization). Up to now, the reported crystalline forms could be α , α' and β (Table 9). These forms have been indexed from powder X-ray scattering by Maini et al [113]. Accounting for the fact that PEF crystallization is quite difficult and slow, one has to be cautious that a potential difference in lamellae structure could also be argued. The work of Araujo et al. reveals that the same conformations exist in the crystal, for both α and β crystalline structure [102].

Form	Crystallization conditions
α [55]	Thermodynamically stable form, obtained from static crystallization and $T_c \geq 170^\circ\text{C}$
α' [55]	Defective form obtained from static crystallization and $T_c \leq 170^\circ\text{C}$
α' [65]	Crystalline form obtained after strain induced crystallization
β [56]	Crystalline form obtained after solvent crystallization

Table 9. Crystalline forms reported in PEF.

In this work, the analysis is based on the Mao's crystal structure, which is closer to our experimental protocol [58,59]. Firstly, SIC is analysed and compared to the crystal induced upon static crystallization, under the α' -form, for PEF. The WAXS indexation is reported [65]. Then, both crystals are characterized in terms of crystal definition and conformational changes [67]. The results are compared with PET.

2. Analysis of the crystalline structure of PEF

2.1 Crystalline structure induced by the stretching

For clarity, the exhaustive analysis is described using only one of the stretching conditions presented in the previous chapter for PEF and PET. The experimental settings are mentioned in Table 10. According to the stretching settings reported, for PEF and PET, one sample has been stretched up to the rupture and then air-quenched, while another one has been stretched up to a defined strain and then air-quenched before the unloading. This last sample is named “interrupted”. It has been chosen to stop the stretching below and far from the NDR, at $\epsilon_{xx} = 0.90$ and $\epsilon_{xx} = 1.20$ for respectively PET and PEF. The stress-strain curves and the associated Debye-Scherrer of each samples are represented in Figure 29. The distance between the sample and the screen is of 75 mm (D). The Miller’s indices of each family of planes are reported for both materials. On the true stress/strain curves the crosses designate the strains at which the stretching has been stopped for the “interrupted” tests.

Materials	Stretching settings ($s^{-1} / ^\circ C$)	Localization on the master curve and equivalent strain rate (s^{-1})	Stretching specificity	Debye-Scherrer pictures
PEF	0.035 / 101	Middle of the rubbery plateau (10^{-2})	Rupture (D-PEF)	Figure 29.c
			Stretched and interrupted, $\epsilon_{xx} = 1.20$ (I-PEF)	Figure 29.e
PET	0.020 / 95	End of the rubbery plateau ($2 \cdot 10^{-3}$)	Rupture (D-PET)	Figure 29.d
			Stretched and interrupted, $\epsilon_{xx} = 0.90$ (I-PET)	Figure 29.f

Table 10. Stretching settings of PEF and PET.

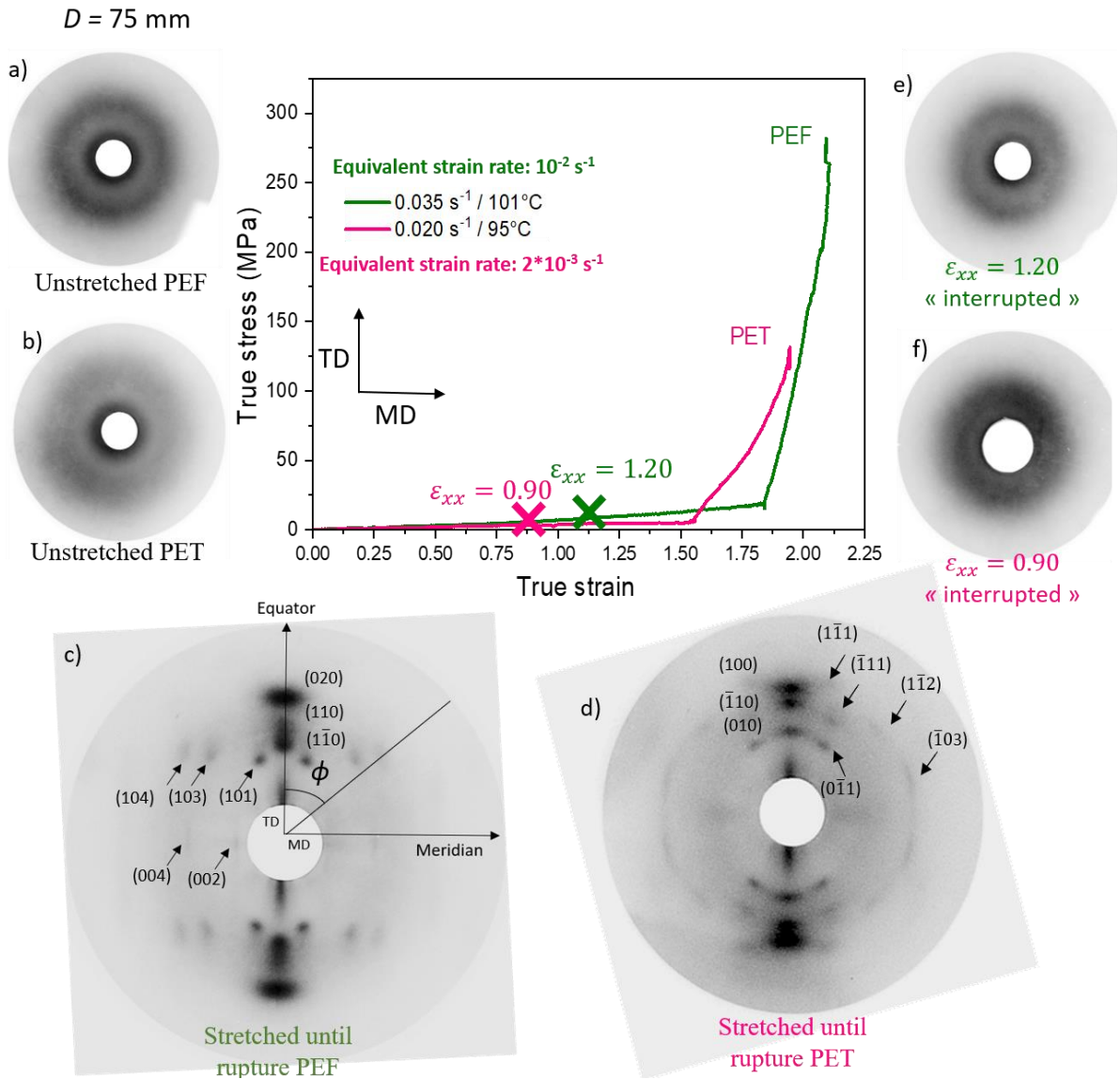


Figure 29. True stress/strain curves of uniaxially stretched PEF and PET with associated Debye-Scherrer of non-stretched (a) PEF and (b) PET; stretched up to rupture (c) PEF and (d) PET; stretched and interrupted (e) PEF and (f) PET. MD is the stretching (or machine) direction whereas TD is the transverse direction [65,67].

On the Debye-Scherrer patterns, a clear fiber-like texture can be observed after the stretching until rupture, (Figures 29.c and 29.d) whereas initial PEF and PET only exhibit an amorphous halo (Figure 29.a and Figure 29.b). In Figures 29.c and 29.d, because of the presence of spots, both the crystalline character of the material and the crystal orientation are manifest. The protocol to identify the Miller's indices (hkl) has been described in the Chapter 1 (7. Determination of the Miller's indices).

According to the fact that the material should develop a fiber texture, with the chain axis c parallel to the stretching direction, the spots in the transverse direction, TD (equatorial

direction), are supposed to be associated with $(hk0)$ planes. These planes contain the chain axis. Moreover, in the meridional direction two spots, which appear with a weaker intensity in this direction, are observed. They are the trace of reflections of the $(00l)$ types that correspond to the crystalline planes oriented perpendicularly to the chain axis and, consequently, to the stretching direction. Other even weaker spots are visible in some positions that are neither equatorial nor meridional. They are associated to (hkl) planes. To summarize eight spots are visible on this first pattern (Figure 29.c): three in the equatorial direction, two in the meridional direction and three others in locations that are neither equatorial nor meridional [65]. PET indexation is coherent with previous works [111].

When the distance between the sample and the imaging plate decreases ($D = 30$ mm), some other spots become observable (Figure 30). The meridional spots, which are difficult to discriminate in this picture, are better evidenced on the radial scan (Figure 31).

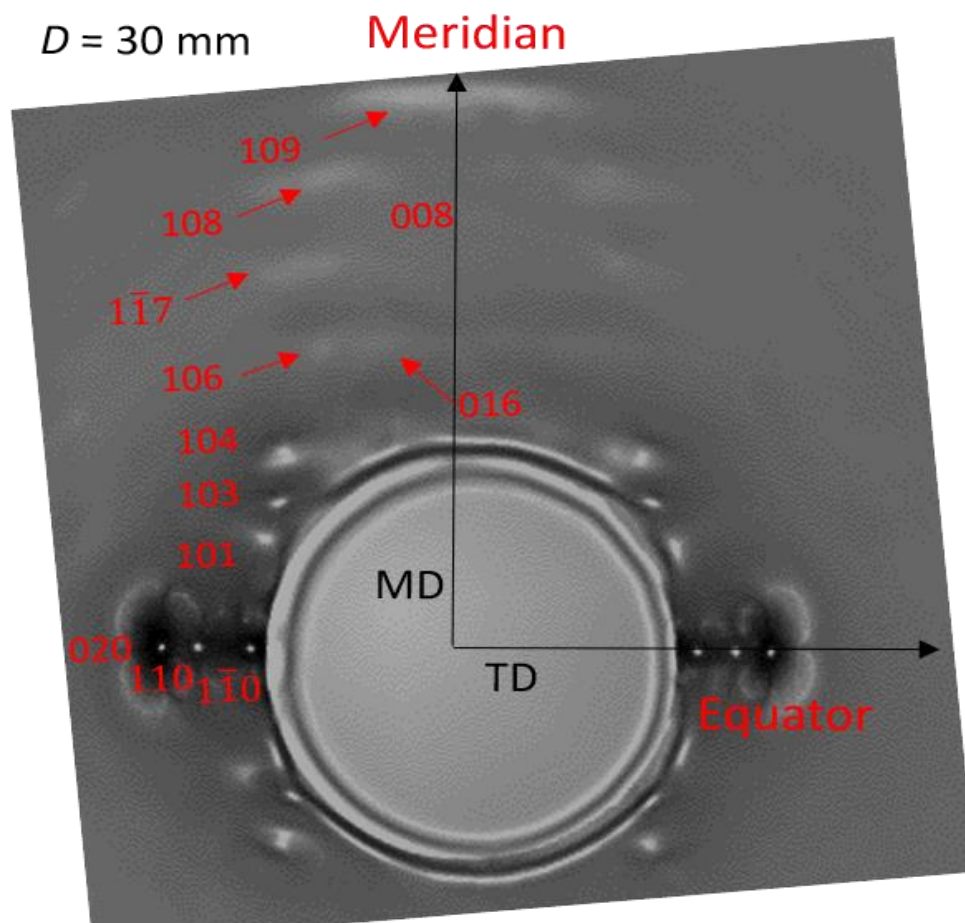


Figure 30. Debye-Scherrer pattern for stretched PEF. MD is the stretching direction whereas TD is the transverse direction [65].

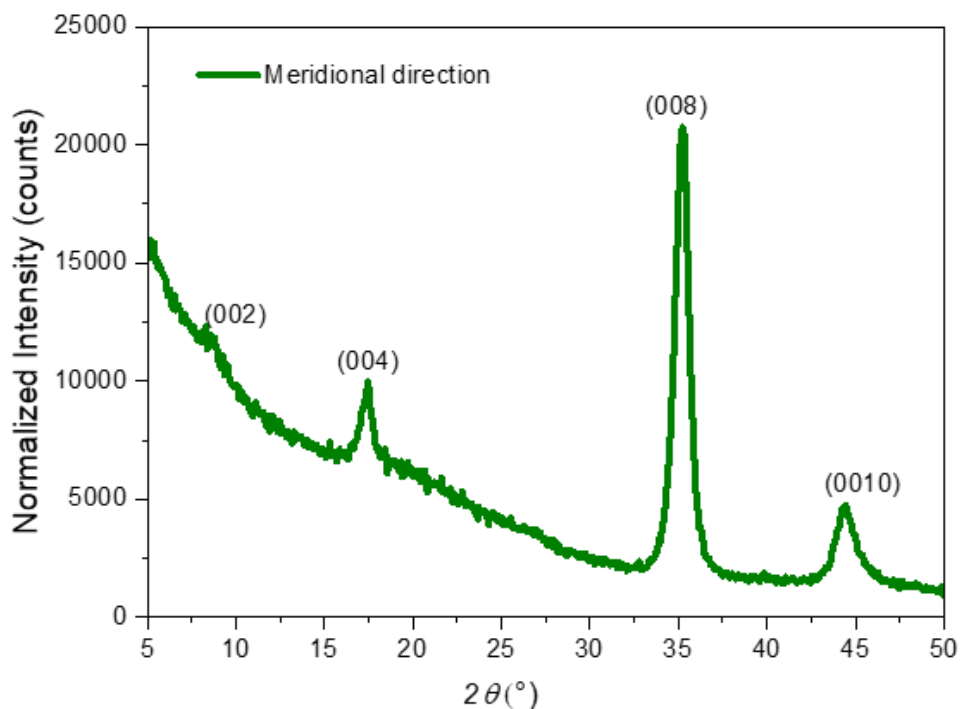


Figure 31. Radial scan diffractogram obtained in transmission mode, in the meridional direction [65].

Then, in Figure 31, four diffraction peaks, hardly noticeable in Figure 30, become visible. The (hkl) indexes are reported in Figure 30. The low intensity spots are designated with arrows to make the reading easier. As classically for a fiber texture, the (hkl) reflections are organized into hyperbolic layers, each layer being labelled by the value of l . For the positive values of l , nine layers can be observed in Figure 30. It is possible to index all the reflexions in agreement with the fact that PEF crystallizes in a monoclinic system [58]. Table 11 reports the values of 2θ ($^\circ$), the (hkl) indexes and the interreticular spacing d_{hkl} (\AA).

Localization	2θ (°)	(hkl)	d_{hkl} (Å)
Meridian	8.70	002	10.148
	16.34	101	5.421
Meridian	17.46	004	5.074
Equator	18.20	$1\bar{1}0$	4.869
	20.52	103	4.325
Equator	23.00	110	3.864
	23.60	104	3.768
Equator	27.00	020	3.299
	29.66	016	3.010
	30.82	106	2.900
Meridian	35.34	008	2.537
	36.02	$1\bar{1}7$	2.491
	38.92	108	2.313
	43.18	109	2.093
Meridian	44.60	0010	2.030

Table 11. Identification of the crystalline families of planes for stretched PEF [65].

For each (hkl) proposal, the indexation considers the eventual multiple orders of l , and it has been checked that the position of the diffraction on the fiber diagram is correct.

Many spots are revealed by the analysis conducted in this work, it testifies of a strong crystalline organization, and of the presence of a fiber texture with a high scale periodic order. Most of the spots are in agreement with the results of Mao et al. [58,59]. The efficiency of the stretching protocol established has to be pointed out, as it allows the observation of the same families of planes as those reported by Mao et al., but without the need of using the synchrotron. Moreover, with this protocol, the samples of this work have a crystal ratio higher than what is reported by Mao et al [58,59] (more than 30% in this work). These results prove that PEF can develop a well-defined SIC, if the relevant stretching parameters are applied. Thus, it can be imagined

that, on the sample of this work, other families of planes can become detectable with the use of a more powerful device, such as the synchrotron.

However, some slight differences exist between the work of Mao et al. and this one.

Firstly, the (002) family of planes, which is the first meridional spot in Figure 29 and the first diffraction peak in Figure 31 is not reported on the indexation of 2018. It is due to the too close position of the peak in relation to the central cone of the wide-angle detector [59]. Secondly, the (110) family of planes is also absent of the indexation made by Mao et al. in 2018 [59]. When the crystal structure is not well-defined and perfected, this family of planes can be superimposed to the ($1\bar{1}0$) family of planes. As the stretching of Mao et al. leads to less than 5% of crystal, it can explain a possible merging of the ($1\bar{1}0$) and (110) families of planes, in their work. Nevertheless, these two reflections are present in another publication of Mao et al. [58]. Finally, the last difference concerns the (019) and (0110) families of planes which cannot be observed in the Debye-Scherrer patterns of this study. It is due to a high wavelength used in the lab, 1.54 Å, instead of the lower wavelength of the synchrotron, 0.7293 Å [59]. The (0010) family of planes is hardly detected on some Debye-Scherrer patterns, but clearly identified on the radial scan (Figure 31).

In the previous Debye-Scherrer pattern (Figure 30), it was noticeable that many families of planes appear rather as arcs than as spots, especially when the angular position increases. Stoclet et al. [61] have also reported the presence of arcs with low intensity close to the meridional direction. They have mentioned the presence of spots with higher intensity in the equatorial direction. The authors have related the meridional arcs to a mesophase, and the spots to a crystalline structure. They have concluded that, contrary to PET which forms a mesophase before its crystal, it seems that PEF mesophase is still there, even after an annealing step, and thus, is able to coexist with a crystalline form. As a consequence, PEF mesophase would not be a crystal precursor as it is in PET [61]. The results of our work are more consistent with the existence of an unique highly defined crystalline phase, with more or less intensity in the diffraction by the families of planes. This will be discussed in the following part.

2.2 Comparison with the crystal formed by static crystallization

A comparison between the crystal induced upon an isothermal cold crystallization (160 °C during 2h from the solid state, crystallization in the α' form) and the one induced by the stretching has been performed. Figure 32 shows the pattern obtained for the isothermal cold crystallization (Figure 32.a), with a distance sample-screen of 75 mm, as well as the associated radial scan performed in transmission mode (Figure 32.b).

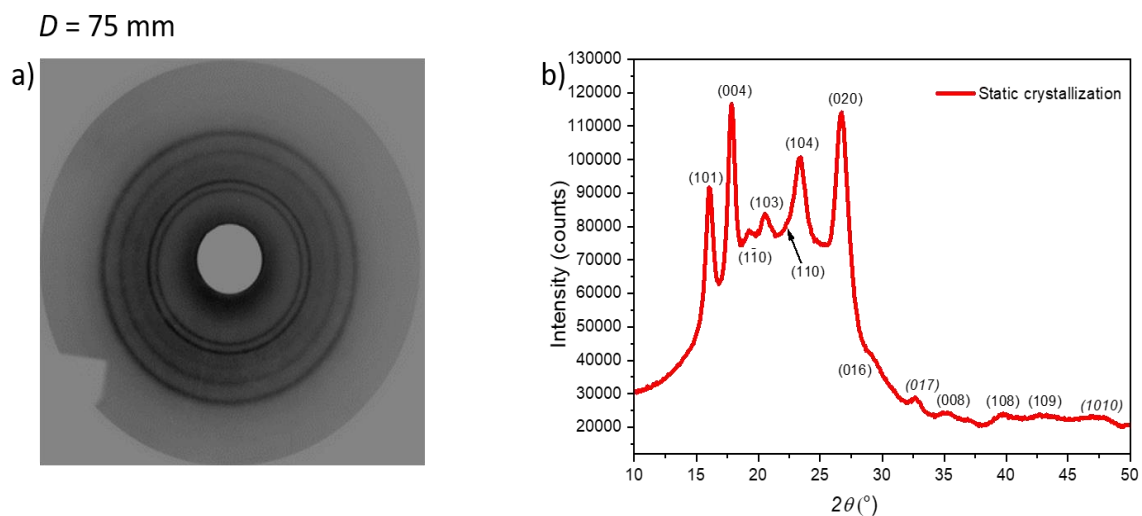


Figure 32. (a) Debye-Scherrer pattern and (b) radial scan, in transmission mode, of a PEF sample crystallized in static conditions, at 160 °C during 2h [65].

The cold crystallization leads to an isotropic well-defined crystalline phase, whose signature is continuous diffraction rings. It is worth noticing that the thermal crystallization required 2h at 160 °C, whereas SIC only took few seconds at 101 °C. It underlines the efficiency of the mechanical loading to promote crystallization, as it orients the chains prior to crystallization. Table 12 gathers the indexation of the families of planes found in SIC and in static crystallization.

SIC		Static Crystallization	
<i>(hkl)</i>	2θ (°)	<i>(hkl)</i>	2θ (°)
002	8.70	Too low intensity	
101	16.34	101	16.00
004	17.46	004	17.87
1 $\bar{1}$ 0	18.20	1 $\bar{1}$ 0	19.20
103	20.52	103	20.55
110	23.00	110	22.40
104	23.60	104	23.37
020	27.00	020	26.77
016	29.66	016	29.33
106	30.82		
		017	32.89
008	35.34	008	35.20
1 $\bar{1}$ 7	36.02		
108	38.92	108	39.67
109	43.18	109	43.20
0010	44.60		
		1010	47.60

Table 12. Comparison of the families of planes existing after SIC and after static crystallization [65].

One unique crystalline phase seems to exist. Additionally, this phase is equivalent to that suggested by Stoclet et al. for the crystallization in the defective α' form (crystallization temperature below 170 °C) [55]. But some angular positions can be slightly different between SIC and static crystallization.

These differences can be associated to the crystallization in an extended conformation in SIC, compared to the static crystallization where more packing can occur. These slight differences

observed can also be due to a lack of precision of the measurement, and to the definition of the families of planes that can change between static crystallization and SIC. Indeed, in the radial scans (Figures 31 and 32.b), the peak associated to the presence of the same family of planes can be more or less wide between SIC and static crystallization.

The (002) family of planes is not discernible on the static crystallization scan, because of its too low intensity it cannot be dissociated from the signal noise. The indexation of ($1\bar{1}0$) and (110) families of planes, which are among the most intense reflections in stretched specimens, raises some problems:

- in the indexation of Figure 32, ($1\bar{1}0$) is the third peak at a 2θ angle close to 19.2° , far from the theoretical one of 18.2° . (110) appears as a shoulder on (104) peak;
- one can also consider that the second peak results from the overlapping of (004) at 17.5° and ($1\bar{1}0$) at 18.2° . In such a case, the third peak remains unexplained.

The bumps detectable for 2θ above 28° , in Figure 32, for the static crystallized sample, could be the diffuse arcs observed on the Debye-Scherrer patterns of the stretched sample. The same indexation protocol is possible for many bumps. The two bumps with italic indexes in Figure 32.b, (017) and (1010), might not be detectable on the stretched sample because of a too low intensity for the (017) family, and a too high wave length for (1010). The presence of these bumps for the static crystallized sample, above 28° , confirms the existence of the same microstructural organization between the stretched samples and the thermally crystallized one. Finally, X-ray analysis corroborates that SIC and the static crystallization under the defective form, α' , are equivalent. Some slight differences subsist, especially in the angular positions, but the indexed crystalline families remain the same. In the frame of this work, PEF seems not to be a polymorphic material, and there is not a coexistence of a mesophase and a crystal, but the existence of only a strong and well-defined crystalline organization.

By analysing the conformational changes found in amorphous, stretched and thermally crystallized PEF samples, the comparison between the two crystallization way and their similarities will add data on the crystal structure of PEF. A comparison with PET (amorphous, stretched and thermally crystallized) can give details on the stretching mechanism in both materials.

3. Conformations involved in PEF and PET

The objectives in this part are firstly to better understand the induced microstructure in PEF. In parallel, comparisons with PET, on one hand, and with PEF crystallized in static conditions are hoped to reveal the effects of respectively the chain architecture and the mechanical loading. The samples crystallized in static conditions are named TC-PEF and TC-PET, while the amorphous ones are referred as A-PEF and A-PET, for respectively PEF and PET. The name of the other samples is visible in Table 10. The two “interrupted” conditions aims at highlighting the first part of the chain that is impacted by the stretching. Moreover, these two “interrupted” samples are still amorphous after the low stretching undergone (as visible in Figure 29.e and 29.f). A special interest is on the carbonyls motions, as they are directly related to the secondary β -relaxation [67]. Table 13 gathers the vibrational bands studied, the chemical group associated as well as the related figures for PEF and PET. Depending on the samples some shift of the vibrational bands can exist, the values reported in Table 13 are then indicative values associated to the amorphous sample or to the static crystallized one.

PET			PEF		
Band (cm ⁻¹)	Chemical group	Figure	Band (cm ⁻¹)	Chemical group	Figure
			609 (bending) / 1576 (stretching)	<i>syn</i> ^{FDCA}	Figure 34.a Figure 34.b
			617 (bending) / 1580 (stretching)	<i>anti</i> ^{FDCA}	Figure 34.a Figure 34.b
975	<i>trans</i> ^{EG}	Figure 36.a	990 / 1040	<i>trans</i> ^{EG} ?	Figure 36.b
1015	<i>C=C-C</i> (<i>bending</i>)	Figure 36.a	1015	<i>C=C-C</i> (<i>bending</i>)	Figure 36.b

1045	<i>cis</i> ^{EG}	Figure 36.a				
1090	C-O-C (<i>stretching</i>)	Figure 37.a		1115	C-O-C (<i>stretching</i>)	Figure 37.b
1236	O=C-O-C (<i>stretching</i>)	Figure 37.a		1225-1275	O=C-O-C (<i>stretching</i>)	Figure 37.b
1340	<i>trans</i> ^{EG} (<i>wagging</i>)	Figure 33.a		1340	<i>trans</i> ^{EG} (<i>wagging</i>)	Figure 33.b
1380	<i>gauche</i> ^{EG} (<i>wagging</i>)	Figure 33		1380	<i>gauche</i> ^{EG} (<i>wagging</i>)	Figure 33.b
1460	<i>gauche</i> ^{EG} (<i>bending</i>)	Figure 33.a		1460	<i>gauche</i> ^{EG} (<i>bending</i>)	Figure 33.b
1480	<i>trans</i> ^{EG} (<i>bending</i>)	Figure 33.a		1480	<i>trans</i> ^{EG} (<i>bending</i>)	Figure 33.b
1710	C=O (<i>stretching</i>)	Figure 38.a		1718	C=O (<i>stretching</i>)	Figure 38.b
				1732	C=O (<i>syn-shoulder</i>)	Figure 38.b
				3120 / 3160	=C-H (<i>furan</i>)	Figure 35

Table 13. Values of the vibrational bands with the chemical groups associated and the related figures.

3.1 Conformational changes due to crystallization occurrence

As for PET [66,74,77,107,108], it is proposed that the crystallization increases the proportion of EG in *trans* conformation, in the PEF samples [67,102]. Figure 33 (a and b) deals with these changes for respectively amorphous, thermally crystallized and stretched PET and PEF.

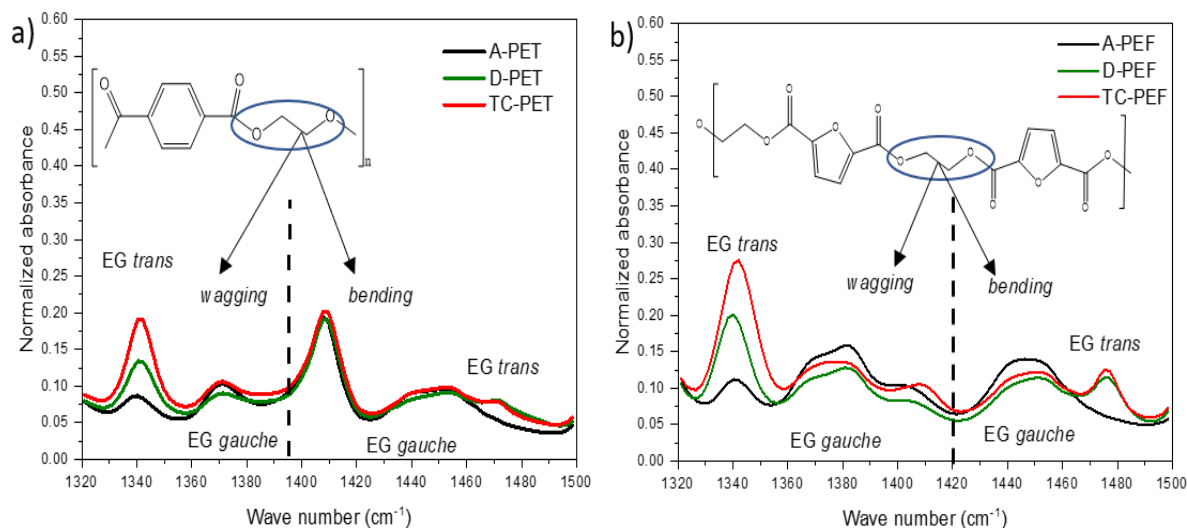


Figure 33. FT-IR spectra from 1320 to 1500 cm^{-1} of amorphous (black, A-PET/A-PEF), stretched until rupture (green, D-PET/D-PEF) and thermally crystallized (red, TC-PET/TC-PEF) [67].

The stretched (D-PET/D-PEF) and the thermally crystallized (TC-PET/TC-PEF) samples exhibit almost the same trend, with a coexistence of *gauche*^{EG} and *trans*^{EG} conformations. On the all, the signature of the *gauche* conformation decreases in “D” and “TC” samples, whereas the signature of the *trans* conformation increases, compared to the amorphous materials (“A”). The bending phenomena indicate that, whatever the source of crystallization is, the *trans* conformation occurrence increases and the *gauche* one decreases, which could be the signature of the crystallization. The wagging of the EG is different in D-PEF samples compared to TC-PEF, for *gauche* and *trans* conformations. However, the crystalline fraction are equivalent for D-PEF and for TC-PEF (around 35%, more details in Chapter 5). This suggests, in agreement to what is known for PET, that probably the amorphous phase could be constrained by the stretching. Then, the shape of the band associated to the *gauche* conformation appears different for the stretched samples. Thus, the stretching can impact the occurrence of conformational changes, and/or can change the mobility of the EG in *gauche* and

trans conformations. The band at 1340 cm^{-1} seems wider for TC-PEF compared to D-PEF, it could be the result of a different chemical environment.

Figure 34 (a and b) compares the absorbance between the amorphous (A-PEF) and the crystallized samples (TC-PEF and D-PEF), in the furan ring deformation regions.

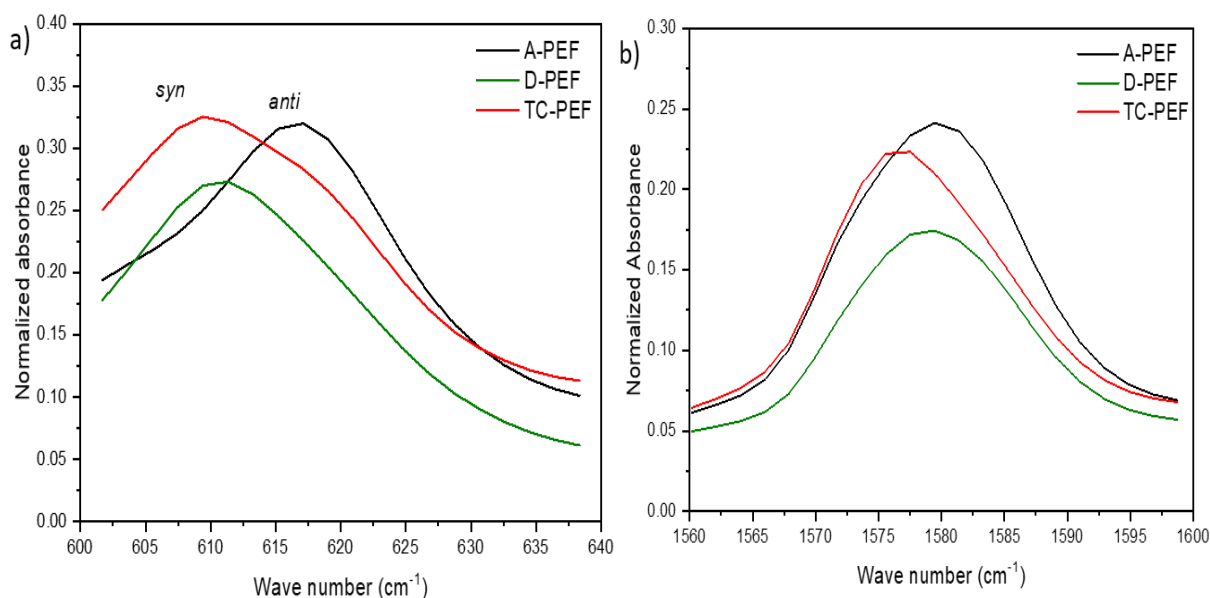


Figure 34. FT-IR spectra from (a) 600 to 640 cm^{-1} and (b) from 1560 to 1600 cm^{-1} of amorphous (black, A-PEF), stretched (green, D-PEF) and thermally crystallized (red, TC-PEF) [67].

The *syn* conformation is characterized by a peak at 609 cm^{-1} , while the *anti* conformation exhibits a peak around 617 cm^{-1} (Figure 34.a) [102]. This corresponds to what is observed for amorphous (A-PEF) and static crystallized samples (TC-PEF). Nevertheless, the stretched sample (D-PEF) exhibits a peak maximum at 610 cm^{-1} . Thus, it can be concluded that SIC results in an increase of the absorption energy of the existing *syn* groups or, leads to the formation of groups in *anti* conformation with a much lower absorption energy. If it is stated that the crystal is only constituted of *syn* conformation. Then, the first hypothesis may be retained, and it can be concluded that SIC induces a slight shift to the higher energy for the *bending* of the furan cycle in *syn* conformation.

A shoulder is detectable at 618 cm^{-1} for the thermally crystallized sample which can be the signature of the presence of furans in *anti* conformation in the amorphous phase. But, the signal corresponding to the furan cycles in *syn* conformation dominates, in the semi-crystalline samples. The thermally crystallized sample (TC-PEF) exhibits a broader peak with a shoulder

for the *anti*^{FDCA} conformation, while D-PEF shows predominantly the *syn* conformation. It is likely that the stretching has led to more homogeneous chemical environment.

Figure 34.b shows the C=C stretching of the furan ring, in the 1550–1660 cm⁻¹ region. The amorphous PEF presents a band at 1580 cm⁻¹, while TC-PEF, as the consequence of the predominance of the *syn*^{FDCA} conformation, shows a broadening of the band to lower wave numbers, with a maximum at 1576 cm⁻¹. In agreement with Figure 34.a, the band of D-PEF in the 1550–1660 cm⁻¹ region is thinner compared to those of A-PEF and TC-PEF (Figure 34.b). It would mean that the statistical distribution of the conformations is more limited in D-PEF, due to the mechanical stretching that imposes the alignment of the chains. Thus, it limits the discrepancies of conformations compared to un-oriented chains. In Figure 34.b, a real difference is noticeable between D-PEF and TC-PEF. Indeed, the band of D-PEF appears shifted to higher energy, compared to the one of TC-PEF. Nevertheless, the presence of furans in *syn* conformation has been demonstrated in Figure 34.a. Thus, this shift can be due to a higher constrain of the furan ring in the stretched sample. Furans are fixed in *syn* conformation and they need more energy to allow the vibration.

3.2 Aromatic =C-H and cycle breathing

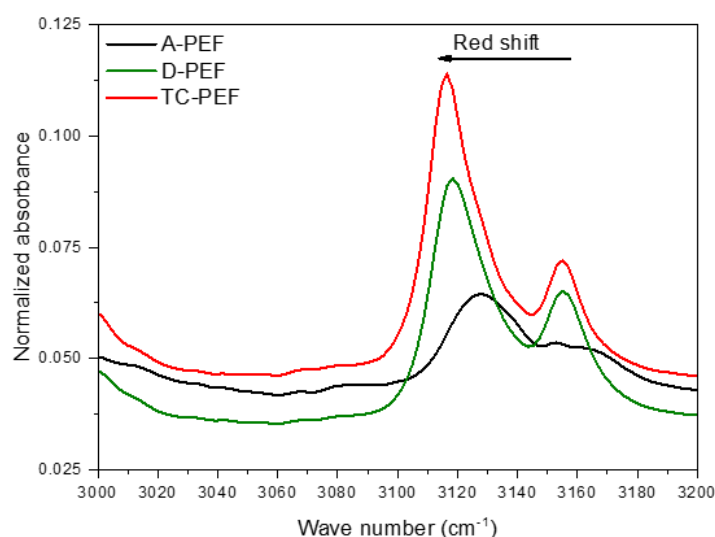


Figure 35. FT-IR spectra from 3000 to 3200 cm⁻¹ of amorphous (black, A-PEF), stretched until rupture (green, D-PEF) and thermally crystallized (red, TC-PEF) PEF [67].

Figure 35 focuses on the region of absorption of the methylene group =C-H of the furan cycles. Two populations of ring stretching can be identified with different neighbourhoods: one absorption band around 3120 cm^{-1} (i.e. symmetric stretching of C-H from furan), and the other around 3160 cm^{-1} (overtone of the asymmetric C=C stretching). Both crystallization paths result in an intensification of these two bands together with a red-shift. It is consistent with Araujo et al. [102], and with the intensification of C-H stretching band due to the hydrogen bonding between the furan and the carbonyl (=C-H--O=C). The red shift and the peak intensification are similar between TC-PEF and D-PEF, suggesting similar inter-locking between the chains for the two crystallization paths.

Figure 36 compares the IR spectra obtained in the region of the cycle breathing (C=C-C) for PET (Figure 36.a) and PEF (Figure 36.b).

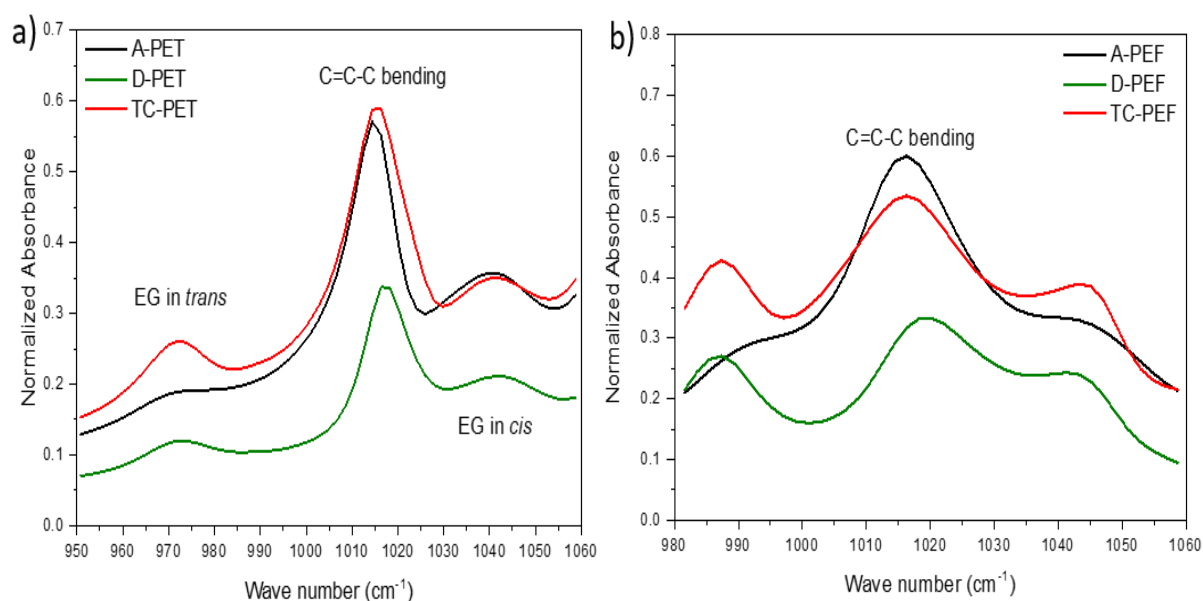


Figure 36. FT-IR spectra from (a) 950 to 1060 cm^{-1} and (b) 980 to 1060 cm^{-1} of respectively amorphous (black, A-PET/A-PEF), stretched (green D-PET/D-PEF) and thermally crystallized (red, TC-PET/TC-PEF) [67].

For PET (Figure 36.a), the shoulder at 973 cm^{-1} is associated to the EG in *trans* conformation [66], and increases for TC-PET and D-PET. For them, a peak is observed. As A-PET has more *gauche* conformation, it can explain the lower intensity of this peak. Whereas, the bump at 1042 cm^{-1} is associated to the EG in *cis* conformation. The band intensity associated to this conformation decreases after the stretching process, which is in agreement with a crystallization

process [66]. For PET, both crystallization paths seem to shift slightly the peak at 1015 cm^{-1} to 1018 cm^{-1} , i.e. to higher energy. This peak is ascribed to the in plane stretching of the C-H bending of the benzene cycle [46], and its shift witnesses of a higher constrained of the benzene ring for TC-PET and D-PET.

Regarding PEF (Figure 36.b), there is the apparition of two peaks at 986 cm^{-1} and 1045 cm^{-1} on the crystallized samples, that can be ascribed to the signature of the crystal apparition. In a similar manner than in PET, the peak around 974 cm^{-1} can be related to an increase of the EG in *trans* conformation. The main peak is observed at 1016 cm^{-1} , for A-PEF, and is shifted towards higher values for D-PEF. This is explained by a more constrained ring in stretched sample, in comparison with A-PEF and TC-PEF.

The following section aims at exploring, more deeply, the differences existing on the aliphatic part of PEF and PET.

3.3 Transformations in the aliphatic part in PEF and PET

Figures 37 focus on the absorption band linked to the ether group, especially the $\text{O}=\text{C}-\text{O}-\text{CH}_2$ (named C-O-C) stretching ($1050\text{-}1150\text{ cm}^{-1}$), and to the ester, the $\text{O}=\text{C}-\text{O}-\text{C}$ stretching ($1200\text{-}1300\text{ cm}^{-1}$) both for PET (Figure 37.a) and PEF (Figure 37.b). Moreover, the comparison with the interrupted PET and PEF samples, stretched to respectively a strain of $\epsilon_{xx} = 0.90$ (I-PET) and $\epsilon_{xx} = 1.20$ (I-PEF), has been added to get information on the influence of the first stretching steps on the vibrational modes of the aliphatic part of the chain. As a remind, these two samples are still amorphous despite the stretching (Figures 29.e and 29.f).

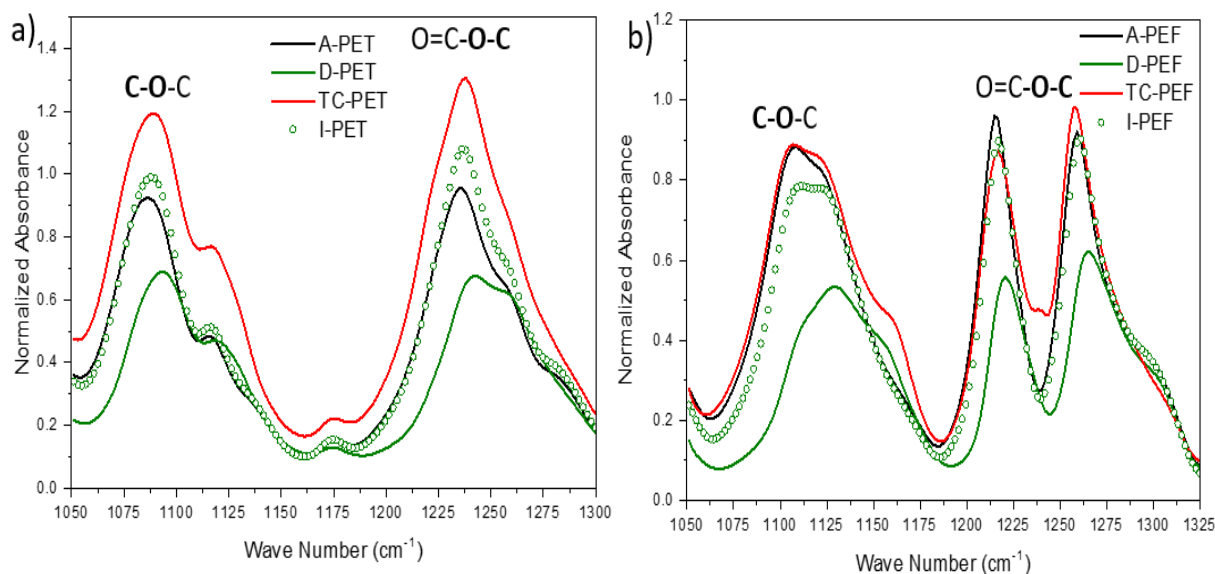


Figure 37. FT-IR spectra from (a) 1050 to 1300 cm⁻¹ and (b) 1050 to 1325 cm⁻¹ of amorphous (black, A-PET/A-PEF), stretched (green lines, D-PET/D-PEF), stretched and interrupted (green dots, I-PET/I-PEF) and thermally crystallized (red, TC-PET/TC-PEF) [67].

A limited shift towards higher energy (around +3 cm⁻¹) appears for TC-PET compared to A-PET (Figure 37.a). It suggests that the crystal formed upon static crystallization impacts slightly the C-O-C (1086 cm⁻¹), or the O=C-O-C stretching (1236 cm⁻¹). On the other hand, a clear cut shift of about 7-8 cm⁻¹ is highlighted for D-PET, compared to A-PET. It could indicate that the ester and ether groups are more constrained after SIC than after the static crystallization [67].

About PEF the same trend, as in PET, is highlighted (Figure 37.b): TC-PEF shows ester stretching bands at the same chemical position than A-PEF. The blue-shift due to PEF stretching is highlighted for the O=C-O-C band (+ 5-6 cm⁻¹), in the same line as PET. However the shift of the C-O-C peak, around 1128 cm⁻¹ (i.e. + 22 cm⁻¹), is much more pronounced for D-PEF compared to D-PET. It would indicate that the C-O-C linkage in PEF becomes more constrained upon stretching. In PEF, the shoulder at 1150 cm⁻¹ can be considered as the signature of the crystal apparition, as it is detectable only on D-PEF and TC-PEF [67].

Interestingly, the spectra of interrupted PEF and PET samples (I-PEF and I-PET) in Figures 37 shed new light on the development of the microstructure upon stretching. Indeed, when the stretching of PET is interrupted before its NDR, the spectral signature is almost comparable to the amorphous sample with only a limited shift on the peak maxima for the ester region (Figure 37.a). For I-PEF, the contribution of the peak at 1107 cm⁻¹ decreases and broadens to higher wavenumbers, with a higher contribution of the band at 1125 cm⁻¹. This represents an intermediary situation between the amorphous and the stretched PEF. A slight shift towards

higher energy is detectable on the ether and ester groups. The initial steps of PEF stretching have a particular influence on the C-O-C stretching, while the O=C-O-C band is less affected. Indeed the C-O-C is directly in the alignment of the chain, and thus is more sensitive to the strain. Thus, the band representative of the C-O-C appears at higher energy, in D-PEF, and can be considered as a signature of the mechanical stretching [67].

Figure 38 shows the carbonyl band of PET and PEF for the amorphous, the thermally crystallized, the mechanically crystallized, and the stretched and interrupted samples [67].

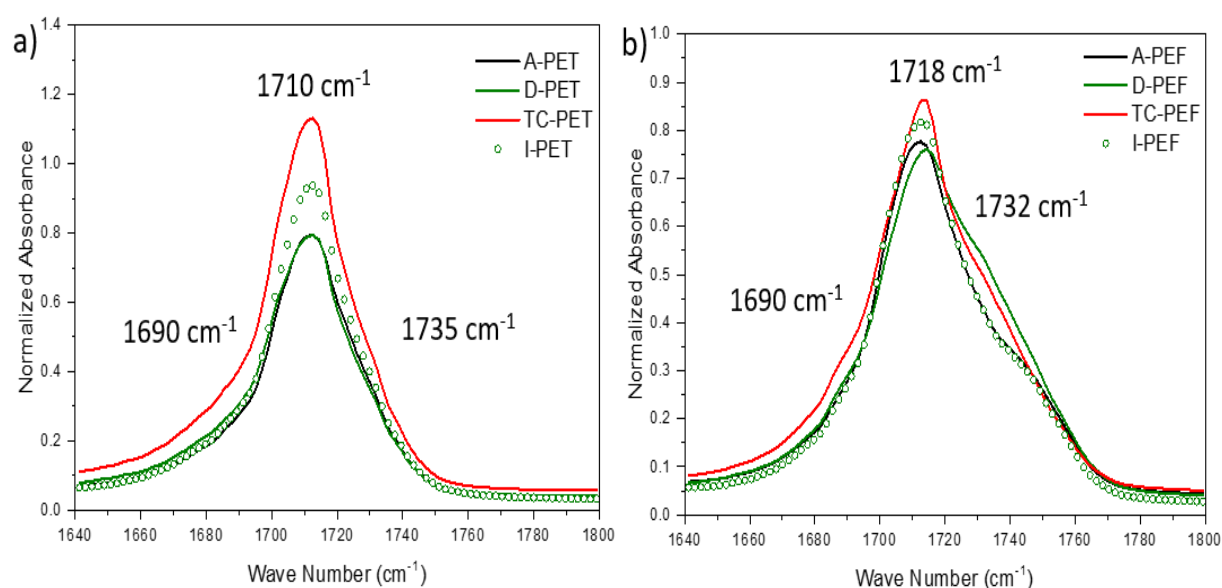


Figure 38. FT-IR spectra from 1640 to 1800 cm^{-1} of amorphous (black line), stretched up to rupture (green line), stretched and interrupted (green dots) and thermally crystallized (red) of (a) PET and (b) PEF samples [67].

Concerning PET, a main peak is observed at 1710 cm^{-1} and is attributed to C=O stretching. A weak shoulder can be noticed at 1735 cm^{-1} , for all the samples. Another shoulder which can be attributed to the signature of the carbonyl stretching in the crystalline region appears at 1690 cm^{-1} . Upon thermal crystallization, more hydrogen bonds are created, thus shifting the carbonyl band to slightly lower wavenumbers. However, D-PET and I-PET spectra are very close to the one of A-PET, indicating a limited influence of the mechanical stretching on the carbonyl response [67].

For PEF, the situation is a bit more controversial since, on one hand the C=O undergoes a change from *anti* to *syn* upon crystallization [102]. It leads to a shift to higher energy (i.e. shoulder at 1732 cm^{-1} visible on TC-PEF and D-PEF). While in the meantime a red-shift is also

expected from the creation of H-bond during the crystallization. However, this red-shift is not visible in Figure 38.b. It can be supposed that the stretching has not allowed the formation of additional hydrogen bonds. Indeed, the aliphatic part has been stretched, the furan cycle also has restricted motions and, by this way, it can be more difficult for the carbonyl groups to promote the formation of many hydrogen bonds.

Interestingly, the spectra of I-PEF is quite similar to the one of A-PEF, and it does not present the *syn*-shoulder at 1732 cm^{-1} . It indicates that this conformational change is reached after a sufficient draw ratio, i.e. when SIC is created [67].

The FT-IR analysis has shown that the first part of the chain influenced by the stretching is the aliphatic part. An increase of the number of *trans* conformation is visible for the EG. Moreover, the furan cycle seems to be more constrained due to the stretching. The carbonyl groups are not very different before and after stretching in PET, whereas in PEF carbonyls seem to have a restricted mobility, according to FT-IR analysis.

Finally, when the crystallization occurs there is a change of EG from *gauche* to *trans* and of the furan from *anti* to *syn* conformations. There is also the apparition of several bands: two bands at 3110 and 3145 cm^{-1} with a red shift due to the presence of H bonding (aromatic =C-H); two bands at 1000 cm^{-1} and 1045 cm^{-1} probably due to the increase of EG in *trans* conformation (cycle breathing); and the *syn* shoulder at 1732 cm^{-1} . The main changes observed between the static crystallization and SIC are the shift to higher wave number of the *syn* band (1575 to 1580 cm^{-1}), for the C=C-C bending band (1015 to 1020 cm^{-1}), for the ether and ester bands (1103 to 1125 cm^{-1} and $1220/1270$ to $1225/1275\text{ cm}^{-1}$)

Globally, the same conformations have been found between SIC and the thermally crystallized PEF. The major differences result in the existence of more constrained conformations, for stretched PEF. DMTA measurements were performed in the next part to get additional information about the carbonyl motions, and their influence on the β -transition [67].

3.4 Impact on the β -transition

According to Araujo et al. [102], the carbonyl groups are really sensitive to the intramolecular and the intermolecular changes. As the β -transition is associated to low energetical and local motions around the principal chain axis, it has been proposed that the carbonyls are the functional groups involved in this transition for PEF and PET [46,114].

Figure 39 shows the DMTA scans associated to the β -transition of the amorphous, the thermally crystallized, the stretched until rupture, and stretched and interrupted samples. The interest of the DMTA is that only the motional processes of the amorphous phases, influenced or not by the crystal, are highlighted [67].

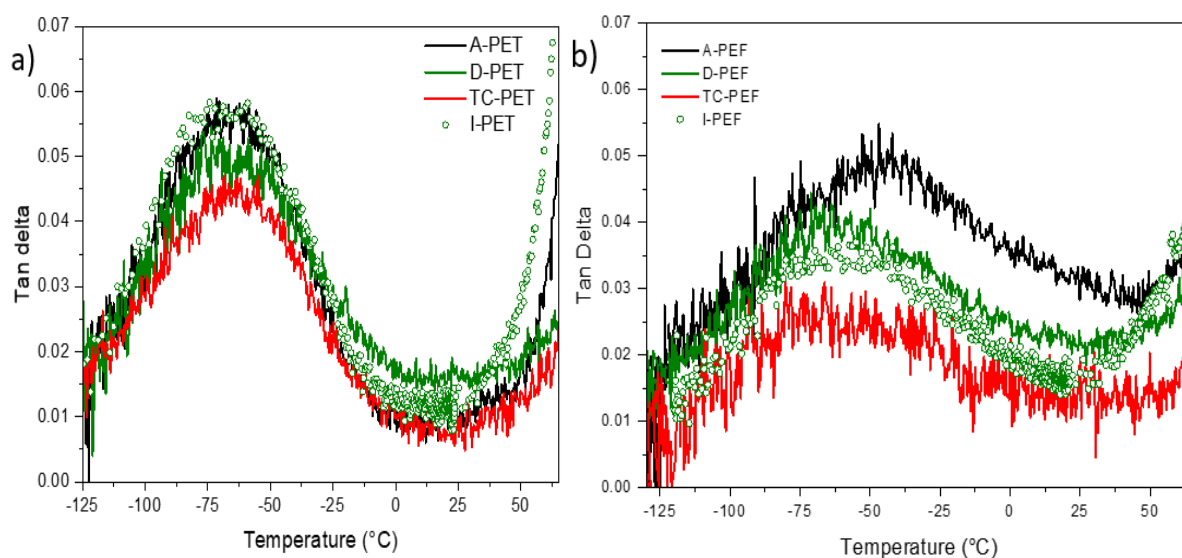


Figure 39. DMTA measurements in the low temperature region of amorphous (black, A-PET/A-PEF), stretched (green, D-PET/D-PEF), stretched and interrupted (green dots, I-PET/I-PEF) and thermally crystallized (red, TC-PET/TC-PEF) [67].

In the case of PET, the β -transition seems to appear at slightly higher temperatures for the semi-crystalline samples, as it was found in biaxial stretching by Zekriardehani et al. [115]. For I-PET, the temperature at the peak maximum and the peak magnitude remain nearly equal to the amorphous sample. The formation of new hydrogen bonds, from PET crystal, does not really impact the local mobility of the amorphous carbonyls [67].

As shown in Figure 39.b, the β -transition of A-PEF occurs on a much broader temperature range (i.e. -120 °C to 45 °C) compared to the other samples (-120 °C to 0 °C). Such results are consistent with the previous investigation, on PEF and PET, of Burgess et al. [46]. They have explained that the lower magnitude, and the shift to higher temperature of the PEF β -relaxation peak is due to the existence of some concerted motion for the PEF carbonyls that are possibly coupled with small scale oscillations of the furan ring. Moreover, the larger possibilities of amorphous conformational state for PEF, in comparison with PET [102], is also in agreement with a broader relaxation peak for carbonyl motions.

This broad relaxation peak might be the result of the convolution of several local relaxation processes. The lower temperature side of the peak would represent the motions from the “freer” C=O, predominantly in the *anti* conformation. On the other hand, the high temperature side of the peak would be more associated to restricted C=O motions, both due to H-bond or to the *syn* conformation.

For D-PEF and TC-PEF, the peak amplitude decreases as the consequence of crystallization which induces a decrease of the amorphous part in the material and then, a reduced mobility compared to A-PEF. Moreover, the peak maximum of the β -transition of both D-PEF and TC-PEF appears at lower temperature (shift of -10 °C), compared to A-PEF (but remains at higher temperatures compared to PET). Such shift to lower temperature would mean that the motional processes of amorphous C=O in both TC-PEF and D-PEF would be less restricted compared to A-PEF. Another explanation would be that the high temperature side of the β -relaxation peak (typically between -50 °C and 25 °C), i.e. corresponding to restricted C=O in A-PEF, is much less expressed in TC-PEF and D-PEF. It would mean that the restricted C=O, already in the *syn* conformation in the amorphous state, have been preferentially transformed into crystals. As the consequence of this, only the less restricted C=O in *anti* conformation, which were not transformed into crystals, are expressed in the β -transition peak of both TC-PEF and D-PEF, resulting in a shift to lower temperature [67].

Interestingly, the same situation is observed in I-PEF, for which the peak amplitude decreases and the peak maximum is shifted to lower temperature, compared to A-PEF. It would mean that only the less restricted carbonyls are expressed in the β -relaxation peak of I-PEF, compared to A-PEF. As I-PEF has been stretched to a low strain, its microstructure is slightly different from the one of A-PEF. This can be explained as follows:

First, the chains having carbonyls with some very restricted motions (like in crystals) do not show any visible β -relaxation. They are normally those corresponding to the right side of the A-PEF peak (Figure 39.b). On the other hand, there is still some amorphous carbonyls with a certain degree of liberty which are expressed in the left side of the A-PEF β -peak, thus leading to a global shift to lower temperature. Moreover, the decrease in the peak intensity between A-PEF and I-PEF, which is not observed between A-PET and I-PET, is the indication that a higher level of cooperativity is needed for the carbonyl motions in I-PEF. We have shown that connections with neighbouring CH₂ unit (throughout the C-O-C stretching, FT-IR peak in Figure 37) requires higher energy in I-PEF, i.e. after stretching. In that respect, the cooperativity required in I-PEF to allow concerted motions of carbonyls with EG groups has a higher energy

penalty compared to A-PEF. It logically leads to lower peak magnitude as shown in Figure 39.b [67].

4. Conclusions

This chapter has demonstrated that the crystal induced by the stretching, in PET and in PEF, is almost similar to the one formed with static crystallization. Thanks to the stretching protocol defined, PEF is able to form a crystal with a high level of definition. Miller's indices have been found in PEF, and associated to the angular positions and to the interreticular distance. Moreover, this work suggests that there is no coexistence of a mesophase and a crystal in PEF, but only the presence of a crystal.

In a more local point of view, the main differences between these two crystallization paths remain in the level of constrained for each groups, especially in PEF for the furan and the ether. Because of the stretching, the groups are more constrained than with the static crystallization. It can be the result of the extension of the chains and of their orientation in the stretching direction. It is presently interesting to follow the crystal formation during stretching for PEF and PET. It will be done in the next chapter.

Chapter 4

The formation of a crystal upon stretching in PEF and PET

Table of contents

1. Introduction.....	99
2. Mechanical description	100
2.1 Behaviour of PET under loading-unloading tests.....	102
2.2 Behaviour of PEF under loading-unloading tests.....	104
3. Crystal development scenario.....	106
3.1 PET and PEF thermal behaviour	106
3.2 PET and PEF crystal building.....	110
3.2.1 PET crystal formation	111
3.2.2 PEF crystal formation	114
4. Properties induced by the stretching.....	118
4.1 PET amorphous phase mobility and rigidity evolution	118
4.2 PEF amorphous phase mobility and rigidity evolution.....	120
4.3 Modification of the local motions by the stretching.....	122
4.4 PET and PEF thermal deformation	124
5. Conformational analysis.....	126
6. Conclusions.....	128
7. Annexes.....	130

Chapitre 4

L'apparition d'un cristal sous étirage pour le PEF et le PET

Stoclet et al. ont proposé que le PEF formait en plus de sa phase cristalline une mésophase et, à la différence du PET, cette mésophase persisterait après l'étirage [61]. Pour assoir notre hypothèse selon laquelle le PEF ne forme pas de mésophase, mais uniquement une phase cristalline, et confirmer les résultats obtenus en cristallographie, différents tests mécaniques ont été réalisés. A partir des mêmes échantillons que ceux du chapitre précédent, des tests « interrompus » et « déchargés » ont été réalisés le long de la courbe de traction. Un test « interrompu » consiste à étirer un échantillon jusqu'à une certaine déformation, à le tremper directement, puis à le décharger ; tandis que lors d'un test « déchargé », l'échantillon est étiré, déchargé jusqu'à une force nulle, puis trempé. La décharge est réalisée avec les mêmes paramètres que la charge (vitesse de déformation et température). Ces différents tests permettent d'évaluer le degré de viscoélasticité des échantillons le long de la courbe de traction, la quantité de viscoélasticité diminuant avec la création d'un cristal.

D'après les différents résultats obtenus à travers plusieurs techniques d'analyses complémentaires, il a été trouvé une différence réelle de formation du cristal sous étirage entre le PEF et le PET. Le PET forme sa microstructure de façon progressive, en induisant d'abord une mésophase. La décharge aide grandement à perfectionner la microstructure formée lors de la charge, et ce jusqu'à la fin de l'essai. D'un point de vue cristallographique, cette mésophase est une phase organisée comportant seulement certaines périodicités du cristal. Pour le PEF, la situation est plutôt binaire : soit le cristal n'existe pas, soit il existe. En effet, le cristal avec toutes ses périodicités serait formé avant le NDR, et n'évoluerait que légèrement jusqu'à la fin de l'étirage. Cette différence majeure est en accord avec la plus grande complexité de la chaîne du PEF, sa mobilité réduite, la nécessité d'opérer deux changements de conformations pour former un cristal qui est constitué de deux unités constitutives. De ce fait, il semblerait que le durcissement structural prenne place seulement lorsque les conditions de cristallisation complète sont remplies. L'absence de mésophase dans le PEF rend la pente du durcissement structural plus abrupte que celle observée dans le PET.

1. Introduction

This chapter is based on a paper published in the journal *Polymer*, and is focused on the steps leading to the apparition of SIC, during PEF and PET stretching [116]. The same stretching conditions as in the previous chapter have been used to define the tests analysed thereafter (Chapter 3, Table 10). The microstructural analyses are conducted in parallel with the mechanical characterization in tension, on PEF and PET, to confirm or not the previous assumptions, specially concerning the mesophase presence.

The microstructural changes over the stretching and the microstructural organization are depicted at different strain steps. The purpose is to understand the crystal building, for PEF and PET [116]. It is established that PET forms progressively its stable crystal, and starts with the development of an intermediate organized phase, prior to crystallize [75–78,81,83–92,95,117,118]. During the stretching, firstly the benzene rings flip in the stretching direction [76,88,117,118], and concomitantly the quantity of EG in *trans* conformations increases progressively. Finally, the crystal appears when the interactions (hydrogen bonding) are created, and when the structure is stabilized.

Concerning PEF, a coexistence between a mesophase and a crystal was proposed by Stoclet et al. [61]. Based on the crystallographic and the conformational analysis made previously [65,67], this hypothesis seems to be not relevant and complementary stretching tests are needed.

Firstly, the samples have been stretched up to controlled strains, at given temperature and strain rate. Then, they have been quenched to the room temperature either immediately after the stretching end, or after an additional unloading step, up to a zero force, performed with the same settings as those applied during the loading (strain rate and temperature). The main objective is to release the stress while avoiding the buckling or the compression, that would have damaged the specimen. The samples quenched before the unloading are referred as “interrupted” in the following, while the samples quenched after the unloading are referred as “unloaded”.

The stretching tests are presented and commented in both materials. Then, the crystal development is followed. The microstructure in the different samples, i.e. “interrupted” and “unloaded”, is analysed to suggest a possible scheme of structural development under stretching.

2. Mechanical description

Different key localizations on the stress/strain curves have been selected:

1. Far from the NDR ($\epsilon_{xx} = 0.90$ for PET and $\epsilon_{xx} = 1.20$ for PEF);
2. Close but before the NDR ($\epsilon_{xx} = 1.45$ for PET and $\epsilon_{xx} = 1.75$ for PEF);
3. Close but after the NDR ($\epsilon_{xx} = 1.60$ for PET and $\epsilon_{xx} = 1.93$ for PEF);
4. During the strain hardening ($\epsilon_{xx} = 1.72$ for PET and $\epsilon_{xx} = 2.06$ for PEF);
5. After the rupture ($\epsilon_{xx} = 1.94$ for PET and $\epsilon_{xx} = 2.12$ for PEF).

These conditions are marked by crosses on the mechanical curves in Figure 40.a and Figure 40.b for respectively PET and PEF [116].

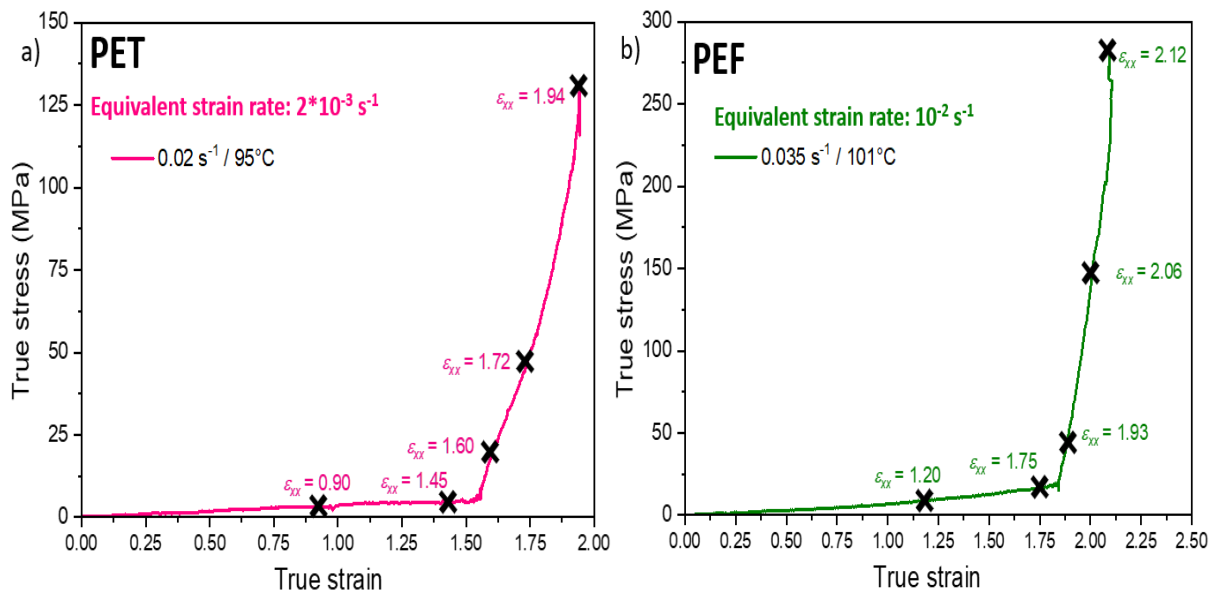


Figure 40. (a) PET and (b) PEF true stress/strain curves and associated staged explored for the mechanical and microstructural analysis [116].

Table 14 summarizes the conditions that are explored for the “interrupted” and the “unloaded” tests, for both materials. The grey boxes correspond to the non-explored cases (i.e. only “interrupted” or only “unloaded”).

The shape of the unloading loop gives information on the amount of in-elasticity (such as visco-elasticity or plasticity) after the stretching. The unloading time depends on this amount. This degree of in-elasticity is assumed to decrease with the progression of the crystallization.

Unloading time ranged from 32 s to less than 1 s depending on the samples, the unloading time being longer in case of a stretching below the NDR (Table 14), and close to 0 in case of a stretching above the NDR.

PET					
Unloaded	$\epsilon_{xx} = 0.90$	$\epsilon_{xx} = 1.45$	$\epsilon_{xx} = 1.60$	$\epsilon_{xx} = 1.72$	
Unloading time (s)	32	11	<2	<2	
Interrupted	$\epsilon_{xx} = 0.90$	$\epsilon_{xx} = 1.45$	$\epsilon_{xx} = 1.60$		$\epsilon_{xx} = 1.94$
PEF					
Unloaded	$\epsilon_{xx} = 1.20$	$\epsilon_{xx} = 1.75$	$\epsilon_{xx} = 1.93$	$\epsilon_{xx} = 2.06$	
Unloading time (s)	26	5	<1	<1	
Interrupted	$\epsilon_{xx} = 1.20$	$\epsilon_{xx} = 1.75$	$\epsilon_{xx} = 1.93$		$\epsilon_{xx} = 2.12$

Table 14. Summary of the mechanical “interrupted” and “unloaded” tests performed in PET and PEF. The unloading time is added.

Figures 41 and 42 depict the mechanical behaviour of respectively PET and PEF, for the “unloaded” tests. For clarity, the true stress/strain curves issuing from “interrupted” tests are not presented, as the responses are pretty well superimposed to the “unloaded” ones, accounting for the experimental scattering.

Nevertheless, one has to emphasize that this scattering induces some apparent lack in reproducibility of the NDR. A typical order of magnitude of such scattering can be estimated in Figure 41, by comparing the stress/strain curves up to strains of 1.60 and to 1.72, for PET. The main effect is observed on the NDR, it is not surprising. Indeed, the local strain rate is not controlled per se and is impacted by the strain hardening itself that constrains the local deformation. As a consequence, the exact strain rate could vary from one sample to another as soon as the strain hardening occurs. Indeed, even if the technological loading rate is controlled in the same manner, the local strain rate can depend on some small local fluctuations in size (thickness), or microstructure, or temperature. Moreover, it has been observed in the second chapter that the strain rate and the temperature increase slightly during the first stages of the stretching. However, the minor differences remain reasonable and do not modify the analysis. The corresponding Debye-Scherrer patterns, realised with a sample-screen distance of 75 mm, are associated to each test. Unstretched PEF and PET exhibit a clear amorphous structure.

The comparison between the two kinds of post stretching treatment, “interrupted” and “unloaded”, allows estimating the potential microstructural evolution taking place during the unloading path.

2.1 Behaviour of PET under loading-unloading tests

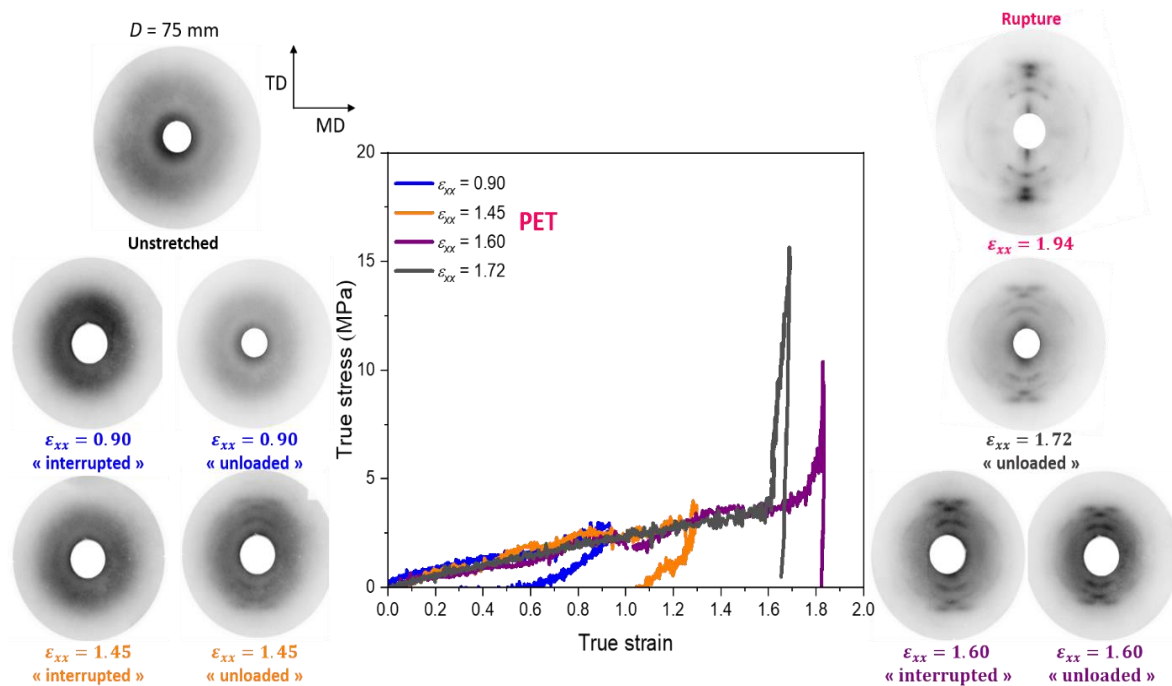


Figure 41. Loading/unloading true stress/strain curves of PET for strains up to 0.90; 1.45; 1.60 and 1.72. Debye-Scherrer patterns before unloading (“interrupted” tests) and after unloading (“loaded/unloaded” and “rupture”) are added. TD is the transverse direction while MD is machine (or stretching) direction [116].

Through the analysis of the two first unloading conditions ($\epsilon_{xx} = 0.90$ and $\epsilon_{xx} = 1.45$), PET exhibits a mainly visco-elastic behaviour, as previously observed [77,91,95]. The existence of a residual strain after the unloading suggests that some deformation was not recovered instantaneously after this step, but this residual strain could be recovered within hours or days. The concept of “blocked elastic energy” could be explained that. This concept can be related to the entropic elasticity of the chains that are locked by the precursors of the crystallization. They act as crosslinking nodes. Because of the high mobility of the chains, in PET, the organization seems to be progressive. Then, such precursors can exist for low strains, and then disappear. Finally, with time, the system can return at its initial state and release the energy stored. It

testifies of a visco-elastic behaviour. The shape of the unloading is very different at and after the NDR: the strain appears to be 100 % irreversible. It can suggest the occurrence of irreversible microstructural changes.

The Debye-Scherrer patterns do not reveal a well-defined periodic organisation (i.e. crystallization) below a strain of 1.60. However, while at low strain ($\epsilon_{xx} = 0.90$) the diffraction pattern is a characteristic amorphous halo, there is some trace of periodicity for a strain of 1.45. This latter pattern is quite incomplete, and the spots appear diffuse, but the organisation is clearly not isotropic. The unloading at the temperature of the test seems to improve the microstructure, as there is a better definition of the diffractions spots for the unloaded sample. This aspect is completed further in the text (3.2 PET and PEF crystal building).

To conclude, at this level, these observations suggest that the stretching induces some periodic arrangements in the material, below a strain of 1.45. It is difficult to discriminate if it is discrete nuclei or a global organisation. However, the distribution is not isotropic and the periodicity could be improved upon the unloading, without promoting a complete diffraction pattern. To go further, it can be added that the first traces of periodicity are seemingly oriented parallel to the tensile axis, in the equatorial direction, and correspond to the $(hk0)$ families of planes. Close to the meridional direction, some low intensity traces of families of planes, related to $(00l)$ type, can be foreseen. It suggests that the chains are extended and oriented by tension, and nucleated an organized phase that develops itself toward a crystal during the unloading. It can be a mesophase, a crystal precursor or an imperfect crystal. This scenario has already been reported in the literature [77,119,120].

After the NDR ($\epsilon_{xx} = 1.60$ and $\epsilon_{xx} = 1.72$) the mechanical response is different: the reversibility of the deformation drastically decreases. On the Debye-Scherrer patterns, some differences between the strains of 1.45 and 1.60 are observed: there is an increase of the spots intensity. It can be due to a higher amount of crystal. Indeed, when $\epsilon_{xx} = 1.60$ the formation of an anisotropic and periodic structure is observed, whatever the cooling conditions are. Once again, the equatorial dots $(hk0)$ are mainly visible. For the last unloading condition ($\epsilon_{xx} = 1.72$), an organized microstructure, with intense spots in the equatorial direction, is also noticeable. The dots become more defined and less diffused after the rupture. To understand that point, one has to consider that the rupture corresponds to a rapid unloading of the sample. A better-defined crystal is then consistent with the observation concerning the unloaded sample. This possible crystallization during the unloading was already suggested in the past [77,91]. Additionally, in that case, the quenching was not possible and consequently, the cooling down after unloading

is slower than in the other tests. It can favour the crystallization too [77], and explain that some diffractions (different from the $(hk0)$ and $(00l)$ ones) such as $(\bar{1}11)$, $(\bar{1}12)$, $(\bar{1}03)$ and $(0\bar{1}1)$ become observable. A typical indexed Debye-Scherrer pattern for PET was visible in the previous chapter (Figure 29.d). After the rupture at high strain, it appears that the final microstructure is very close to the perfect fibre texture one, as referred in the literature by Liu & Geil [111,112].

To sum-up, these observations are coherent with the formation of the definitive crystal (with all its periodicities) after the stretching in PET, as reported in previous works [75,86,90,92,121], whereas the strain hardening could be due to imperfect crystal, mesophase or precursors.

In any case, these observations confirm that the strain hardening, as well as the organized microstructure, appear step by step for PET [116].

2.2 Behaviour of PEF under loading-unloading tests

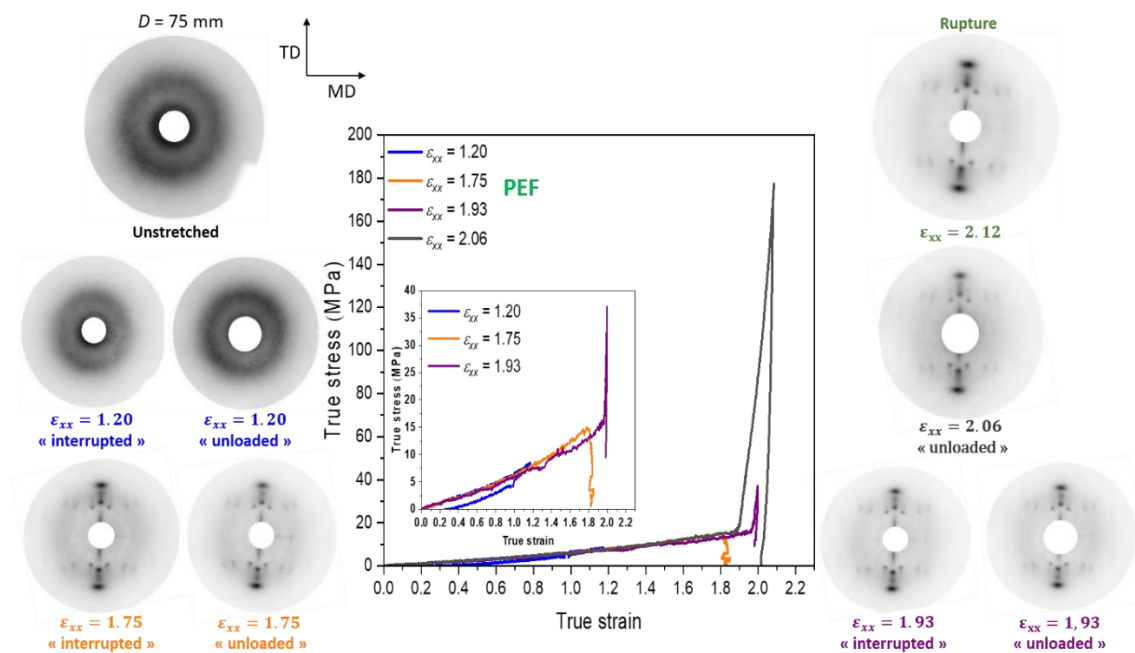


Figure 42. Loading/unloading true stress/strain curves of PEF for strains up to 1.20; 1.75; 1.93; and 2.06. Debye-Scherrer patterns before unloading (“interrupted” tests) and after unloading (“loaded/unloaded” and “rupture”) are added. TD is the transverse direction while MD is machine (or stretching) direction [116].

The stress in PEF reaches higher values than those reached in PET, even during the first deformation stages. Consequently, a zoom is added for the first three unloading conditions ($\epsilon_{xx} = 1.20$; $\epsilon_{xx} = 1.75$; $\epsilon_{xx} = 1.93$), in Figure 42. The first unloaded test ($\epsilon_{xx} = 1.20$) leads to a visco-elastic loop, as in PET. This loop seems to be more “closed” for PEF. Because of its lower chain mobility, in comparison with PET, some crystallization precursors cannot be able to exist for a such low strain level. Then, the unloading path is closer to the loading one.

For the lower strain level ($\epsilon_{xx} = 1.20$), whatever the cooling conditions are, the structure of the “interrupted” and “unloaded” samples is close to the amorphous state. When the strain is closer to the NDR ($\epsilon_{xx} = 1.75$ and $\epsilon_{xx} = 1.93$), a well-defined crystalline structure which is not sensitive to the unloading conditions is visible. This is obviously different from PET, as the crystal structure is already clearly defined at once, prior to the mechanical strain hardening. There is the presence of intense and defined spots on the Debye-Scherrer patterns. The impossibility to observe a mesophase prior to the crystallization is contradictory to the work of Stoclet et al. [61], but it is in agreement with the crystallographic and conformational analysis conducted in the Chapter 3 [65,67]. It is also coherent with some observations on the stress/strain curves of the Chapter 2. The sharper strain hardening of PEF can be due to the presence of the crystal before the NDR, while in PET the crystal does not exist yet at this stage. The presence of the crystal in PEF restricts the strain evolution during the strain hardening, while the mesophase in PET has a lower impact on the strain. It can also fit with the temperature increase observed up to the NDR, that can potentially be ascribed to the formation of a crystal or to a part of it.

The need to form a crystal before the NDR occurrence in PEF is compatible with what can be imagined concerning its slow crystallization. PEF crystal is formed of segments composed of two repeating units [58], instead of one in PET. It should slow down the crystallisation. Moreover, the crystal is composed of chains that have made two conformational changes. These both aspect can explain the later NDR apparition in PEF, compared to PET.

Finally, the architecture of PEF chain should lead to weaker interactions between the segments and to a less stable crystal, as well as a less stable potential mesophases, than the PET one. It agrees with the lower PEF melting temperature. Due to those characteristics one possible conclusion is that no intermediate organized metastable phases, that could contribute to harden the material, can be promoted in PEF. The strain hardening could occur only when the conditions of complete crystallization are reached. On the contrary, during the early stages of the crystallization, PET can exhibit a mesophase whose life time is long enough to contribute to the strain hardening. Hence, the strain hardening and the crystal development can coexist.

The “interrupted” and “unloaded” conditions at higher strain ($\epsilon_{xx} = 1.93$ and $\epsilon_{xx} = 2.06$) show that the microstructure seems completed, and is the same before and after the unloading, as well as after the rupture ($\epsilon_{xx} = 2.12$).

To conclude on this part, some metastable phases of lower level of organization than the final crystal exist in PET, and contribute to the strain hardening, making it more progressive. Whereas in PEF, the final crystal has first to be stable to allow the strain hardening development. As the Debye-Scherrer patterns only gives qualitative results, some complementary measurements must be performed to better understand the two polymers crystalline development.

3. Crystal development scenario

3.1 PET and PEF thermal behaviour

The thermal behaviour is analysed through DSC measurements, to complement the Debye-Scherrer analysis. The curves are depicted in Figures 43.a and 43.b, for respectively PET and PEF. Table 15 gathers the temperature of the cold crystallization peak during the heating program. The resulting crystal, MAF and RAF ratios are gathered in Table 16. For some samples, it was not possible to obtain the values investigated, because of the measurement sensitivity, they are represented by red boxes. However, global trends can be drawn. The uncertainty of measurement is estimated at around 5%.

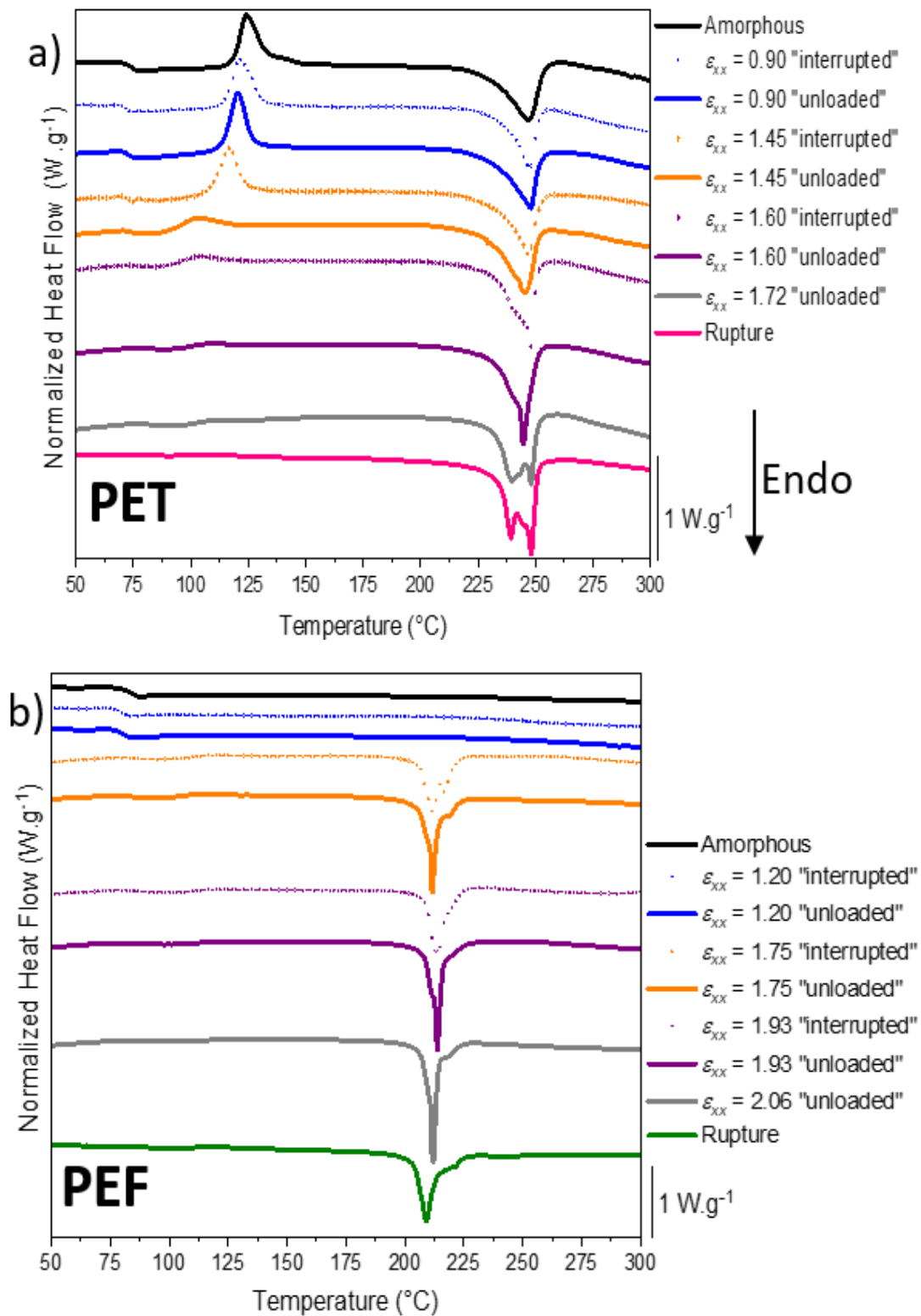


Figure 43. Thermal behaviour of (a) PET and (b) PEF, measured by DSC at a heating rate of 10 °C/min from 50 °C to 300 °C. Comparison is made between amorphous, “unloaded” samples (lines) and “interrupted” samples (dots). Endothermic phenomena are top-down [116].

PET						
Interrupted	Amorphous	$\epsilon_{xx} = 0.90$	$\epsilon_{xx} = 1.45$	$\epsilon_{xx} = 1.60$		$\epsilon_{xx} = 1.94$
T_c (°C)	124	121	117	104		105
Unloaded		$\epsilon_{xx} = 0.90$	$\epsilon_{xx} = 1.45$	$\epsilon_{xx} = 1.60$	$\epsilon_{xx} = 1.72$	
T_c (°C)		121	103	107	111	
PEF						
Interrupted	Amorphous	$\epsilon_{xx} = 1.20$	$\epsilon_{xx} = 1.75$	$\epsilon_{xx} = 1.93$		$\epsilon_{xx} = 2.12$
T_c (°C)			118	121		117
Unloaded		$\epsilon_{xx} = 1.20$	$\epsilon_{xx} = 1.75$	$\epsilon_{xx} = 1.93$	$\epsilon_{xx} = 2.06$	
T_c (°C)			114	120	128	

Table 15. PEF and PET cold crystallization temperature at 10 °C/min for amorphous and samples that have been stretched at different strains.

PET					
Interrupted	$\epsilon_{xx} = 0.90$	$\epsilon_{xx} = 1.45$	$\epsilon_{xx} = 1.60$		$\epsilon_{xx} = 1.94$
χ_c (%)	7	12	36		47
χ_{RAF} (%)	1	26	32		
χ_{MAF} (%)	92	62	32		
Unloaded	$\epsilon_{xx} = 0.90$	$\epsilon_{xx} = 1.45$	$\epsilon_{xx} = 1.60$	$\epsilon_{xx} = 1.72$	
χ_c (%)	11	29	42	43	
χ_{RAF} (%)	9	34	24	35	
χ_{MAF} (%)	80	37	34	22	
PEF					
Interrupted	$\epsilon_{xx} = 1.20$	$\epsilon_{xx} = 1.75$	$\epsilon_{xx} = 1.93$		$\epsilon_{xx} = 2.12$
χ_c (%)	0	27	28		35
χ_{RAF} (%)	24	54	54		37
χ_{MAF} (%)	76	19	18		28
Unloaded	$\epsilon_{xx} = 1.20$	$\epsilon_{xx} = 1.75$	$\epsilon_{xx} = 1.93$	$\epsilon_{xx} = 2.06$	
χ_c (%)	0	32	35	32	
χ_{RAF} (%)	15	48	47	56	
χ_{MAF} (%)	85	20	18	12	

Table 16. PEF and PET crystal, RAF and MAF ratios for samples that have been stretched at different strains.

The conclusions drawn from the Debye-Scherrer patterns are confirmed through this analysis. As demonstrated by the progressive decrease of the temperature of cold crystallization and of the associated enthalpy with the increasing strain, SIC seems to be a progressive phenomenon in PET. The glass transition temperature increases also slightly with the strain. The melting peak, which is a single peak-shaped when amorphous PET cold crystallizes, progressively becomes a double-peak shaped, suggesting the existence of two crystallization regimes (perhaps one during the loading and another one during the unloading).

The scheme in PEF is much simpler: the material being amorphous far below the NDR, and semi-crystalline close to it and above.

For the same level of strain, the crystal ratio increases between the “interrupted” and the “unloaded” samples. This trend is visible on the Figures 44.a and 44.b for respectively PET and PEF.

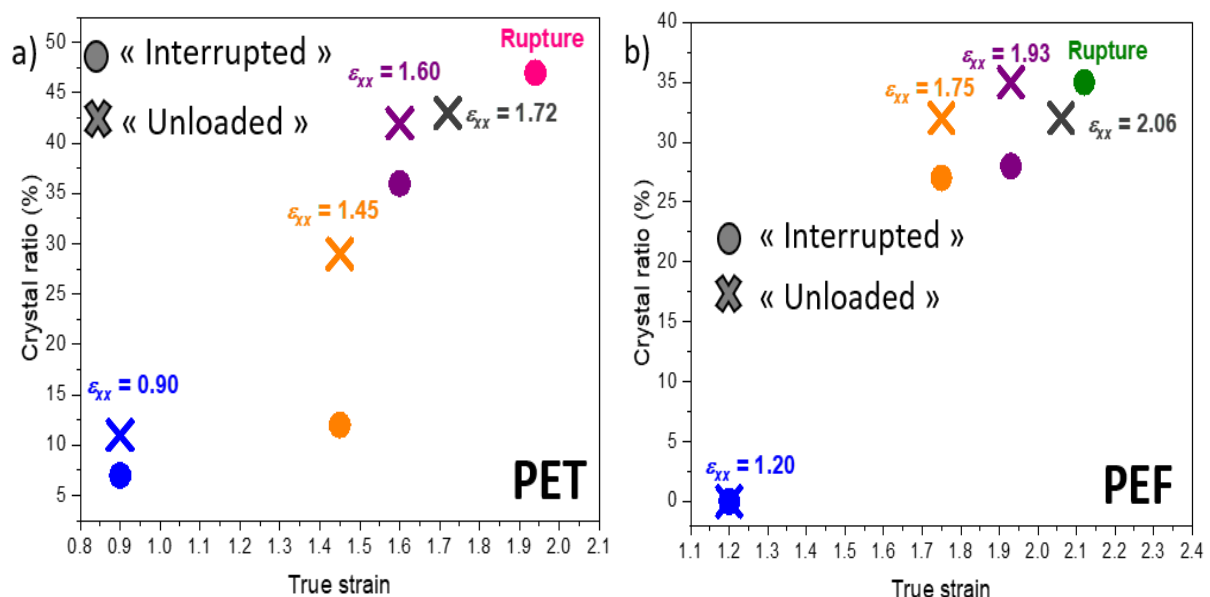


Figure 44. Evolution of the crystal ratio depending on the true strain for “interrupted” and “unloaded” samples.

It confirms that the unloading step helps to form and improve the crystal. It is particularly true in PET. For the samples in which a well-defined periodic organization was not observable on the Debye-Scherrer patterns, below $\epsilon_{xx} = 1.60$, it seems that the MAF is dominant (Table 16). For $\epsilon_{xx} = 1.45$ “unloaded”, in comparison with $\epsilon_{xx} = 0.90$ tests (“interrupted” and “unloaded”) and $\epsilon_{xx} = 1.45$ “interrupted”, the χ_{MAF} is lower while χ_{RAF} and χ_c increase. For PEF, the MAF

is dominant only for the sample far from the NDR ($\epsilon_{xx} = 1.20$). In PEF, a higher amount of RAF is found for the “interrupted” tests compared to the “unloaded” ones. It has been observed by Harmonic et al., that in PET stretched samples the MAF part is also oriented, and then impacted by the stretching [122]. The same thing can be concluded for PEF.

Finally, for all the samples, PEF seems to form a higher part of RAF and a lower crystal ratio, compared to PET. It fits with the more complex required conditions of crystal apparition reported. Then, when the crystallization cannot occur, some chains can remain in an intermediary constrained state, that is different from the amorphous and the crystal phases. As the mobility of the PET chain is higher, the chains can probably more easily become amorphous again, if crystallization is not realised.

Next two parts analyse the crystal apparition thanks to WAXS radial scans.

3.2 PET and PEF crystal building

Figures 45 and 47 show the diffraction scans in the transverse direction (equatorial direction, analysis of $(hk0)$ plans), for respectively PET and PEF. In Figure 46, the development of the $(\bar{1}05)$ diffraction in PET, which is associated to a plane quasi-perpendicular to the chain axis, is represented through the analysis of the meridional direction. The many meridional diffractions of PEF are visible in Figure 48 [116].

3.2.1 PET crystal formation

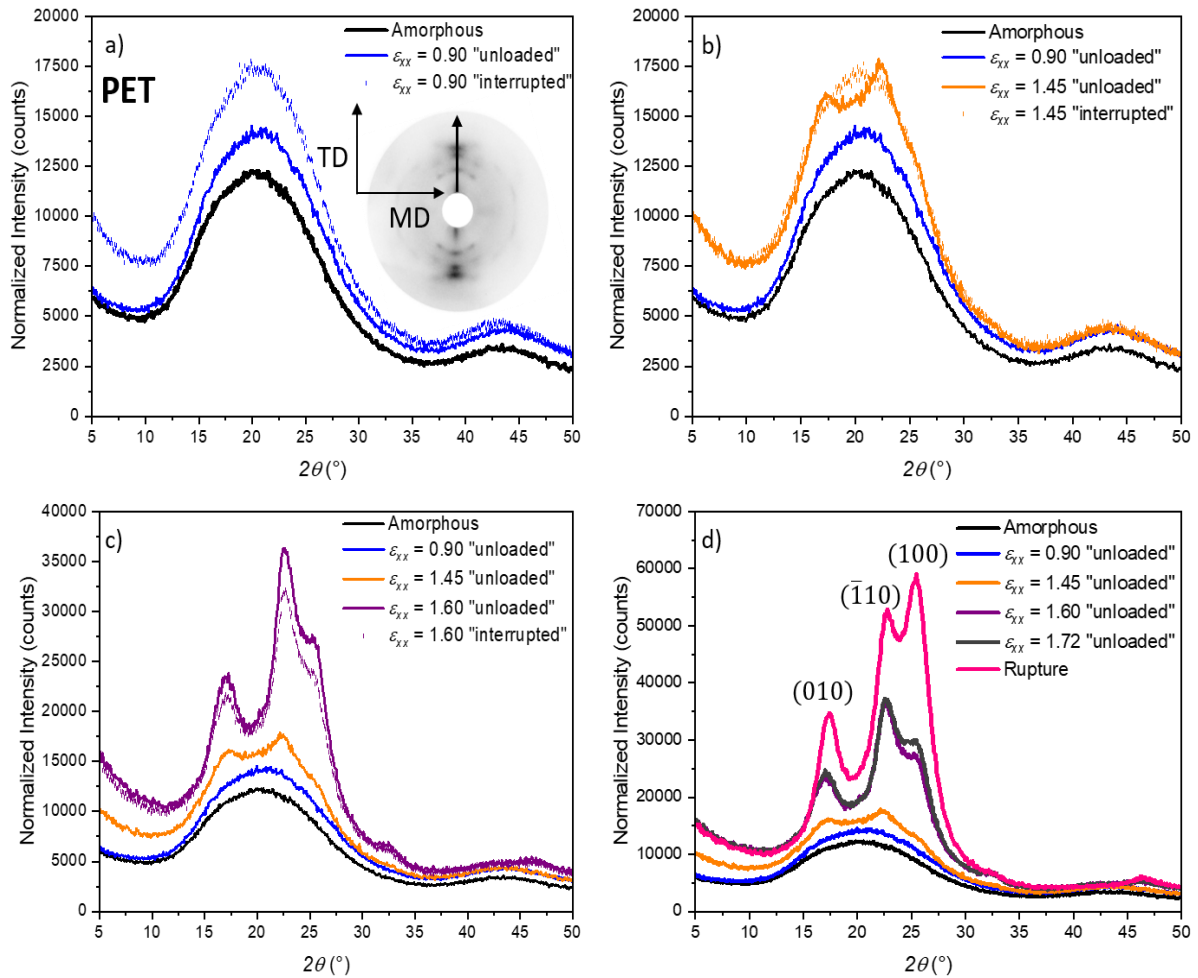


Figure 45. Diffraction scans in the transverse direction (TD): development of the PET crystalline phase for “interrupted” (dots) and “unloaded” (lines) tests up to a strain of (a) 0.90; (b) 1.45; (c) 1.60; and (d) up to the rupture [116].

Figure 45 confirms the qualitative observations deduced from Figure 41, and agrees with the data previously reported [91,95]. PET remains amorphous, up to a strain of 1.45 (Figures 45.a and 45.b), despite an increase in the diffracted intensity. In the earlier steps ($\epsilon_{xx} = 0.90$), the unloading in temperature results in a decrease in the intensity (compared to the interrupted test). It is worth noticing that the early stages of the stretching lead to an amorphous-like X-ray diffraction. But, according to the DSC measurements, these samples can be slightly crystalline (8 % if “interrupted” and 11 % if “unloaded”). One could argue that this contradiction results from experimental artefact or could be overestimated due to experimental uncertainty, and to the dependence of enthalpy upon temperature (Chapter 1, Equation 1).

However, from a strain of 1.45, the unloading makes possible the observation, of two diffractions related to the (010) and ($\bar{1}10$) families of planes, whereas the (100) family of planes is still very weak, but is distinguishable as a shoulder. Conversely, the interrupted sample could still be considered as amorphous based on X-ray diffraction. DSC measurements, for their parts, lead to crystal ratios of around 12 %, if “interrupted”, and to around 29 % when “unloaded”. Before the NDR, the crystal ratio increase confirms the organization during the unloading. For the “interrupted” and the “unloaded” samples stretched up to strains of 0.90 and 1.45, in comparison with the amorphous sample, the cold crystallization is fastened (Figure 43.a). Moreover, the continuous, and coherent, evolution in the crystal ratios (Figure 44.a) encourages to draw some conclusions, even if the evaluation of the crystal ratio with DSC measurements on these materials is subjected to non-negligible experimental errors. Indeed, the previous observations suggest that a certain level of organization could exist, even if this last is not immediately visible through X-ray diffraction. It could be some small nuclei, the number or the size of them increasing upon the unloading.

For $\epsilon_{xx} = 0.90$, the amorphous phase appears less oriented in the case of the “unloaded” tests, as this path can authorize the chains relaxation in temperature. Moreover, if some denser zones are too small to be stable, they disappear upon unloading. Whereas for a strain of 1.45 (Figure 45.b), with the unloading, PET begins to form an organized microstructure, which is not yet a well-defined crystal (only some periodicities are visible). It is a metastable phase named mesophase, which could be the crystal precursor or which could disappear. For $\epsilon_{xx} = 1.60$ (Figure 45.c), there are much less differences between the “interrupted” and the “unloaded” tests, even if the diffracted intensity increases with the unloading. Despite the close diffracted intensity observed in this direction, the crystal ratios increase with the unloading (36% for the “interrupted” test vs 42% for the “unloaded” test, Table 16). It confirms the crystallization occurrence during the unloading. The last unloaded condition before the rupture, ($\epsilon_{xx} = 1.72$, Figure 45.d), results in a structure closer to a “perfect” crystal, compared to $\epsilon_{xx} = 1.60$. The crystal ratios remain approximately equal (42% for $\epsilon_{xx} = 1.60$ “unloaded” vs 43% for $\epsilon_{xx} = 1.72$ “unloaded”). The mesophase is still better defined with the stretching and with the unloading. However, there is a significant change with the sample stretched up to the rupture (Figure 45.d). The diffracted intensities are higher than in the other cases, and the crystal ratio reaches 47% (instead of 43% for $\epsilon_{xx} = 1.72$ “unloaded”). In PET, the crystal continues to be improved as the stretching goes on. It illustrates the efficiency of combining stress relaxation and low cooling rate to develop crystallinity after stretching (as discussed during the Debye Scherrer patterns analysis).

To complete the analysis in the stretching direction, the other direction (perpendicular to the stretching) can inform on the $(\bar{1}05)$ family of planes, which is the signature of the periodicity along the chain skeleton [91]. The initial amorphous halo consists of two bumps, the second at an angle of 43° corresponds to this diffraction. The following meridional scans give more information on the evolution of this diffraction, during the tests and from one test to another. This periodicity is not visible on the Debye Scherrer patterns but is detectable on the scans in the machine direction (MD) (Figure 46).

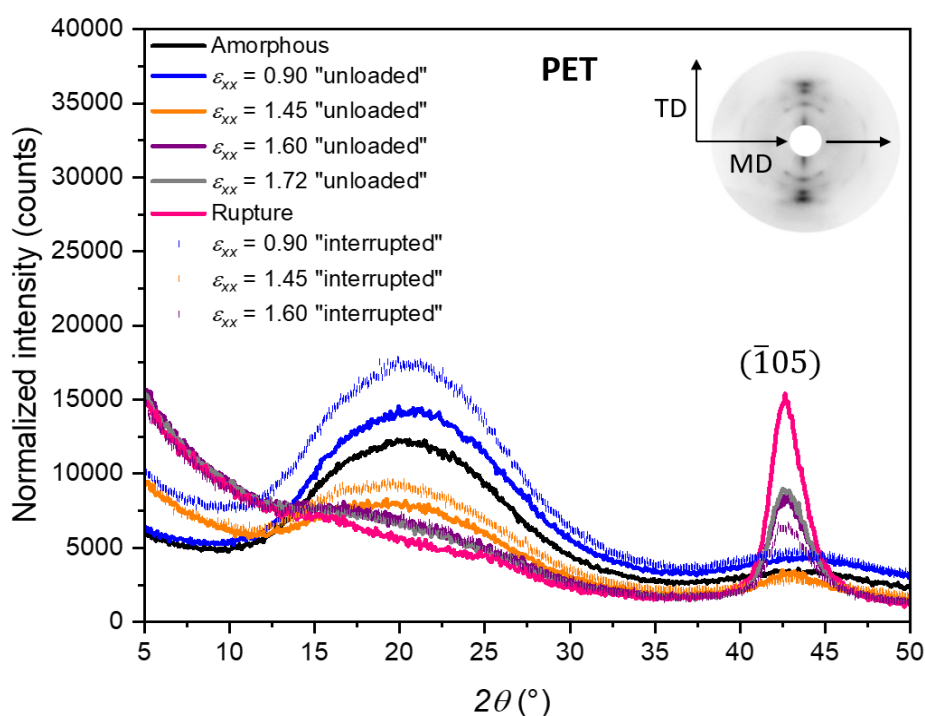


Figure 46. Diffraction scans in the machine direction (MD) for PET. Dots and lines are respectively relative to “interrupted” and “unloaded” samples [116].

In the meridional direction (machine direction), the intensity of the amorphous halo increases, as a function of the stretching up to a deformation of 0.90, and then decreases. In parallel, the intensities are relatively equivalent for both “interrupted” and “unloaded” tests. Some local organization of the amorphous phase could take place with no clear anisotropy.

For the strains above 1.45, the microstructural anisotropy develops, as described on the Debye-Scherrer patterns. Step by step, the mesophase is getting more and more obvious, followed by the crystal appearance. The bump around 43° , observable in the amorphous PET, as well as for the low strain stretched samples, becomes thinner from strain of 1.45. This peak is more intense

for the “unloaded” test (orange line), compared to the “interrupted” one (orange dots). After the unloading, the lateral arrangement is visible in Figure 45.b, but the organization perpendicularly to the stretching direction is not yet evidenced (Figure 46). At higher strain, from $\epsilon_{xx} = 1.60$, the peak is formed, and is once again more intense after the unloading. The chains organization is then optimum, and promotes along and perpendicularly to the chain axis some longitudinal and lateral periodicities, which allow the optimization of the interactions in all the planes (H and ϕ - ϕ bonds). The chains packing is then improved, and this organization becomes more and more probable as the stretching goes on [116].

3.2.2 PEF crystal formation

The microstructural development observed, in Figure 42 for PEF stretching, is illustrated in Figure 47 from the diffraction scans in the transverse direction (TD).

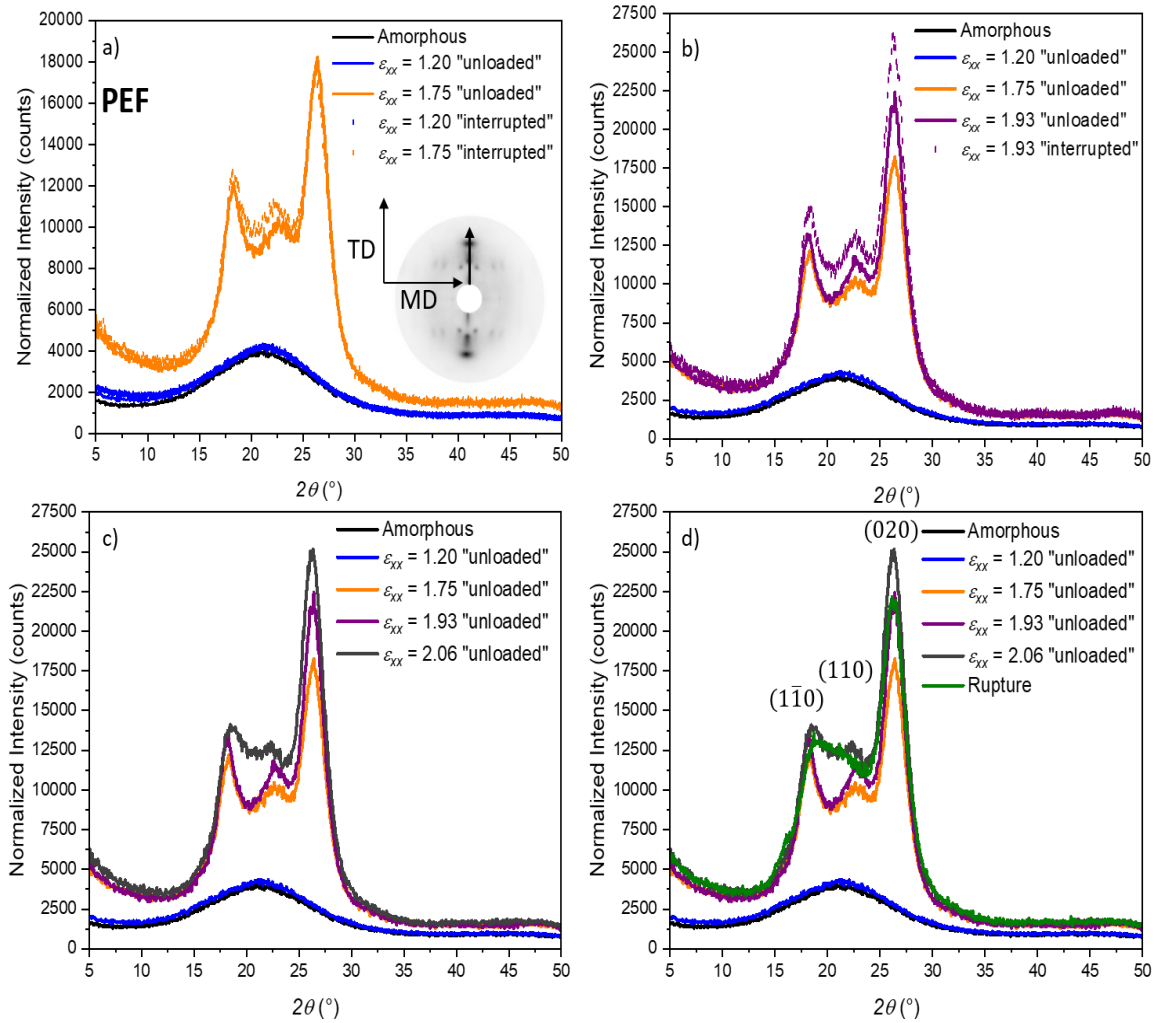


Figure 47. Diffraction scans obtained in the transverse direction (TD) : development of the PEF crystalline phase for “interrupted” and “unloaded” tests; up to a strain of (a) 1.75; (b) 1.93; (c) 2.06 and (d) up to the rupture. Dots and lines are respectively relative to “interrupted” and “unloaded” samples [116].

The first “interrupted” and “unloaded” stretching conditions (Figure 47.a, $\epsilon_{xx} = 1.20$) exhibits a close to a fully amorphous microstructure, as it was observed in Figure 42 for both samples. The associated crystal ratios are close to 0%. When the deformation is stopped just before the NDR ($\epsilon_{xx} = 1.75$, Figure 47.a), the crystal is wholly formed, even before the unloading. The crystal ratios are of 27 % and 32%, for respectively “interrupted” and “unloaded” tests. Contrary to PET, three intense diffraction peaks can already be observed. Moreover, the peaks intensity decreases slightly with the unloading. It can be explained by a disorientation of the crystal towards others directions (not observable on this scan), or by a disappearance of PEF crystal during the unloading. As the crystal ratio increases slightly, and as it was shown in previous

works that PEF crystal is defined in equatorial, meridional but also in other directions, the first hypothesis could be more relevant [58,59,65].

The same scenario is found just after the NDR ($\varepsilon_{xx} = 1.93$, Figure 47.b). The “interrupted” sample is associated to more intense peaks, compared to the “unloaded” one. The crystal ratio is lower for the “interrupted” test (28 %) than for the “unloaded” one (35 %). For a strain of 1.93, both samples exhibit higher peaks intensity than the sample unloaded before the strain hardening occurrence (orange curve, $\varepsilon_{xx} = 1.75$). The last unloaded condition ($\varepsilon_{xx} = 2.06$, Figure 47.c) exhibits again an increase of the peak intensity. The crystal ratio is close to the previous unloaded condition (34 %). Nevertheless, the definition of the peaks changes. Up to now, three well-defined peaks were observable but from this point, the first and the second peaks become closer and wider. This trend continues to exist when the sample is stretched up to its rupture. The peak intensity of the (020) family of planes decreases slightly. The merging of the first and the second peak is clearly visible, as a bump is formed, while the two families of planes remain distinguishable. It seems that when PEF is stretched to high level of deformation, its first crystal formed (before the NDR) can be deformed, and maybe slightly unstructured, if the stretching goes on. This observation is realistic as it was observed in the second Chapter that the process zone of the sample is deformed a last time after the NDR and before the rupture. Moreover, the crystal deformation that could occur during the NDR, can explain the slight differences in angular position that have been observed in the Chapter 3, between SIC and the static crystallization. It confirms the unicity of the crystal structure. The final crystal ratio does not change and is of 35%. Unlike PET, the crystal ratios measured in PEF, do not really evolve from the NDR.

When the sample to screen distance decreases down to 30 mm, some additional and diffuse diffractions become observable (Figure 48), close to the meridional direction [65,116].

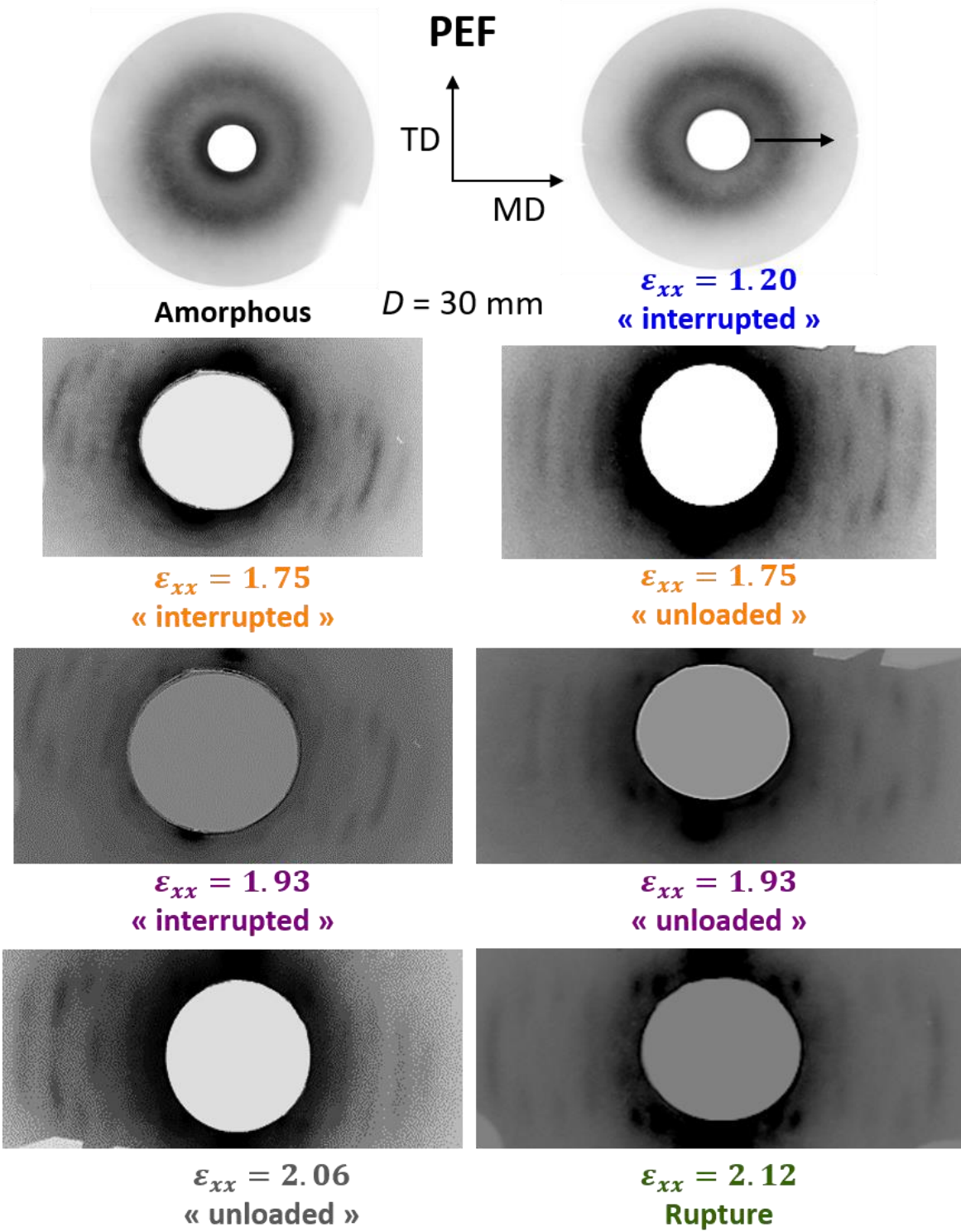


Figure 48. Debye Scherrer analysis of "interrupted" and "unloaded" PEF samples at several strains [116].

In Figure 48, two situations are depicted. When the deformation has been performed up to $\varepsilon_{xx} = 1.20$, similarly to the initial amorphous sample the amorphous halo is observable through an isotropic structure. This is observed for both “interrupted” and “unloaded” samples, even if only the result of “interrupted” sample is presented here. When the stretching develops, the diffuse arcs become observable on all the patterns. These diffractions appear at the same time as those observed in Figure 42. It is difficult to discuss the intensity of the spots, as they correspond more to diffuse arcs rather than spots.

Nevertheless, it can be concluded that a crystalline phase appears as a whole in PEF, and that no intermediate organizations are stable enough to be observed after the unloading. It is different from PET where the stretching seems to firstly lead to a metastable phase, and then the crystal with all its periodicities is formed as the stretching continues. It can be suggested that the main responsible of these differences is the limited mobility of the furan ring that cannot flip into the tensile plane, and does not promote the same level of interactions between the constitutive units.

4. Properties induced by the stretching

Figures 49 and 50 show DMTA measurements carried out for the samples of this study. DMTA analysis is expected to address residual mobility of amorphous phase in a quite indirect manner.

4.1 PET amorphous phase mobility and rigidity evolution

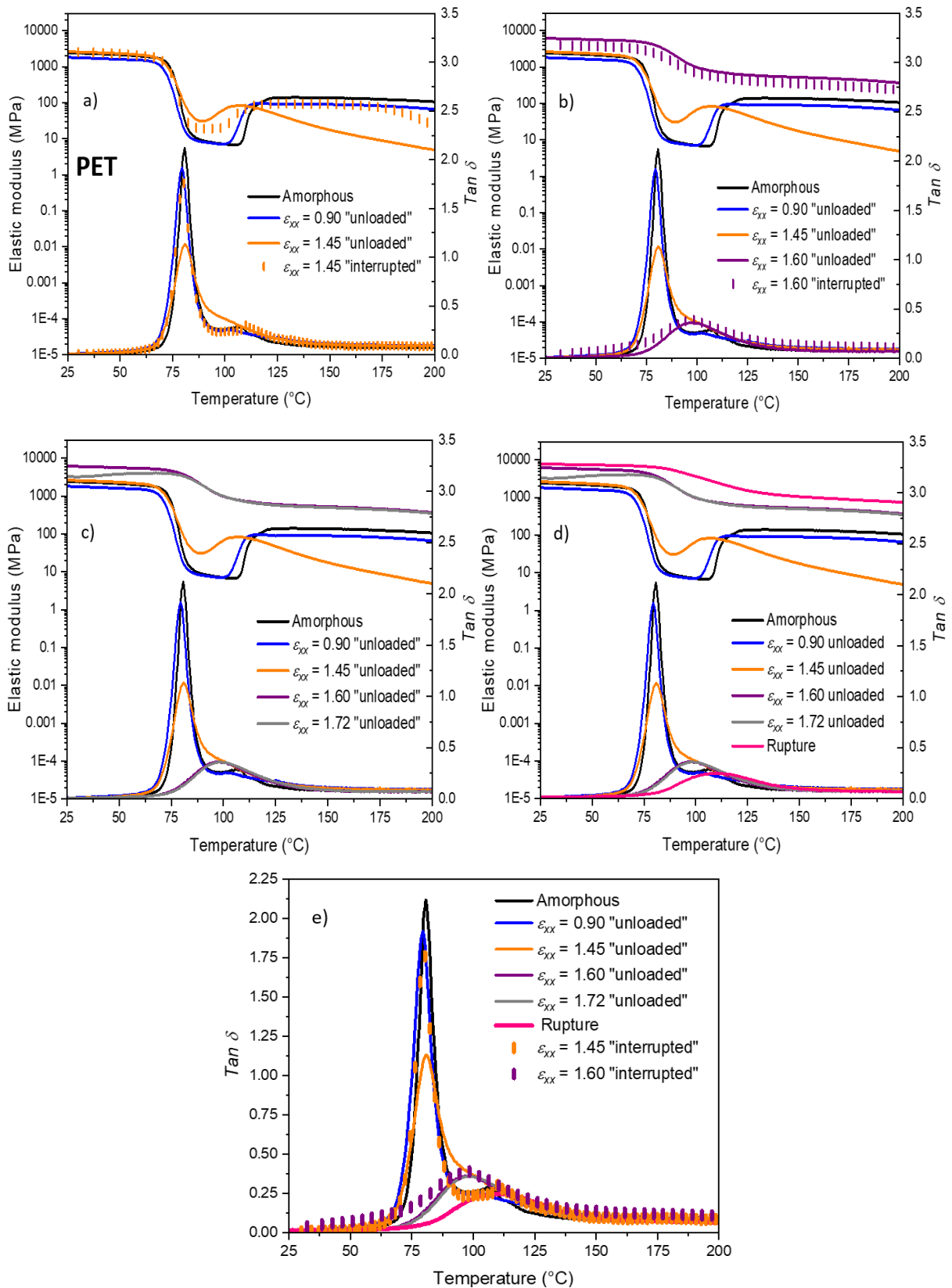


Figure 49. PET measurement of the viscoelastic behaviour through a DMTA analysis performed at 1 °C/min for “interrupted” and “unloaded” tests up to a strain of (a) 1.45; (b) 1.60; (c) 1.72 and (d) up to the rupture; (e) zoom on the $Tan \delta$ evolution. Dots and lines are respectively relative to “interrupted” and “unloaded” samples [116].

For the low strain condition ($\epsilon_{xx} = 0.90$), the elastic modulus, at the glassy plateau, is slightly lower than the one of the amorphous sample (Figure 49.a). It is likely that the processing of the films has induced some rigid zones in the material, that were relaxed during the pre-heating stage of the tensile protocol. The stretching up to strain of 0.90 could not be enough to re-create some rigid areas to the same extent as in the initial material. In an equivalent manner to DSC, during a DMTA test, the cold crystallisation occurs at lower temperature for this sample stretched up to a low strain compared to the amorphous one. Nevertheless, the modulus at the rubbery plateau does not vary. It suggests that the apparent entanglement density does not significantly evolve during the stretching (or decreased while reaching the glass transition during DMTA test). The microstructural change remains weak. When a strain of 1.45 is reached (orange dots curve and orange line), the elastic modulus of the glassy plateau slightly increases, and the crystallization temperature is decreased in such a way that the rubbery plateau almost disappears. In the case of “interrupted” samples, this effect is less important. It confirms the DSC observations, with a real difference in the cold crystallization between the “interrupted” and “unloaded” PET, for this strain level. The α -relaxation temperature does not increase significantly and ranges from 79 °C to 81 °C, when the strain ranges from 0 to 1.45. For higher strains, no evidence of the cold crystallisation is observed anymore, and the α -relaxation temperature increases from 98 °C to 110 °C (Figures 49.c to 49.d). Both the glassy and rubbery plateaux increase. In the $Tan \delta$ signal (Figure 49.e), the decrease of the peak amplitude as the mesophase is formed, followed by the crystal apparition, testifies of the restricted mobility of the amorphous domain.

4.2 PEF amorphous phase mobility and rigidity evolution

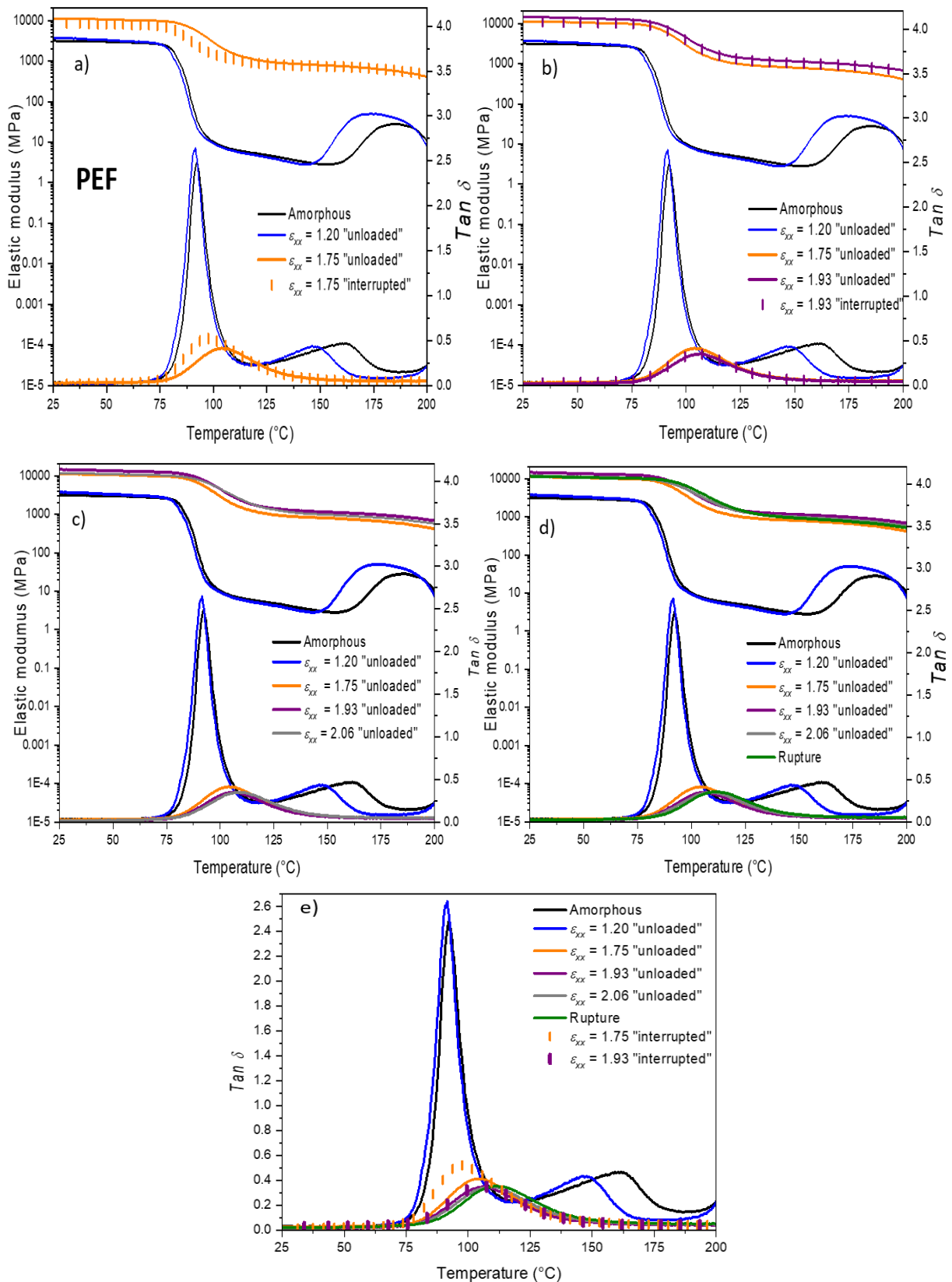


Figure 50. PEF measurement of the viscoelastic behaviour through a DMTA analysis performed at 1 °C/min for “interrupted” and “unloaded” tests up to a strain of (a) 1.75; (b) 1.93; (c) 2.06 and (d) up to the rupture; (e) zoom on the $Tan \delta$ evolution. Dots and lines are respectively relative to “interrupted” and “unloaded” samples [116].

The same qualitative observations can be done for PEF (Figure 50). The stretching up to a low strain ($\epsilon_{xx} = 1.20$) results in a decrease of the cold crystallisation temperature. It was not visible on the DSC scans, as the heating rate was ten times higher (1 °C/min vs 10 °C/min), and consequently too high to fit with the low mobility of the chain. The stretching up to high strains leads to an increase in T_α (up to 112 °C) and to an increase of the modulus. The increase of the α -relaxation temperature along the stretching, as well as the decrease of the chain mobility, is clearly visible in Figure 50.e. The amorphous phase is getting more and more constrained by the crystalline phase. This evolution is not really progressive and, is more brutal than for PET. Some microstructural improvement until the sample rupture, in terms of rigidity and thermal stability, may still exist in PEF, even if the crystal is formed before the strain hardening. To conclude, the formation of PEF crystal occurs before the NDR. The DMTA results are in good agreement with the previous results, and give additional information on the potential remaining crystallisation and on the α -relaxation temperature evolution. The relatively slow heating rate in DMTA suits better with the PEF crystallization rate compared to the one used in DSC, as it allows to observe the crystallization.

4.3 Modification of the local motions by the stretching

Figures 51.a and 51.b represent the β -relaxation of respectively PEF and PET, which is more related to the small local motions such as the one of the carbonyls [46,114]. By this way, one can wonder if “interrupted” and “unloaded” tests reveal progressive changes in this local transition.

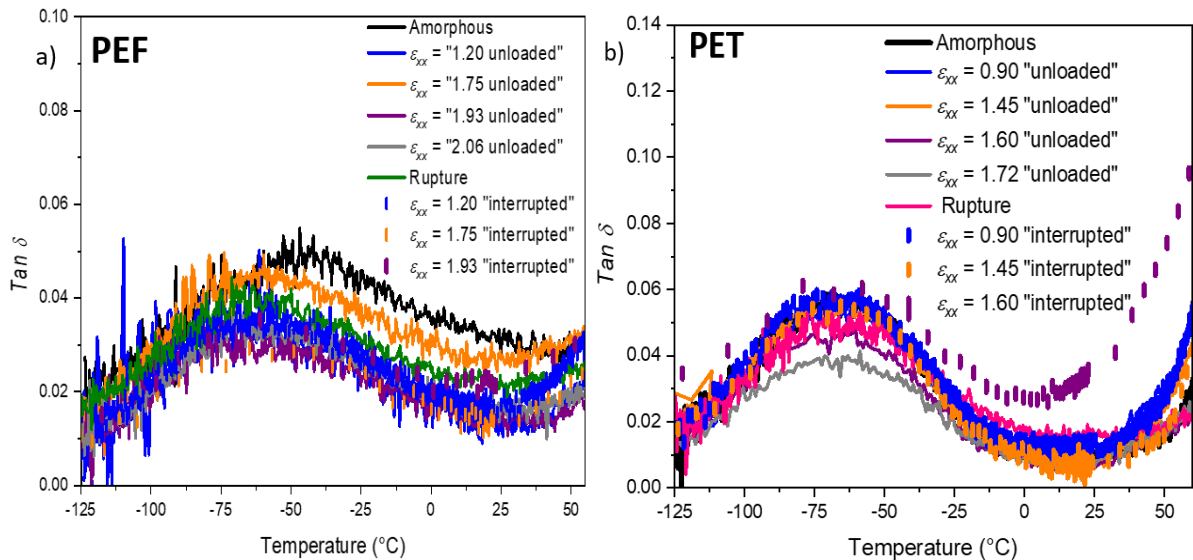


Figure 51. DMTA measurements in the low temperature region of amorphous, stretched and interrupted, stretched and unloaded of (a) PEF and (b) PET.

The β -transition of PEF seems to be shifted to lower temperature for stretched samples. It is true even for the really first deformation stages, and no changes occur afterward [67]. As a remind, it was proposed that the broad amorphous peak could be decomposed into two parts. This decomposition could explain the shift towards the lower temperature range in the case of the stretched samples:

- The left side represents the mobility of the “freer“ carbonyls, the ones in *anti* conformation: predominantly present in the amorphous domain;
- The right side is associated to the more constrained carbonyls, such as those in *syn* conformation, present in the crystal but even in the amorphous domain.

When crystallization occurs, the amount of *syn* conformations increases and, in the fully amorphous area there is mainly the presence of *anti* conformations. Hence, only the left side of the peak remains. It can explain the impression of temperature decreasing. However, no progressive shift towards the lower temperature is noticeable for the “interrupted” and “unloaded” PEF samples.

Concerning PET, the β -transition remains almost the same for the stretched and the amorphous samples. A slight temperature increase is visible for the crystallized samples, but it is too weak to argue on the progressivity or not of the phenomenon. It means that all along the stretching process, there is the existence of strong hydrogen bonds in PET.

4.4 PET and PEF thermal deformation

Thermal deformation measurements have been performed to quantify the dilatation or the contraction of the material during the heating. It can give highlights on the amount of shrinkage of the stretched samples. Indeed, during the heating, the chains that have been extended can relax their extension, or the crystallization can occur.

Figures 52.a and 52.b show the relative length evolution, during DMTA analysis performed on the “interrupted” and “unloaded samples”, for respectively PEF and PET. The behaviour of the amorphous and the static crystallized samples have been added.

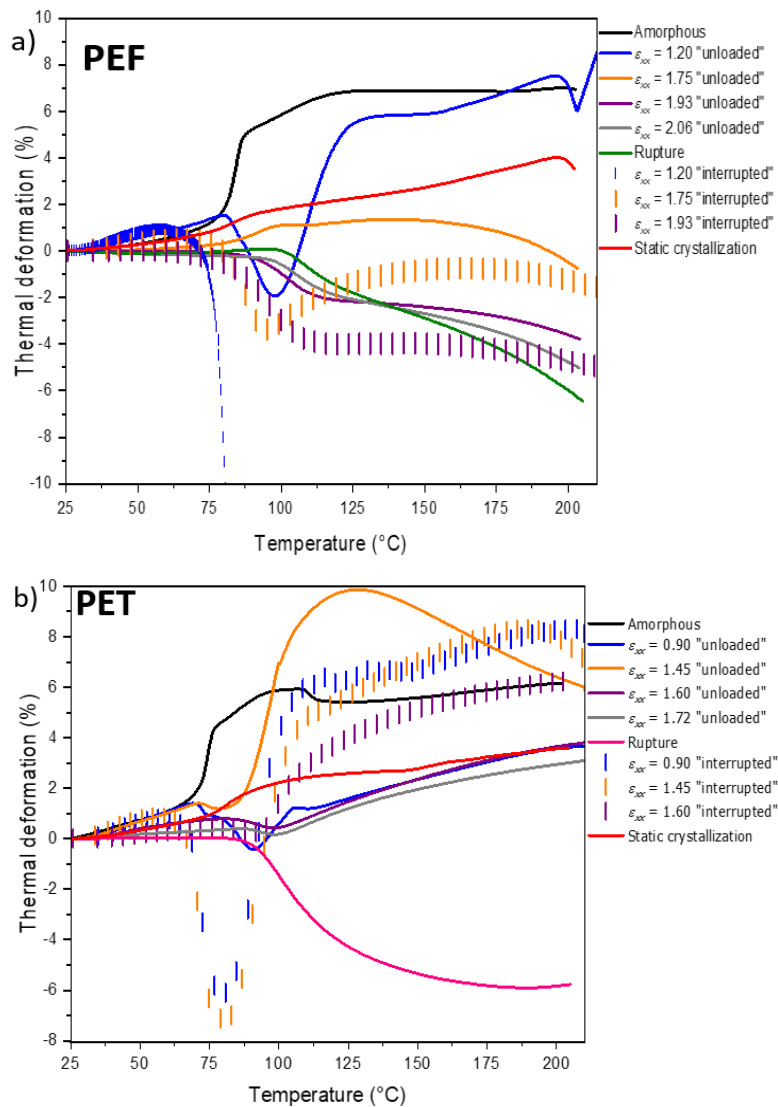


Figure 52. Thermal deformation of amorphous, “interrupted”, “unloaded” and static crystallized (a) PEF; (b) PET from 25 °C to 210 °C measured by DMTA at 1 Hz and 1 °C/min.

Firstly, the continuous dilatation of the amorphous samples (black curves) during the heating is visible for PEF and PET. The thermal deformation is increasing at the crossing of T_α , and a sharp increase is visible at this moment. When the cold crystallization occurs a slight decrease of the curve, which represents the contraction of the structure, is observable. As the cold crystallization is faster in PET this phenomenon is more marked in Figure 52.b, but exists also in PEF (Figure 52.a). The static crystallized sample acts in the same way as the amorphous one, but exhibits a lower amount of dilatation because of the presence of the crystal. At the crossing of T_α the increase of the curve is much less marked.

The shape of the curves for the stretched samples is slightly different from the amorphous case. A drop is visible close to the occurrence of the glass transition. This drop is more pronounced for the “interrupted” tests (dots) compared to the “unloaded” ones (lines), and especially intense for the samples in which a well-defined crystal structure has not been reported. According to the impressive amount of contraction reported, it cannot be only due to the crystallization. It is mainly the result of the relaxation of the extended chains that is possible with the thermal energy brought to the system during the measurement. This drop is less marked for the “unloaded” samples as during the unloading, because of the mechanical energy, these samples have already been able to relax the chain extension in temperature. In PEF, the first “interrupted” sample ($\epsilon_{xx} = 1.20$) is subjected to a too high amount of relaxation that makes the measurement impossible for the device with the settings applied. No stable microstructural organization induced by the stretching can compensate the elastic recovery of the material. During the heating of the stretched samples, there is a concomitantly existence and a competition between the relaxation of the chains, the dilatation and the crystal perfection. The relaxation is dominant firstly, and then dilatation becomes predominant. The crystal perfection seems to have a relatively low contribution, in these samples. The relaxation of the chains is less marked, and appears at higher temperatures for the “unloaded” samples stretched to strains higher than the NDR. The dilatation is also less marked for these samples.

For PET, the shape of the curve of the sample that has been stretched up to the rupture is slightly different from the others “interrupted” and “unloaded” tests. The thermal deformation measurement is sensitive to the thermomechanical path of the samples. With the rupture the unloading of the material cannot be completely known. The impact of “non-controlled” end of test is less marked in PEF, stretched up to the rupture, as it seems that PEF microstructure is less sensitive than PET one.

5. Conformational analysis

This part deals with the existence of progressive, or not, conformational changes for stretched PEF and PET through the analysis of the “interrupted” and “unloaded tests”. Figures 53.a and 53.b analyse the conformational changes in the region of the EG for respectively PET and PEF.

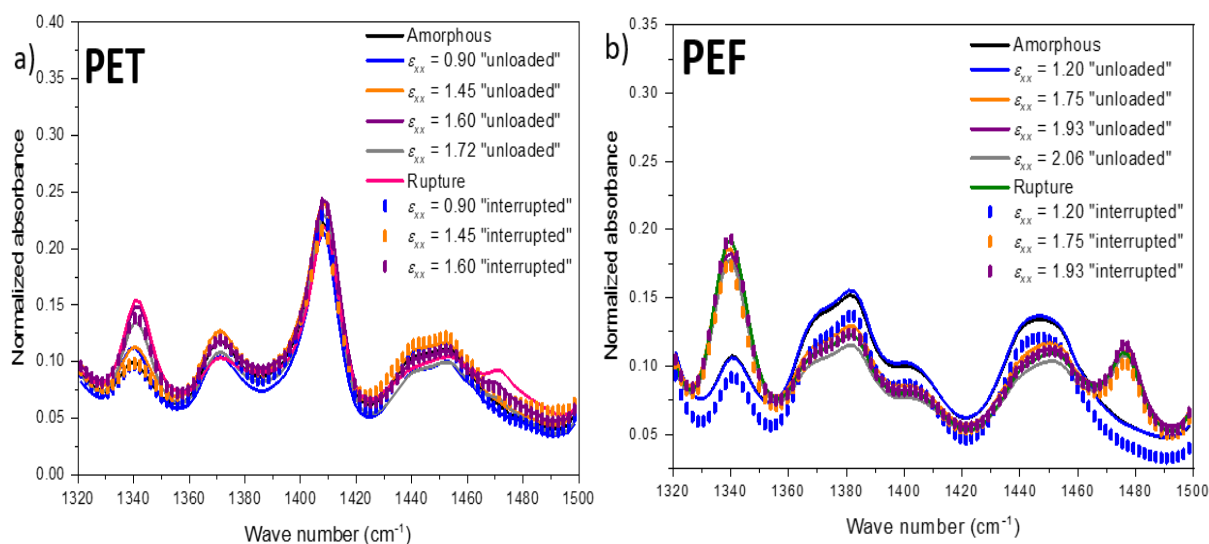


Figure 53. FT-IR spectra from 1320 to 1500 cm^{-1} of (a) PET and (b) PEF for “unloaded” and “interrupted” samples. Dots and lines are respectively relative to “interrupted” and “unloaded” samples [116].

Concerning PET, it is possible to distinguish three cases (Figure 53.a).

For both “interrupted” and “unloaded samples”, when $\epsilon_{xx} = 1.60$; $\epsilon_{xx} = 1.72$ and when the sample has been stretched up to its rupture, there is a significative increase of the peak at 1340 cm^{-1} . With the stretching, the number of EG in *trans* conformation increases: the creation of a crystal, or of a more constrained amorphous phase, takes place.

The two others “interrupted” conditions ($\epsilon_{xx} = 0.90$, blue dots, and $\epsilon_{xx} = 1.45$, orange dots) are well superimposed with the amorphous sample. It means that, there is a minority of EG in *trans* conformation in all these samples, and a majority of *gauche* conformations. It is coherent with their amorphous state.

For the two others “unloaded” conditions ($\epsilon_{xx} = 0.90$, blue line, and $\epsilon_{xx} = 1.45$, orange line), there is an increase of the amount of *trans* conformations, leading to an intermediary state between the amorphous phase, with a majority of *gauche* conformations, and the crystal presence with the *trans* conformation. It is relevant with the previous observations. For the peak

at 1470 cm^{-1} , the same conclusions can be drawn. These progressive changes in PET are noticeable for all the others band that are presented in Annex (Annexes 1 to 3).

About PEF, the situation is more binary as shown in Figure 53.b.

The spectra corresponding to the amorphous sample, the “unloaded” and the “interrupted” samples for the strain of $\varepsilon_{xx} = 1.20$ are well superimposed. It is in adequation with the previous result and with the amorphous structure of these samples (with a majority of *gauche* conformation). For all the other conditions, the number of *trans* conformation increases, as illustrated by the rise of the peaks at 1340 cm^{-1} and 1480 cm^{-1} . All the curves are superimposed. It confirms that the crystal of PEF is well-defined before the beginning of the strain hardening, and remains almost the same after the unloading or the rupture (despite some microstructural improvements). In Annexes 4 to 8, this binary situation is also visible. The amorphous and the interrupted/unloaded conditions far from the NDR ($\varepsilon_{xx} = 1.20$) are almost always superimposed.

In the case of the ester/ether band (Figure 54), a slight difference exists between the amorphous, the “unloaded” and the “interrupted” samples. The band of the “interrupted” sample has been slightly shifted to higher energy. This is the signature of a more constrain environment. For the “unloaded” condition, the band is almost superimposed to the one of the amorphous sample. This aliphatic part of the material, is the easier part to deform. Hence, the observation of some slight changes and orientation on the ether/ester groups is understandable. Moreover this shift can be correlated with the values of RAF (Table 16). Indeed, the χ_{RAF} of the “interrupted” sample is higher than the one of the “unloaded” sample (24% vs 15%). It can explain the localization of this band at higher wave number.

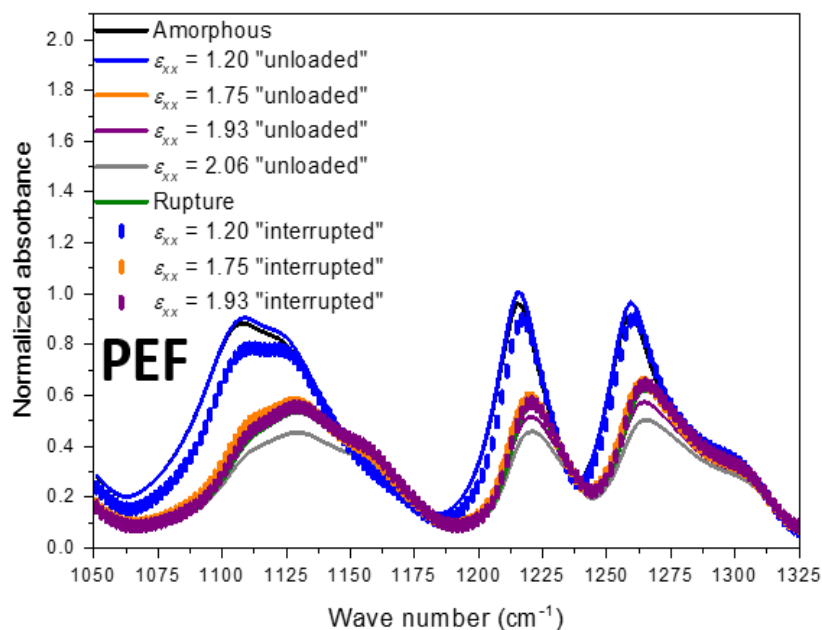


Figure 54. FT-IR spectra from 1050 to 1325 cm^{-1} of amorphous, stretched, stretched and interrupted, and stretched and unloaded PEF.

All this study proves that PEF crystal is formed before the strain hardening and continues to be improved up to the stretching end, while PET is able to promote intermediary metastable phases before the apparition of its final crystal.

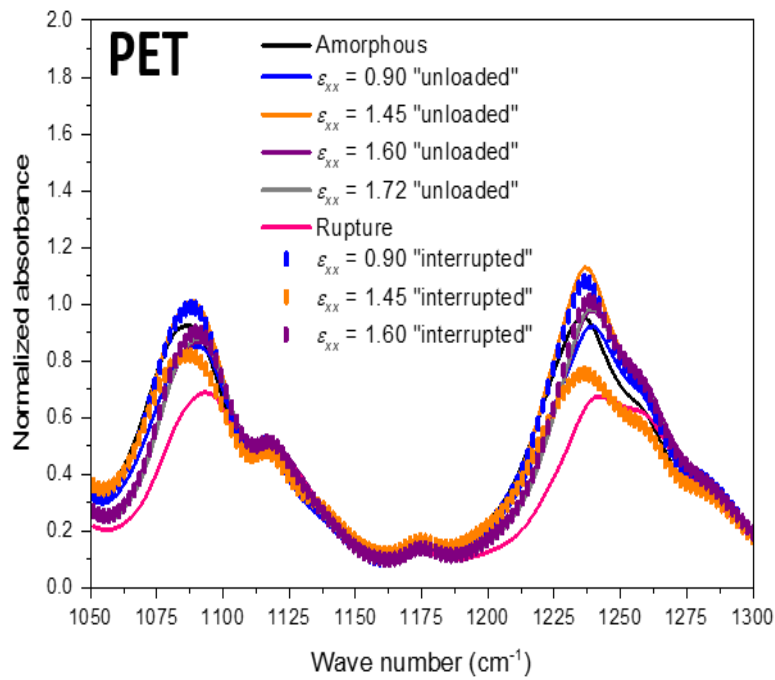
6. Conclusions

To conclude, this chapter has focused on the crystal development scenario over stretching for PEF, in comparison to the better known PET. PET exhibits an easier chain mobility and can develop strong interactions (hydrogen bonds and C_6 interactions). This makes it easier for PET to promote SIC. As soon as some thermal and mechanical energies are given, PET is able to form a mesophase. This mesophase can be an oriented amorphous phase, that will help its crystallization to occur, and that will develop up to the end of the stretching. The definitive PET crystal, with all its periodicities and interactions, is formed only after the stretching end and can be improved during the unloading, or some relaxation steps. Some clear differences are noticeable between the samples “interrupted” or “unloaded” and the one stretched up to its rupture: it testifies the progressive organization in PET.

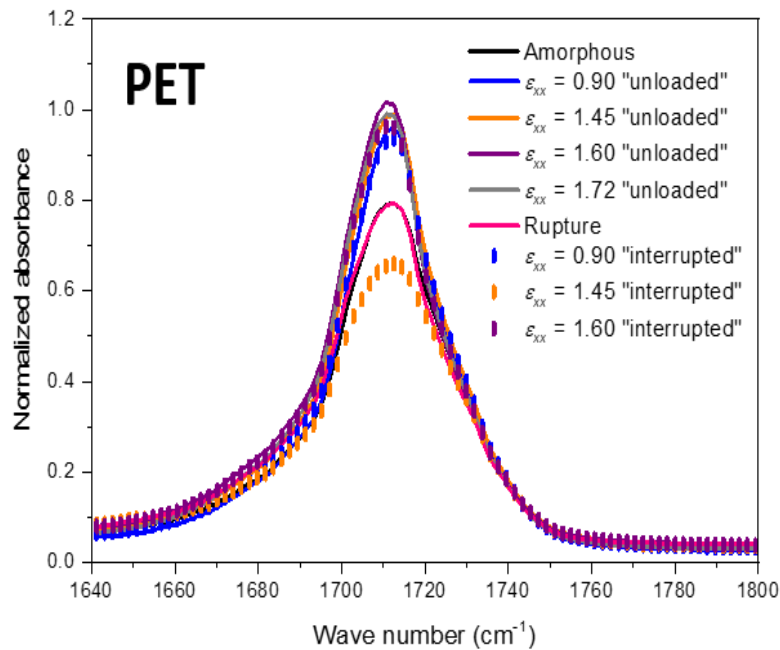
PEF has a real hindered mobility because of the furan ring. The material will need time, and energy to organize its microstructure into a crystal. Moreover, because of the low symmetry of the furan ring, two repeat units are needed in the crystal and two conformational constraints exist: *gauche* to *trans* for the EG, and *anti* to *syn* for the furan groups. As it is a complex process, PEF crystallizes only when its structure can be stabilized. From a mechanical point of view, PEF strain hardening appears only when a crystal is formed. More constrained areas can exist and remain in PEF than in PET. Despite a crystallization before the strain hardening, some microstructural improvements (crystal perfection and *RAF* fraction increase) occur up to the end of the stretching for PEF.

The impact of the stretching settings on the microstructural development, and the associated final properties, in PEF and PET samples, are now going to be analysed.

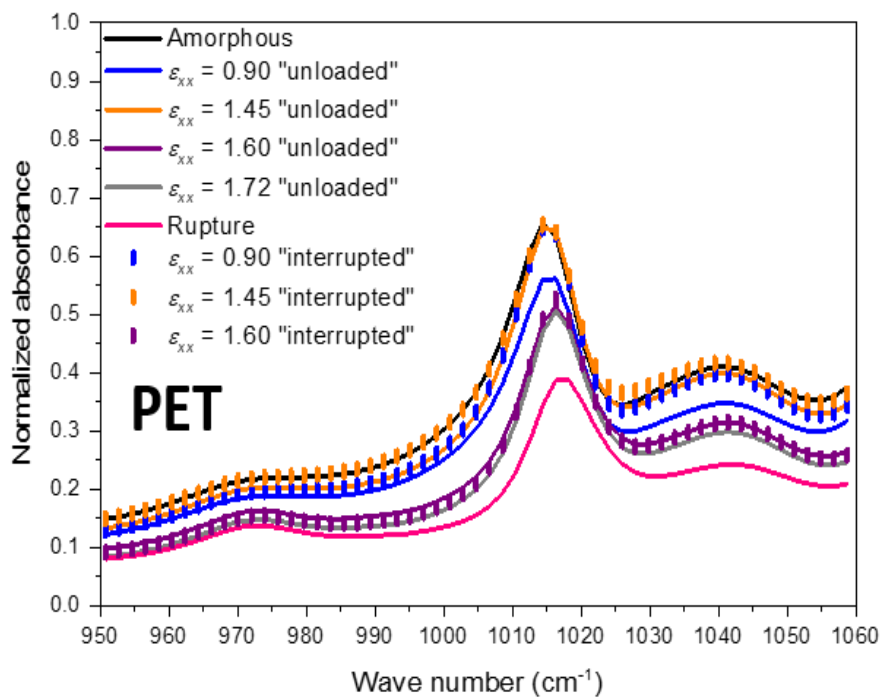
7. Annexes



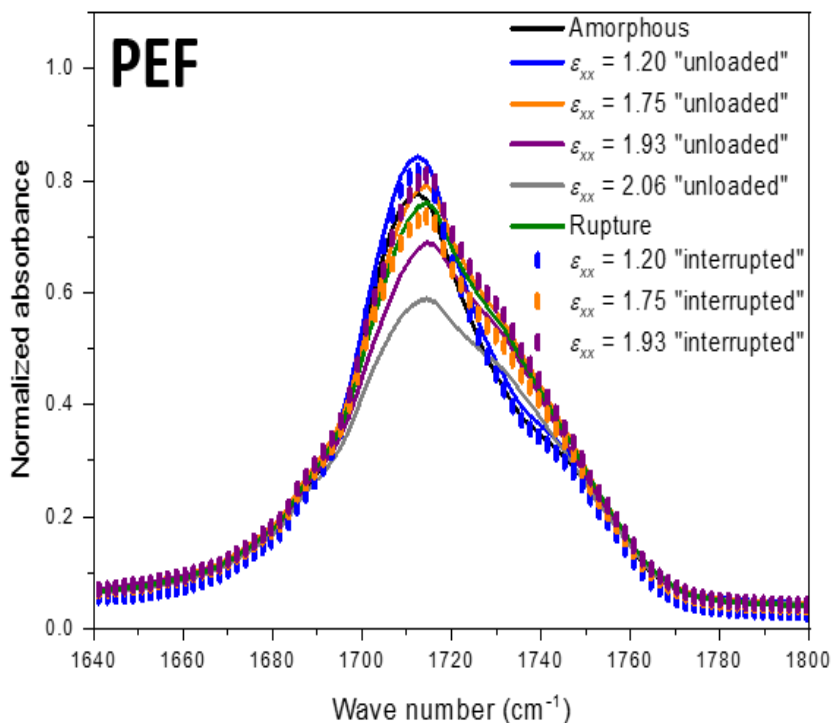
Annex 1. FT-IR spectra from (a) 1050 to 1300 cm⁻¹ of amorphous, stretched, stretched and interrupted, and stretched and unloaded PET.



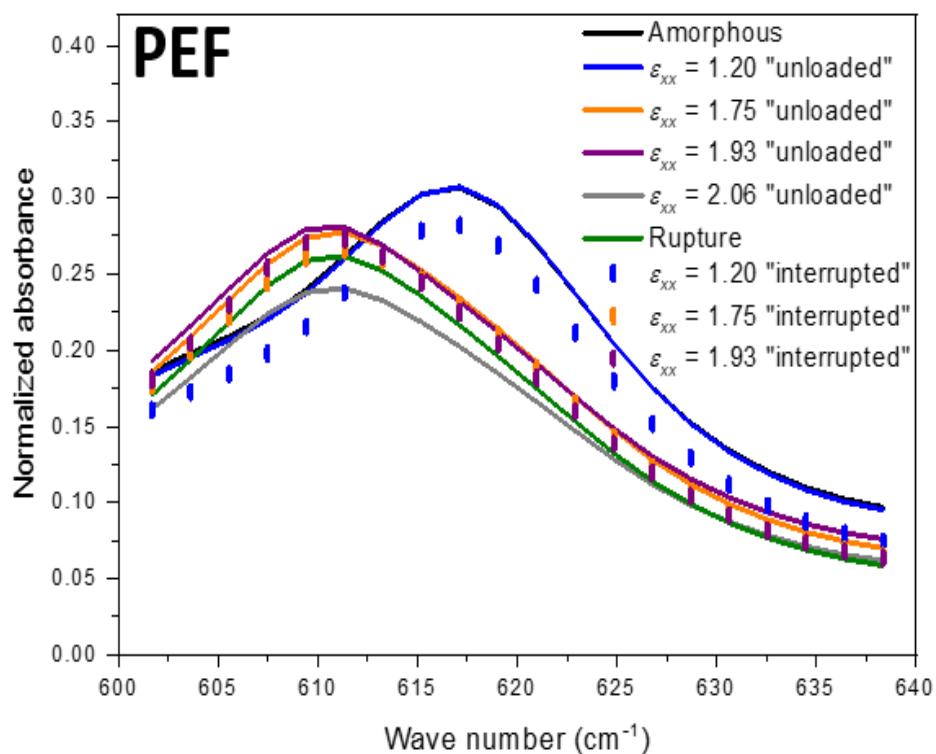
Annex 2. FT-IR spectra from 1640 to 1800 cm⁻¹ of amorphous, stretched up to rupture, stretched and interrupted, and stretched and unloaded PET.



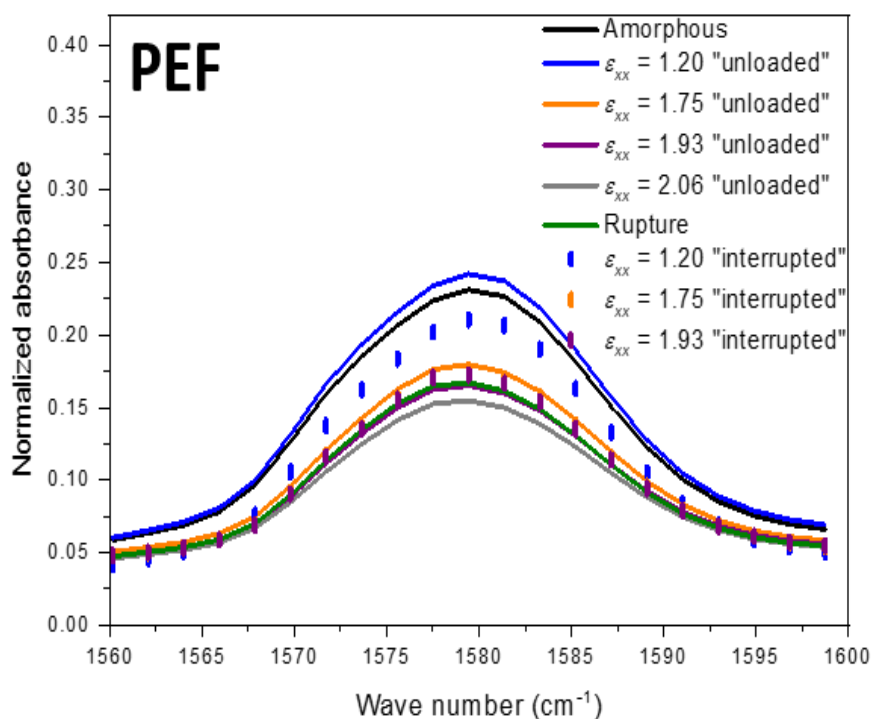
Annex 3. FT-IR spectra from 950 to 1060 cm^{-1} of amorphous, stretched up to the rupture, stretched and interrupted and stretched and unloaded PET.



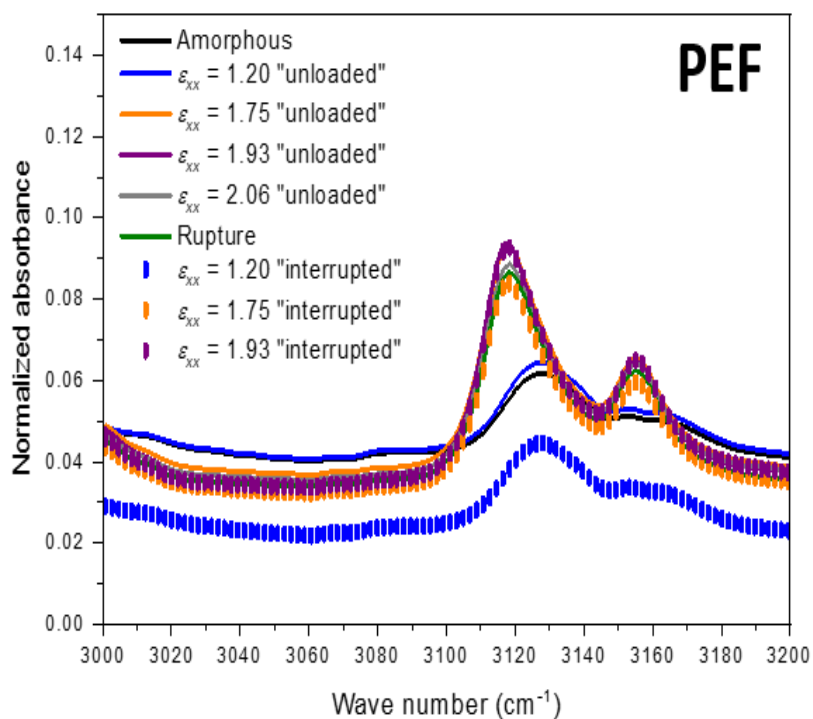
Annex 4. FT-IR spectra from 1640 to 1800 cm^{-1} of amorphous, stretched up to rupture, stretched and interrupted, and stretched and unloaded PEF.



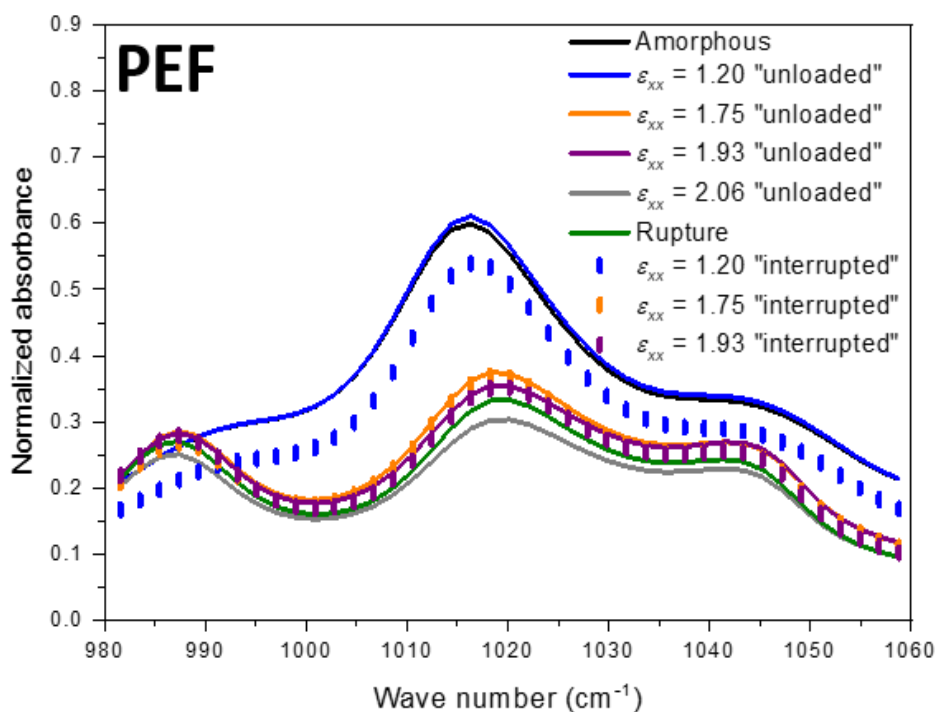
Annex 5. FT-IR spectra from 600 to 640 cm^{-1} of amorphous, stretched until rupture, stretched and interrupted, stretched and unloaded PEF.



Annex 6. FT-IR spectra from 1560 to 1600 cm^{-1} of amorphous, stretched until rupture, stretched and interrupted, stretched and unloaded PEF.



Annex 7. FT-IR spectra from 3000 to 3200 cm^{-1} of amorphous, stretched until rupture, stretched and interrupted, stretched and unloaded PEF.



Annex 8: FT-IR spectra from 980 to 1060 cm^{-1} of amorphous, stretched up to the rupture, stretched and interrupted and stretched and unloaded PEF.

Chapter 5

Characterization of the microstructure and of the thermo-mechanical behaviour of the uniaxially stretched PEF and PET samples

Table of contents

1. Introduction.....	138
2. Stretching of PEF up to close strains	141
3. PET sensitivity to the stretching conditions	146
4. Comparison with the tests performed up to higher strains.....	152
5. Conclusions.....	159
6. Annexes	160

Chapitre 5

Caractérisation de la microstructure et des propriétés thermomécaniques des échantillons de PEF et de PET étirés uniaxialement

Ce chapitre a pour but de déterminer l'influence des conditions d'étirage sur le développement microstructural. Les échantillons étirés uniaxialement et présentés au second chapitre sont ainsi analysés pour le PEF et le PET. Deux paramètres semblent importants pour analyser la microstructure induite par l'étirage : le niveau de déformation final et le couple vitesse de déformation/température utilisé. En effet, les essais réalisés avec une vitesse de déformation dite « rapide », dans le cadre de cette étude, ont probablement été soumis à un auto-échauffement apparaissant durant les dernières étapes de l'étirage. Cet auto-échauffement n'apparaît pas ou bien n'est pas observable sur les essais dits « lents ». Cette constatation est vraie pour le PEF, ainsi que pour le PET. L'auto-échauffement est visible uniquement pour les échantillons ayant un comportement viscoélastique. Les échantillons étirés à la fin des plateaux caoutchoutiques, étant plutôt hyper-élastiques, ne semblent pas le présenter.

Il semblerait que la phase cristalline, aussi bien pour le PEF que pour le PET, soit dépendante du niveau de déformation final atteint. Ainsi, la quantité de cristal mesurée augmente avec la déformation finale. Ceci est vrai pour les échantillons présentant un comportement viscoélastique. Pour les autres échantillons, étant plutôt dans un état hyper-élastique durant l'étirage, les taux de cristallinité mesurés sont plus faibles pour le PET et assez similaires aux autres conditions pour le PEF. La définition des familles de plans du PEF est dépendante de la présence ou non de l'auto-échauffement.

La phase amorphe, quant à elle, est directement soumise aux conditions d'étirage. Lors des différentes mesures, les échantillons se classent selon une vitesse de déformation « lente » ou « rapide ». En effet, les essais réalisés avec une vitesse dite « lente » ont un module élastique plus élevé sur le plateau vitreux que les échantillons « rapides ». Les températures de cristallisation froide sont également plus basses pour les tests « lents ». Ceci signifie que la phase amorphe est pré-orientée et plus contrainte. En effet, les essais « lents » n'ayant pas

bénéficié de l'auto-échauffement, leur domaine amorphe est sûrement plus contraint que celui des essais « rapides », qui ont pu plus facilement relaxer leurs chaînes ou finaliser leur cristal durant la fin de l'étirage.

Malgré la classification par vitesse de déformation « lente » ou « rapide », les différents échantillons de PEF semblent plus proches que ceux du PET, pour lesquels plus de disparités existent. Ceci confirme que le PEF est capable, une fois que les paramètres d'étirage adéquats sont trouvés, de former une microstructure bien définie et similaire. Il faut réussir à dépasser le NDR. Au contraire, le PET affiche une plus grande sensibilité aux conditions expérimentales. Si le PEF et le PET sont comparés, il semble que le PEF soit plus rigide que le PET sur le plateau vitreux. Cependant, le PET forme plus de cristal et a, pour quelques échantillons, une température de transition α plus élevée.

1. Introduction

The uniaxial stretching of PEF and PET has been introduced in Chapter 2. This chapter focuses on the influence of the stretching parameters on the microstructural development, and on the final properties. Based on the time/temperature equivalence principle, several mechanical conditions have been chosen, but one can wonder if an equivalent mechanical behaviour (i.e. the same equivalent strain rate at a reference temperature) leads to the same microstructure, and to the same resulting properties. All the tests of Chapter 2 were settled up to the rupture, and the NDR was reached in any case.

For PET, it is reported in the literature that the microstructural perfection is dependent on the initial physical state: it means the localization of the tests on the master curve [95]. Moreover, the post-stretching treatment also influences the microstructure observed *ex situ* [91]. Concerning PEF, one study deals with the comparison of some samples stretched at various equivalent strain rates [60]. According to their stretching protocol, the authors have found that SIC is improved when the stretching is performed at a stretching temperature 10 °C higher than the T_g . For them, there is the presence of organized phases with a better definition and a higher crystalline fraction than with the other stretching conditions.

This chapter, aims at establishing a wider comparison of PEF and PET stretched samples. In the previous chapter, the influence of the strain level on the microstructural development has been observed through “unloaded” and “interrupted” tests. Thus, the influence, on the microstructural development, of a stretching performed up to higher strains must be quantified. Table 17 and 18 remind, respectively, the PEF and PET stretching tests conditions that have been presented in Chapter 2, and add the final strain reached for each of them.

	Equivalent strain rate at the reference temperature of 100 °C (s ⁻¹)	Stretching settings (s ⁻¹ / °C)	Final strain (ϵ_{xx}^{final})
PEF	10⁻¹	Slow (0.02 / 96)	1.92
		Rapid (0.20 / 101)	1.92
	10⁻²	Slow (0.035 / 101)	2.08
		Rapid (0.13 / 109)	2.15
	5*10⁻⁴	Slow (0.015 / 109)	2.67
		Rapid (0.040 / 117)	2.74

Table 17. Summary of PEF stretching conditions with the associated final strain reached.

	Equivalent strain rate at the reference temperature of 90 °C (s ⁻¹)	Stretching settings (s ⁻¹ / °C)	Final strain (ϵ_{xx}^{final})
PET	$2 \cdot 10^{-2}$	Slow (0.01 / 87)	1.75
		Rapid (0.06 / 92)	1.91
	$2 \cdot 10^{-3}$	Slow (0.02 / 95)	1.94
		Rapid (0.07 / 101)	1.96
	$2.5 \cdot 10^{-4}$	Slow (0.009 / 101)	2.77
		Rapid (0.030 / 106)	2.34

Table 18. Summary of PET stretching conditions with the associated final strain reached.

Concerning PEF, the final strains are slightly different from an equivalent strain rate to another, but relatively similar within the same equivalent strain rate. Thus, a comparison of all the stretching conditions together can be slightly tricky. The equivalent strain rates of 10⁻¹ s⁻¹ and of 10⁻² s⁻¹, defined at a reference temperature of 100 °C, have reached really close level of final strains. In PET, the same final strain can be found for different equivalent strain rates. For both materials, these similarities are in bold in Table 17 and Table 18. The final strain increases with the state of the material : higher strains are reached when the stretching is performed on samples in a “pronounced” rubbery state.

In order to make a correct comparison, the samples that have been stretched up to the same, or to a really close, final strain (ϵ_{xx}^{final}) are firstly compared for PEF, and then for PET. After that,

to get a database on the microstructural development under a stretching performed with several conditions, the others tests are presented.

2. Stretching of PEF up to close strains

Firstly, only the analysis of the tests that exhibit a viscoelastic behaviour during the stretching are presented: it means the tests performed for equivalent strain rates of 10^{-1} s^{-1} and 10^{-2} s^{-1} , at a reference temperature of $100 \text{ }^\circ\text{C}$.

Despite the reaching of the same or close final strains, some differences can exist between the samples. It is true for the crystal ratios, as visible in Figure 55. These ratios have been obtained with a DSC measurement performed at $10 \text{ }^\circ\text{C}/\text{min}$ from $50 \text{ }^\circ\text{C}$ to $250 \text{ }^\circ\text{C}$.

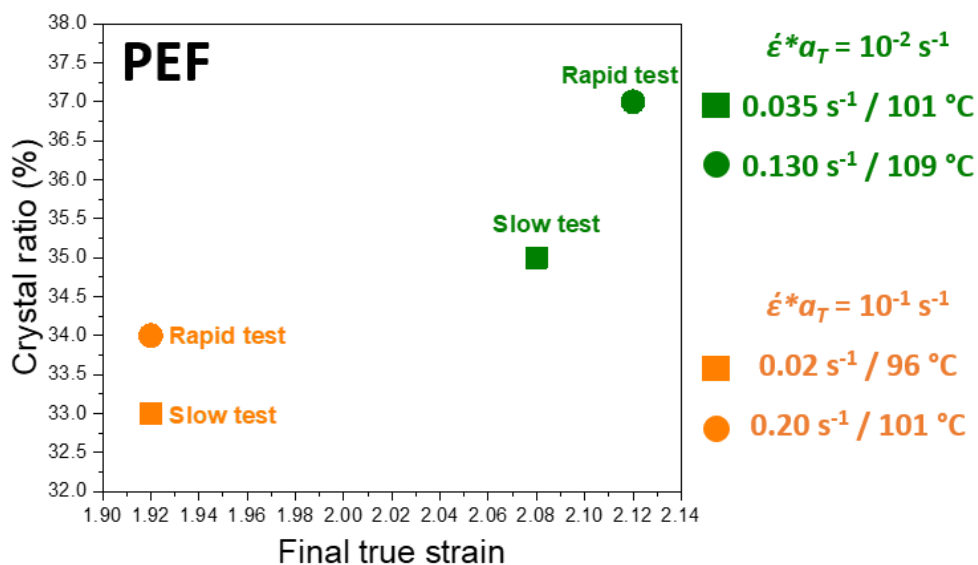


Figure 55. Evolution of the crystal ratio depending on the final strain reached for samples stretched with "slow" and "rapid" strain rates for the equivalent strain rates of 10^{-1} s^{-1} (orange) and 10^{-2} s^{-1} (green) defined at a reference temperature of $100 \text{ }^\circ\text{C}$.

By comparing the two equivalent strain rates, it appears that the reaching of higher level of final strains leads to higher crystal ratios. Within an equivalent strain rate, some slight disparities exist: the tests performed with "rapid" strain rates lead to higher crystal ratios.

The indexed radial scans in TD (Figures 56.a and 56.b) confirm an apparent difference between the samples stretched up to the same final strain, and specially an influence of the stretching settings on the crystal perfection. The Debye-Scherrer pattern of one stretching condition is depicted in Figure 56.c, as an example of the pattern obtained (“rapid” test performed for an equivalent strain rate of 10^{-2} s^{-1} defined at a reference temperature of $100 \text{ }^\circ\text{C}$). The other ones are in Annex 1. To perform these experiments, the sample to screen distance (D) of 75 mm is used [65,67,116].

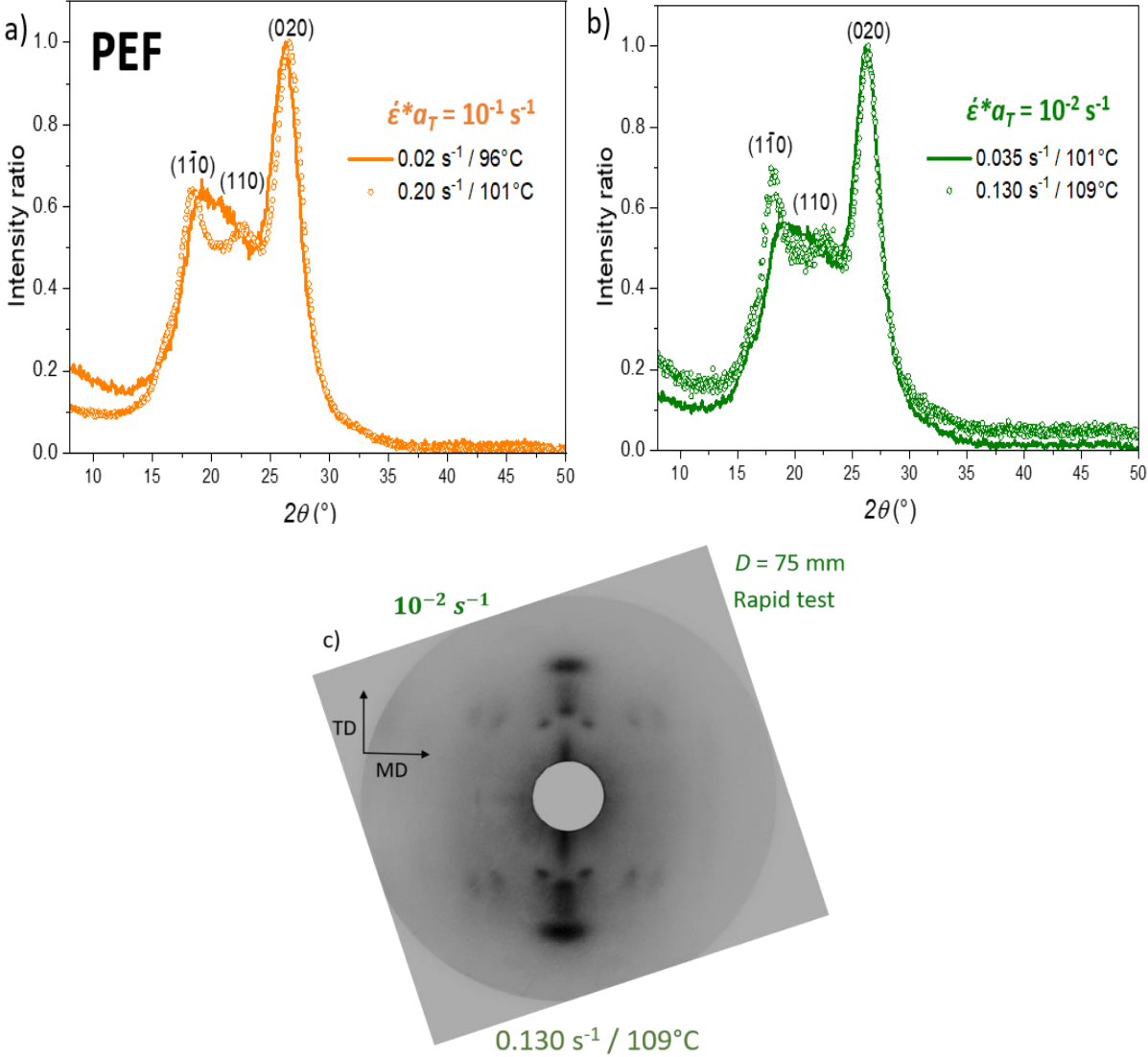


Figure 56. Radial scans from 5° to 50° of PEF, in TD direction, for equivalent strain rates of (a) 10^{-1} s^{-1} (orange) and (b) 10^{-2} s^{-1} (green) defined at a reference temperature of $100 \text{ }^\circ\text{C}$, (c) Debye-Scherrer pattern performed on PEF stretched with “rapid” strain rate at an equivalent strain rate of 10^{-2} s^{-1} , at the reference temperature of $100 \text{ }^\circ\text{C}$.

The orientation of the crystal induced by the stretching is clearly visible through the presence of intense spots, in Figure 56.c and in Annex 1 [65]. The scans in the stretching direction (Figures 56.a and 56.b) lead to the observation of three separated peaks (17.72 °, 22.62 ° and 26.21 °), or to one bump and one intense peak at 26.21 °. If a deconvolution is made, the bump has to be decomposed into two peaks (one around 18.20 ° and the other one around 23.00 °, the exact angular values depend on the stretching settings).

The apparent merging of the peaks appears to be slightly dependent on the stretching conditions. Indeed, it seems that the scans of the samples stretched with “rapid” strain rates (dot curves) exhibit three separated peaks; while the one of the slower strain rates (lines) conduct to the observation of one bump and one peak. This trend is true for all the samples even those stretched up to exactly the same final strain (Figure 56.a). Thus, the only difference between these two tests is the stretching temperature and the strain rate applied. In the previous chapter, the interrupted and loaded/unloaded tests, realised on a “slow” test (0.035 s⁻¹ / 101 °C), had informed that the crystal is formed before the NDR, and that three separated peaks are distinguishable at this moment [116]. It means that the families of planes are well-separated. During the strain hardening, the first two peaks start to merge creating the bump. It has been associated to the deformation of the crystal during the last stages of the stretching. According to the strain rate evolution during the stretching (Chapter 2, Figure 22 and Annexes 1 to 3), the deformation of the crystal takes place for the “slow” and the “rapid” strain rates [65].

An explanation concerning the presence of three peaks in the case of the samples stretched with a “rapid” strain rates is the temperature evolution during the last stages of the stretching. In fact, as visible in Chapter 2, during the last stages of the stretching, the “rapid” tests exhibit a continuous increase of the temperature, while the “slow” tests have a relative constant temperature evolution. By this way, it is possible that a self-heating occurs during the last stages of the stretching, for the “rapid” tests only. Thus, the stretching deforms the crystal but the thermal energy given by the self-heating acts as an annealing step, and then leads to the observation of three separated peaks for these samples. Three separated peaks can also be observed in the work of Menager et al [60], in which an annealing step has been applied after the stretching. On the contrary, in the “slow” tests the deformation of the crystal is made without an additional thermal energy: it leads to the observation of a merging of the first two peaks.

The influence of the stretching settings on the microstructural development (additionally to the final strain) is confirmed through other measurements. Figure 57 represents the analysis of the viscoelastic behaviour of the stretched samples, performed with a DMTA measurement, at 1

°C/min, 1 Hz and from -150 °C up to 200 °C. Table 19 gathers the cold crystallization temperatures obtained with a DSC measurement performed at 10 °C/min from 50 °C to 300 °C. The DSC curves are in Annex 2.

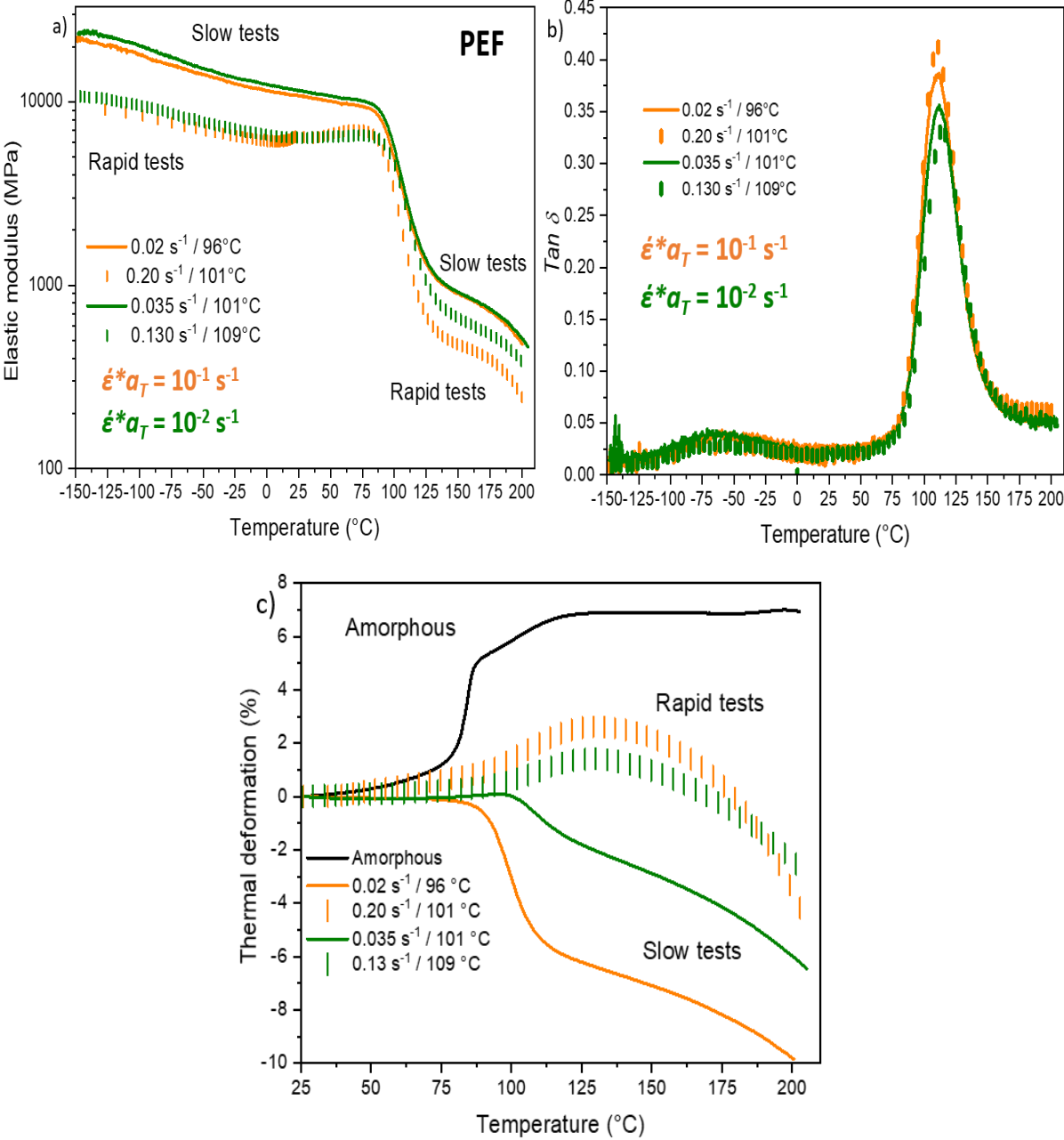


Figure 57. (a) Elastic modulus (E'), (b) $Tan \delta$ and (c) thermal deformation evolutions with the temperature, performed by DMTA at an heating rate of 1° C/min, from (a) and (b) -150 °C to 210 °C and (c) from 25 °C to 210 °C, for stretched PEF.

	Equivalent strain rate (s^{-1}) defined at a reference temperature of 100 °C	Samples	T_c (°C)
PEF	10^{-1}	0.02 s^{-1} / 96°C	112
		0.20 s^{-1} / 101°C	135
	10^{-2}	0.035 s^{-1} / 101°C	117
		0.130 s^{-1} / 109°C	135

Table 19. Cold crystallization temperatures of stretched PEF, measured by DSC with a heating rate of 10 °C/min and from 25 °C to 250 °C.

Some slight disparities are noticeable even if the same level of final deformation has been reached. A similar amorphous domain seems to exist for the “slow” tests, and another one for the “rapid” tests, as visible in Figure 57.a and Figure 57.c. The curves drawn on these figures are classed by strain rates first and then, by the value of the final strain.

The “slow” tests exhibit a really close glassy and rubbery plateaux. For the “rapid” tests, the glassy plateaux are close too. The glassy and rubbery plateaux are slightly higher for the samples that have been stretched up to a higher final strain (green curve, equivalent strain rate of $10^{-2} s^{-1}$ at a reference temperature of 100 °C). This trend is more marked on the rubbery plateau.

The amorphous domain of the “slow” tests seems to be more rigid than the one of the “rapid” tests. The self-heating occurring for only the “rapid” tests can slightly relax some part of the amorphous domain of the material, or can help to turn others towards a crystal. This last hypothesis fits with the higher crystal ratios obtained, for the “rapid” tests. By this way, there is the presence of a lower part of oriented and constrained amorphous domain, and then the elastic modulus on the glassy plateau appears lower for the “rapid” tests, compared to the “slow” tests that have not be submitted to a self-heating process.

The $Tan \delta$ curves are really similar. No real changes are noticeable on the α - and β -relaxations. A close T_α is found between all the samples, but this temperature seems to increase with the reaching of higher strains (tests of the equivalent strain rate of $10^{-2} s^{-1}$ defined at a reference temperature of 100 °C). Indeed, the highest temperature is of 114 °C, and belongs to the sample stretched up to 2.15 (“rapid” test stretched at an equivalent strain rates of $10^{-2} s^{-1}$ defined at the reference temperature of 100 °C). The three others tests exhibit a T_α close to 110 °C. The magnitude of the peak, which is linked to the mobility of the amorphous domain, seems to be dependent on the level of the final strain, and of the crystal ratio value. Then, the samples

stretched with an equivalent strain rate of 10^{-2} s^{-1} , at the reference temperature of $100 \text{ }^\circ\text{C}$, exhibit the lower chain mobility.

The cold crystallization temperature, measured in DSC, seems to fit with the DMTA results, and specially with the thermal deformation behaviour (Figure 57.c). Indeed, as it is visible in Table 19, the cold crystallization occurs always at lower temperatures for the samples stretched with “slow” strain rates. It lets suppose that these samples are composed of amorphous areas that are highly pre-organized, but not in an enough periodic way to form a crystal, then, they remain in the amorphous state. But, as soon as the thermal energy is given to them, they can crystallize. On the contrary, the “rapid” tests have already given this thermal energy to the amorphous domain during the last stages of the stretching, through the self-heating contribution. Then, the cold crystallization takes place at higher temperatures.

Moreover, with the observation of the thermal deformation (Figure 57.c), the relaxation of the stretched chains seems to occur right after the glass transition for the “slow” tests, while for the “rapid” ones this relaxation occurs, as the cold crystallization, at higher temperatures. The self-heating contribution has already given the thermal energy needed to allow the relaxation of the chains in the “rapid” samples.

To conclude this part, it seems that some differences exist between the “slow” and “rapid” stretched samples, especially in the organization of the amorphous domain. The level of the final strain impacts the crystal ratios values, while the amorphous domain and its stability is clearly dependent on the presence or not of the self-heating. The amorphous domain of the “slow” tests seems less stable compared to the one of the “rapid” tests. Nevertheless, the differences appear to be relatively low.

3. PET sensitivity to the stretching conditions

Some PET tests (in bold in Table 18) have reached close final strains. It is the case for the “rapid” test performed at an equivalent strain rate of $2 \cdot 10^{-2} \text{ s}^{-1}$, as well as for the “slow” and “rapid” tests performed at an equivalent strain rate of $2 \cdot 10^{-3} \text{ s}^{-1}$, defined at a reference temperature of $90 \text{ }^\circ\text{C}$. Then, these tests are going to be compared. To broaden the discussion, another test is added: the “slow” test performed at an equivalent strain rate of $2 \cdot 10^{-2} \text{ s}^{-1}$ defined at a reference temperature of $90 \text{ }^\circ\text{C}$ (italic line in Table 18). This test has reached the lowest

final strain but its analysis can help to determine the influence of the strain level on the microstructural development. The comparison with PEF is also conducted.

Figure 58 represents the indexed radial scans performed in TD, as well as the typical Debye-Scherrer pattern obtained for these samples. The Debye-Scherrer patterns of the other tests are represented in Annex 3.

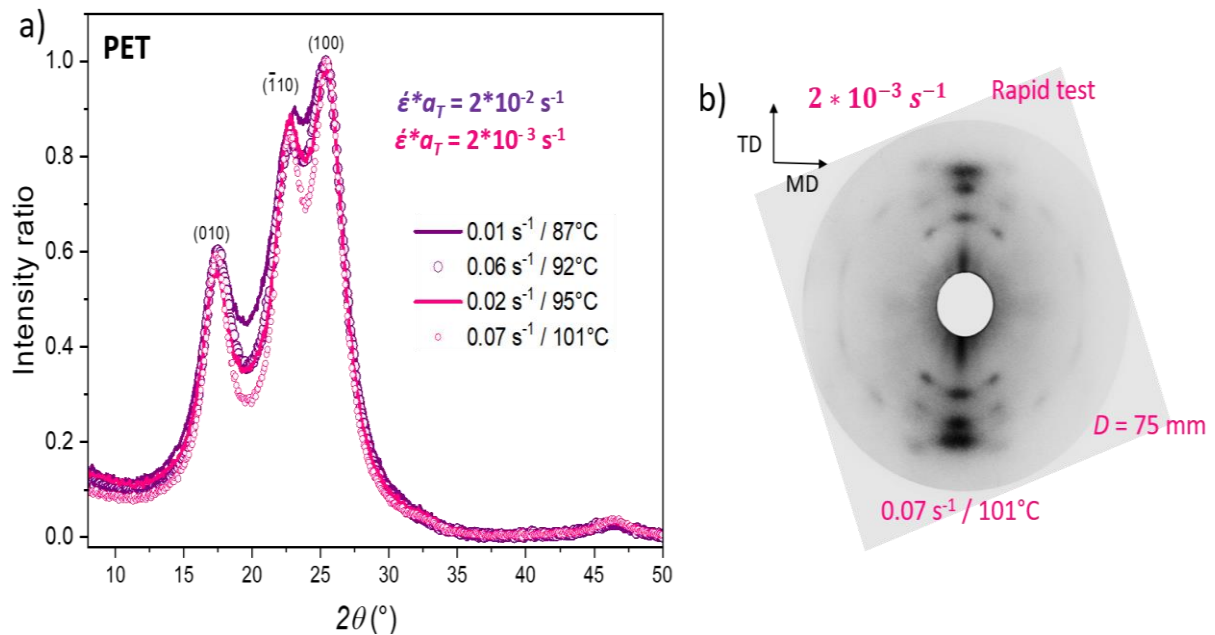


Figure 58. (a) Radial scans from 5 ° to 50 ° of PET in TD, (b) Debye-Scherrer pattern performed on PET stretched with “rapid” strain rates at an equivalent strain rate of $2 * 10^{-3} s^{-1}$ at the reference temperature of 90 °C.

The scans are in agreement with the observations of the previous chapter, made with the “interrupted” and “unloaded” samples. After the stretching end, three thin and separated peaks are noticeable on the scan performed in the equatorial direction (Figure 58.a). The crystal, with all its periodicities, has been formed at the end of the stretching. Then, it appears that the crystal definition of these samples is less sensitive to the strain rate, and thus to the temperature. Indeed, as in PEF, during the strain hardening there is the presence of a self-heating, for only the “rapid” tests (Chapter 2, Annexes 1 and 3). This self-heating does not impact the crystal definition.

The crystal perfection and the definition of the families of planes are sensitive to the final strain reached, as visible in Figure 58.a. The scan of the “rapid” sample stretched at an equivalent strain rate of $2 * 10^{-3} s^{-1}$ is the one that exhibits the thinner peaks and that has been stretched up to the higher strain. Thus, the families of planes seem to be well-defined. The two other samples

stretched to a close final strain exhibit a similar, almost superimposed, scan. The influence of the final strain is confirmed through the analysis of the test stretched up to the lowest final strain (“slow” test of an equivalent strain rate of $2 \cdot 10^{-2} \text{ s}^{-1}$ at a reference temperature of $90 \text{ }^\circ\text{C}$): the peaks are less separated, thus the families of planes have a lower definition. Despite the slight changes observed, the crystal perfection seems to be close between these tests.

The dependence of the final strain on the crystal ratio exists, as in PEF, and is visible in Figure 59. Crystal ratios have been measured through DSC measurements performed at $10 \text{ }^\circ\text{C}/\text{min}$ from $50 \text{ }^\circ\text{C}$ to $300 \text{ }^\circ\text{C}$. Table 20 gathers the cold crystallization temperatures measured in DSC. The DSC curves are visible in Annex 4.

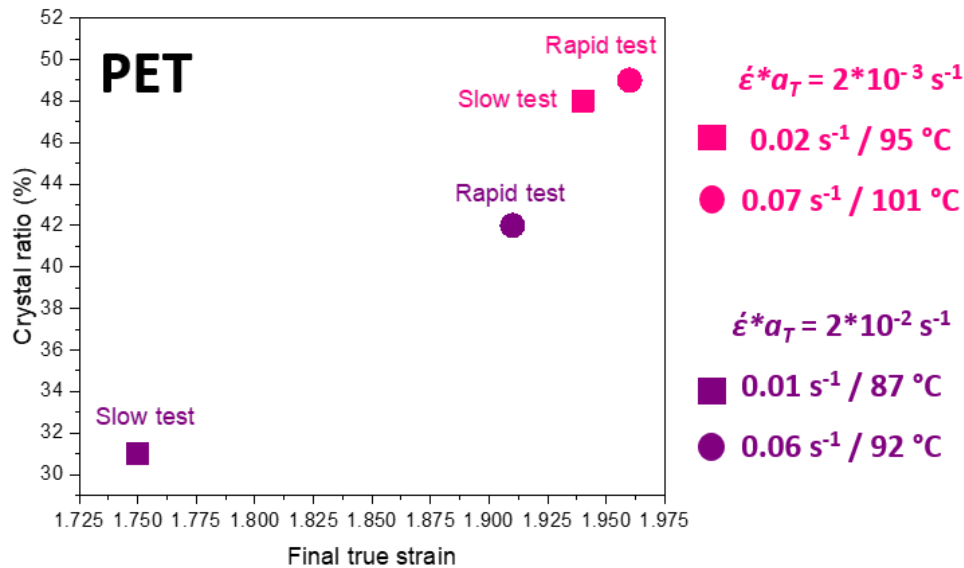


Figure 59. Evolution of the crystal ratio depending on the final strain reached for samples stretched with "slow" and "rapid" strain rates for the equivalent strain rates of $2 \cdot 10^{-2} \text{ s}^{-1}$ and $2 \cdot 10^{-3} \text{ s}^{-1}$, defined at a reference temperature of $90 \text{ }^\circ\text{C}$.

	Equivalent strain rate (s^{-1}) defined at a reference temperature of $100 \text{ }^\circ\text{C}$	Samples	T_c ($^\circ\text{C}$)
PET	$2 \cdot 10^{-2}$	$0.01 \text{ s}^{-1} / 87^\circ\text{C}$	155
		$0.06 \text{ s}^{-1} / 92^\circ\text{C}$	142
	$2 \cdot 10^{-3}$	$0.02 \text{ s}^{-1} / 95^\circ\text{C}$	105
		$0.07 \text{ s}^{-1} / 101^\circ\text{C}$	158

Table 20. Cold crystallization temperatures measured in DSC with a heating rate of $10 \text{ }^\circ\text{C}/\text{min}$ and from $50 \text{ }^\circ\text{C}$ to $300 \text{ }^\circ\text{C}$.

The formation of higher crystal ratios when the stretching has been performed up to a higher final strains is clearly visible. For the conditions that have a similar final strain (around 1.90), the crystal ratio is higher than 40 %. While for the test stretched up to 1.75, the crystal ratio is around 30 %. It is possible that the crystal ratio has been slightly overestimated by DSC (as discussed previously), but the trend seems quite in agreement with the WAXS analysis (Figure 58). Thus, the trend is relatively close to the one of PEF. Nevertheless, the crystal ratios are globally higher for stretched PET compared to stretched PEF. It confirms the complexity of the PEF crystallization in comparison with the PET one.

As in PEF, the cold crystallization of the samples stretched with “slow” strain rates starts at lower temperatures compared to the “rapid” strain rates. For the test stretched at 96 °C, even if the maximum of the crystallization is reported at 155 °C, it is visible in Annex 4, that the cold crystallization starts at the glass transition. It is due to a pre-organization of the microstructure. The variations of the cold crystallization temperatures let suppose, as in PEF, that the microstructural development is not dependent on the final strain only.

As a matter of fact, some major differences exist when the mobility of the amorphous domain is observed on the PET stretched samples. DMTA measurement, performed with a heating rate of 1 °C/min between -150 °C and 210 °C and at 1 Hz, is visible in Figure 60.

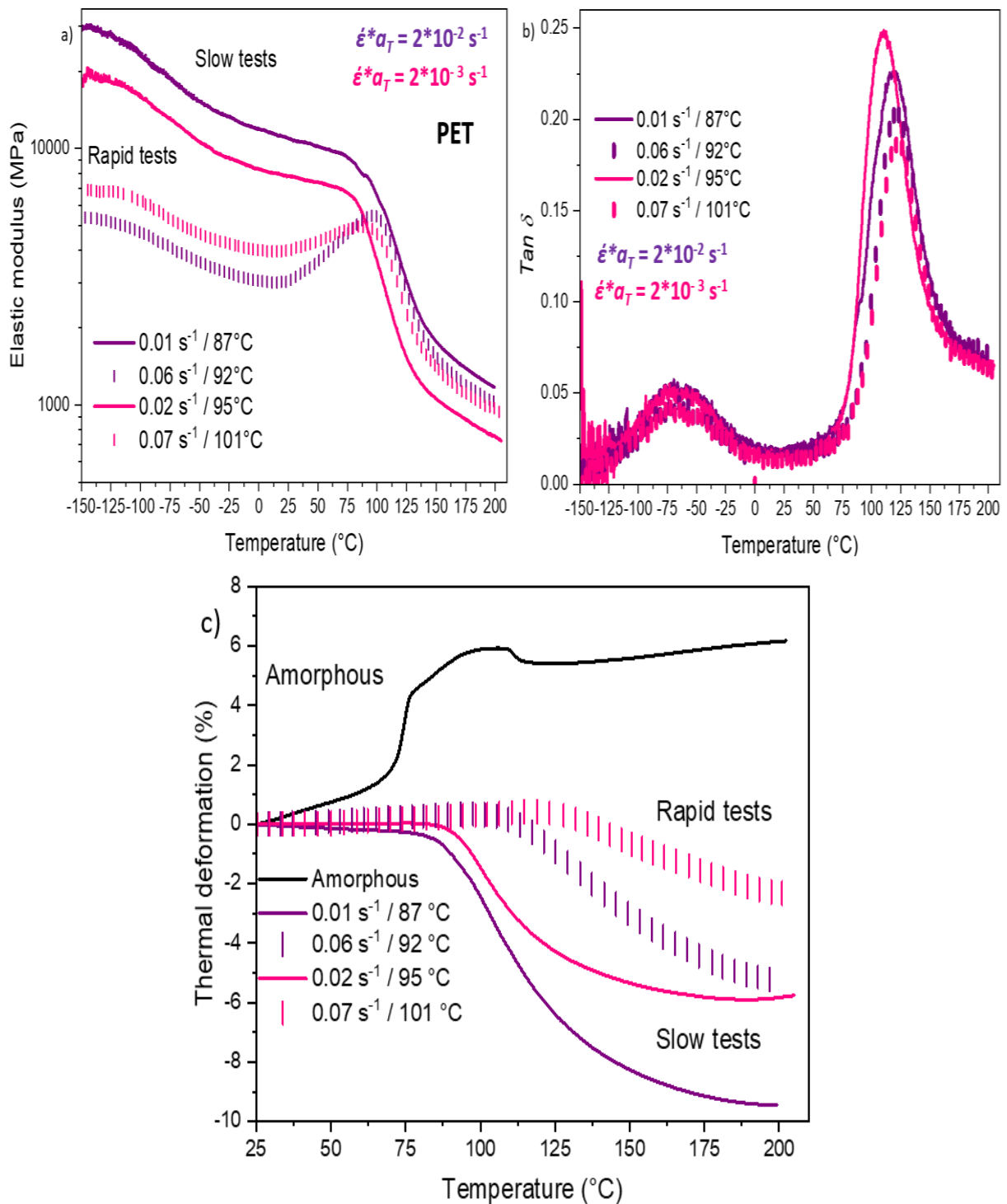


Figure 60. (a) Elastic modulus (E'), (b) $\text{Tan } \delta$ and (c) thermal deformation evolutions with temperature, performed by DMTA at an heating rate of $1^{\circ}\text{C}/\text{min}$, from (a) and (b) -150°C to 210°C and (c) from 25°C to 210°C , for stretched PET.

The trend in PET is similar to the one of PEF, as the tests are also classed by “slow” and “rapid” strain rates on the glassy plateau. But more disparities exist between the PET samples compared

to the PEF ones. The “slow” tests exhibit the higher elastic modulus, as in PEF. It agrees with the high orientation and constraint existing in the amorphous domain of the “slow” tests. But in PET, the highest value does not belong to the higher final strain but to the lowest one: the test stretched up to 1.75. This test, which has the lower crystal ratio, also has the higher glassy and rubbery plateaux. This high elastic modulus can be explained by a high portion of pre-organized amorphous domain that has not been turned into the crystal, during the stretching. But the rigidity of its amorphous domain seems to slightly compensate its lack of stability, as it is developed further.

Concerning the “rapid” tests, the opposite trend is observed: the highest glassy plateau belongs to the sample stretched up to the highest strain (1.96). On the rubbery plateau, the trend is inverted, the rubbery plateaux are close for the two “rapid” tests. It seems that a higher gap exists in the glassy and rubbery plateaux between the “slow” tests, compared to the one existing between the “rapid” tests.

As in PEF, these differences between the amorphous domains of “slow” and “rapid” tests can be explained by presence or not of self-heating during the last stages of the stretching. The amorphous domain of the “rapid” tests can be slightly relaxed compared to the one of the “slow” tests. Moreover, as the “rapid” tests have formed a higher crystal ratio compared to the “slow” tests, the proportion of oriented amorphous domain is lower and the elastic modulus appears less rigid. On the opposite, the amorphous domain of the “slow” tests becomes pre-organized during the last stages of the stretching. It fits with the occurrence of the cold crystallization at lower temperature in DSC, and with the thermal behaviour observed in Figure 60.c.

Concerning the T_α , a higher diversity exists compared to PEF. The peak is wider for the “slow” tests, as a confirmation of the concomitant presence of the crystal, the amorphous domain and the pre-organized domain in these samples. These results on “slow” samples also fit with the low cold crystallization temperatures, and with the high relaxation of the stretched chains in Figure 60.c.

The magnitude of the T_α is lower for the “rapid” tests, compared to the “slow” tests. It is probably due to a better definition of the microstructure (as visible in Figure 60.c with the relaxation of the stretched chains that occurs at a high temperature). Moreover, the highest T_α (around 120 °C) belong to both the “rapid” tests, and to the one stretched up to the lowest strain. On the other hand, the T_α is of 110 °C for the “slow” test performed at 95 °C. It seems that this test is the less rigid, probably because the strain rate is too slow and the temperature too low accounting for the high rubbery state of this material. No real differences exist on the β -relaxation.

To conclude this part, the occurrence of the self-heating impacts the amorphous domain definition, as in PEF. The crystal ratio is clearly dependent on the final strain. On the contrary to PEF, it seems that the stretching leads to more variability in the amorphous domain definition. In terms of rigidity, the stretched PEF samples exhibit a slightly higher modulus for “slow” and “rapid” tests, in comparison with PET.

4. Comparison with the tests performed up to higher strains

As the microstructure has been compared and analysed for the samples stretched in a similar way, in terms of initial rubbery state and final strain, the analysis can be widened to the other samples: those with a hyper-elastic behaviour that have reached higher strain levels. They have been stretched at higher temperatures, and as it was visible in Chapter 2 (Figure 23 and Annex 4), the temperature variation is different from the other tests. In PET and PEF, no or a very low self-heating seems to occur in the final stretching stages (Figure 23 and Annex 4).

Figure 61 represents the Debye-Scherrer patterns of the PET tests stretched up to the highest final strains, while being in a “pronounced” rubbery state.

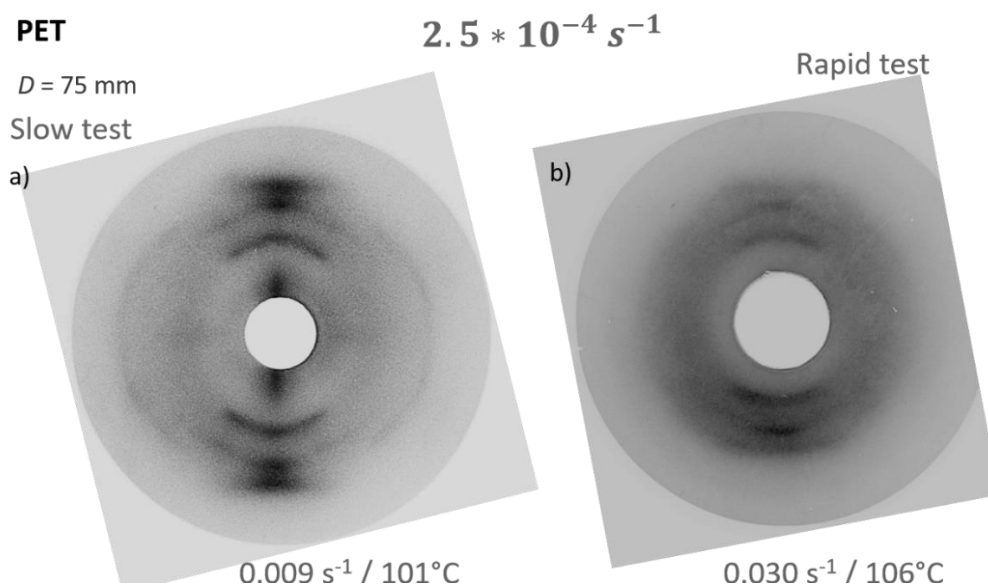


Figure 61. Debye-Scherrer patterns performed on PET stretched with (a) “slow” and (b) “rapid” strain rates at an equivalent strain rate of $2.5 * 10^{-4} \text{ s}^{-1}$ at the reference temperature of 90°C .

These two samples exhibit different patterns compared to the previous ones presented (Figure 58.b and Annex 3): the spots appear to be spreader. It is especially true on the pattern of the sample stretched at 106 °C (Figure 61.b): arcs rather than spots are visible. Thus, the crystal perfection of these samples can be lower compared to the other tests. The indexed radial scans of these conditions confirm this observation and are represented, with the other conditions, in Annex 5, for TD and MD. In Chapter 2, it has been suggested that the PET sample that has been stretched with the highest temperature (106 °C) can have developed a microstructure which is a mix between SIC and some nucleation occurring during the pre-heating step. The “slow” test of this equivalent strain rate has a lower but relatively similar crystal ratio compared to the other conditions (36%), while the “rapid” test has the lowest crystal ratio (22%).

FT-IR measurements have been performed to highlight the differences observed in terms of conformations for these two samples. The “slow” test of this equivalent strain rate seems to be slightly less constrained, on the ether and ester part of the chain, compared to the other samples (as visible in Figure 62), while the sample stretched at 106 °C exhibits constrained groups in a state between the amorphous sample and the stretched ones. The other graphs in agreement with this observation are in Annex 6. As it has been observed previously, no real changes are visible on the carbonyl groups (Annex 6.a).

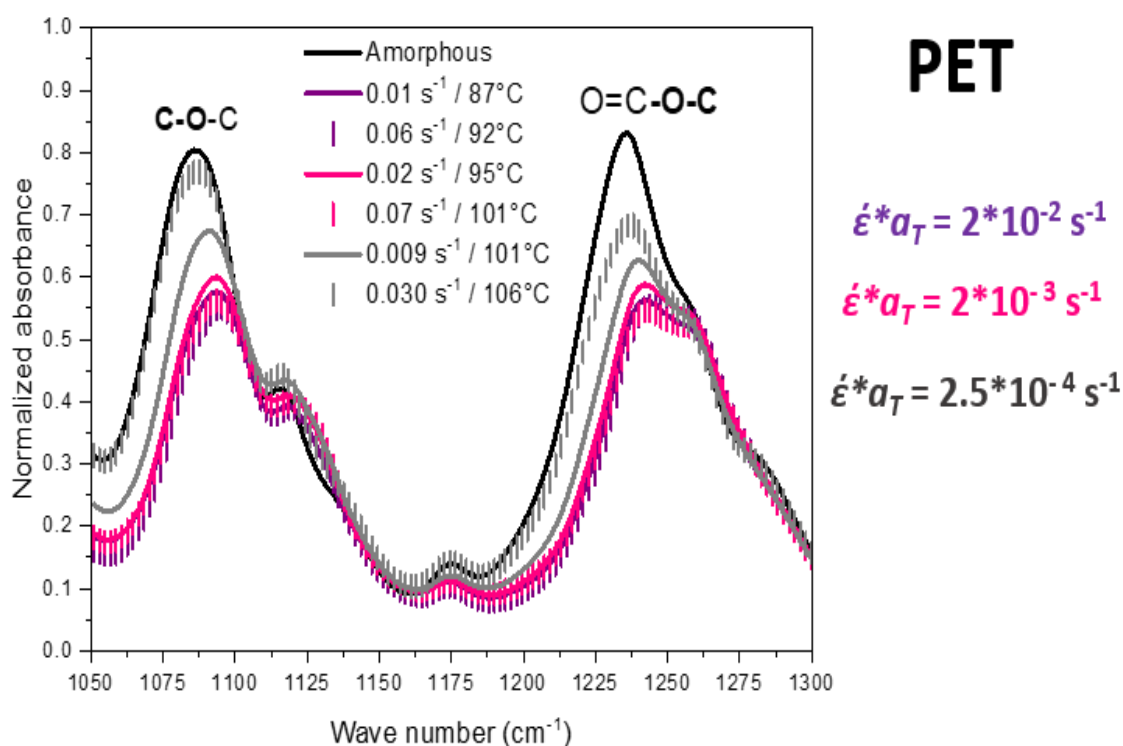


Figure 62. FT-IR spectra from 1050 to 1300 cm^{-1} for stretched and amorphous PET.

These results confirm that the microstructure of the sample stretched at 106 °C is closer to the one of the amorphous sample and then, slightly different from the others samples, in which only SIC has occurred. The other condition of this equivalent strain rate, the “slow” test appears to be closer to the other samples presented in the previous part, in terms of crystal definition, crystal ratio and conformational changes.

The analysis of the amorphous domain through a DMTA measurement is going to add more details on this sample (Figure 63).

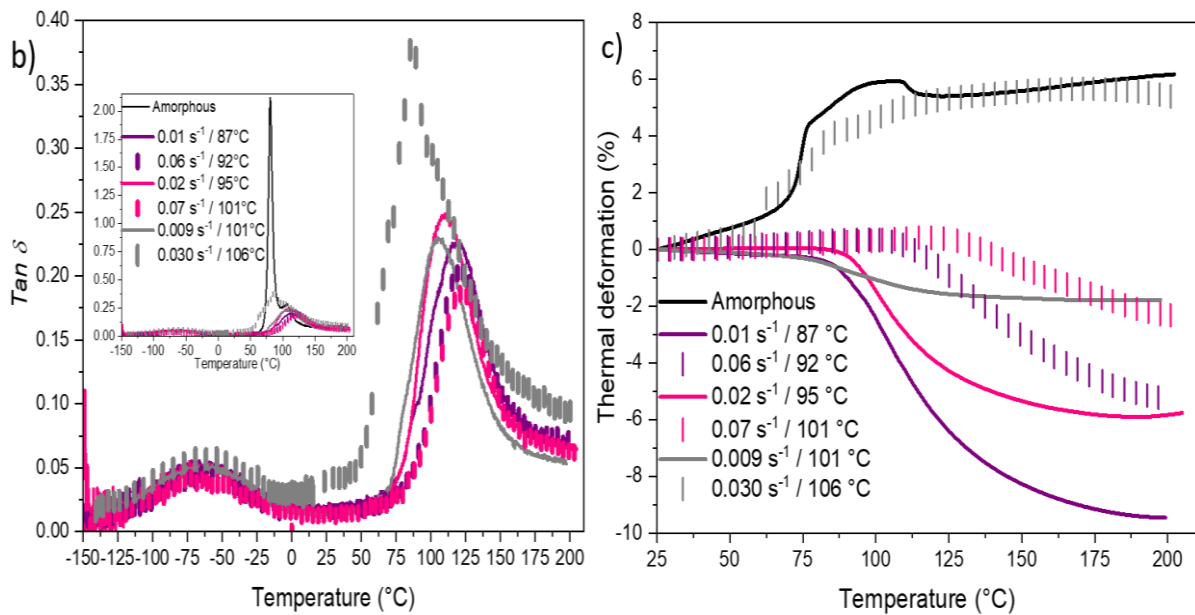
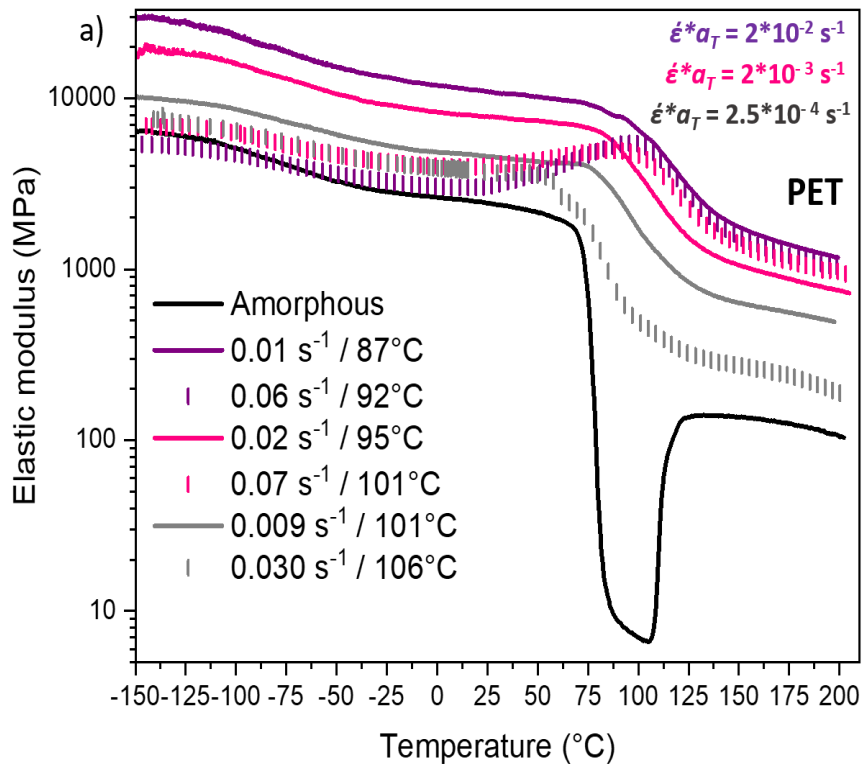


Figure 63. (a) Elastic modulus (E'), (b) $Tan \delta$ and (c) thermal deformation evolutions with temperature, performed by DMTA at an heating rate of $1^\circ \text{C}/\text{min}$, from (a) and (b) -150°C to 210°C and (c) from 25°C to 210°C , for stretched PET.

The “slow” test performed at 101°C , for an equivalent strain rate of $5 \cdot 10^{-4} \text{ s}^{-1}$, presents an elastic modulus closer to the “rapid” tests, in comparison to the other “slow” tests. It is possible that when being in a high rubbery state, the combination of a stretching at 101°C with the

“slow” strain rate does not allow the formation of an amorphous domain as rigid as the one of the other “slow” tests (performed at lower temperature and equivalent strain rate). The α -relaxation of this sample also occurs at lower temperature (105 °C) and its T_α peak is wide. The major difference existing between this sample and the other “slow” tests is visible on the thermal deformation. Indeed, the chains relaxation with the temperature is almost neglectable, it means that the amorphous domain is relatively stable. The temperature of cold crystallization of this sample (measured in DSC) is of 116 °C, which is higher compared to the other “slow” tests and also close to what can be observed for an amorphous sample (124 °C). It can let suppose that this sample does not have pre-organized amorphous domains. The DSC graphs are in Annex 7. Thus, because of the stretching settings and its initial physical state, this sample is different from the other ones. It confirms that the microstructural development of PET samples is highly submitted to the stretching conditions.

On the contrary, once the NDR has been crossed in PEF, it seems that the obtained microstructure is relatively similar. It has been observed in the first part, and it is confirmed with the analysis of the samples stretched at an equivalent strain rates of $5 \cdot 10^{-4} \text{ s}^{-1}$, defined at a reference temperature of 100 °C. The microstructure of the samples in a “pronounced” rubbery state (blue curves) is close to the one of the other conditions, as it is visible in Figure 64.

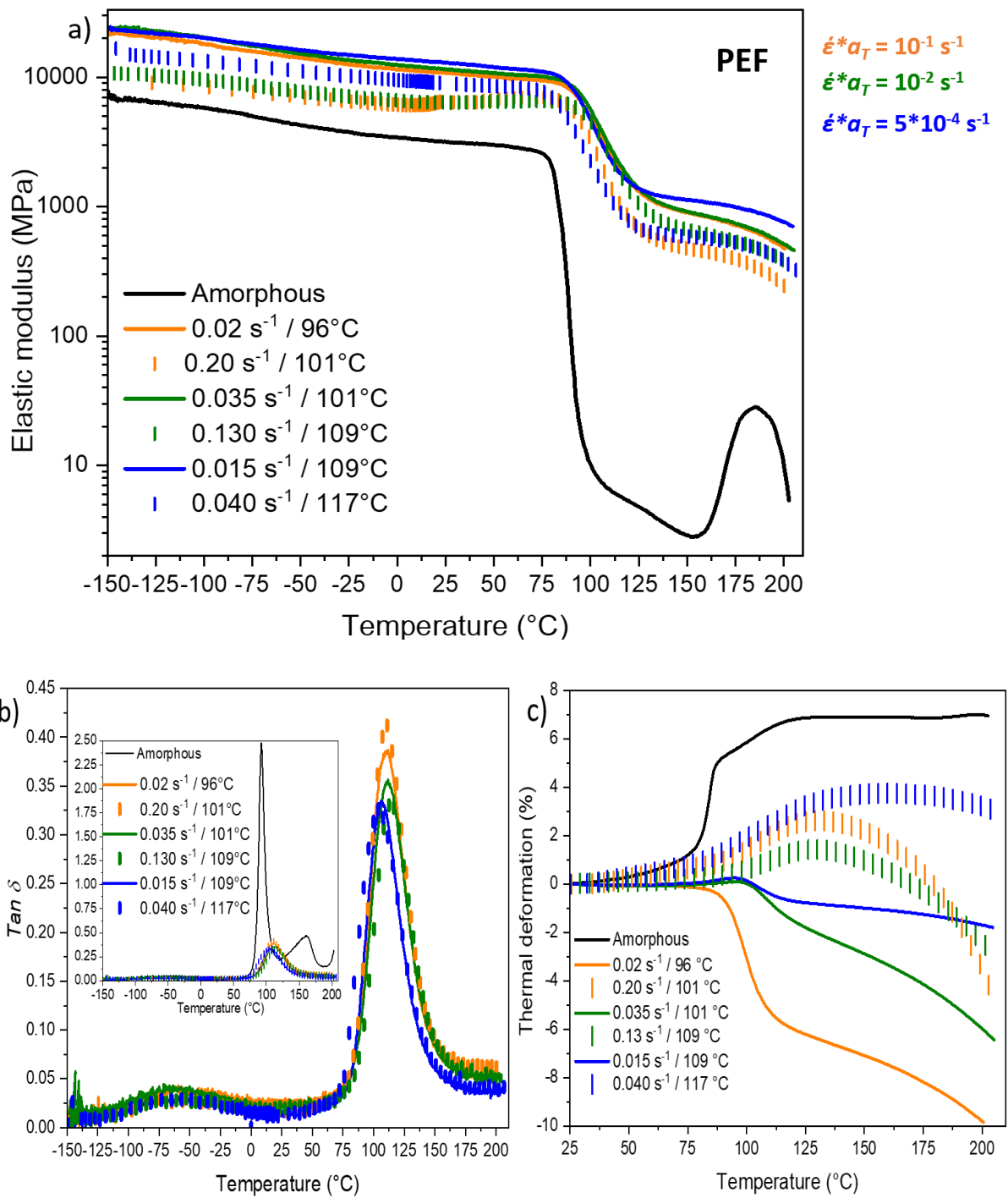


Figure 64. (a) Elastic modulus (E'), (b) $Tan \delta$ and (c) thermal deformation evolutions with temperature, performed by DMTA at an heating rate of 1° C/min, from (a) and (b) -150 °C to 210 °C and (c) from 25 °C to 210 °C, for stretched PEF.

A totally different trend is visible on the previous PEF graphs, in comparison to what has been observed in PET. The behaviour of the amorphous domain of the samples stretched with an

equivalent strain rate of $5 \cdot 10^{-4} \text{ s}^{-1}$, at the reference temperature of $100 \text{ }^\circ\text{C}$, is really close to the one of the others conditions. Moreover, these samples exhibit the highest elastic modulus on the glassy and rubbery plateaux, in comparison to respectively the other “slow” and “rapid” tests. There is the existence of low disparities between all the PEF stretched samples

The high temperatures used for the stretching of the samples stretched at an equivalent strain rate of $5 \cdot 10^{-4} \text{ s}^{-1}$ has led to a relatively stable amorphous domain, as it is visible in Figure 64.c. As in PET, the “slow” test exhibits an almost neglectable relaxation of the stretched chains, while the “rapid” test acts similarly to the others “rapid” tests, with a constant dilatation of the amorphous domain. But on the contrary to the other “rapid” tests, there is no contraction of the chains during the last step of the measurement. Concerning the T_a values of the samples stretched in the highest rubbery state, they are close to the ones of the others tests. The peak is relatively thin, and these samples seem to have the lowest chains. mobility

In parallel, the crystal ratios are lower compared to the other conditions (30% for the “slow” test and 22% for the “rapid” one). Thus, the low mobility of the amorphous domain can probably be explained by the RAF and MAF values. These fractions have not been commented for the others samples stretched up to the same strains because the values are relatively close (around 40% of RAF and around 25% of MAF). But for these samples stretched up to higher strains, the RAF are of 40% for the “slow” test (similar to the other test) but of 60% for the “rapid” test. Then, it explains the low mobility of its amorphous domain. For PET, the RAF and MAF fractions have not been commented because the values have not been obtained for the “slow” tests, because of the existence of several thermic phenomenon (glass transition, cold crystallization, thermal deformation...).

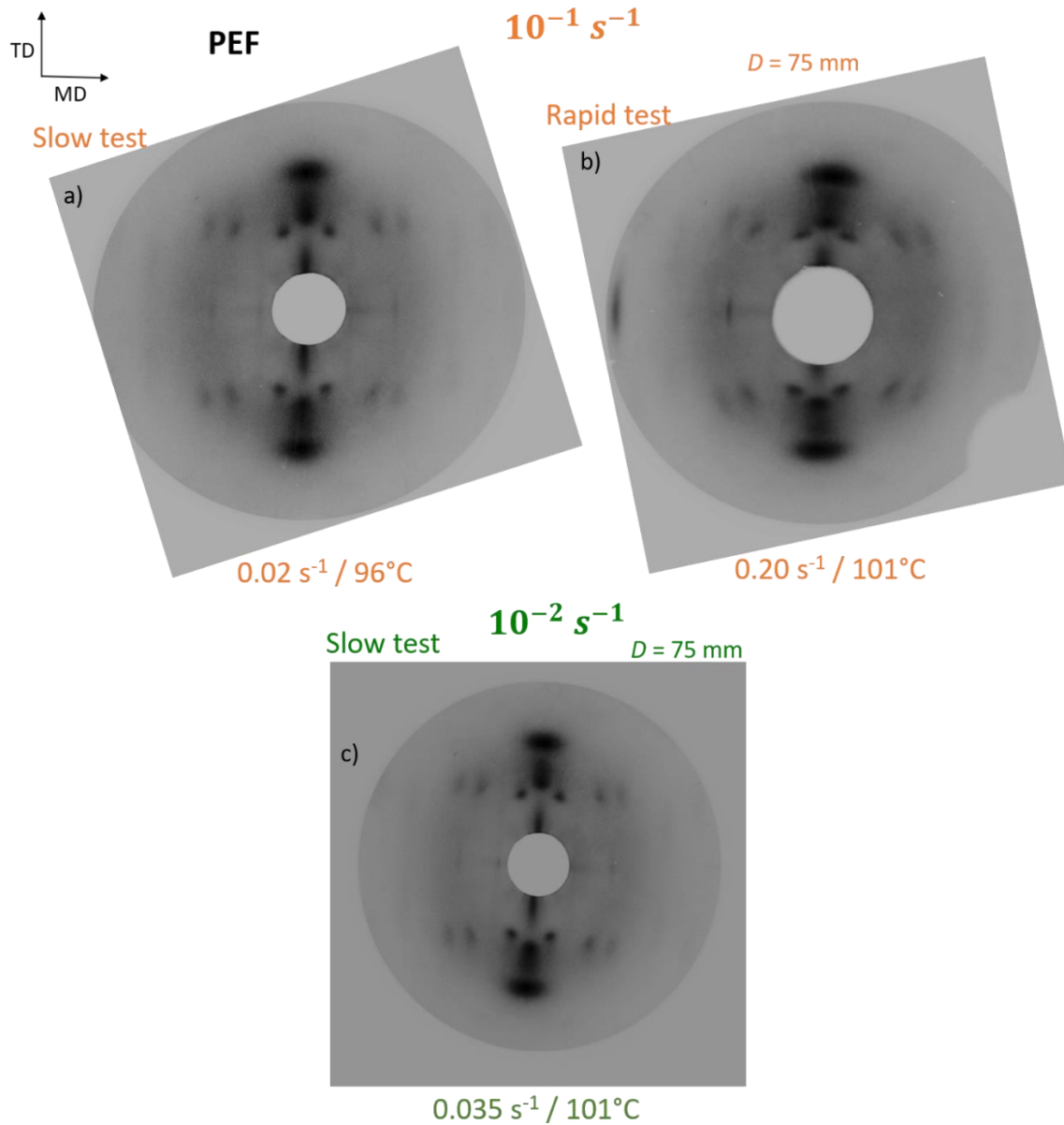
The cold crystallization temperatures appear at around $141 \text{ }^\circ\text{C}$ and at $151 \text{ }^\circ\text{C}$, for respectively the “slow” and the “rapid” tests. The DSC scans are in Annex 8. These temperatures are higher compared to the other tests, and then confirm the well stability of the amorphous domain, and the presence of a low proportion of pre-organized areas. These samples have not benefited of a thermal energy given by the self-heating, but the temperature of the stretching and the time of the experiment have been sufficient to promote a stable microstructure, and similar to the one of the other tests. In Annexes 9 to 11, other complementary measurements (WAXS and FT-IR measurements) do confirm the PEF similarities in terms of microstructural development.

In a nutshell, it seems that PEF is able to form a very close microstructure whatever the stretching conditions are, supposing that the material is in a rubbery-like state and is stretched until impressive strain levels (above the NDR).

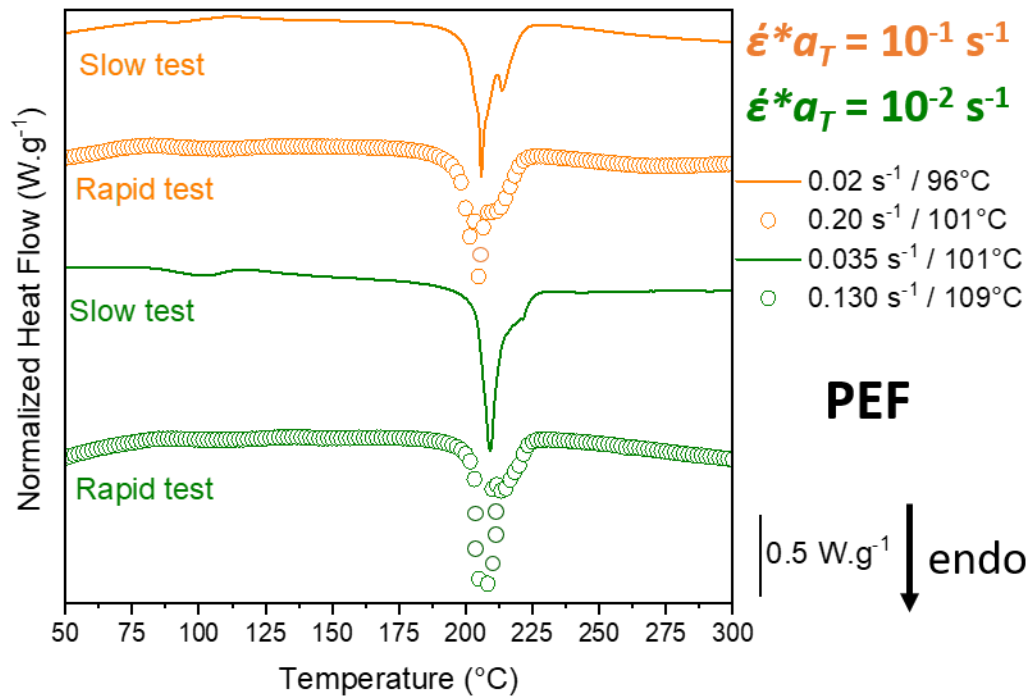
5. Conclusions

This chapter has shown that for PEF and PET, the final strain level is important for the crystal definition and the crystal ratios. However, the thermo-mechanical behaviour during the stretching is the dominant parameter that masters the properties of the amorphous domain. The presence or not of the self-heating during the stretching modifies directly the microstructure and its stability. This chapter has also highlighted that once the NDR of PEF has been reached, the microstructures developed are very similar whatever the stretching conditions may be. In PET, the stretching settings have a higher influence on the microstructural definition, and more variability exists.

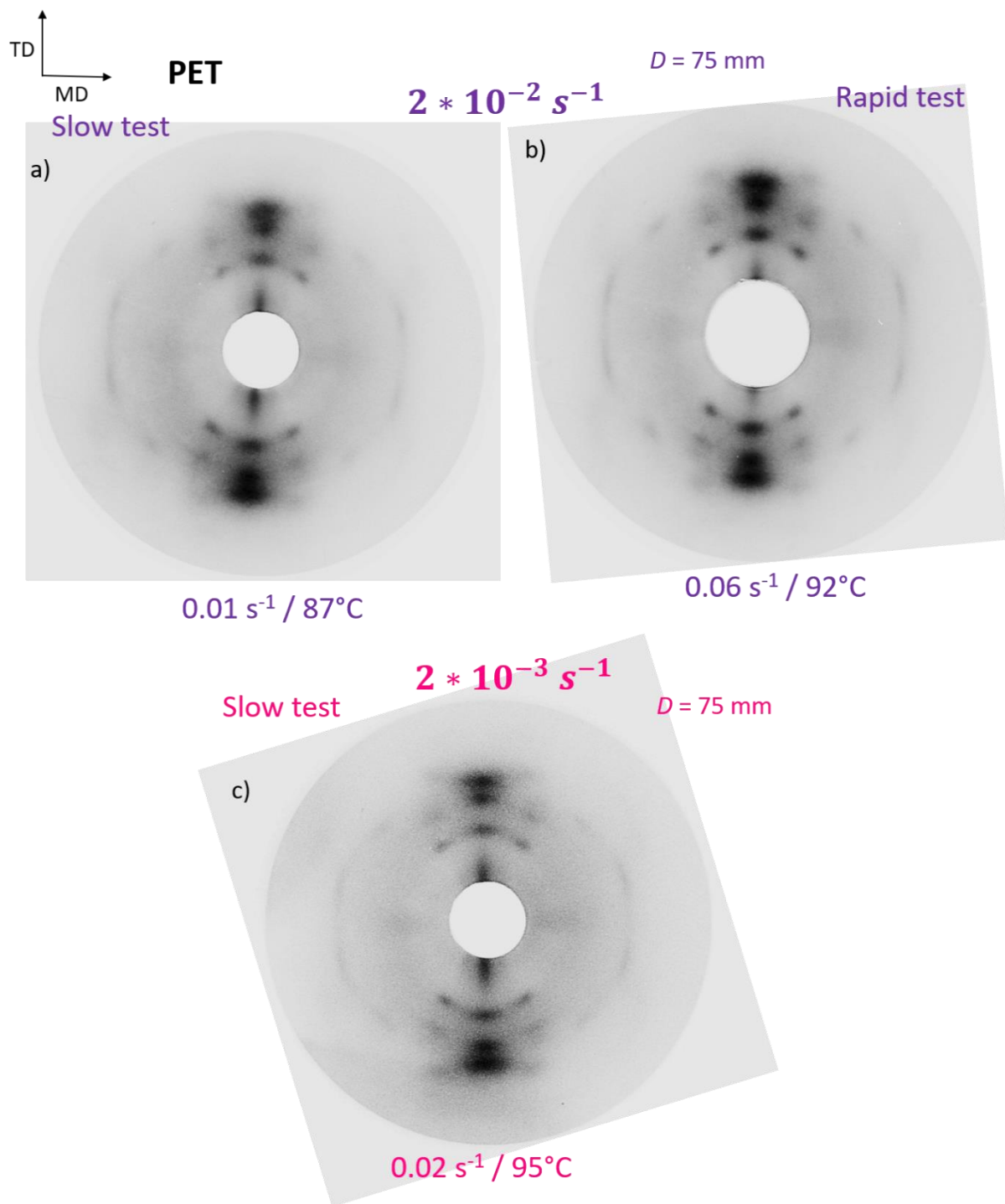
6. Annexes



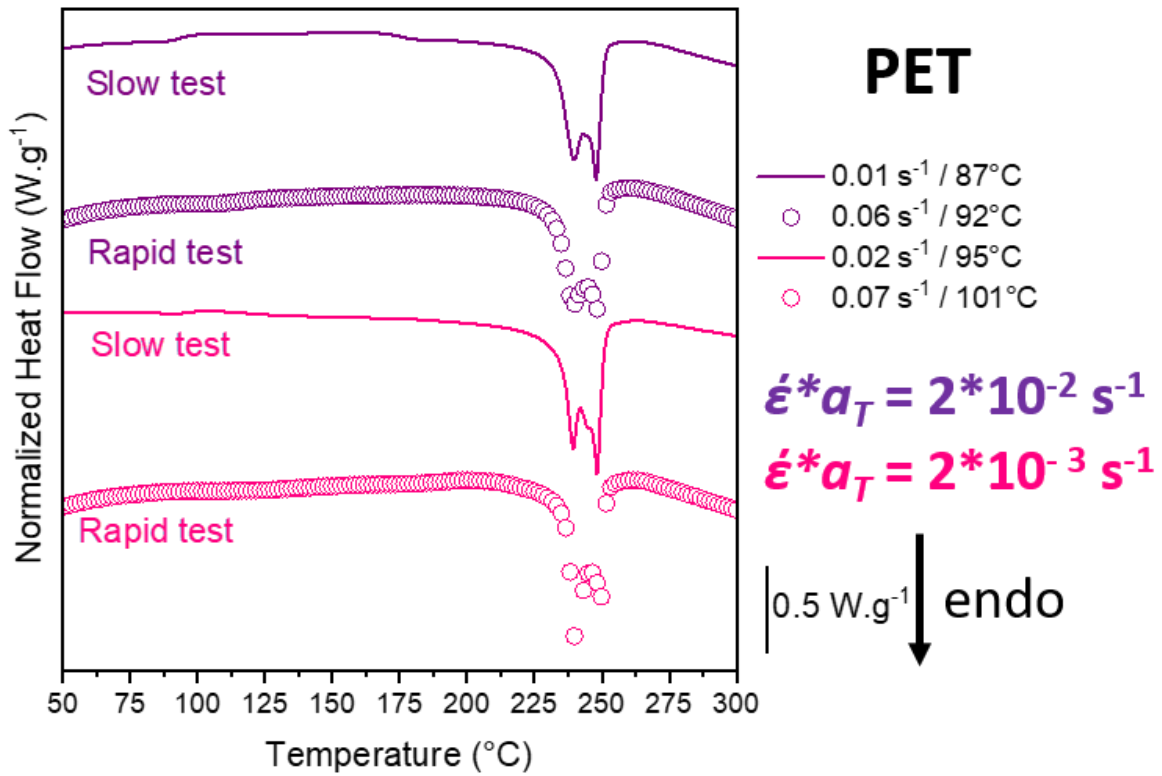
Annex 1. Debye-Scherrer patterns of stretched PEF, (a) “slow” and (b) “rapid” strain rates, at an equivalent strain rate of 10^{-1} s^{-1} (orange); and (c) “slow” test of an equivalent strain rate of 10^{-2} s^{-1} (green), defined at the reference temperature of 100°C .



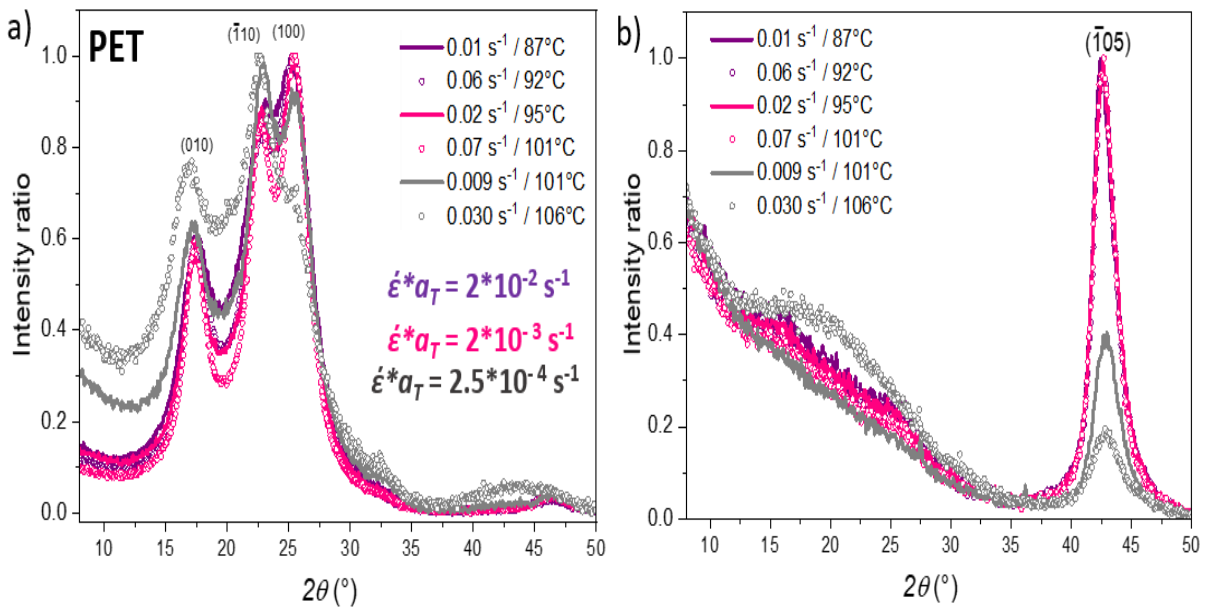
Annex 2. Thermal behaviour of PEF, measured by DSC with an heating rate of 10 °C/min from 50 °C to 300 °C, for the “slow” and “rapid” tests defined from equivalent strain rates of 10⁻¹ s⁻¹ (orange) and of 10⁻² s⁻¹ (green) at the reference temperature of 100 °C. Lines are for “slow” strain rates while dots are for “rapid” strain rates.



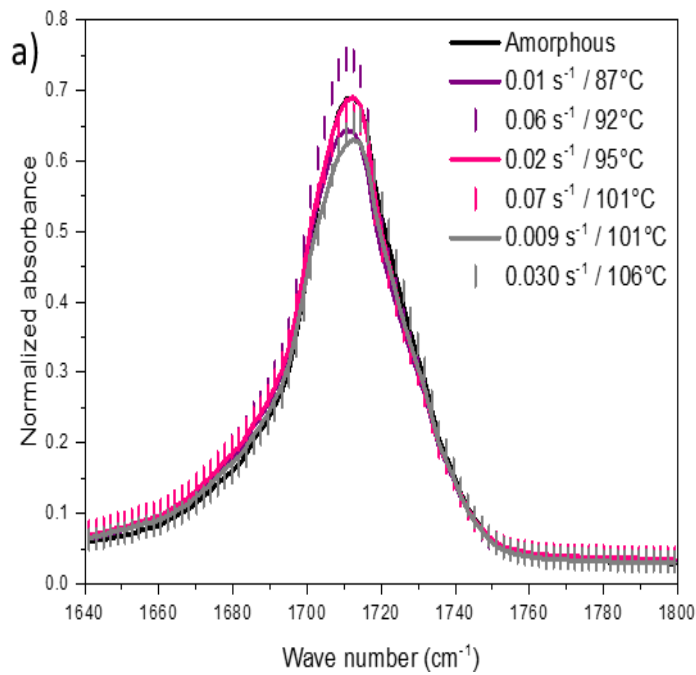
Annex 3. Debye-Scherrer patterns of stretched PET, (a) “slow” and (b) “rapid” strain rates at an equivalent strain rate of $2 * 10^{-2} \text{ s}^{-1}$ (purple); and (c) “slow” test of an equivalent strain rate of $2 * 10^{-3} \text{ s}^{-1}$ (pink) defined at the reference temperature of 90°C .



Annex 4. Thermal behaviour of PET, measured by DSC with an heating rate of $10^{\circ}\text{C}/\text{min}$ from 50°C to 300°C , for the “slow” and “rapid” tests defined from an equivalent strain rate of $2 \cdot 10^{-2} \text{ s}^{-1}$ and of $2 \cdot 10^{-3} \text{ s}^{-1}$ at the reference temperature of 90°C . Lines are for “slow” strain rates while dots are for “rapid” strain rates.



Annex 5. Radial scans from 5° to 50° of PET in (a) TD and (b) MD.

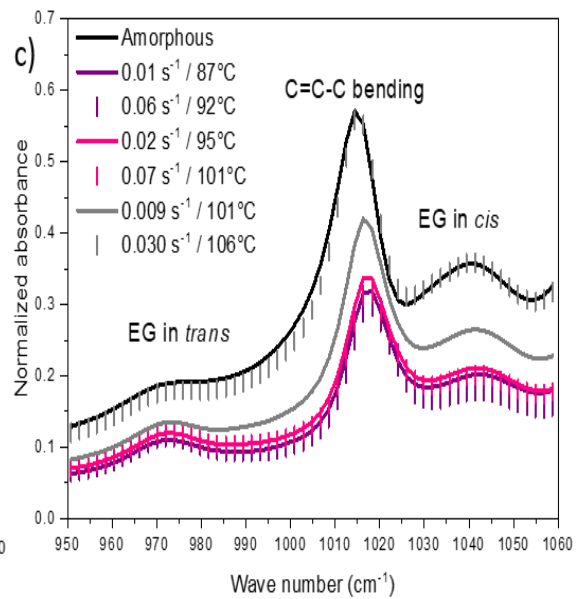
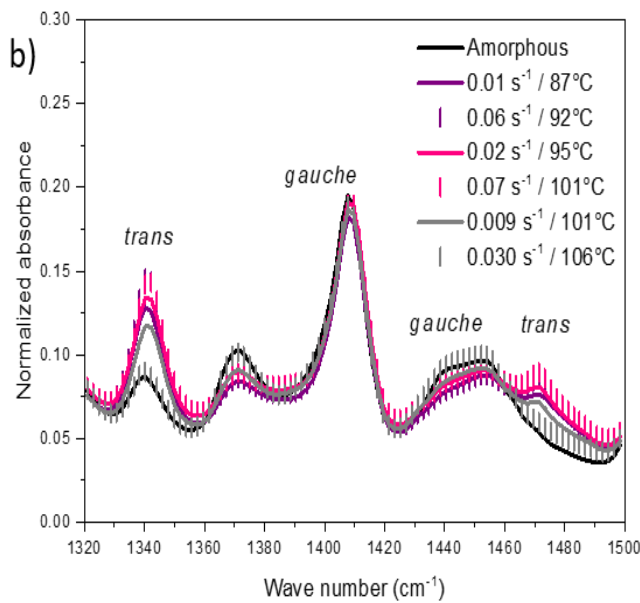


PET

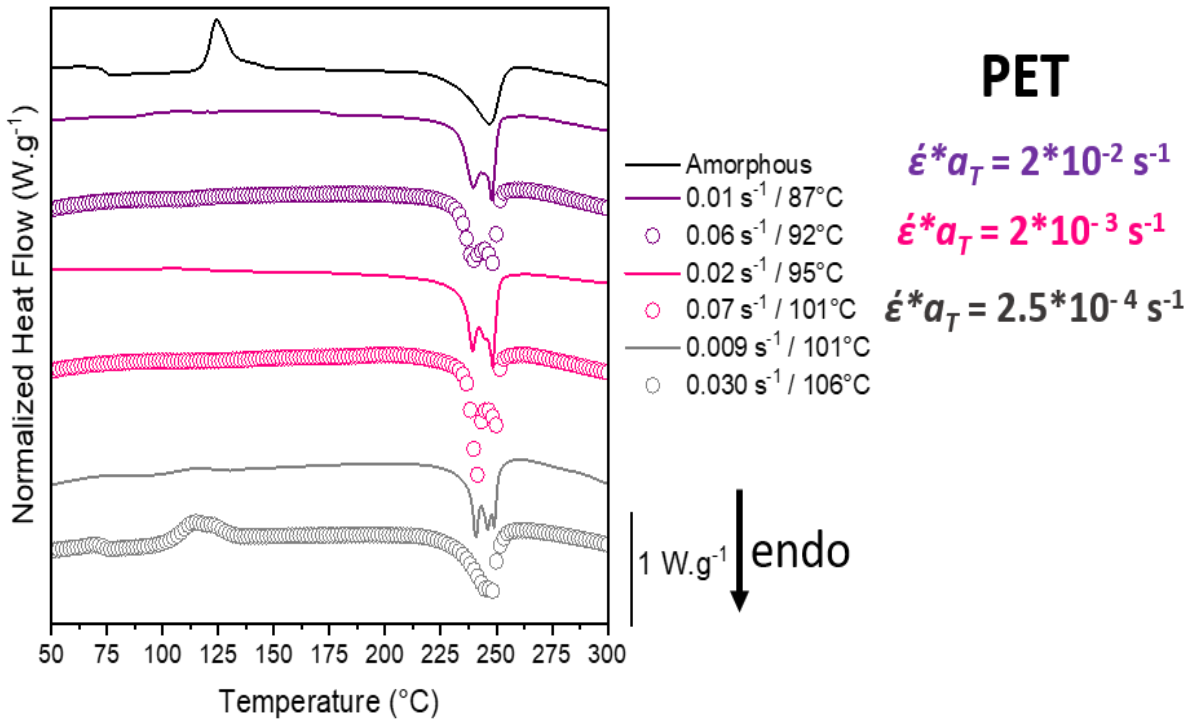
$$\dot{\epsilon}^* a_T = 2 \cdot 10^{-2} \text{ s}^{-1}$$

$$\dot{\epsilon}^* a_T = 2 \cdot 10^{-3} \text{ s}^{-1}$$

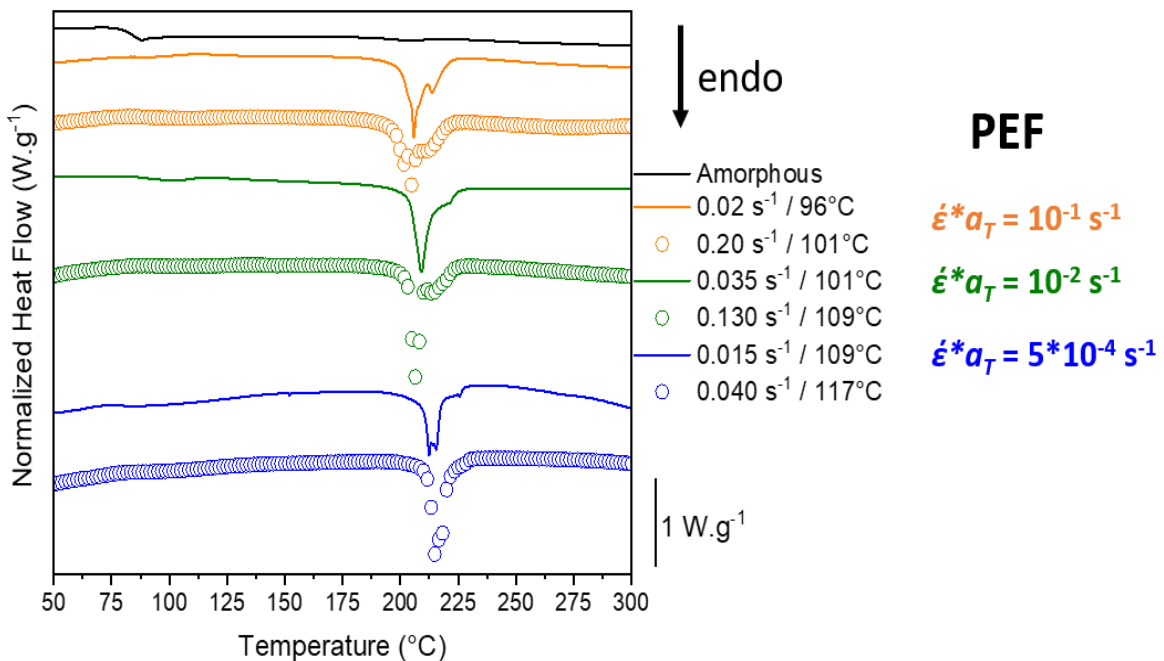
$$\dot{\epsilon}^* a_T = 2.5 \cdot 10^{-4} \text{ s}^{-1}$$



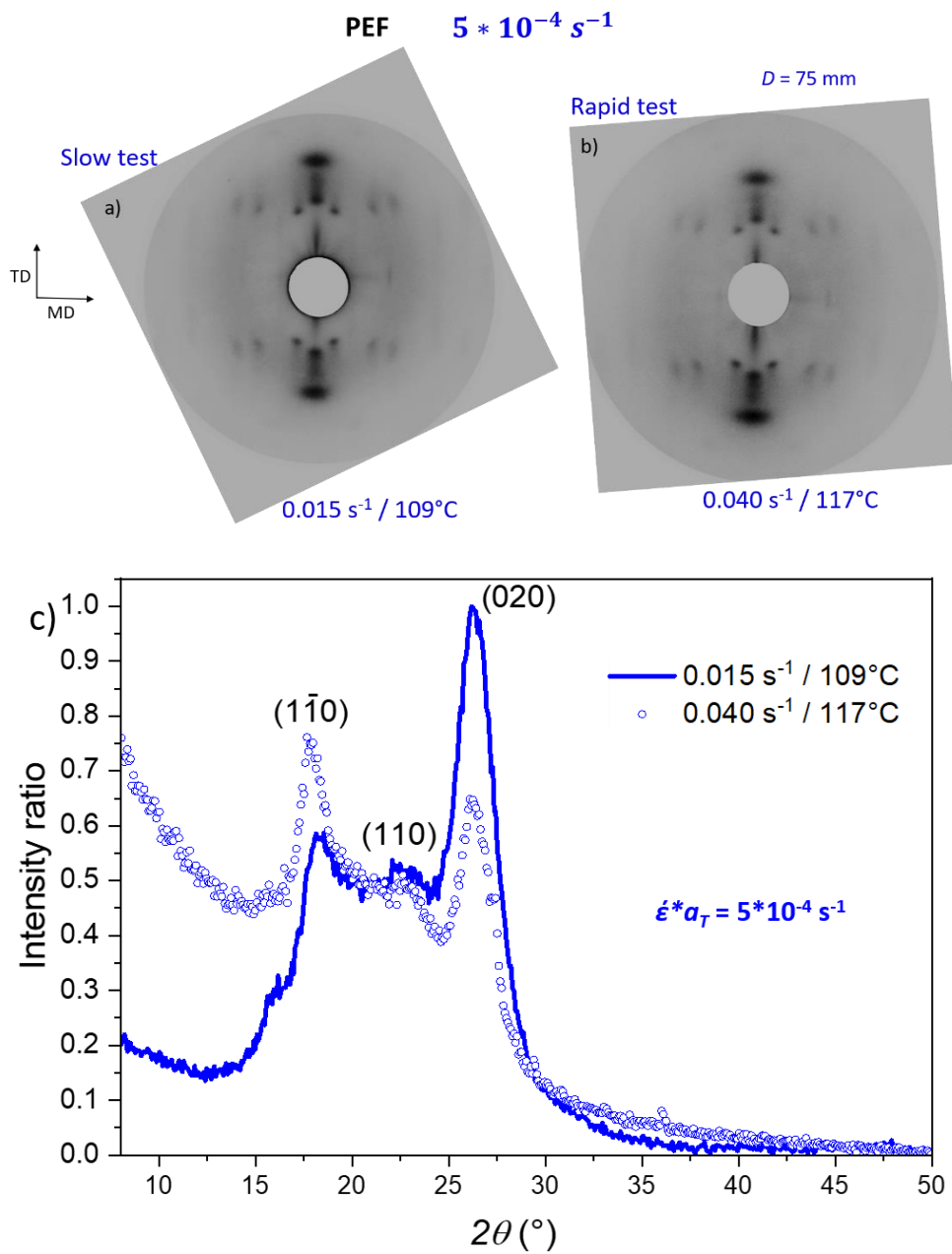
Annex 6. FT-IR spectra from of amorphous and stretched PET from (a) 1640 to 1800 cm^{-1} ; (b) 1320 to 1500 cm^{-1} and (c) 950 to 1060 cm^{-1} .



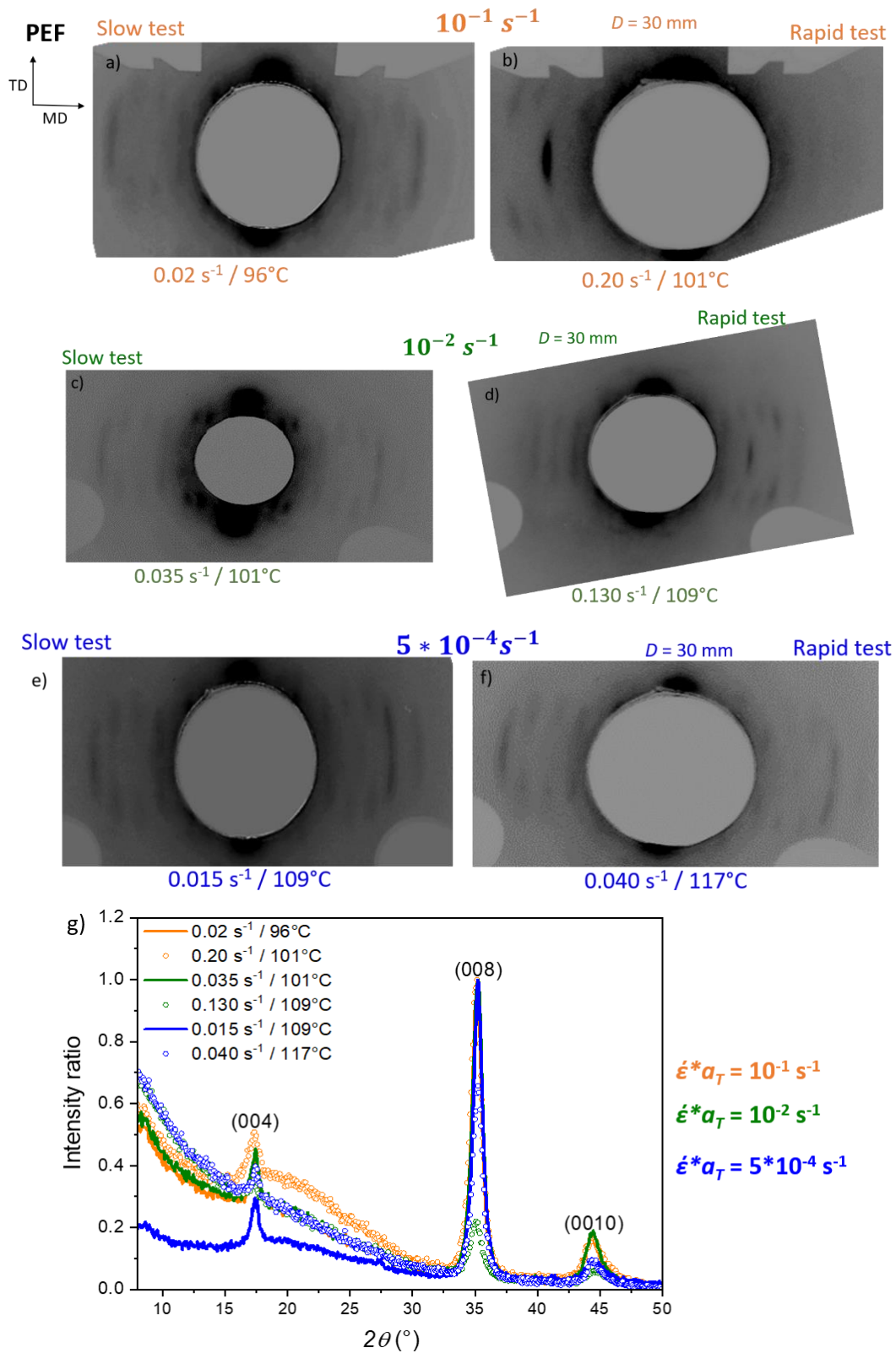
Annex 7. Thermal behaviour of PET, measured by DSC with an heating rate of 10 °C/min from 50 °C to 300 °C, for all the stretching conditions. Lines are for “slow” strain rates while dots are for “rapid” strain rates.



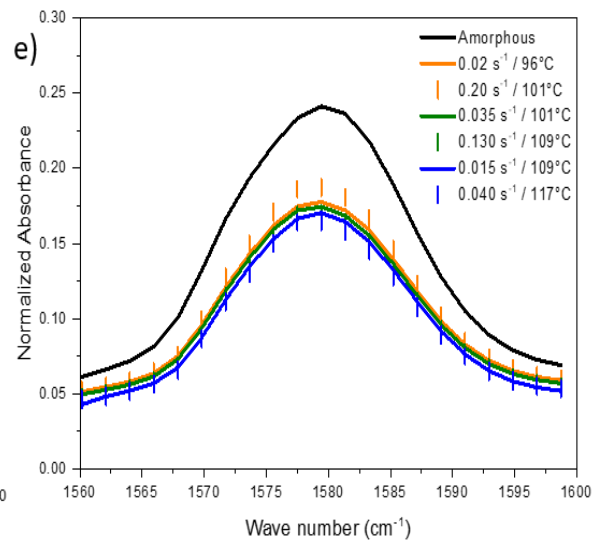
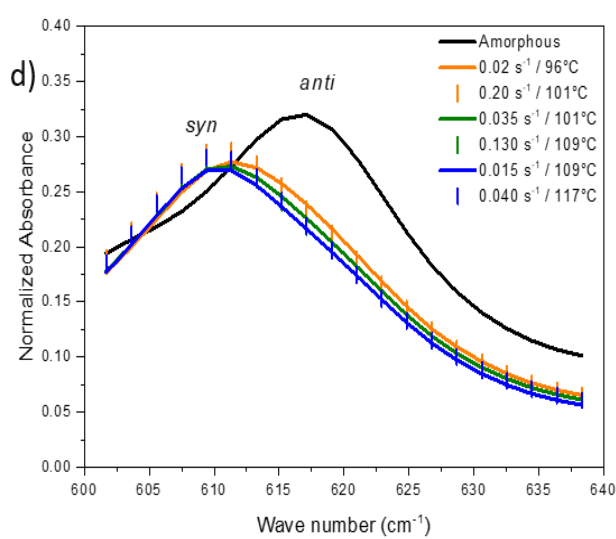
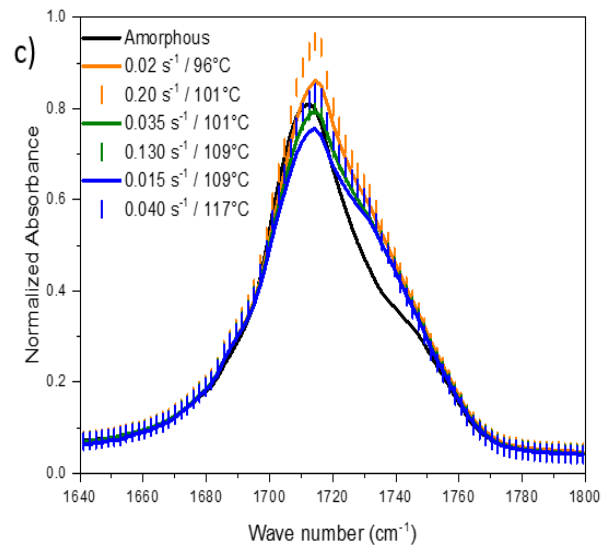
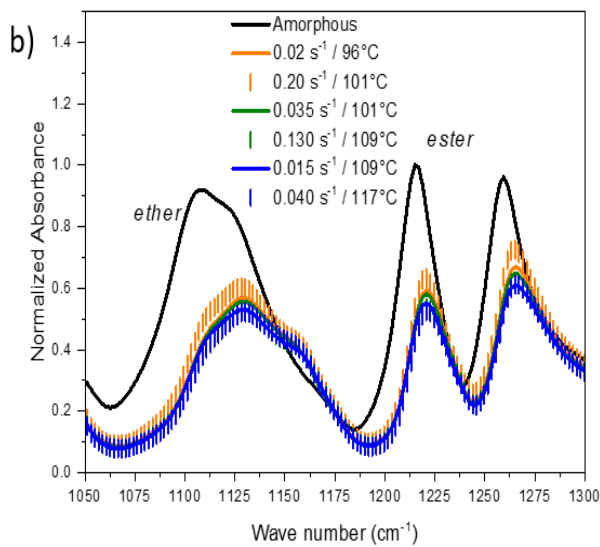
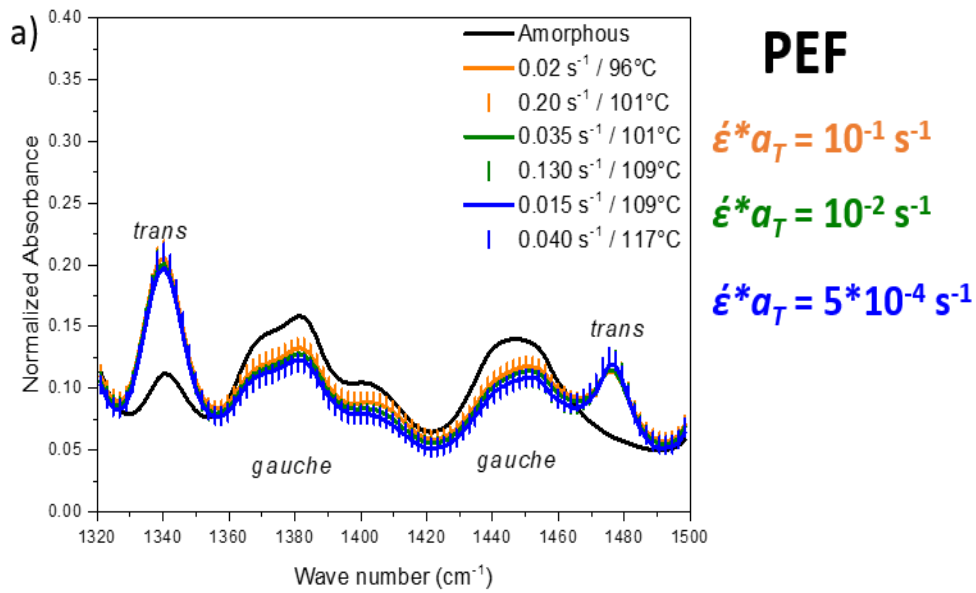
Annex 8. Thermal behaviour of PEF, measured by DSC with an heating rate of 10 °C/min from 50 °C to 300 °C, for all the stretching conditions. Lines are for “slow” strain rates while dots are for “rapid” strain rates.

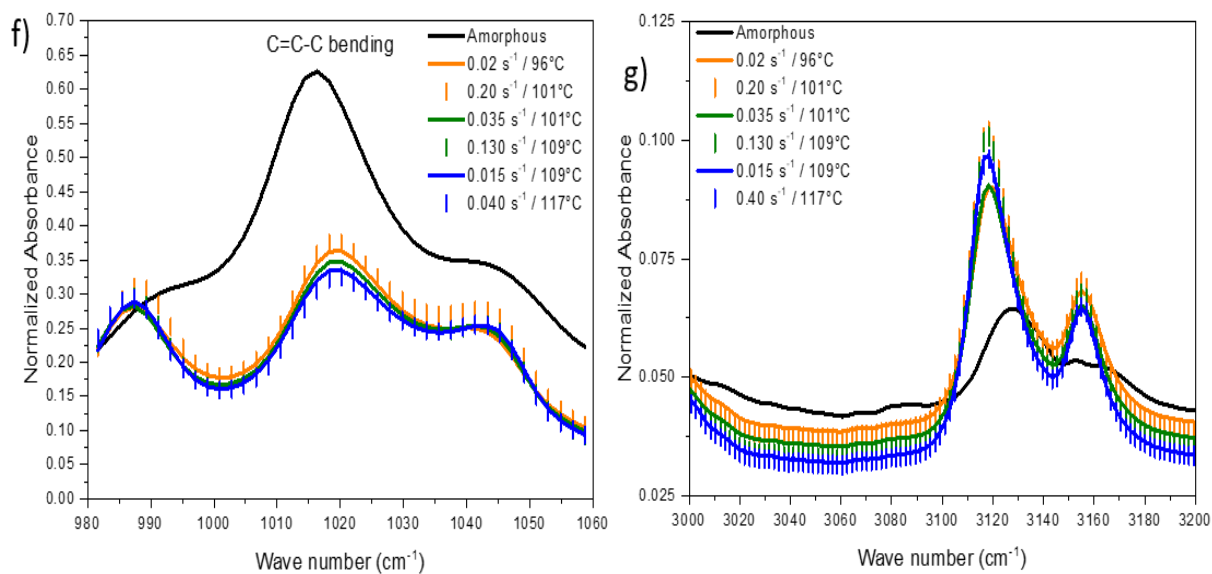


Annex 9. Debye-Scherrer patterns of stretched PEF, (a) “slow” and (b) “rapid” strain rates and (c) radial scans in TD “slow” and “rapid” tests at an equivalent strain rate of $5 * 10^{-4} s^{-1}$ defined at the reference temperature of $100^{\circ}C$.



Annex 10. Debye-Scherrer patterns of stretched PEF, with (a), (c), (e) “slow” and (b), (d), (f) “rapid” strain rates; (g) radial scans in MD from 5° to 50° . All the stretching conditions are represented.





Annex 11. FT-IR spectra of amorphous and stretched PEF from (a) 1320 to 1500 cm⁻¹ ; (b) 1050 to 1300 cm⁻¹; (c) 1640 to 1800 cm⁻¹; (d) 600 to 640 cm⁻¹; (e) 1560 to 1600 cm⁻¹; (f) 980 to 1060 cm⁻¹; (g) 3000 to 3200 cm⁻¹.

Chapter 6

PEF biaxial stretching and associated microstructural development

Table of contents

1. Introduction.....	174
2. Biaxial stretching	175
2.1 Protocol	175
2.1.1 Definition of the tests.....	175
2.1.2 Heating protocol.....	177
2.1.3 Strain rate, temperature and equivalent strain rate evolution	179
2.2 True stress/strain curves	180
3. Microstructural development and properties	182
4. Microstructural evolution upon biaxial stretching.....	192
5. Conclusions.....	198
6. Annexes	199

Chapitre 6

Étirage biaxial du PEF et développement microstructural associé

Ce chapitre a pour but de présenter l'étirage biaxial simultané et équilibré du PEF. Le même protocole que celui utilisé pour l'étirage uniaxial est employé. Cependant, en raison de la géométrie massive des éprouvettes biaxiales, le protocole de chauffage a dû être ajusté. En effet, pour réussir à localiser la déformation au centre de l'éprouvette, il a été choisi de la chauffer spécifiquement par conduction, en son centre, avec une pince thermique. Par la suite, pour maintenir la température la plus constante possible, le chauffage par convection est assuré par l'intermédiaire du four chaud disposé sur l'éprouvette durant l'étirage.

Avec le protocole d'étirage mis en place, il apparaît que des tests relativement isothermes sont réalisables. Ainsi, le PEF est capable de durcir sous étirage tout en modifiant sa microstructure et en formant un cristal. Une des conditions mécaniques testée semble conduire à un taux de cristallinité assez élevé (19 %), ainsi qu'à une microstructure rigide, bien définie et stable thermiquement. Lorsque les conditions mécaniques ne permettent pas d'induire un cristal avec toutes ses périodicités, une étape de recuit, à la température du four pendant 3 minutes, conduit à un perfectionnement de la microstructure. Initialement, la microstructure est une phase amorphe orientée. Cependant, une quantité insuffisante de cristal, inférieure à 10 %, ne permet pas d'induire une microstructure rigide, ni stable thermiquement.

D'un point de vue cristallographique, moins de familles de plans sont observables avec notre protocole de mesure, en comparaison avec ce qui a été trouvé en uniaxe. Ceci est sûrement dû à une trop faible quantité de ces familles diffractantes. Il est également confirmé, comme en uniaxe, que la formation d'un cristal est dépendante d'un nombre suffisant d'éthylènes glycols en conformation *trans*, mais également de cycles furaniques en conformation *syn*. Pour tous les échantillons isothermes, l'étirage conduit à une phase amorphe contrainte. Tout comme en uniaxe, la chaîne aliphatique est la première impactée par l'étirage.

Pour suivre le développement microstructural durant l'étirage biaxial, quelques essais déchargés et interrompus sont conduits. Ils confirment que sans une quantité suffisante de cristal, les échantillons ont principalement un domaine amorphe contraint. Leur stabilité

thermique et leur rigidité sont ainsi limitées. Certains des résultats obtenus peuvent également laisser supposer qu'une microstructure différente peut être induite à la charge et à la décharge. Pour les niveaux de déformation explorés, la décharge peut légèrement faire revenir vers un état amorphe moins contraint, la microstructure induite lors de la charge.

1. Introduction

To enlarge the analysis of PEF, some biaxial stretching tests are performed. Indeed, local loading during ISBM is a combination of uni and biaxial tests (partly sequential, partly simultaneous) [94]. As a first approach, only simultaneous and equilibrated tests are considered (the same loading sequences are applied in the two orthogonal directions).

PEF biaxial stretching has been investigated through only one paper [62], while PET biaxial stretching and the associated microstructural development have already been studied in previous works [91,95,110,115,123–132]. In PET, it is well accepted that this loading induces an equivalent type of microstructure as in uniaxial stretching [133–135]. The stretching induces the elongation of the chains, and an increase in the number of *trans* conformations [136]. The crystal appears when a sufficient level of deformation is reached [91,134]. Cakmak et al. have shown that, with biaxial stretching, the planes of the phenyl rings switch to the plane of the film [126].

This level of understanding is still missing in PEF. Thus, this work aims at going further on the biaxial stretching, and on the associated microstructural development of PEF. Firstly, the stretching protocol and the true stress/strain curves are presented, then the induced microstructure and the thermal and mechanical properties are analysed. Finally, interrupted and unloaded tests have been conducted, in PEF, in order to analyse the microstructural changes that occur during the first stages of the stretching.

2. Biaxial stretching

Because of a lack of time, PET mechanical behaviour in biaxial stretching conditions has not been investigated. However, the results found concerning PEF are going to be compared with some existing results in the literature.

2.1 Protocol

2.1.1 Definition of the tests

To account for potential scattering a master curve is rebuilt with the sheet that has been used for PEF biaxial stretching (Chapter 2, Table 2). The resulting curve is depicted in Figure 65. As previously, the stretching conditions chosen correspond to the middle of the PEF rubbery plateau.

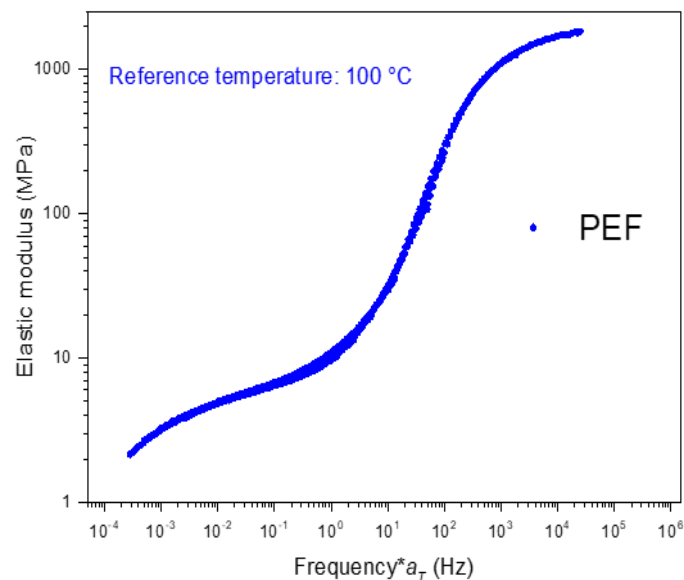


Figure 65. Master curve of PEF at a reference temperature of 100 °C.

The shape and dimensions of the samples are illustrated in Figure 66. The true stress/strain curves are drawn as for the previous tensile tests, and the microstructure is analysed in the same manner.

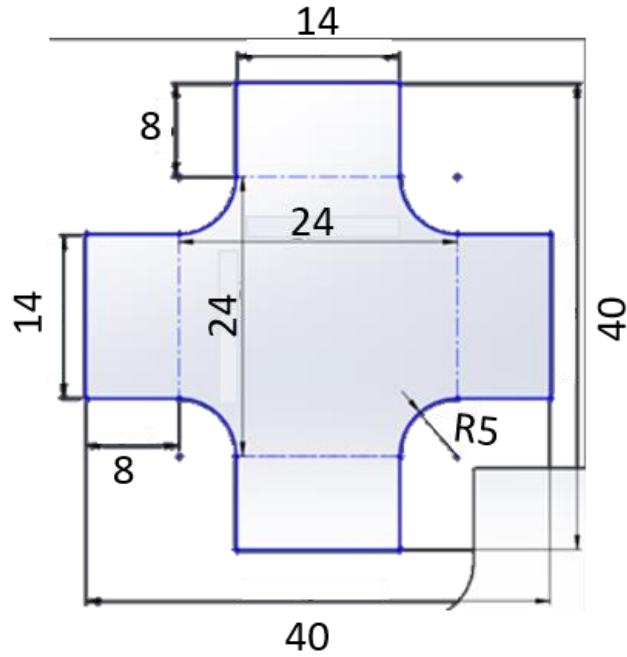


Figure 66. Geometry of the biaxial samples. R5 is the curvature radius.

The displacement of each arms is again controlled with an exponential velocity for PEF (Chapter 2, Equations 9.a to 9.c). As the loading is equilibrated, the stress and Hencky's strain are averaged on the diagonal of the central zone. Equation 12 reminds the calculation of the stress in biaxial stretching.

$$\sigma(t) = \frac{\sqrt{2}F(t)}{e_0 * L_{diagonal} * e^{-\varepsilon_{diagonal}}} \quad (12)$$

with $L_{diagonal}$ the length of the diagonal, and $\varepsilon_{diagonal}$ the Hencky's strain on one diagonal.

Figure 67.a compares the typical evolution of the longitudinal true strain upon time as extracted from the two diagonals. On the other side, in Figure 67.b is drawn the evolution of the longitudinal, the transversal as well as the main strains (ε_1 and ε_2 , are respectively the major and minor strains).

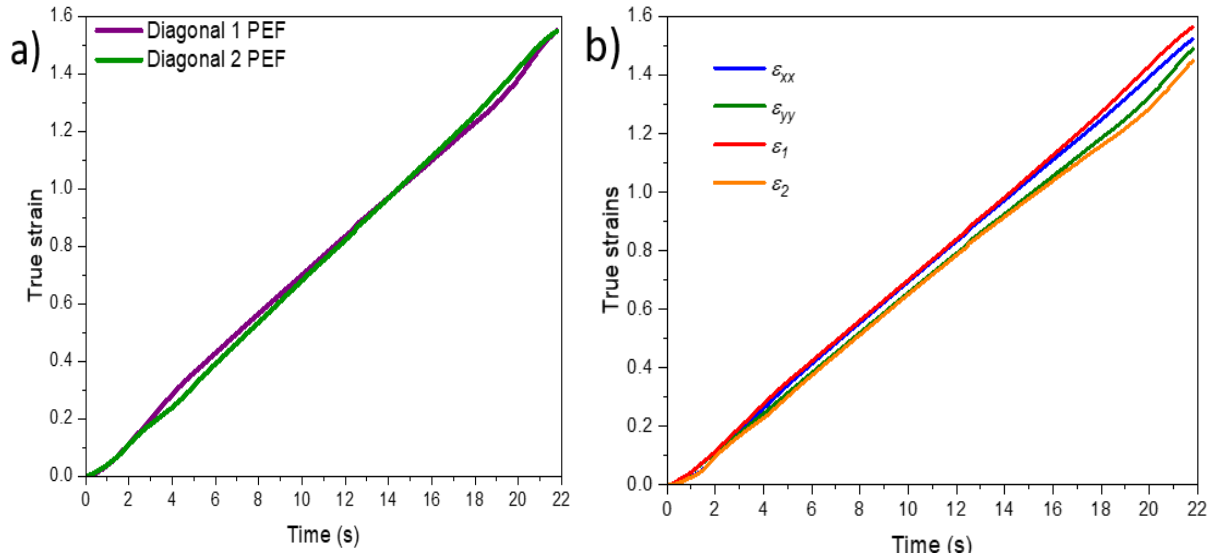


Figure 67. (a) Evolution of the true longitudinal strain (Hencky's strain) with the time on the two diagonals, (b) evolution of the true longitudinal, transversal, major and minor strains for one stretching test of PEF.

The correctness of the test is visible with the equivalence of the measurement on both the two diagonals. The quality of the control of the strain rate is visible by the linearity of the evolution for PEF. The closeness of the strain curves in Figure 67.b confirms the quality of the biaxial loading in the central zone.

2.1.2 Heating protocol

An uniform heating of the “cross” sample in Figure 66, and the associated clamping device do not allow an uniform deformation of the central zone, as the deformation would be located close to the clamping zone of smaller sections. To localize the deformation, it is then necessary to weaken the central zone. Tooling, as usual for massive samples, is not possible with thin films. Then, a thermal weakening, as in a previous study, has been chosen [91].

The challenge is to ensure that the central zone (square in Figure 66) is uniform in temperature, and hotter than the material in the clamps that should remain glassy. The idea of cooling down the clamps to ensure the uniformity and to control the temperature in the process zone was technically complex, and would necessitate to design a protocol [77,137]. Following the work of Quandalle [91], the heating is made thanks to a pinch at a temperature, T_{pinch} , during 3 minutes. Then, the pinch is taken off and immediately the hot oven, at a temperature T_{oven} (T_{oven}

$< T_{pinch}$), is placed on the sample. Stretching is performed without an additional delay. This protocol aims at reducing the thermal losses, as the film would cool down in the ambient air. It aims at ensuring a temperature variation as low as possible. The actual temperature of the film is measured continuously, and enables to calculate the equivalent strain rate at reference temperature, which is the controlling parameter of this work. As the pinch is directly in contact with the painted sample, the temperature of the pinch has to be sufficiently low to avoid the paint removal. The stretching is stopped before the rupture of the sample, in order to perform microstructural analysis on the biaxial stretched samples.

2.1.3 Strain rate, temperature and equivalent strain rate evolution

The control of the equivalent strain rate during the stretching has to be validated. The evolution of the temperature, the strain rate and the equivalent strain rate is represented in respectively Figures 68.a to 68.c

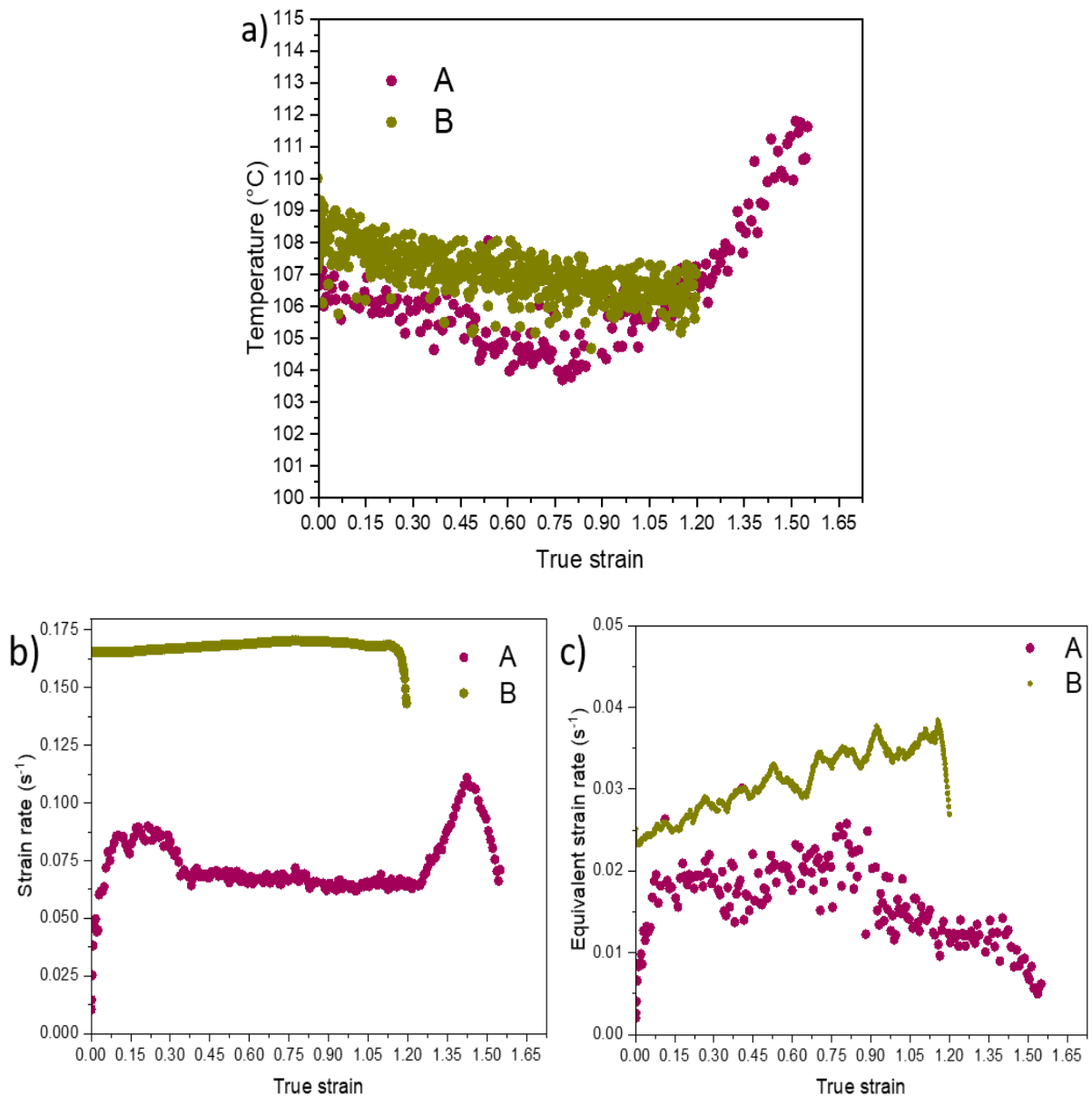


Figure 68. Evolution of (a) the strain rate, (b) the temperature and (c) the equivalent strain rate for biaxial stretching tests of PEF.

These results prove that it is possible to keep the temperature and the strain rate constant during the tests with the stretching protocol applied. Firstly, the strain rate and the temperature are relatively constant. Then, an increase of the temperature is observed for A test. As for the uniaxial tests, this increase can be due to crystallization or to self-heating. This increase occurs during the strain hardening, as confirmed further. On the contrary, the B test does not reveal such phenomenon. The previous observations explain the evolution of the equivalent strain rates at the reference temperature of 100 °C. The equivalent strain rates of the A and B tests appear relatively constant (they remain in the same decade), and are of respectively 0.02 s^{-1} and 0.025 s^{-1} , at the reference temperature of 100 °C. These equivalent strain rates are relevant, and correspond to the expected localization on the master curve.

The microstructural development is less discernible in biaxial stretching, than in uniaxial stretching. Thus, two post-stretching treatments have been applied on the stretched samples: quenched with cold-air or annealed during 3 minutes at the stretching temperature. The aim of the annealing is to reveal the existence of weak organizations, that were not able to appear during the stretching.

2.2 True stress/strain curves

In the seminal work on PEF biaxial stretching [62], the settings did not allow the development of a strain hardening nor crystallisation. Figure 69.a represents the true stress/strain curves of both A and B tests. In Figure 69.b, the deformation fields, at several strains, are depicted for the A test.

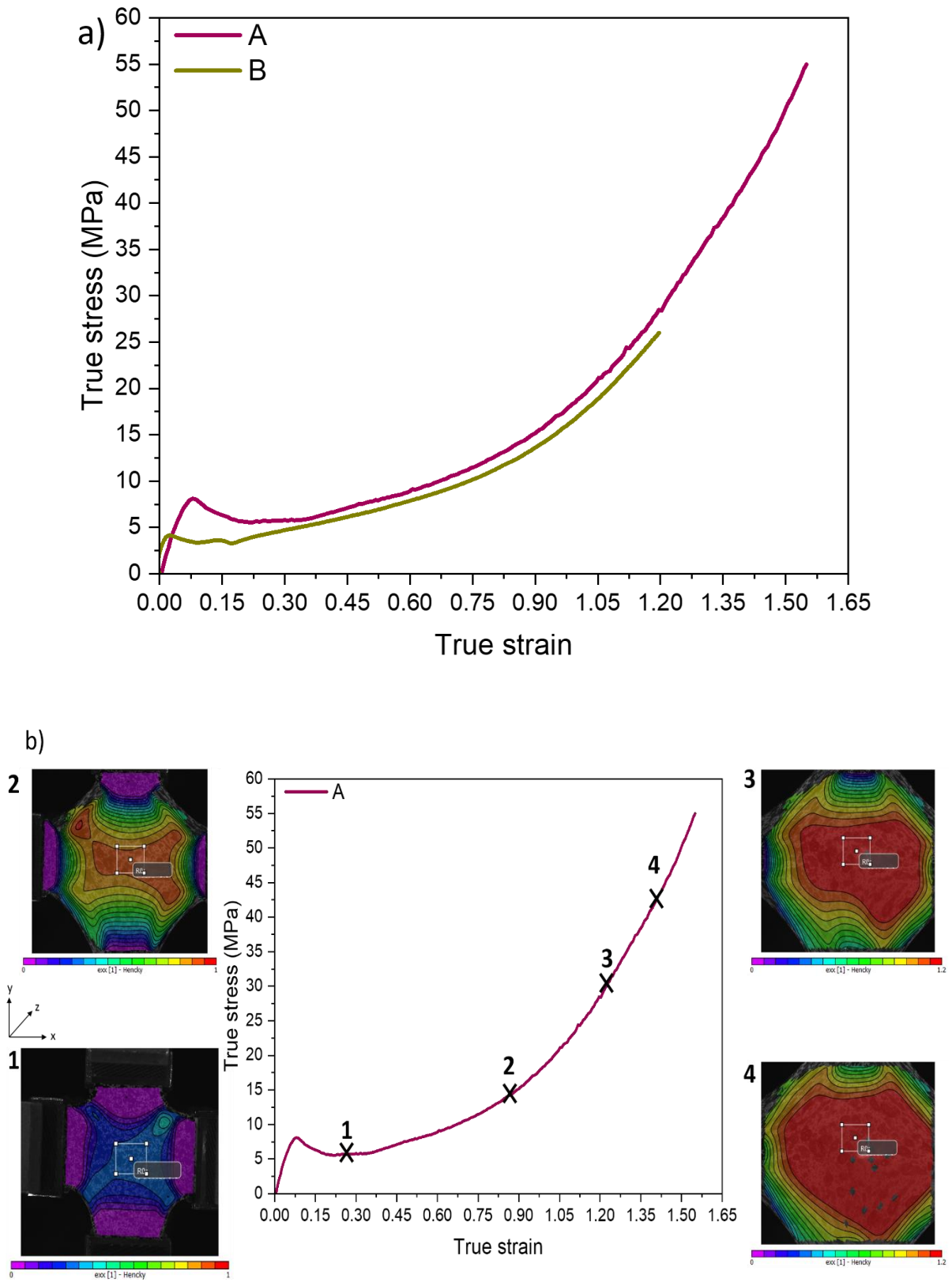


Figure 69. (a) True stress strain curves of PEF during biaxial stretching, (b) strain fields at several longitudinal true strains of the A test.

Both tests reveal that PEF can be biaxially stretched, and is able to strain harden. Moreover the deformation is well localized in the central zone (Figure 69.b). For the two stretching settings, the curves are relatively close. The strain hardening occurrence is less sharp than what has been observed in uniaxial stretching. Table 21 sums up the biaxial draw ratio ($\lambda_{biaxial}$), which is calculated according to Equation 13.

$$\lambda_{biaxial} = \lambda_1 * \lambda_2 \quad (13)$$

with λ_1 and λ_2 the draw ratio on each direction.

Material	Test	λ_1	λ_2	$\lambda_{biaxial}$
PEF	A	4.71	4.70	22.2
	B	3.31	3.42	11.3

Table 21. Biaxial draw ratio of biaxial tests.

The biaxial draw ratio reached for the B test is in the range of the classical biaxial draw ratio reported in PET (between 8 and 12). The biaxial draw ratio of the A test is relatively high, confirming the high stretch ability of PEF, even in biaxial stretching.

Next part deals with the microstructural development of the tests. The measurements are performed on a rectangular sample cut in the middle of the process zone.

3. Microstructural development and properties

The A and B tests exhibit a close mechanical behaviour. The only difference between them is the faster strain rate applied in the B test. Then, according to the previous observations of the uniaxial stretching campaign one can ask the influence of it concerning the SIC occurrence.

The quantity of crystal for the quenched and annealed samples has been estimated with a DSC measurement (Figure 70) performed at 10 °C/min from 25 °C to 275 °C. The cold crystallization temperatures, χ_c , χ_{RAF} and χ_{MAF} are reported in Table 22.

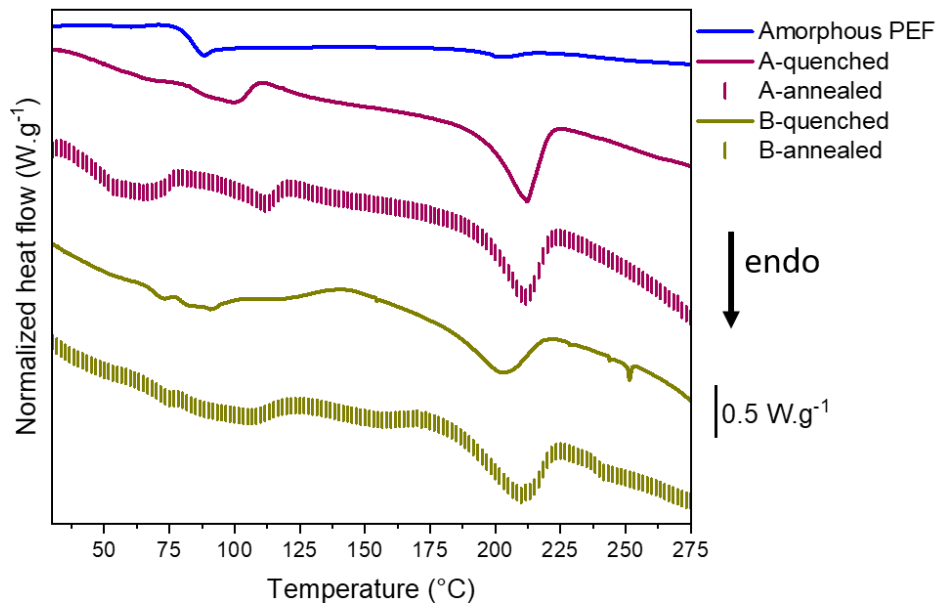


Figure 70. Thermal behaviour of annealed (dots) and quenched (lines) samples, measured by DSC scans performed at 10 °C/min from 30 °C to 275 °C. Endothermic phenomena are top-down.

Samples	χ_c (%)	χ_{RAF} (%)	χ_{MAF} (%)	T_c (°C)
Amorphous PEF	0	0	100	
A-quenched	19	33	48	111
A-annealed	19	26	55	120
B-quenched	6	41	53	140
B-annealed	11	39	50	126

Table 22. χ_c , χ_{RAF} , χ_{MAF} and cold crystallization temperatures of biaxially stretched samples.

The A test samples (quenched and annealed) have developed relatively high crystal ratios (19%), while for the B tests (quenched and annealed) the crystal ratio is much lower, and increases with the annealing step. For the samples of the A test, the χ_{MAF} and χ_{RAF} are relatively similar, but the quantity of RAF decreases with the annealing step. The B samples exhibit a slightly higher χ_{RAF} , in comparison with the A tests. It is probably due to the higher strain rate used in the B tests, in comparison to the A tests. Moreover, the stretching of B test has been performed up to a lower strain level. It has an impact on the microstructural development.

On the contrary to the amorphous sample (because of a too fast heating rate), the cold crystallization occurs in all the stretched samples and at low temperature, as it is visible in Figure 70. It confirms the influence of the stretching on the microstructure. The temperature of

cold crystallization is lower for A-quenched, in comparison with A-annealed. It fits with the values found for the χ_{RAF} . It is likely that the annealing has allowed a slight release of the pre-organized areas. On the contrary to the A tests, the B-annealed sample has a lower cold crystallization temperature, in relation with the B-quenched. The annealing of this sample has allowed to improve the microstructure induced during the stretching. Then, the crystal ratio is higher. During the DSC measurement the B-annealed sample continues its crystallization, while B-quenched has not been able to develop pre-organized zones, its cold crystallization appears at higher temperature.

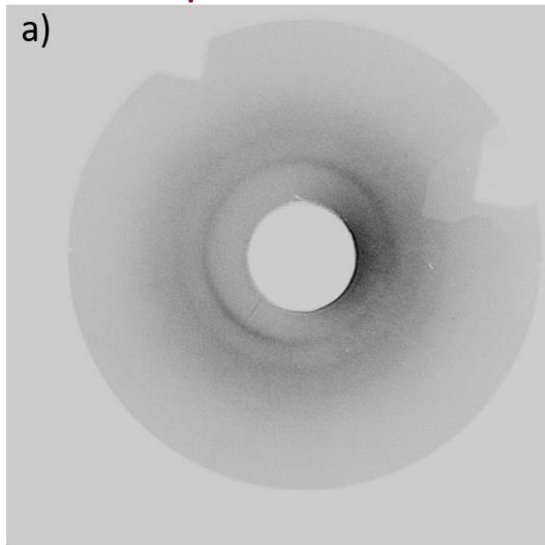
These results, concerning the cold crystallization temperature decrease, agree with what has previously been observed by van Berkel et al [62]. Nevertheless, the crystal ratios found in PEF (A tests) in this work are higher compared to this previous work.

The existing differences between the samples in terms of crystallinity are confirmed with the crystallographic analysis. The Debye-Scherrer patterns of the quenched and annealed samples are represented in Figure 71 ($D = 75$ mm), while the radial scans in transmission and reflexion are depicted in Figure 72.

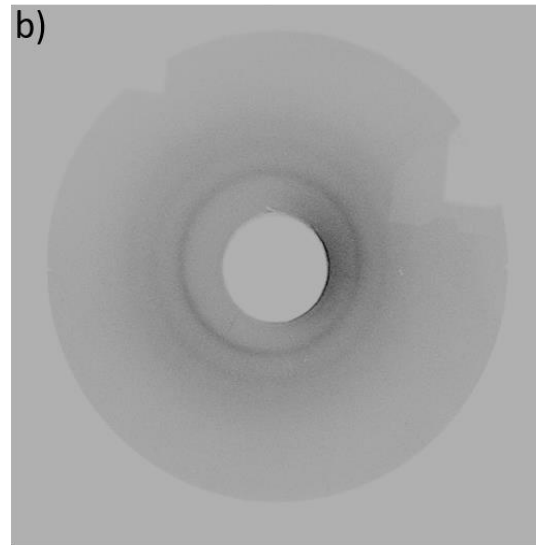
It has been stated in the previous chapters that the samples were amorphous before the stretching. Thus, for ease of reading, the associated Debye-Scherrer pattern is not reported in this chapter.

$D = 75 \text{ mm}$

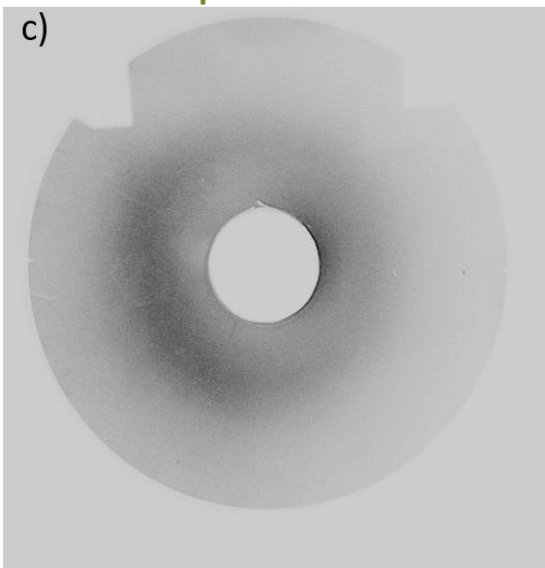
A-quenched



A-annealed



B-quenched



B-annealed

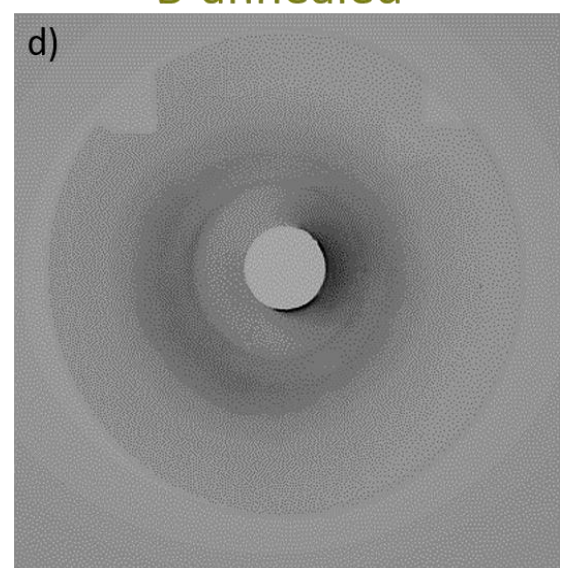


Figure 71. Debye-Scherrer patterns of the A and B tests for the (a) and (c) quenched samples; (b) and (d) the annealed samples.

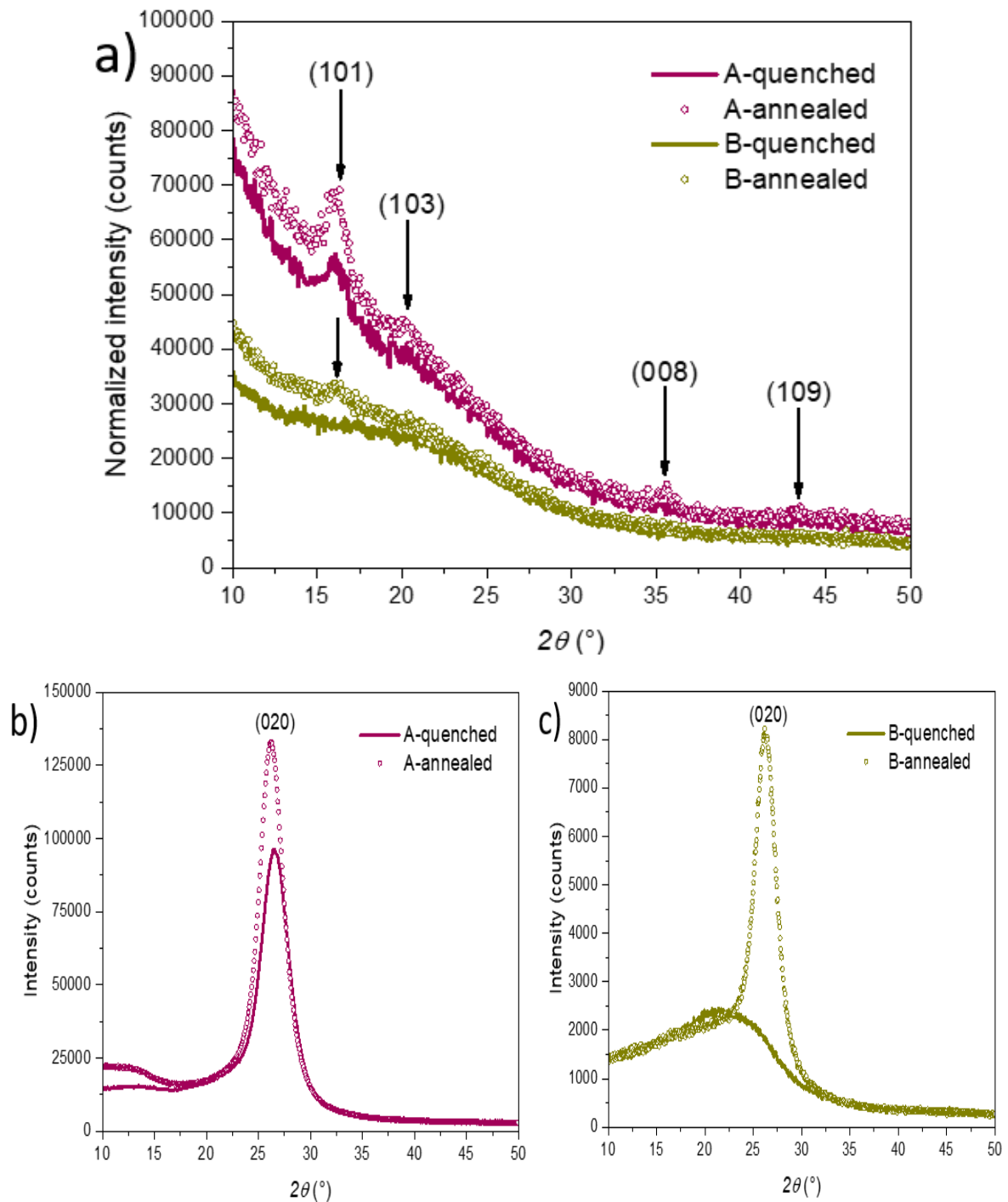


Figure 72. Radial scans in (a) transmission; (b) and (c) reflexion mode of the quenched (lines) and the annealed (dots) biaxially stretched samples of the A and B tests.

The diffraction of the families of planes is visible on the patterns of the A test, with or without the annealing step. They appear as continuous circles, on the contrary to the spots observed in the patterns of the uniaxial stretching tests. It is in agreement with some previous works [91,121,124,125,127,138]. The annealing seems to slightly improve the definition of the

families of planes. On the patterns and scans, the diffraction of less crystalline families is visible (in comparison with the uniaxial stretching [65]). It is probably due to a lower quantity of them. The indexation of the families of planes is reported (Figure 72), and made according to the existing indexation in PEF [65]. Some slight disparities, relative to the 2θ values, can exist but it has already been pointed out between the SIC (during uniaxial stretching) and the cold crystallization. However, these disparities remain acceptable.

Different families of planes are observed in transmission and in reflexion. It has already been pointed out for PET free-blown bottles, in a previous work [95]. In transmission, the planes observed are those perpendicular to the surface of the sample, while in reflexion the planes parallel to the surface of the samples are analysed. According to the work of Mao et al [58], the (020) family of planes could represent the alignment of the furan cycle face to face in the stretching plane of the sample. It can explain why this intense family can be observed only for the scans performed in the reflexion mode.

The scans of the B-annealed test, in Figure 72, reveal the presence of only some families of planes. It is possible that the others families of planes are not observable with these measurements because of a too low intensity and quantity of them. Their observation is not possible for the quenched sample. Thus, the quenched sample appears relatively amorphous, maybe with only some oriented areas or some nuclei, but there is not the existence of a well-defined crystal.

To get more data on the samples of the B test, FT-IR measurements have been conducted. The relevant spectra, focused on certain wavenumber domains, are shown in Figure 73, while the other regions are in Annex 1.

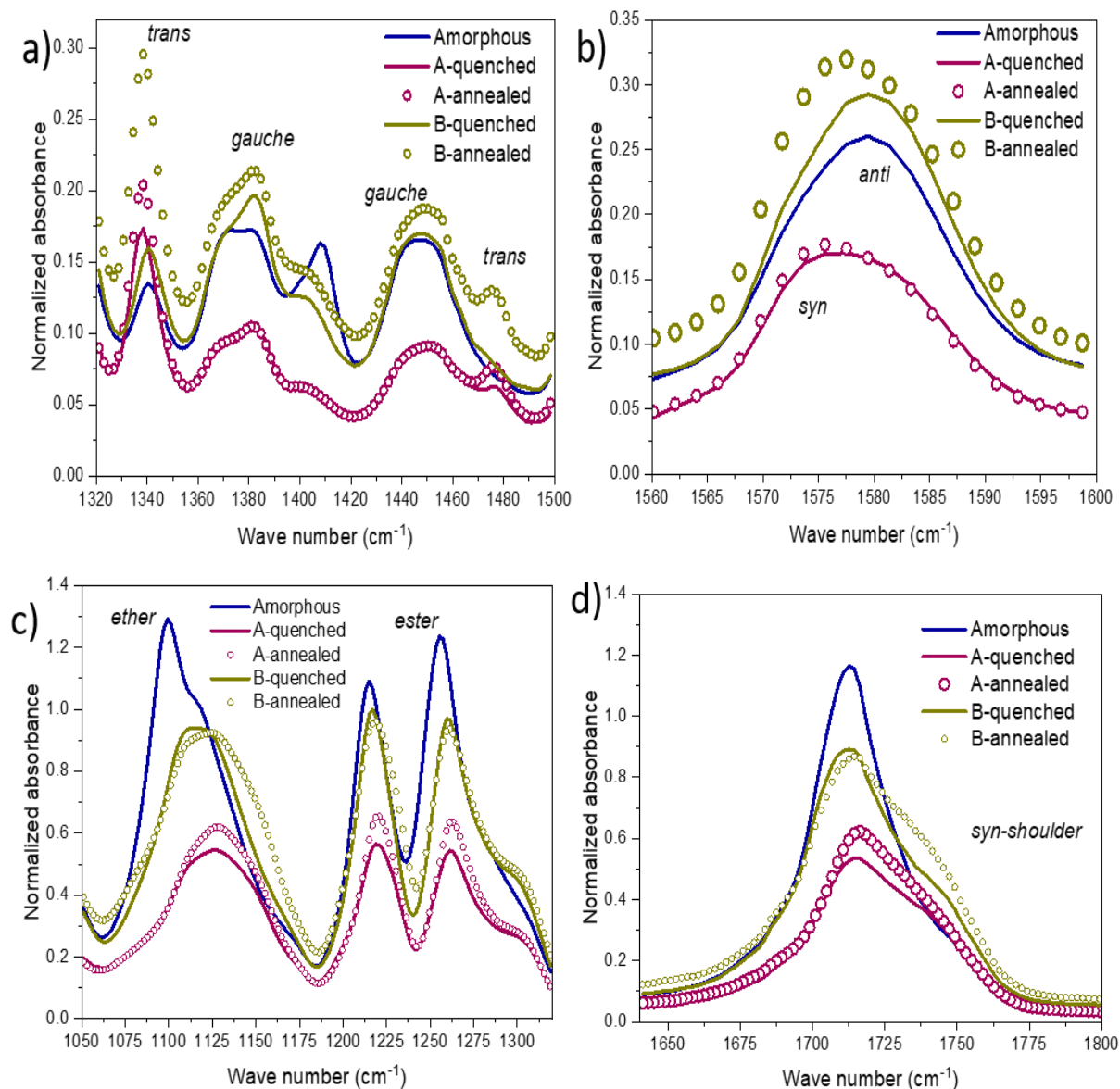


Figure 73. FT-IR spectra of amorphous, quenched (lines) and annealed (dots) PEF from (a) 1320 cm^{-1} to 1500 cm^{-1} ; (b) 1560 cm^{-1} to 1600 cm^{-1} (c) 1050 cm^{-1} to 1320 cm^{-1} ; and (d) 1630 cm^{-1} to 1800 cm^{-1} .

In the crystal, there is the existence of EG in *trans* and of furan cycles in *syn* conformations [67,102]. The increase of the quantity of groups in these conformations is clearly visible on the previous graphs (Figures 73.a and 73.b) for the A samples (quenched and annealed) and the B-annealed one, confirming the presence of crystals. Figure 73.b attests that the crystal apparition under biaxial stretching is dependent on the furan cycles in *syn* conformations. As it is visible for the A samples, the maximum of the band is localized at 1575 cm^{-1} compared to 1580 cm^{-1} in the amorphous PEF. This shift was observed when the samples are cold crystallized [67,102]. The increase of the quantity of furan cycles in *syn* conformations in the B-annealed sample is

well-visible, compared to the B-quenched in which only a shoulder is noticeable at the wave number associated to the *syn* conformations (Figure 73.b).

The amorphous domain is mainly composed of a majority of EG in *gauche* conformation and of furans in *anti* conformation. The stretching has an influence on the amorphous domain. If the stretched samples and the amorphous one are compared, clear differences are visible in Figure 73.c, with the band representative of the ether ($1050 - 1180 \text{ cm}^{-1}$) and of the ester groups ($1180 - 1350 \text{ cm}^{-1}$), and in Figure 73.a, with the signal of the *gauche* conformations. Upon biaxial stretching, these groups become more constrained. Then, the B-quenched sample exhibits mainly constrained EG in *gauche* conformations, furans in *anti* conformations and constrained ether and ester groups. Thus, the B-quenched has mainly developed a constrained amorphous domain.

The same conformational changes as in uniaxial stretching seem to be involved in SIC with biaxial stretching, confirming the existence of an unique crystal structure [65,116].

The analysis of the amorphous domain mobility can complete the previous observations. Figure 74 shows the viscoelastic properties of the quenched and annealed samples of the A and B tests. On the contrary to the static crystallization, and to the uniaxial stretching, no real changes between the amorphous and the biaxially stretched samples are visible on the β -relaxation (see Annex 2).

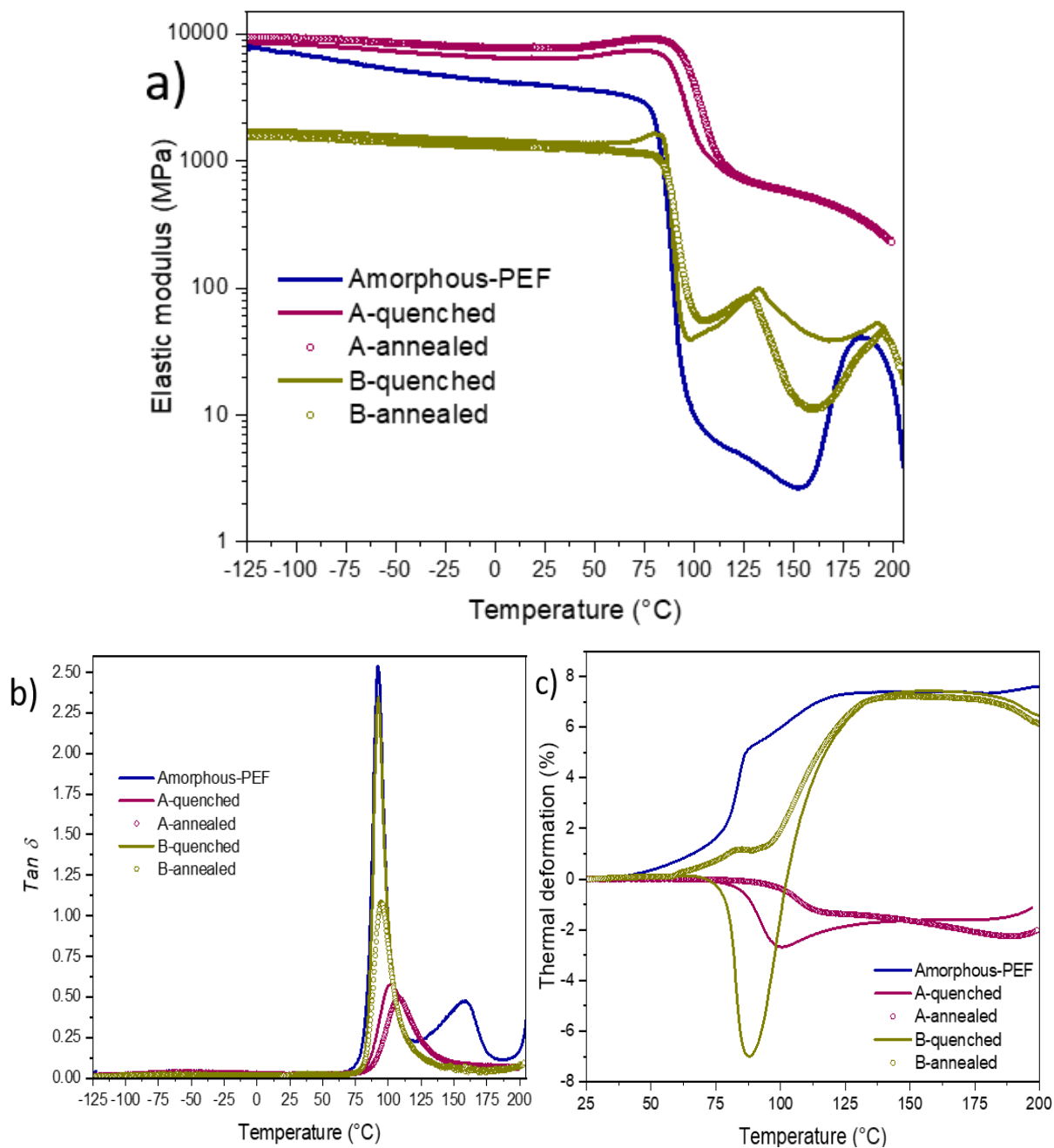


Figure 74. (a) Elastic modulus (E'), (b) $\text{Tan } \delta$ and (c) thermal deformation evolutions with the temperature, performed by DMTA at an heating rate of $1^{\circ}\text{C}/\text{min}$, from (a) and (b) -150°C to 210°C and (c) from 25°C to 210°C , for stretched PEF.

The quenched and annealed samples of the A test are relatively similar. There is an increase of the elastic modulus values and of the T_{α} , in comparison with the amorphous sample. The annealed sample has a slightly higher glassy plateau and a higher α -relaxation temperature, compared to the quenched one (108°C for the annealed sample and 103°C for the quenched one). It is the consequence of a reduced mobility of the amorphous domain after the biaxial

stretching and the annealing. These T_α are close to previous work on biaxially-oriented PEF [62]. The thermal stability of the annealed sample is also better, as the relaxation of its stretched chains seems to be lower and occurs at higher temperatures, compared to the quenched one. However, these two samples remain relatively similar.

The mobility and the orientation of the amorphous domain is completely different between the A and B tests. Thus, it seems that the stretching settings and the biaxial draw ratios have a real influence on the microstructural development.

The α -relaxation of the B-samples (quenched and annealed) occurs at the same temperature as the amorphous sample, and the cold crystallization takes place readily during the α -relaxation. The magnitude of the $Tan \delta$ peak is lower for the B-annealed (Figure 74.b), while the peak magnitude of the B-quenched does not change compared to the amorphous sample. It confirms that the annealing step has reduced the mobility of the amorphous domain.

The B-samples exhibit a lower glassy plateau compared to the amorphous sample. With these stretching settings, the stretching has led to the formation of low crystal ratios and then, it is possible that the amorphous domain has been slightly relaxed. It is in adequation with what has been observed in the previous chapter with “slow” and “rapid” strain rates. Then, the global response in DMTA appears less rigid. The low stability of the amorphous domain of the B tests is confirmed with the thermal deformation measurement (Figure 74.c). For the quenched sample the relaxation of the stretched chains occurs during the α -relaxation and is more pronounced, compared to A test. The B-annealed exhibits a behaviour close to the one of the amorphous sample. It is likely that the stretched chains have already been relaxed during the annealing step.

To conclude this part, the defined protocol has led to the realization of isothermal stretching tests. However, the microstructure of the samples is different between the two stretching conditions. The samples of the A test exhibit a high crystal ratio and a good stability of their microstructure. On the other hand, the samples of the B test, performed at higher strain rates and up to lower biaxial draw ratio, leads to a lower quantity of crystal, and to a less stable microstructure. Without the annealing step, the sample exhibits mainly a constrained amorphous domain. The following part aims at investigating the microstructural evolution during biaxial stretching.

4. Microstructural evolution upon biaxial stretching

In order to get additional data on the microstructural development of PEF during the biaxial stretching, some “interrupted” and “unloaded” tests have been realised. The A test is used as a reference for the stretching settings, and two levels of strain have been chosen on the stress/strain curve. The stretching protocol is the same as the one presented at the beginning of this chapter. The samples are quenched at the end of the test.

Figure 75 depicts this selection, as well as the associated “interrupted” and “loaded/unloaded” curves. Debye-Scherrer patterns are also added.

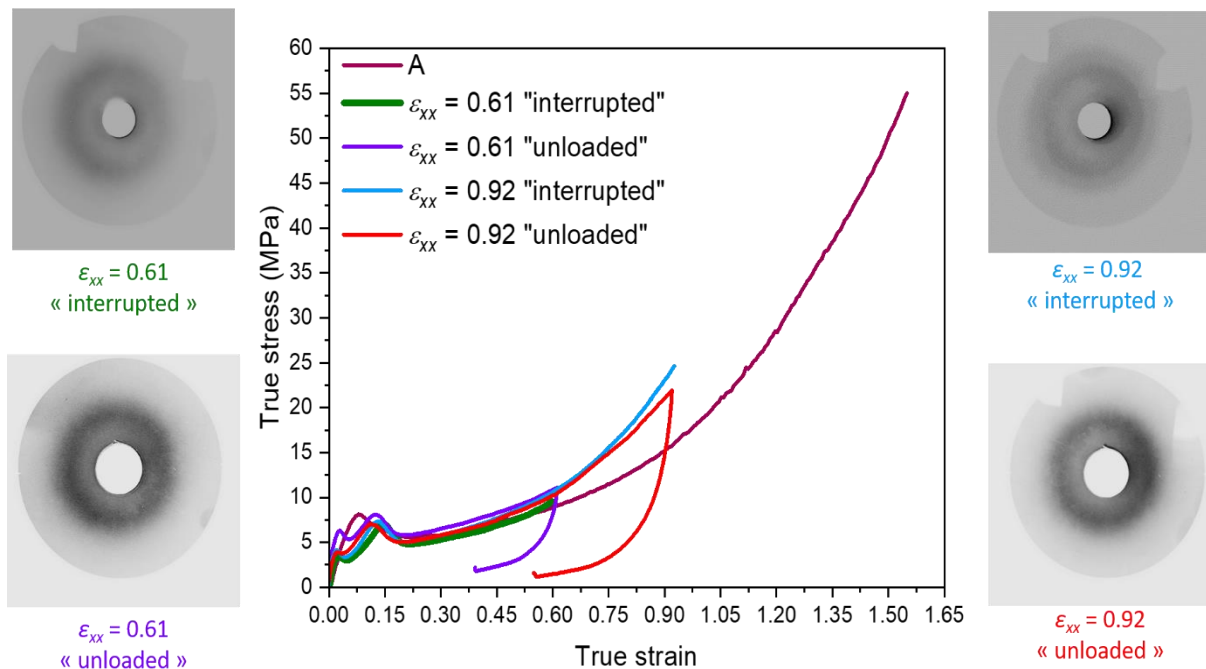


Figure 75. PEF true stress strain curves of “interrupted”, “unloaded” tests and of the test stretched to a higher strain (A).

The superposition of the “interrupted” and “unloaded” tests with the A test is well visible. The slight disparities are related to the experimental scattering (sample localization on the sheet and temperature for example). However, the unloaded loop is different from what has been observed during uniaxial stretching [116]. For both tests, the unloading loop reveals a visco-hyperelastic behaviour, and probably a low level of plasticity. On the Debye-Scherrer patterns, only an

amorphous halo is visible. It is possible to notice a really low anisotropy of the amorphous halo on the patterns related to the “interrupted” tests ($\varepsilon_{xx} = 0.61$ and $\varepsilon_{xx} = 0.92$).

The radial scans, in transmission (Figure 76.a) and in reflexion (Figure 76.b), are going to complete the Debye-Scherrer observations. The crystal ratios as well as the cold crystallization temperatures (measured by DSC) are gathered in Table 23. It was not possible to calculate the χ_{MAF} and χ_{RAF} of the two “unloaded” tests, thus the values are not reported for all the “unloaded” and “interrupted” samples. This difficulty of integration can be due to a different microstructure induced during the loading and, another one induced during the unloading. It has already been proposed for PET loaded/unloaded tests in Chapter 4. The DSC scans are in Annex 3.

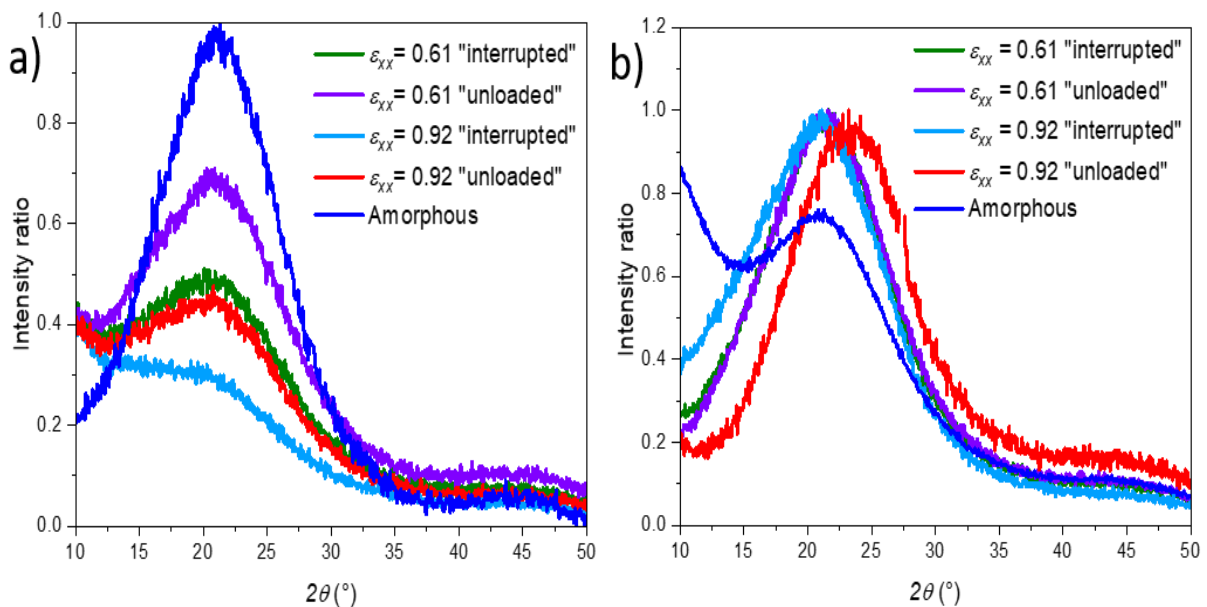


Figure 76. (a) Radial scans in transmission and (b) in reflexion from 10 ° to 50 ° of amorphous, interrupted and unloaded tests.

Samples	χ_c (%)	T_c (°C)
Amorphous PEF	0	
$\epsilon_{xx} = 0.61$ “interrupted”	1	105
$\epsilon_{xx} = 0.61$ “unloaded”	0	
$\epsilon_{xx} = 0.92$ “interrupted”	14	107
$\epsilon_{xx} = 0.92$ “unloaded”	5	160
A-quenched	19	111

Table 23. χ_c and cold crystallization temperatures of amorphous, interrupted, unloaded and A-quenched tests of PEF.

These two scans are different from those of the A test (Figures 72). It confirms that no SIC has occurred in these samples, and that chains have probably only be extended. These samples remain in a predominantly amorphous state. It suggests that some local organized zones may exist. The sample stretched up to 0.61 and unloaded seems to be the closest to the amorphous sample. The unloading at this strain erases the influence of the first stages of the stretching. Finally, the sample stretched up to 0.61 and interrupted, and the one stretched up to 0.92 and unloaded look relatively similar with these scans.

The DSC scans in the glass transition region (Annex 3) show, through the presence of many bumps, the complexity of the microstructure. The thermogram of the sample stretched up to a strain of 0.61 and then unloaded shows no traces of cold crystallization nor melting. It indicates an amorphous sample. The other DSC traces reveal the existence of cold crystallization occurring under a relatively “fast” heating rate (i.e. 10 °C/min), while no crystallization is observed at such heating rate for amorphous PEF. This is due to the creation of pre-organized areas with the stretching. The crystal ratios remain low for these samples, and then according to the previous results, a doubt exists on the 14% of crystal found for the samples stretched up to a strain of 0.92 and then interrupted. However, the temperature of cold crystallization seems relatively trustable and decreases for the “interrupted” samples. It confirms that up to these levels of strains, the stretching has formed some local organized areas that can be suppressed during the unloading.

Figure 77 shows the FT-IR measurements of the “interrupted” and “unloaded” samples for the relevant bands. The other regions, for which no changes are clearly visible, are in Annex 4.

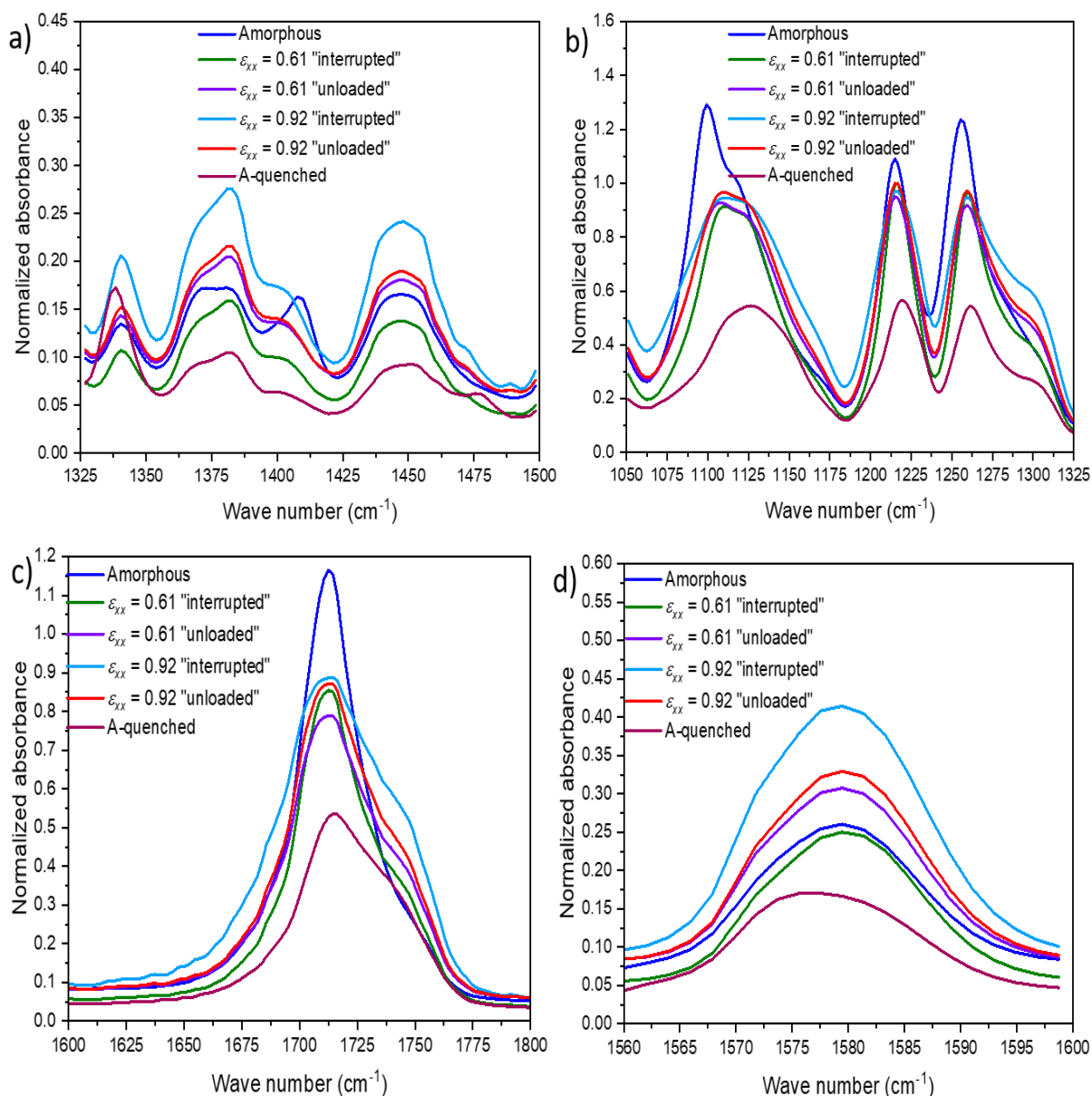


Figure 77. FT-IR measurement of amorphous, interrupted, unloaded and A-quenched tests from (a) 1325 cm^{-1} to 1500 cm^{-1} , (b) 1050 cm^{-1} to 1325 cm^{-1} , (c) 1600 cm^{-1} to 1800 cm^{-1} , (d) 1560 cm^{-1} to 1600 cm^{-1} .

Figure 77 reveals that there is only the existence of a constrained amorphous domain in the “interrupted” and “unloaded” samples. The bands have the same shape, as for the B-quenched test. It confirms that the first stages of the stretching, even the biaxial one, has an influence mainly focused on the aliphatic part of the chain [67]. Thus, for the samples exhibiting a low crystal ratio, the visible changes can be highlighted on the bands corresponding to the amorphous domain: constrained ether and ester groups, furan in *anti* conformations and ethylene glycol in constrained *gauche* conformations.

Figure 78 represents the viscoelastic behaviour of the amorphous domain of the “interrupted” and “unloaded” samples in comparison with the A-quenched test.

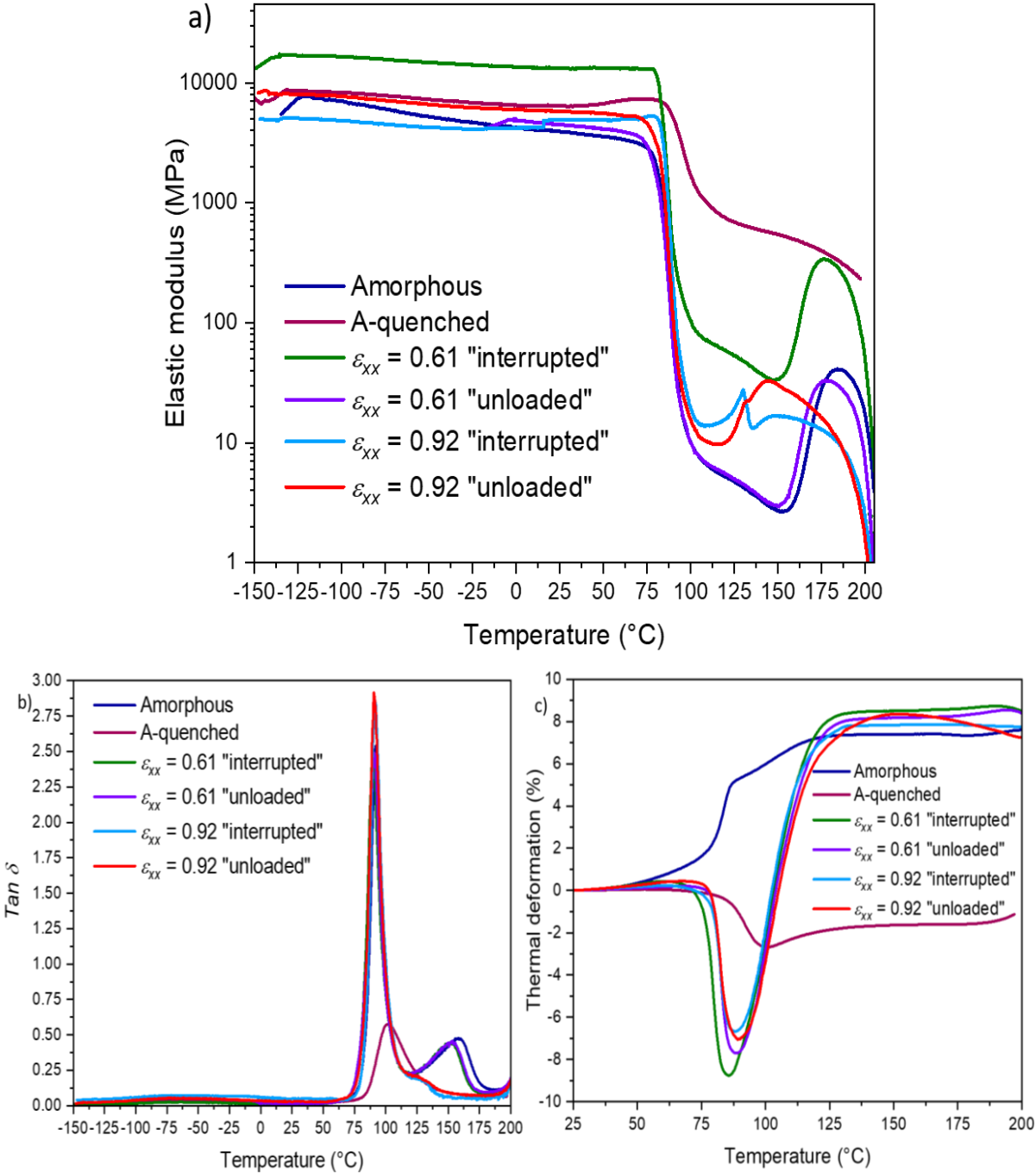


Figure 78. (a) Elastic modulus (E'), (b) $Tan \delta$ and (c) thermal deformation evolutions with the temperature, performed by DMTA at an heating rate of 1° C/min, from (a) and (b) -150 °C to 210 °C and (c) from 25 °C to 210 °C, for stretched PEF.

Figure 78.a attests of the mainly amorphous state of the “interrupted” and “unloaded” samples. Indeed, as in the B tests (Figure 74), the cold crystallization is well visible for all the samples. The heating rate of 1 °C/min (used in DMTA) suits better with the complex microstructure of these samples, than the one of 10 °C/min in DSC. However, it is well-visible in Figure 78.a and 78.b, that the cold crystallization occurs at lower temperature compared to the amorphous sample. The cold crystallization is also more visible than with the B tests. It agrees with the presence of some areas with a local pre-organization that can crystallize when some thermal energy is given to them. The cold crystallization appears sooner and is faster for the samples stretched up to $\epsilon_{xx} = 0.92$ compared to those stretched up to a strain of 0.61. It means that the stretching up to this strain has led to more changes in the amorphous domain of these two samples, whatever if they have been unloaded or not.

For the sample stretched up to 0.92 and interrupted, the shape of the curve during the cold crystallization is close to the one of the B samples. Moreover, on the sample stretched up to 0.92 and unloaded, a shoulder is visible during the cold crystallization at the same temperature as the peak temperature of the sample stretched up to 0.92 and interrupted. The “unloaded” sample exhibits its main peak at a temperature around 12 °C higher. It would mean that a part of the microstructure has been induced during the loading, while another part has been formed during the unloading. The magnitude of the *Tan δ* peak and its maximum peak temperature are similar for the amorphous sample, as well as for the “interrupted” and “unloaded” ones.

Some differences exist concerning the height of the glassy and rubbery plateaux, especially for the $\epsilon_{xx} = 0.61$ “interrupted”. However, the microstructure of these biaxial samples is too complex to draw clear conclusions. Depending on the settings, and as there is no crystal, more or less rigid areas can exist in the amorphous domain (as it has been also observable for B tests). Thus, the global response of the amorphous domain can appear more or less rigid.

To conclude on this part, Figure 78.c shows that the “interrupted” and “unloaded” samples still behave in a similar way, mainly caused by the absence of a well-defined crystal, like in the case of the B-quenched test. The relaxation of the stretched chains occurs close to the α -transition and, the highest magnitude of relaxation is attributed to the $\epsilon_{xx} = 0.61$ “interrupted”. This sample has the highest modulus on the glassy plateau, maybe due to a strong extension of the chains and the presence of domains with a high rigidity. The relaxation of the chains is less and less pronounced as the strain of the biaxial test increases. Then, for all the samples the dilatation occurs, and they behave like amorphous PEF. It confirms that without a sufficient amount of

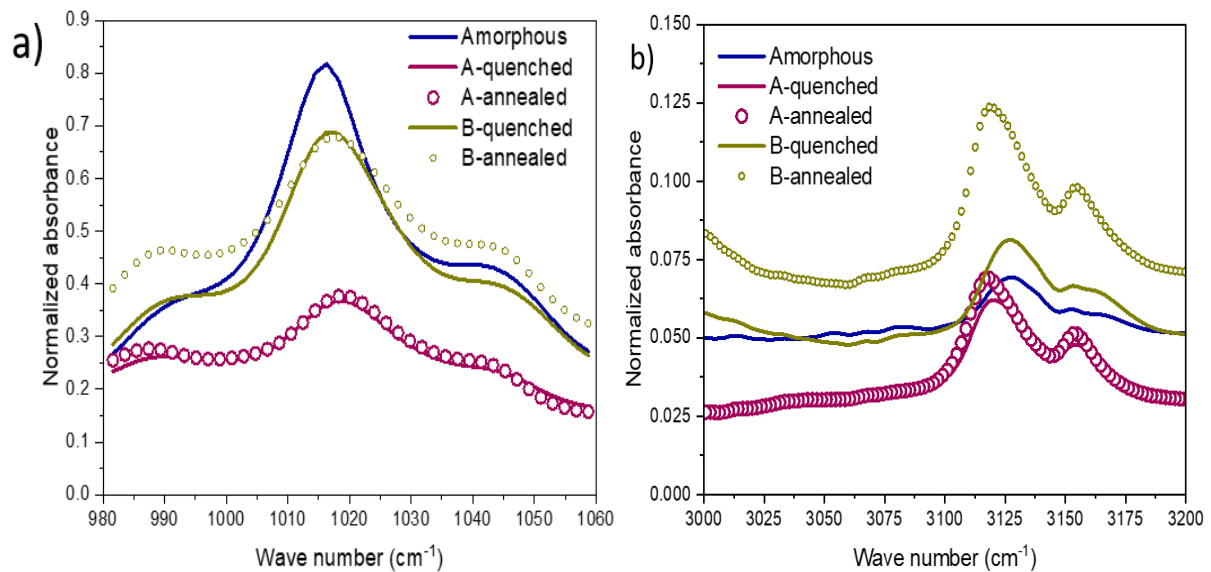
crystal (as in B-quenched sample), the local organizations of the amorphous zone is not sufficient to obtain a stable structure.

5. Conclusions

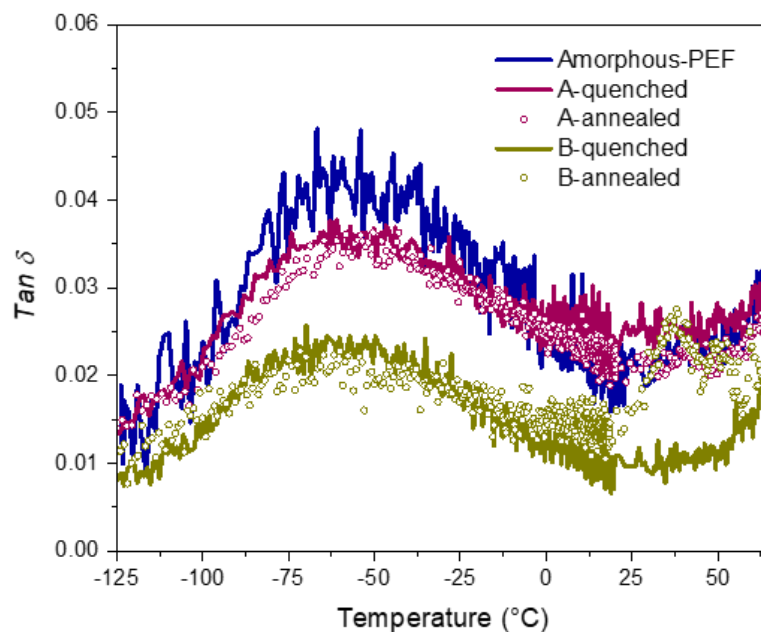
To conclude, it has been shown that PEF is able to form a crystal during biaxial stretching, but the stretching settings are determinant for the amorphous domain stability. Once the crystal is formed, less crystalline families are observed, in comparison with uniaxial stretching. However, as in uniaxial stretching, the same conformational changes are involved, and the aliphatic part of the chain is still the first one impacted by the stretching. The tests, for which a well-defined crystal was not formed, have a constrained microstructure, close to the one of the “interrupted” and “unloaded” tests. Only the aliphatic part of the chain has undergone changes, but the microstructure seems to be not stable.

Some others “unloaded” and “interrupted” tests must be performed at higher strains to compare the kinetic of crystal apparition in uniaxial and biaxial stretching.

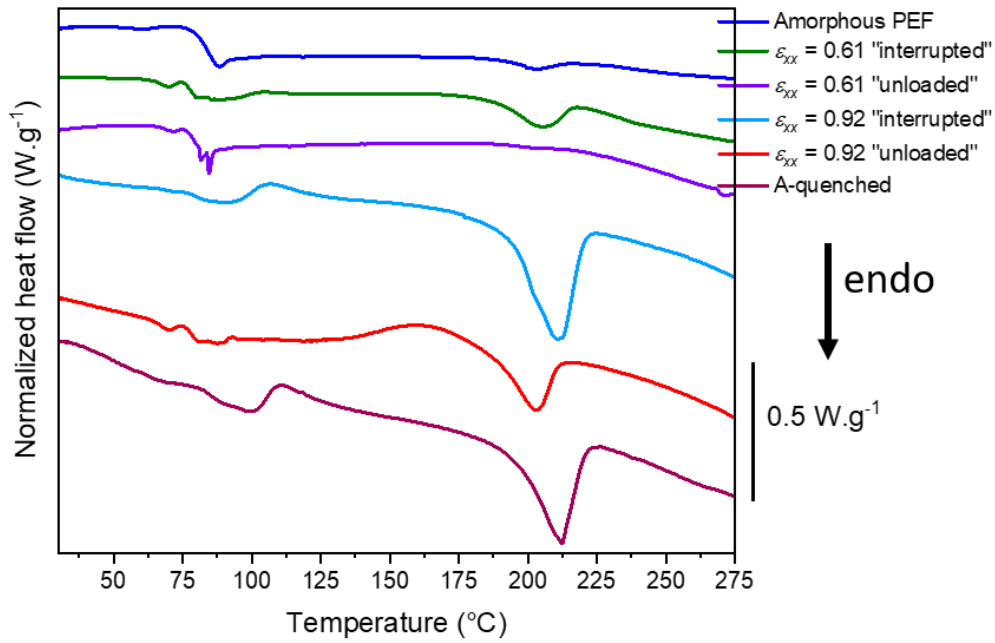
6. Annexes



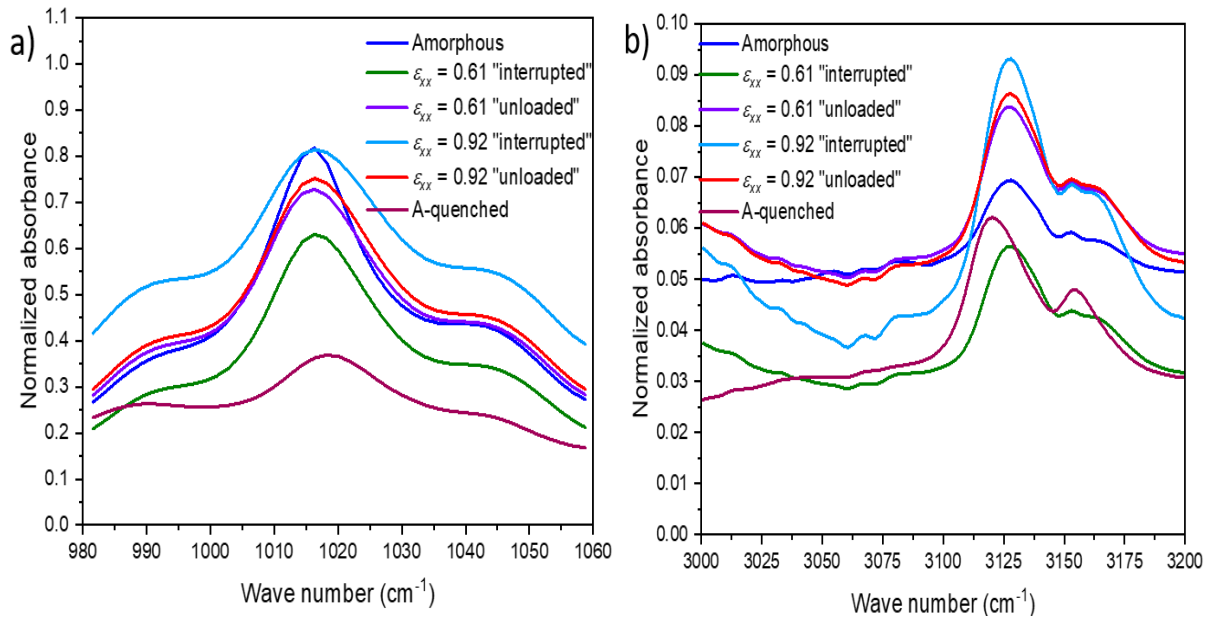
Annex 1. FT-IR measurement of amorphous, quenched (lines) and annealed (dots) PEF from (a) 980 cm⁻¹ to 1060 cm⁻¹ and (b) 3000 cm⁻¹ to 3200 cm⁻¹.



Annex 2. Viscoelastic measurement in the low temperature region of A and B tests (quenched and annealed), measured by DMTA at 1 Hz and 1 °C/min.



Annex 3. Thermal behaviour of amorphous, interrupted, unloaded and A tests. DSC measurement performed from 30 °C to 275 °C at 10 °C/min. Endothermic phenomena are top-down.



Annex 4. FT-IR measurement of amorphous, interrupted, unloaded and C-tests from (a) 980 cm^{-1} to 1060 cm^{-1} and (b) 3000 cm^{-1} to 3200 cm^{-1} .

Conclusions and perspectives

1. Conclusions of the work

The aim of this work was to get more data on the PEF mechanical behaviour, as well as on its associated microstructural development during some mechanical loadings that are close to those occurring during the ISBM process (uniaxial and biaxial stretching). Another fundamental point was to have a direct comparison with the material currently used for this application, PET.

Thus, it has been demonstrated that if the uniaxial stretching of PEF is performed with the correct stretching settings, an impressive strain hardening occur and a crystal is formed. These stretching parameters cannot be the same as those of PET: they have to take into account the initial physical state of the material. It means to consider the gap from the α -relaxation. The interest of using a master curve is then completely proved.

It also seems that the induced microstructure in PEF is not really dependent on the stretching parameters, but mainly on the reaching or not of the NDR. For all the stretching tests that have reached strains higher than the NDR, the microstructure obtained was similar. On the contrary, because of its high chain mobility, PET microstructural development is more sensitive to the stretching settings. This analysis has been confirmed with the realisation and the analysis of the “interrupted” and “unloaded” tests.

The crystal of PEF is formed before the NDR, while the one of PET appears at the end of the stretching. It limits the microstructural disparities between the stretching settings. It means that for an industrial process, the reaching of the NDR is necessary to ensure a stable microstructure. The presence of a microstructural unicity fits with the similar crystal ratios obtained in PEF, in comparison with the higher variability existing in PET. It has also been noted that the crystal

formed with SIC is similar to the one existing with static crystallization. The same conformations exist. The influence of the stretching in the first stages of the deformation is clearly visible on the aliphatic part of the chain. The furan change, from *anti* to *syn* conformation, is determinant to form a crystal. PEF is able to be stretched efficiently in biaxial stretching too. When the temperature remains isotherm during the stretching, the microstructure obtained seems to be relatively well-defined and stable, if a sufficient crystal ratio has been reached.

Overall, when PEF and PET are compared, it seems that once the stretching is completely mastered the resulting properties are relatively close in terms of thermal stability, α -relaxation, crystal ratios and amorphous domain mobility. The influence of the temperature, during the stretching, on the microstructural development has been shown as relatively similar for PEF and PET. The temperature evolution during the stretching is the determinant parameter to ensure the stability of the amorphous domain.

In a nutshell, it seems that it is possible to replace PET by PEF and to obtain similar microstructural developments, during a stretching process step. Moreover, some others results (not reported in this work) have proven the improved stability of stretched PEF, in comparison with amorphous one, when the materials are in contact with water or another acid solvent, air or heat.

2. Perspectives

Despite the synthesis shown, some questions still remain concerning PEF, and starting from this work complementary measurements must be performed. For example, it can be interesting to focus on the thermal behaviour existing during uniaxial stretching. The quantification of the temperature increase, and its comparison with a temperature increase due to the self-heating or to a crystallization process can be helpful to improve the stretching settings and the understanding. With this in mind, the realization of complementary “interrupted” and “unloaded” tests with “rapid” strain rates can confirm the kinetic of crystal formation found with a “slow” strain rate, and can highlight or not some differences in terms of crystal perfection.

The realization of complementary biaxial tests and of poles figures can also add details concerning the PEF crystal, its orientation and its spatial organization. To finish this non-

exhaustive list, the barrier properties of stretched PEF in comparison with stretched PET must be explored.

From our point of view, the path existing to form PEF bottles can be successful if some differences between the two materials are taken into account. For example, according to the occurrence of the NDR at higher strains, it can be better to design smaller preform for PEF. The process temperatures must also be higher for PEF in comparison with PET: as an example PEF can be stretched at the end of its rubbery plateau and form a stable and well-defined microstructure; while PET microstructure seems to be more stable when the stretching is performed close to the α -relaxation.

3. Environmental impact of PEF

From an environmental side, the introduction of PEF in the industrial market can have a positive impact, as it can reduce the use of non-renewable energy use (NREU) by 40 % to 50 %, in comparison with PET. The same reduction is almost observable for the greenhouse gas emissions [139]. The use of packaging made from renewable resources can reduce the environmental impact, increase the acceptance by the consumers and could also save 315 millions of tons of CO₂ annually [26,140].

Then, switching from PET to PEF, and in a general from petroleum based materials to biobased plastics, can help to reach the Europe 2020 targets for greenhouse gas emissions [26]. Moreover, PEF could be used in other fields than only food packaging, such as textile, medical packaging, home building, insulating... Up to now, the cost of biobased plastics is still high, but tends to decrease in the next years with their implantation on the market. Concerning the end of life, PEF can be recycled in the same way as PET, and then provides a material which fits well with the circular economy, and the will of consumers to use now “greener” products. However, the introduction of PEF in the global market would necessitate a complete substitution of PET. Indeed, if not the recycling of both materials is going to be handled and the separation of them can be complicated. At the present time, PEF, and other materials are allowed to be introduced on the PET recycling stream if they do not exceed 5% of the total weight. Thus, right now, complementary works on PEF must be accomplished to implant it on all the PET markets.

References

- [1] H. Namazi, Polymers in our daily life, *BioImpacts*. 7 (2017) 73–74.
doi:10.15171/bi.2017.09.
- [2] J. Haudin, Processus de déformation des polymères semi-cristallins. Effets de mise en œuvre, (n.d.) 2–3. <https://www.lavoisier.fr/livre/chimie/structure-et-morphologie-des-polymeres/descriptif-9782746249141> (accessed 1 December 2020).
- [3] Natural Polymers | Polymers | Chemistry|Source of Polymers | Byju's, (n.d.).
<https://byjus.com/chemistry/natural-polymers/> (accessed 26 November 2020).
- [4] Natural Polymer - an overview | ScienceDirect Topics, (n.d.).
<https://www.sciencedirect.com/topics/materials-science/natural-polymer> (accessed 26 November 2020).
- [5] By Design: World War II, plastics, and NPE, (n.d.).
<https://www.plasticstoday.com/business/design-world-war-ii-plastics-and-npe>
(accessed 25 November 2020).
- [6] Disneyland 'house of the future' from the 1960s: Photos are fascinating, (n.d.).
<https://www.news.com.au/finance/economy/world-economy/fascinating-photos-show-the-plastic-house-of-the-future-that-20-million-disneyland-visitors-flocked-to-in-the-1960s/news-story/1fbff5f11caeabc8f681cd9d9cf42e41> (accessed 26 November 2020).
- [7] A History of Plastics, (n.d.).
https://www.bpf.co.uk/plastipedia/plastics_history/Default.aspx (accessed 26 November 2020).

- [8] S.J. Risch, Food Packaging History and Innovations, *J. Agric. Food Chem.* 57 (2009) 8089–8092. doi:10.1021/jf900040r.
- [9] History and Timeline | Crown, (n.d.). <https://www.crowncork.com/about-crown/history-and-timeline> (accessed 26 November 2020).
- [10] The History of Plastic Bottles – RecycleNation, (n.d.). <https://recyclenation.com/2011/03/history-plastic-bottles-recycle/> (accessed 26 November 2020).
- [11] R.D. B. Daubeny, The crystal structure of polyethylene terephthalate, *Proc. R. Soc. London. Ser. A. Math. Phys. Sci.* 226 (1954) 531–542. doi:10.1098/rspa.1954.0273.
- [12] K. Ben Hafsia, Identification des micro-mécanismes de déformation du PET amorphe et semi-cristallin in situ au cours d'un essai mécanique, HAL Id Tel-01752357. (2016).
- [13] Planetoscope - Statistiques : Ventes de bouteilles en plastique dans le monde, (n.d.). <https://www.planetoscope.com/dechets/1990-ventes-de-bouteilles-en-plastique-dans-le-monde.html> (accessed 27 November 2020).
- [14] LSP Patrice NATIER 13 décembre ppt télécharger, (n.d.). <https://slideplayer.fr/slide/11877235/> (accessed 27 November 2020).
- [15] F. Alvarado Chacon, M.T. Brouwer, E.U. Thoden van Velzen, Effect of recycled content and rPET quality on the properties of PET bottles, part I: Optical and mechanical properties, *Packag. Technol. Sci.* 33 (2020) 347–357. doi:10.1002/pts.2490.
- [16] G.Z. Papageorgiou, V. Tsanaktis, D.N. Bikiaris, Synthesis of poly(ethylene furandicarboxylate) polyester using monomers derived from renewable resources: Thermal behavior comparison with PET and PEN, *Phys. Chem. Chem. Phys.* 16 (2014) 7946–7958. doi:10.1039/c4cp00518j.
- [17] F. Zouai, S. Bouhelal, M.E. Cagiao, F.Z. Benabid, D. Benachour, F.J.B. Calleja, Study of nanoclay blends based on poly(ethylene terephthalate)/poly(ethylene naphthalene 2,6-dicarboxylate) prepared by reactive extrusion, *J. Polym. Eng.* 34 (2014) 431–439. doi:10.1515/polyeng-2013-0244.
- [18] T.N. Blanton, An X-ray diffraction study of poly(ethylene-2,6-naphthalate), PEN,

- Powder Diffr. 17 (2002) 125–131. doi:10.1154/1.1446861.
- [19] C.I. Martins, M. Cakmak, Large deformation mechano-optical and dynamical phase behavior in uniaxially stretched poly(ethylene naphthalate), *Macromolecules*. 38 (2005) 4260–4273. doi:10.1021/ma047499s.
- [20] S. Murakami, M. Yamakawa, M. Tsuji, S. Kohjiya, Structure development in the uniaxial-drawing process of poly(ethylene naphthalate), *Polymer (Guildf)*. 37 (1996) 3945–3951. doi:10.1016/0032-3861(96)00209-1.
- [21] M. Cakmak, Y.D. Wang, M. Simhambhatla, Processing characteristics, structure development, and properties of uni and biaxially stretched poly(ethylene 2,6 naphthalate) (PEN) films, *Polym. Eng. Sci.* 30 (1990) 721–733. doi:10.1002/pen.760301205.
- [22] LES BIOPLASTIQUES BIODÉGRADABLES ET COMPOSTABLES ÉTAT DES LIEUX RAPPORT D'INFORMATION R A P P O R T D'INFORMATION, 2019.
- [23] POUR UNE NOUVELLE ÉCONOMIE DES PLASTIQUES, n.d.
- [24] sustainable development goals, agenda 2030 | Global Taskforce, (n.d.). <https://www.global-taskforce.org/tags/sustainable-development-goals-agenda-2030> (accessed 2 December 2020).
- [25] What is a Circular Economy? | Ellen MacArthur Foundation, (n.d.). <https://www.ellenmacarthurfoundation.org/circular-economy/concept> (accessed 2 December 2020).
- [26] C.L. Reichert, E. Bugnicourt, M.-B. Coltelli, P. Cinelli, A. Lazzeri, I. Canesi, F. Braca, B.M. Martínez, R. Alonso, L. Agostinis, S. Verstichel, L. Six, S. De Mets, E.C. Gómez, C. Ißbrücker, R. Geerinck, D.F. Nettleton, I. Campos, E. Sauter, P. Pieczyk, M. Schmid, Bio-Based Packaging: Materials, Modifications, Industrial Applications and Sustainability, *Polym.* 2020, Vol. 12, Page 1558. 12 (2020) 1558. doi:10.3390/POLYM12071558.
- [27] R.A. Lee, J.-M. Lavoie, From first- to third-generation biofuels: Challenges of producing a commodity from a biomass of increasing complexity, *Anim. Front.* 3 (2013) 6–11. doi:10.2527/af.2013-0010.
- [28] J. Payne, P. McKeown, M.D. Jones, A circular economy approach to plastic waste,

- Polym. Degrad. Stab. 165 (2019) 170–181.
doi:10.1016/j.polymdegradstab.2019.05.014.
- [29] R.A. Auras, B. Harte, S. Selke, R. Hernandez, Mechanical, Physical, and Barrier Properties of Poly(Lactide) Films, *J. Plast. Film Sheeting*. 19 (2003) 123–135.
doi:10.1177/8756087903039702.
- [30] J. Mulligan, M. Cakmak, Nonlinear mechano-optical behavior of uniaxially stretched poly(lactic acid): Dynamic phase behavior, *Macromolecules*. 38 (2005) 2333–2344.
doi:10.1021/ma048794f.
- [31] G. Stoclet, R. Seguela, J.M. Lefebvre, S. Elkoun, C. Vanmansart, Strain-induced molecular ordering in polylactide upon uniaxial stretching, *Macromolecules*. 43 (2010) 1488–1498. doi:10.1021/ma9024366.
- [32] G. Kokturk, E. Piskin, T.F. Serhatkulu, M. Cakmak, Evolution of phase behavior and orientation in uniaxially deformed polylactic acid films, *Polym. Eng. Sci.* 42 (2002) 1619–1628. doi:10.1002/pen.11057.
- [33] X. Ou, M. Cakmak, Comparative study on development of structural hierarchy in constrained annealed simultaneous and sequential biaxially stretched polylactic acid films, *Polymer (Guildf)*. 51 (2010) 783–792. doi:10.1016/j.polymer.2009.11.058.
- [34] J.-H. Wu, M.-S. Yen, C.-P. Wu, C.-H. Li, • M C Kuo, Effect of Biaxial Stretching on Thermal Properties, Shrinkage and Mechanical Properties of Poly (Lactic Acid) Films, Springer. 21 (2013) 303–311. doi:10.1007/s10924-012-0523-5.
- [35] N. Guigo, E. Forestier, N. Sbirrazzuoli, Thermal Properties of Biobased Polymers: Furandicarboxylic Acid (FDCA)-Based Polyesters, in: Springer, Cham, 2019: pp. 189–217. doi:10.1007/12_2019_51.
- [36] A.F. Sousa, C. Vilela, A.C. Fonseca, M. Matos, C.S.R. Freire, G.-J.M. Gruter, J.F.J. Coelho, A.J.D. Silvestre, Biobased polyesters and other polymers from 2,5-furandicarboxylic acid: a tribute to furan excellency, *Polym. Chem.* 6 (2015) 5961–5983. doi:10.1039/C5PY00686D.
- [37] K. Loos, R. Zhang, I. Pereira, B. Agostinho, H. Hu, D. Maniar, N. Sbirrazzuoli, A.J.D. Silvestre, N. Guigo, A.F. Sousa, A Perspective on PEF Synthesis, Properties, and End-Life, *Front. Chem.* 8 (2020) 585. doi:10.3389/fchem.2020.00585.

- [38] G.Z. Papageorgiou, D.G. Papageorgiou, Z. Terzopoulou, D.N. Bikiaris, Production of bio-based 2,5-furan dicarboxylate polyesters: Recent progress and critical aspects in their synthesis and thermal properties, *Eur. Polym. J.* 83 (2016) 202–229. doi:10.1016/j.eurpolymj.2016.08.004.
- [39] A. Gandini, A.J.D. Silvestre, C.P. Neto, A.F. Sousa, M. Gomes, The furan counterpart of polyethylene terephthalate: An alternative material based on renewable resources, *J. Polym. Sci. Part A Polym. Chem.* 47 (2009) 295–298. doi:10.1002/pola.23130.
- [40] R.-J. van Putten, J. C. van der Waal, E. de Jong, C. B. Rasrendra, H. J. Heeres, J. G. de Vries, Hydroxymethylfurfural, A Versatile Platform Chemical Made from Renewable Resources, *Chem. Rev.* 113 (2013) 1499–1597. doi:10.1021/cr300182k.
- [41] YXY - Avantium, (n.d.). <https://www.avantium.com/technologies/yxy/#> (accessed 4 December 2020).
- [42] M. Volanti, D. Cespi, F. Passarini, E. Neri, F. Cavani, P. Mizsey, D. Fozar, Terephthalic acid from renewable sources: Early-stage sustainability analysis of a bio-PET precursor, *Green Chem.* 21 (2019) 885–896. doi:10.1039/c8gc03666g.
- [43] E. De Jong, M.A. Dam, L. Sipos, G.J.M. Gruter, Furandicarboxylic acid (FDCA), A versatile building block for a very interesting class of polyesters, in: *ACS Symp. Ser.*, American Chemical Society, 2012: pp. 1–13. doi:10.1021/bk-2012-1105.ch001.
- [44] J.J. Bozell, G.R. Petersen, Technology development for the production of biobased products from biorefinery carbohydrates—the US Department of Energy’s “top 10” revisited, *Green Chem.* 12 (2010) 539–55. doi:10.1039/b922014c.
- [45] J. Wu, P. Eduard, S. Thiyagarajan, J. van Haveren, D.S. van Es, C.E. Koning, M. Lutz, C. Fonseca Guerra, Isohexide Derivatives from Renewable Resources as Chiral Building Blocks, *ChemSusChem.* 4 (2011) 599–603. doi:10.1002/cssc.201100076.
- [46] S.K. Burgess, J.E. Leisen, B.E. Kraftschik, C.R. Mubarak, R.M. Kriegel, W.J. Koros, Chain Mobility, Thermal, and Mechanical Properties of Poly(ethylene furanoate) Compared to Poly(ethylene terephthalate), *Macromolecules.* 47 (2014) 1383–1391. doi:10.1021/ma5000199.
- [47] R.J.I. Knoop, W. Vogelzang, J. van Haveren, D.S. van Es, High molecular weight poly(ethylene-2,5-furanoate); critical aspects in synthesis and mechanical property

- determination, *J. Polym. Sci. Part A Polym. Chem.* 51 (2013) 4191–4199.
doi:10.1002/pola.26833.
- [48] S.K. Burgess, G.B. Wenz, R.M. Kriegel, W.J. Koros, Penetrant transport in semicrystalline poly(ethylene furanoate), *Polymer (Guildf)*. 98 (2016) 305–310.
doi:10.1016/j.polymer.2016.06.046.
- [49] S.K. Burgess, O. Karvan, J.R. Johnson, R.M. Kriegel, W.J. Koros, Oxygen sorption and transport in amorphous poly(ethylene furanoate), *Polymer (Guildf)*. 55 (2014) 4748–4756. doi:10.1016/j.polymer.2014.07.041.
- [50] S.K. Burgess, R.M. Kriegel, W.J. Koros, Carbon dioxide sorption and transport in amorphous poly(ethylene furanoate), *Macromolecules*. 48 (2015) 2184–2193.
doi:10.1021/acs.macromol.5b00333.
- [51] S.K. Burgess, D.S. Mikkilineni, D.B. Yu, D.J. Kim, C.R. Mubarak, R.M. Kriegel, W.J. Koros, Water sorption in poly(ethylene furanoate) compared to poly(ethylene terephthalate). Part 1: Equilibrium sorption, *Polymer (Guildf)*. 55 (2014) 6861–6869.
doi:10.1016/j.polymer.2014.10.047.
- [52] S.K. Burgess, D.S. Mikkilineni, D.B. Yu, D.J. Kim, C.R. Mubarak, R.M. Kriegel, W.J. Koros, Water sorption in poly(ethylene furanoate) compared to poly(ethylene terephthalate). Part 2: Kinetic sorption, *Polymer (Guildf)*. 55 (2014) 6870–6882.
doi:10.1016/j.polymer.2014.10.065.
- [53] J.G. van Berkel, N. Guigo, J.J. Kolstad, L. Sipos, B. Wang, M.A. Dam, N. Sbirrazzuoli, Isothermal Crystallization Kinetics of Poly (Ethylene 2,5-Furandicarboxylate), *Macromol. Mater. Eng.* 300 (2015) 466–474.
doi:10.1002/mame.201400376.
- [54] A. Codou, M. Moncel, J.G. van Berkel, N. Guigo, N. Sbirrazzuoli, Glass transition dynamics and cooperativity length of poly(ethylene 2,5-furandicarboxylate) compared to poly(ethylene terephthalate), *Phys. Chem. Chem. Phys.* 18 (2016) 16647–16658.
doi:10.1039/C6CP01227B.
- [55] G. Stoclet, G. Gobius du Sart, B. Yeniad, S. de Vos, J.M. Lefebvre, Isothermal crystallization and structural characterization of poly(ethylene-2,5-furanoate), *Polymer (Guildf)*. 72 (2015) 165–176. doi:10.1016/j.polymer.2015.07.014.

- [56] V. Tsanakis, D.G. Papageorgiou, S. Exarhopoulos, D.N. Bikiaris, G.Z. Papageorgiou, Crystallization and Polymorphism of Poly(ethylene furanoate), *Cryst. Growth Des.* 15 (2015) 5505–5512. doi:10.1021/acs.cgd.5b01136.
- [57] A. Codou, N. Guigo, J. Van Berkel, E. De Jong, N. Sbirrazzuoli, Non-isothermal Crystallization Kinetics of Synthesized via the Direct Esterification Process, (n.d.) 2065–2074.
- [58] Y. Mao, R.M. Kriegel, D.G. Bucknall, The crystal structure of poly(ethylene furanoate), *Polymer (Guildf)*. 102 (2016) 308–314. doi:10.1016/j.polymer.2016.08.052.
- [59] Y. Mao, D.G. Bucknall, R.M. Kriegel, Synchrotron X-ray scattering study on amorphous poly(ethylene furanoate) under uniaxial deformation, *Polymer (Guildf)*. 139 (2018) 60–67. doi:10.1016/j.polymer.2018.01.062.
- [60] C. Menager, N. Guigo, L. Martino, N. Sbirrazzuoli, H. Visser, S.A.E. Boyer, N. Billon, G. Monge, C. Combeaud, Strain induced crystallization in biobased Poly(ethylene 2,5-furandicarboxylate) (PEF); conditions for appearance and microstructure analysis, *Polymer (Guildf)*. 158 (2018) 364–371. doi:10.1016/J.POLYMER.2018.10.054.
- [61] G. Stoclet, J.M. Lefebvre, B. Yenzi, G. Gobius du Sart, S. de Vos, On the strain-induced structural evolution of Poly(ethylene-2,5-furanoate) upon uniaxial stretching: An in-situ SAXS-WAXS study, *Polymer (Guildf)*. 134 (2018) 227–241. doi:10.1016/j.polymer.2017.11.071.
- [62] J.G. van Berkel, N. Guigo, J.J. Kolstad, N. Sbirrazzuoli, Biaxial Orientation of Poly(ethylene 2,5-furandicarboxylate): An Explorative Study, *Macromol. Mater. Eng.* 303 (2018) 1–9. doi:10.1002/mame.201700507.
- [63] R. Androsch, B. Wunderlich, The link between rigid amorphous fraction and crystal perfection in cold-crystallized poly(ethylene terephthalate), *Polymer (Guildf)*. 46 (2005) 12556–12566. doi:10.1016/j.polymer.2005.10.099.
- [64] J.G. van Berkel, On the Physical Properties of poly(ethylene 1,5-furandicarboxylate), These Dr. (2018). <http://joi.jlc.jst.go.jp/JST.Journalarchive/jaqua1957/7.109?from=CrossRef>.
- [65] E. Forestier, C. Combeaud, N. Guigo, G. Monge, J.M. Haudin, N. Sbirrazzuoli, N.

- Billon, Strain-induced crystallization of poly(ethylene 2,5-furandicarboxylate). Mechanical and crystallographic analysis, *Polymer (Guildf)*. 187 (2020). doi:10.1016/j.polymer.2019.122126.
- [66] Z. Chen, J.N. Hay, M.J. Jenkins, FTIR spectroscopic analysis of poly(ethylene terephthalate) on crystallization, *Eur. Polym. J.* (2012). doi:10.1016/j.eurpolymj.2012.06.006.
- [67] E. Forestier, N. Guigo, C. Combeaud, N. Billon, N. Sbirrazzuoli, Conformational Change Analysis of Poly(ethylene 2,5-furandicarboxylate) and Poly(ethylene terephthalate) under Uniaxial Stretching, *Macromolecules*. (2020). doi:10.1021/acs.macromol.0c00691.
- [68] N. Candau, C. Pradille, J.L. Bouvard, N. Billon, On the use of a four-cameras stereovision system to characterize large 3D deformation in elastomers, *Polym. Test*. 56 (2016) 314–320. doi:10.1016/j.polymertesting.2016.10.017.
- [69] G. LeBourvellec, L. Monnerie, J.P. Jarry, Amorphous orientation and induced crystallization in uniaxially stretched poly(ethylene terephthalate glycol), *Polymer (Guildf)*. 27 (1986) 856–860. doi:10.1016/0032-3861(86)90294-6.
- [70] G. Le Bourvellec, J. Beautemps, Stretching of PET films under constant load. II. Structural analysis, *J. Appl. Polym. Sci.* 39 (1990) 329–339. doi:10.1002/app.1990.070390210.
- [71] D.R. Salem, Development of crystalline order during hot-drawing of poly(ethylene terephthalate) film: influence of strain rate, *Polymer (Guildf)*. 33 (1992) 3182–3188. doi:10.1016/0032-3861(92)90232-L.
- [72] A. Ajji, K.C. Cole, M.M. Dumoulin, J. Brisson, Amorphous orientation of poly(ethylene terephthalate) by X-ray diffraction in combination with Fourier transform infra-red spectroscopy, *Polymer (Guildf)*. 36 (1995) 4023–4030. doi:10.1016/0032-3861(95)90981-7.
- [73] A. Mahendrasingam, C. Martin, A. Jaber, D. Hughes, W. Fuller, R. Rule, R.J. Oldman, D. MacKerron, D.J. Blundell, Time-resolved X-ray wide angle scattering studies of the effect of draw rate and temperature on the development of orientation and crystallinity in PET, *Nucl. Inst. Methods Phys. Res. B*. 97 (1995) 238–241. doi:10.1016/0168-583X(94)00377-7.

- [74] A. Ajji, J. Guèvremont, K.C. Cole, M.M. Dumoulin, Orientation and structure of drawn poly(ethylene terephthalate), *Polymer (Guildf)*. 37 (1996) 3707–3714.
doi:10.1016/0032-3861(96)00175-9.
- [75] D.J. Blundell, D.H. MacKerron, W. Fuller, A. Mahendrasingam, C. Martin, R.J. Oldman, R.J. Rule, C. Riekel, Characterization of strain-induced crystallization of poly(ethylene terephthalate) at fast draw rates using synchrotron radiation, *Polymer (Guildf)*. 37 (1996) 3303–3311. doi:10.1016/0032-3861(96)88476-X.
- [76] A.C. Middleton, R.A. Duckett, I.M. Ward, A. Mahendrasingam, C. Martin, Real-time FTIR and WAXS studies of drawing behavior of poly(ethylene terephthalate) films, *J. Appl. Polym. Sci.* 79 (2001) 1825–1837. doi:10.1002/1097-4628(20010307)79:10<1825::AID-APP110>3.0.CO;2-S.
- [77] E. Gorlier, J.M. Haudin, N. Billon, Strain-induced crystallisation in bulk amorphous PET under uni-axial loading, *Polymer (Guildf)*. 42 (2001) 9541–9549.
doi:10.1016/S0032-3861(01)00497-9.
- [78] D. Kawakami, B.S. Hsiao, S. Ran, C. Burger, B. Fu, I. Sics, B. Chu, T. Kikutani, Structural formation of amorphous poly(ethylene terephthalate) during uniaxial deformation above glass temperature, *Polymer (Guildf)*. 45 (2004) 905–918.
doi:10.1016/j.polymer.2003.11.027.
- [79] D. Kawakami, B.S. Hsiao, C. Burger, S. Ran, C. Avila-Orta, I. Sics, T. Kikutani, K.I. Jacob, B. Chu, Deformation-induced phase transition and superstructure formation in poly(ethylene terephthalate), *Macromolecules*. 38 (2005) 91–103.
doi:10.1021/ma049333x.
- [80] D. Kawakami, S. Ran, C. Burger, C. Avila-Orta, I. Sics, B. Chu, B.S. Hsiao, T. Kikutani, Superstructure evolution in poly(ethylene terephthalate) during uniaxial deformation above glass transition temperature, *Macromolecules*. 39 (2006) 2909–2920. doi:10.1021/ma052589y.
- [81] D. Kawakami, S. Ran, C. Burger, B. Fu, I. Sics, B. Chu, B.S. Hsiao, Mechanism of structural formation by uniaxial deformation in amorphous poly(ethylene terephthalate) above the glass temperature, *Macromolecules*. 36 (2003) 9275–9280.
doi:10.1021/ma034791b.
- [82] D. Kawakami, C. Burger, S. Ran, C. Avila-Orta, I. Sics, B. Chu, S.M. Chiao, B.S.

- Hsiao, T. Kikutani, New insights into lamellar structure development and SAXSA/WAXD sequence appearance during uniaxial stretching of amorphous polyethylene terephthalate above glass transition temperature, *Macromolecules*. 41 (2008) 2859–2867. doi:10.1021/ma702554t.
- [83] F. Chaari, M. Chaouche, J. Doucet, Crystallization of poly(ethylene terephthalate) under tensile strain: Crystalline development versus mechanical behaviour, *Polymer (Guildf)*. 44 (2002) 473–479. doi:10.1016/S0032-3861(02)00739-5.
- [84] P.L. Carr, T.M. Nicholson, I.M. Ward, Mesophase structures in poly(ethylene terephthalate), poly(ethylene naphthalate) and poly(ethylene naphthalate bibenzoate), *Polym. Adv. Technol.* 8 (1997) 592–600. doi:10.1002/(SICI)1099-1581(199710)8:10<592::AID-PAT713>3.0.CO;2-H.
- [85] A. Mahendrasingam, D. Blundell, A. Wright, V. Urban, T. Narayanan, W. Fuller, Observations of structure development during crystallisation of oriented poly(ethylene terephthalate), *Polymer (Guildf)*. 44 (2003) 5915–5925. doi:10.1016/S0032-3861(03)00542-1.
- [86] S. Ran, Z. Wang, C. Burger, B. Chu, B.S. Hsiao, Mesophase as the precursor for strain-induced crystallization in amorphous poly(ethylene terephthalate) film, *Macromolecules*. 35 (2002) 10102–10107. doi:10.1021/ma021252i.
- [87] G.E. Welsh, D.J. Blundell, A.H. Windle, A transient mesophase on drawing polymers based on polyethylene terephthalate (PET) and polyethylene naphthoate (PEN), *J. Mater. Sci.* 35 (2000) 5225–5240. doi:10.1023/A:1004820824004.
- [88] M. Vigny, J.F. Tassin, A. Gibaud, G. Lorentz, Study of the molecular structure of PET films obtained by an inverse stretching process. Part I: Constant speed drawing of amorphous films, *Polym. Eng. Sci.* 37 (1997) 1785–1794. doi:10.1002/pen.11827.
- [89] T. Asano, F.J. Baltá Calleja, A. Flores, M. Tanigaki, M.F. Mina, C. Sawatari, H. Itagaki, H. Takahashi, I. Hatta, Crystallization of oriented amorphous poly(ethylene terephthalate) as revealed by X-ray diffraction and microhardness, *Polymer (Guildf)*. 40 (1999) 6475–6484. doi:10.1016/S0032-3861(98)00839-8.
- [90] D.J. Blundell, A. Mahendrasingam, C. Martin, W. Fuller, D.H. MacKerron, J.L. Harvie, R.J. Oldman, C. Riekel, Orientation prior to crystallisation during drawing of poly(ethylene terephthalate), *Polymer (Guildf)*. 41 (2000) 7793–7802.

doi:10.1016/S0032-3861(00)00128-2.

- [91] G. Quandalle, Study and mechanical modeling of the strain-induced-crystallization of polymers : crosslinked naturel rubber and PET, PSL Research University, 2017. <https://pastel.archives-ouvertes.fr/tel-01774634>.
- [92] A. Mahendrasingam, C. Martin, W. Fuller, D.J. Blundell, R.J. Oldman, D.H. MacKerron, J.L. Harvie, C. Riekkel, Observation of a transient structure prior to strain-induced crystallization in poly(ethylene terephthalate), 2000. doi:10.1016/S0032-3861(99)00461-9.
- [93] N. Billon, M. Picard, E. Gorlier, Stretch blow moulding of PET; structure development and constitutive model, *Int. J. Mater. Form.* 7 (2014) 369–378. doi:10.1007/s12289-013-1131-1.
- [94] Eric Gorlier(Mines-ParisTech), Gorlier, E. (2001). Caractérisation rhéologique et structurale d'un PET. Application au procédé de bi-étirage soufflage de bouteilles. Ecole Nationale Supérieure des Mines de Paris, 2001.
- [95] M. Picard, Strain induced crystallisation during stretch blow moulding of PET; correlation with strain hardening, École Nationale Supérieure des Mines de Paris, 2008. <https://pastel.archives-ouvertes.fr/tel-00343353>.
- [96] C.E. Federico, J.L. Bouvard, C. Combeaud, N. Billon, Large strain/time dependent mechanical behaviour of PMMAs of different chain architectures. Application of time-temperature superposition principle, *Polymer (Guildf)*. (2018). doi:10.1016/j.polymer.2018.02.021.
- [97] V. Fabre, G. Quandalle, N. Billon, S. Cantournet, Time-Temperature-Water content equivalence on dynamic mechanical response of polyamide 6,6, *Polymer (Guildf)*. (2018). doi:10.1016/j.polymer.2017.10.067.
- [98] N. Billon, New constitutive modeling for time-dependent mechanical behavior of polymers close to glass transition: Fundamentals and experimental validation, *J. Appl. Polym. Sci.* 125 (2012) 4390–4401. doi:10.1002/app.36598.
- [99] A. Maurel-Pantel, E. Baquet, J. Bikard, J.L. Bouvard, N. Billon, A thermo-mechanical large deformation constitutive model for polymers based on material network description: Application to a semi-crystalline polyamide 66, *Int. J. Plast.* 67 (2015)

102–126. doi:10.1016/j.ijplas.2014.10.004.

- [100] M.L. Williams, R.F. Landel, J.D. Ferry, Temperature Dependence of Relaxation Mechanisms The Temperature Dependence of Relaxation Mechanisms in Amorphous Polymers and Other Glass-forming Liquids¹, 1955.
<https://pubs.acs.org/sharingguidelines> (accessed 1 July 2020).
- [101] L.G. Kazaryan, F.M. Medvedeva, X-Ray study of the structure of the polyester of furan-2, 5-dicarboxylic acid, *Vysok. Soedin., Ser. B.* 10 (1968).
- [102] C.F. Araujo, M.M. Nolasco, P.J.A. Ribeiro-Claro, S. Rudić, A.J.D. Silvestre, P.D. Vaz, A.F. Sousa, Inside PEF: Chain Conformation and Dynamics in Crystalline and Amorphous Domains, *Macromolecules.* 51 (2018) 3515–3526.
doi:10.1021/acs.macromol.8b00192.
- [103] D. Grime, I.M. Ward, The assignment of infra-red absorptions and rotational isomerism in polyethylene terephthalate and related compounds, *Trans. Faraday Soc.* (1958). doi:10.1039/tf9585400959.
- [104] P. Lapersonne, D.I. Bower, I.M. Ward, Molecular orientation and conformational changes due to uniaxial-planar deformation of poly(ethylene terephthalate) films, *Polymer (Guildf).* 33 (1992) 1277–1283. doi:10.1016/0032-3861(92)90774-Q.
- [105] Z. Chen, J.N. Hay, M.J. Jenkins, The thermal analysis of poly(ethylene terephthalate) by FTIR spectroscopy, *Thermochim. Acta.* (2013). doi:10.1016/j.tca.2012.11.002.
- [106] J. Guévremont, A. Ajji, K.C. Cole, M.M. Dumoulin, Orientation and conformation in poly(ethylene terephthalate) with low draw ratios as characterized by specular reflection infra-red spectroscopy, *Polymer (Guildf).* (1995). doi:10.1016/0032-3861(95)99440-6.
- [107] A. Cunningham, I.M. Ward, H.A. Willis, V. Zichy, An infra-red spectroscopic study of molecular orientation and conformational changes in poly(ethylene terephthalate), *Polymer (Guildf).* (1974). doi:10.1016/0032-3861(74)90028-7.
- [108] S.S. Sheiko, I.S. Vainilovitch, S.N. Magonov, FTIR spectroscopy of polymer films under uniaxial stretching, *Polym. Bull.* (2004). doi:10.1007/bf00310242.
- [109] K.C. Cole, J. Guévremont, A. Ajji, M.M. Dumoulin, Orientation and Conformation in PET: New Information from Specular Reflection FT-IR, in: *Prog. Fourier Transform*

- Spectrosc., Springer Vienna, 1997: pp. 403–405. doi:10.1007/978-3-7091-6840-0_94.
- [110] I.M. Ward, Determination of molecular orientation by spectroscopic techniques, in: Springer, Berlin, Heidelberg, 1985: pp. 81–115. doi:10.1007/3-540-13779-3_18.
- [111] J. Liu, P.H. Geil, Crystal structure and morphology of poly(ethylene terephthalate) single crystals prepared by melt polymerization, *J. Macromol. Sci. - Phys.* 36 (1997) 61–85. doi:10.1080/00222349708220415.
- [112] Handbook of Thermoplastic Polyesters, 2002. doi:10.1002/3527601961.
- [113] L. Maini, M. Gigli, M. Gazzano, N. Lotti, D. Bikiaris, G. Papageorgiou, Structural Investigation of Poly(ethylene furanoate) Polymorphs, *Polymers (Basel)*. 10 (2018) 296. doi:10.3390/polym10030296.
- [114] A.S. Maxwell, L. Monnerie, I.M. Ward, Secondary relaxation processes in polyethylene terephthalate-additive blends: 2. Dynamic mechanical and dielectric investigations, *Polymer (Guildf)*. (1998). doi:10.1016/S0032-3861(98)00138-4.
- [115] S. Zekriardehani, S.A. Jabarin, D.R. Gidley, M.R. Coleman, Effect of Chain Dynamics, Crystallinity, and Free Volume on the Barrier Properties of Poly(ethylene terephthalate) Biaxially Oriented Films, *Macromolecules*. 50 (2017) 23. doi:10.1021/acs.macromol.7b00198.
- [116] E. Forestier, C. Combeaud, N. Guigo, N. Sbirrazzuoli, N. Billon, Understanding of strain-induced crystallization developments scenarios for polyesters: Comparison of poly(ethylene furanoate), PEF, and poly(ethylene terephthalate), PET, *Polymer (Guildf)*. 203 (2020) 122755. doi:10.1016/j.polymer.2020.122755.
- [117] P. Lapersonne, D.I. Bower, W. I.M., Benzene ring orientation in uniaxial planar poly(ethylene terephthalate) films, *Polymer (Guildf)*. (1992). doi:10.1016/0032-3861(92)90773-P.
- [118] J.B.F. de Champchesnel, D.I. Bower, I.M. Ward, J.F. Tassin, G. Lorentz, Development of molecular orientation in sequentially drawn PET films, *Polymer (Guildf)*. 34 (1993) 3763–3770. doi:10.1016/0032-3861(93)90498-Y.
- [119] A. Mahendrasingam, C. Martin, W. Fuller, D.J. Blundell, R.J. Oldman, J.L. Harvie, D.H. MacKerron, C. Riekkel, P. Engström, Effect of draw ratio and temperature on the strain-induced crystallization of poly (ethylene terephthalate) at fast draw rates,

- Polymer (Guildf). 40 (1999) 5553–5565. doi:10.1016/S0032-3861(98)00770-8.
- [120] Y. Fu, W.R. Busing, Y. Jin, K.A. Affholter, B. Wunderlich, Structure analysis of the noncrystalline material in poly(ethylene terephthalate) fibers, *Macromol. Chem. Phys.* 195 (1994) 803–822. doi:10.1002/macp.1994.021950236.
- [121] Y. Marco, L. Chevalier, G. Régnier, A. Poitou, Induced crystallization and orientation of poly(ethylene terephthalate) during uniaxial and biaxial elongation, in: *Macromol. Symp.*, John Wiley & Sons, Ltd, 2002: pp. 15–34. doi:10.1002/1521-3900(200208)185:1<15::AID-MASY15>3.0.CO;2-J.
- [122] F. Hamonic, V. Miri, A. Saiter, E. Dargent, Rigid amorphous fraction versus oriented amorphous fraction in uniaxially drawn polyesters, *Eur. Polym. J.* 58 (2014) 233–244. doi:10.1016/j.eurpolymj.2014.06.014.
- [123] I.M. Ward, The mechanical behavior of poly(ethylene terephthalate), *J. Macromol. Sci. Part B.* 1 (1967) 667–694. doi:10.1080/00222346708212356.
- [124] M.K. Hassan, M. Cakmak, Strain-Induced Crystallization during Relaxation Following Biaxial Stretching of PET Films: A Real-Time Mechano-Optical Study, *Macromolecules.* 48 (2015) 4657–4668. doi:10.1021/acs.macromol.5b00388.
- [125] M. Hassan, M. Cakmak, Mechano optical behavior of polyethylene terephthalate films during simultaneous biaxial stretching: Real time measurements with an instrumented system, *Polymer (Guildf).* 54 (2013) 6463–6470. doi:10.1016/j.polymer.2013.09.045.
- [126] J.E. Spruiell, J.L. White, Structural characterization of crystallinity and crystalline orientation in simultaneously biaxially stretched and annealed polyethylene terephthalate films, *J. Polym. Eng.* 6 (1986) 291–312. doi:10.1515/POLYENG.1986.6.1-4.291.
- [127] M. Cakmak, J.E. Spruiell, J.L. White, J.S. Lin, Small angle and wide angle x-ray pole figure studies on simultaneous biaxially stretched poly(ethylene terephthalate) (PET) films, *Polym. Eng. Sci.* 27 (1987) 893–905. doi:10.1002/pen.760271205.
- [128] R.M. Gohil, J.M. Schultz, Morphology of biaxially stretched poly(ethylene terephthalate) films, *J. Macromol. Sci. Part B.* 32 (1993) 99–123. doi:10.1080/00222349308215474.
- [129] P. Chandran, S. Jabarin, Biaxial orientation of poly(ethylene terephthalate). Part I:

- Nature of the stress—strain curves, *Adv. Polym. Technol.* 12 (1993) 119–132.
doi:10.1002/adv.1993.060120202.
- [130] R.M. Gohil, D.R. Salem, Orientation distribution in the noncrystalline regions of biaxially drawn poly(ethylene terephthalate) film: A chain-intrinsic fluorescence study, *J. Appl. Polym. Sci.* 47 (1993) 1989–1998. doi:10.1002/app.1993.070471109.
- [131] D.I. Bower, D.A. Jarvis, I.M. Ward, Molecular orientation in biaxially oriented sheets of poly(ethylene terephthalate). I. Characterization of orientation and comparison with models, *J. Polym. Sci. Part B Polym. Phys.* 24 (1986) 1459–1479.
doi:10.1002/polb.1986.090240706.
- [132] D.A. Jarvis, I.J. Hutchinson, D.I. Bower, I.M. Ward, Characterization of biaxial orientation in poly(ethylene terephthalate) by means of refractive index measurements and Raman and infra-red spectroscopies, *Polymer (Guildf.)* (1980). doi:10.1016/0032-3861(80)90166-4.
- [133] Y. Marco, Caractérisation multi-axiale du comportement et de la micro-structure d'un semi-cristallin : Application au cas du PET, *École normale supérieure de Cachan - ENS Cachan*, 2003. <https://tel.archives-ouvertes.fr/tel-00005271> (accessed 26 October 2020).
- [134] P. Chandran, S. Jabarin, Biaxial orientation of poly(ethylene terephthalate). Part III: Comparative structure and property changes resulting from simultaneous and sequential orientation, *Adv. Polym. Technol.* 12 (1993) 153–165.
doi:10.1002/adv.1993.060120204.
- [135] Y. Maruhashi, T. Asada, Structure and properties of biaxially stretched poly(ethylene terephthalate) sheets, *Polym. Eng. Sci.* 36 (1996) 483–494. doi:10.1002/pen.10434.
- [136] E.A. Lofgren, S.A. Jabarin, Polarized internal reflectance spectroscopic studies of oriented poly(ethylene terephthalate), *J. Appl. Polym. Sci.* 51 (1994) 1251–1267.
doi:10.1002/app.1994.070510712.
- [137] E. Gorlier, J.F. Agassant, J.M. Haudin, N. Billon, Experimental and theoretical study of uniaxial deformation of amorphous poly(ethylene terephthalate) above glass transition temperature, *Plast. Rubber Compos.* 30 (2011) 48–55.
doi:10.1179/146580101101541435.

- [138] Y. Marco, L. Chevalier, M. Chaouche, WAXD study of induced crystallization and orientation in poly(ethylene terephthalate) during biaxial elongation, *Polymer (Guildf)*. 43 (2002) 6569–6574. doi:10.1016/S0032-3861(02)00488-3.
- [139] A.J.J.E. Eerhart, A.P.C. Faaij, M.K. Patel, Replacing fossil based PET with biobased PEF; Process analysis, energy and GHG balance, *Energy Environ. Sci.* 5 (2012) 6407–6422. doi:10.1039/c2ee02480b.
- [140] X. Fei, J. Wang, J. Zhu, X. Wang, X. Liu, Bio-based Poly(ethylene 2,5-furanoate): No Longer an Alternative, But an Irreplaceable One in Polymer Industry, *ACS Sustain. Chem. Eng.* (2020) acssuschemeng.0c01862. doi:10.1021/acssuschemeng.0c01862.

Acknowledgements / Remerciements

Après trois années riches, tant sur le plan scientifique que sur le plan humain, cette aventure, le doctorat, arrive sur sa fin. Dans tous les cas, elle mérite qu'on remercie les (nombreuses) personnes qui y ont, de près ou de loin, contribué. Durant cette expérience, j'ai eu la chance de côtoyer en simultanée deux laboratoires, et donc de pouvoir rencontrer deux fois plus de personnes formidables qui m'ont épaulée, soutenue, motivée et conseillée. Sans elles, ce grand écart scientifique, ce manuscrit, les journées, les soirées et les week-ends auraient été bien différents.

Je tiens tout d'abord à remercier les directeurs des laboratoires qui m'ont accueillie et qui m'ont permis de travailler dans de bonnes conditions. D'une part, la directrice du Centre de Mise en Forme des Matériaux (CEMEF), Madame Elisabeth Massoni, et d'autre part, les directeurs successifs de l'Institut de Chimie de Nice (ICN), Madame Elisabeth Dunach puis Monsieur Uwe Meierhenrich.

J'aimerais ensuite remercier les membres du jury : Madame Valérie Gaucher et Madame Isabelle Royaud, pour avoir accepté d'être les rapporteurs de ma thèse ; Madame Allisson Saiter-Fourcin ainsi que Monsieur Sylvain Caillol, pour leur présence en tant qu'examineurs au sein du jury.

Ce travail n'aurait pas pu être réalisé sans mon équipe encadrante composée de Noëlle Billon et Nicolas Sbirrazzuoli, mes deux directeurs de thèse, ainsi que de

Christelle Combeaud et Nathanaël Guigo, mes deux encadrants. J'espère réellement avoir la chance de retravailler un jour avec vous.

Noëlle, merci d'avoir été ma directrice de thèse et de m'avoir notamment initiée à la mécanique. J'ai appris beaucoup à vos côtés durant ces années, grâce à votre expertise. Je garderai en mémoire les échanges scientifiques que l'on a pu avoir. Merci également de m'avoir fait confiance dès la fin de ma première année, et de m'avoir ainsi permis de participer à mes deux premières conférences. Je garde également un très bon souvenir de la conférence que nous avons faite toutes les deux à Belfast, en septembre 2019. De même, j'ai été très fière de faire partie de l'organisation du GFP, qui s'est tenu à Sophia en juin 2019, et ainsi de donner, avec Christelle, un atelier sur la mécanique des polymères à des scientifiques bien plus expérimentés que moi. Pour finir, merci également de m'avoir fait entrer dans l'équipe enseignante des Travaux Pratiques pour le cycle ingénieur civil de l'école des Mines de Paris. J'ai adoré initier des groupes d'étudiants au PET, et j'ai également été stupéfaite de voir à quel point la créativité des élèves pouvait donner lieu à une très bonne restitution scientifique.

Nicolas, je suis persuadée que sans la discussion que nous avons eue en 2015, lorsque je ne savais pas encore de quelle façon exploiter ma licence de physique-chimie à venir, je ne serais pas ici aujourd'hui. A cette époque, la seule chose que je souhaitais faire, c'était de la thermochimie ☺. Vous m'aviez dit de revenir vous voir lorsque j'aurais mon diplôme, et je vous ai pris au mot ! Me voilà donc 2 ans plus tard, devant vous et Nathanaël, vous informant que je souhaiterais faire un stage et une thèse. Vous avez été mon premier contact pour démarrer cette aventure, et je ne peux que vous en être sincèrement reconnaissante. Travailler avec quelqu'un d'aussi humain, gentil, et reconnu dans son domaine, est une chance qui devrait être donnée à tous les doctorants. Surtout, ne changez rien ! Merci encore pour tout ce que vous avez fait pour moi, enfin, sachez que j'ai été très fière d'enseigner la cinétique (votre bébé) aux étudiants de L3 chimie.

Nathanaël, tu as été mon premier enseignant à la fac en L1 (en septembre 2012). Je suis intimement convaincue que tu es la personne qui m'a donné goût à l'enseignement 😊. Mis à part cela, tu as également été un encadrant super et toujours à l'écoute, mais par-dessus tout très humain ! Merci pour les longues discussions scientifiques que l'on a eues, les débats sociétaux, les idées farfelues aussi (oui, je n'oublie pas le PEF dans la cuve à ultrasons), et toutes tes nombreuses blagues... Merci également de toujours prendre en compte nos idées, nos avis de doctorants et de nous laisser explorer les pistes qui nous tiennent à cœur. Avec Nicolas, vous m'avez également intégrée à l'écriture d'un chapitre de livre. Cela restera pour moi, une très riche expérience ! Tu as toujours eu un mot réconfortant après et/ou avant chaque réunion, à chaque lecture de document, et tu m'as toujours motivée et encouragée. Tu m'as coachée pour le Prix Pierre Laffitte et, sans toi, je n'aurais jamais obtenu ma deuxième place ! Reste cet encadrant au top !

Et pour finir, Christelle. Je me souviendrai toujours de la première phrase que tu m'aies dite quand on a su que j'avais obtenu le financement (après Félicitations évidemment) : « Tu verras, dans 3 ans tu auras grandi et tu ne seras plus la même personne qu'avant de débiter. Tu vas apprendre sur le plan scientifique, mais également énormément sur toi-même ». Je ne peux que te confirmer à quel point tu avais raison ! Tu m'as accompagnée dans cette transformation, de petite stagiaire à, maintenant, chercheuse. On a toujours été en osmose, et ainsi, les échanges ont été très constructifs. La quantité de thé ingurgité durant ces discussions en est sûrement la clé... On a passé des journées, très très longues et d'une efficacité sans nom devant Etifi, pour la rendre plus performante que jamais ! Merci vraiment pour tout le temps que tu m'as consacré. Je garderai toujours en tête que tous les problèmes se règlent après un bon « chien tête en bas » ! 😊

PS: Il m'a fallu du temps mais j'ai enfin admis que tu avais raison : la perfection n'existe pas... Et c'est bien mieux comme ça! 😊

Then, I have a special word for the industrial side of this project. Roy, Ele, Mikaël and Maxime. Thanks a lot for the following of my work during this thesis, as well as for having provided the materials. You always have questions that have contributed to improve my work and my scientific thought. I hope that you have learned many things from the reading of this manuscript. It was so rewarding to exchange with all of you.

Je remercie également l'ADEME pour le financement de ce projet, et les ingénieures qui m'ont suivie, Céline Scheuer, puis Isabelle Hébé. Merci également à Valérie Pineau pour toute son aide administrative et sa disponibilité.

Une très grande partie de ce travail n'aurait pas pu être réalisée sans les personnes du bâtiment D. Que ce soit une aide matérielle, une blague, un mot gentil, ou encore le partage d'un gâteau ou d'une pause repas, je vous dois un immense merci ! Francis, merci d'avoir géré tous les « petits » problèmes mécaniques que je pouvais rencontrer sur les machines. Marc, sans toi je n'aurais pas eu de four transparent. Erick, merci pour les très nombreuses découpes de plaques. Gilbert, on en a fait des soudures de thermocouple, et tu m'en as lancé des biscuits en fin de journée ! Arnaud, tu peux être fier de ton bébé... Etifi est une machine inégalée (et inégalable), merci pour ta gentillesse, ta bienveillance et ta disponibilité. Tu gardes ton titre de super super choupi ! Gaby, on en a fait des sessions de (rayons) X ! Merci pour ta gentillesse et de m'avoir accordé ta confiance sur les machines ! On n'aura pas pu faire cette journée au ski mais je ne l'oublie pas, ce n'est que partie remise ! J'ai passé de très longues heures en salle de RX, à discuter orientation de chaines avec toi, et j'ai toujours suivi ton conseil : « la lumière reviendra toujours avec la Bible de la cristallo » ! Merci pour tout Gaby, tu as plus que participé au bon déroulement de cette thèse.

Et pour finir, un message spécial pour deux personnes de l'atelier, Christophe et Guillaume... Nos DIC, WORD, EXCEL and THERMIC EXPERT ! On parle toujours d'avoir un esprit sain dans un corps sain, mais il faut avoir deux personnes comme vous pour réussir à faire des essais fructueux dans une thèse productive ! Vous avez toujours été disponible pour un réglage, une blague, une aide quelconque, une écoute, une pause thé, un goûter, un soutien et j'en passe (énormément)... Sans vous c'est sûr qu'il y aurait beaucoup moins de résultats dans cette thèse ! Merci d'avoir rendu plus que géniales mes journées de manip ! Je suis obligée de passer sous silence de nombreuses choses, mais souvenez-vous toujours de la posture du guerrier, de l'ours mal léché, de la danse de l'étirage et surtout, je dis bien surtout, de toujours avoir du chocolat sur vous !!... 😊

J'ai également une pensée particulière pour plusieurs permanents au Cemef et à l'ICN : Jean-Marc, je garde un très bon souvenir de nos discussions de cristallographie et de nos échanges de mails sur ce sujet, pour la publie. Vous avez été mon premier enseignant de polymères, et vous m'avez donné envie de continuer dans cette voie. J'ai adoré enseigner avec vous à Paris. Jean-Luc, je sais qu'au fond de ton âme, tu es persuadé de la grandeur d'Etifi, je te la laisse à présent, prends en grand soin ! Merci encore pour ta gentillesse et tes conseils. Pierre-Olivier, Elie, Gaëlle, Christophe (den Auwer), Tania, Lionel, merci également pour vos nombreux et précieux conseils. Florence, merci ton aide et ta gentillesse. Manu, merci de m'avoir sauvé mon ordi et mon disque dur (plusieurs fois). Luc Vincent, merci d'avoir résolu tous les problèmes que j'ai pu rencontrer dans la salle d'analyses thermiques, et de toujours être là pour nous débloquer les DMA ou DSC capricieuses ! Pierre Ilbizian, nous avons fréquemment partagé de nombreuses discussions dans les couloirs pendant mon doctorat, ton écoute et ta bonne humeur ont toujours été au rendez-vous ! Marie-Françoise, tu as illuminé de paroles réconfortantes mes passages au bâtiment B, et tu as été une vraie source de bonne humeur, à l'écoute et prête à aider. Je me souviendrai toujours des conseils que tu

m'as donnés ! Merci également à Geneviève et Sylvie pour votre aide administrative et votre gentillesse !

Je voudrais également remercier tous mes voisins de bureau, autant ceux de Nice, qui se sont succédés au fil du temps : Rime, Angela, notre dinosaure pirate Pierluigi, Johnny, Giuseppe, Mona, Océane, Pierre, Lucie, Lorenzo, Nicolas (Bosq) et notre chef des stagiaires Corentin, super choupinou, que ceux de Sophia : Shitij et Gabriel, pour vos gâteaux, vos petites attentions, avoir supporté mes rires, avoir écouté mes histoires, puis Luc, pour nos débats sociétaux, écologiques, végétariens et encore féministes, sans compter nos échanges animés sur les séries et les films. Travailler, rigoler et sortir avec vous aura été un réel bonheur et une bouffée d'oxygène ! Je n'oublie pas non plus Mélanie, ma première voisine de bureau en stage, qui m'a bien conseillé à mon arrivée au CEMEF, et avec qui j'ai participé à mon premier DEPOS ! Remerciements chaleureux aussi pour tous ceux avec qui j'ai pu partager mon repas, autant à Nice, la team RHE et les bonnes rigolades le midi, qu'à Sophia avec Lucas, Gabriel, Charlounet, Robin, Jonathan, Ramy, Giulia, et mon inconditionnel soutien féminin envers cette redoutable équipe de garçons, Chahrazade. Ces moments au labo et surtout en dehors, ces discussions et échanges de recettes, font partie de mes meilleurs souvenirs. PS : Oui, Lucas, tu auras un exemplaire de mon livre de cuisine !... 😊

J'ai également une pensée pour Sophie et Lucile avec qui j'ai passé une super (NICE) conférence ! Anélia, on a partagé nos expériences de doctorantes ADEME bien similaires pour des labos si éloignés ! Vivement la prochaine mise à jour de nos vies !

J'ai un mot particulier pour mes très chères Charlotte et Anna ! On a passé une très grande partie de notre temps au labo ainsi qu'en dehors, ensemble. Je garderai en tête tous ces moments ! Depuis que vous êtes parties, vous avez suivi de très

près les diverses péripéties liées à ma thèse, tant en live que par skype. On a tellement partagé de bons moments, animant le bureau des MAPEC (et le couloir), râlant aussi parfois, toujours alliées, que ce soit pour commander nos incontournables repas soigneusement réfléchis (à heure fixe !) afin de recharger nos neurones, que pour des « mégas goûters », des points shopping, des conseils cuisine, du sport, des sorties mais aussi des vacances. Notre traditionnel « A taaaaable » est gravé dans NOTRE bureau... Et surtout, on a réussi à toujours s'entraider, se soutenir et se reconforter. La team ACE a continué de briller, et ce, malgré les kilomètres qui malheureusement nous séparent. Vous avez fidèlement été avec moi durant la fin de cette aventure 😊 J'ai aussi un mot spécial pour Emilie, qui, du bout du monde a continué, elle aussi, à être très présente, à me motiver et me soutenir (même dans mes trajets sur l'autoroute le matin). J'apprécie beaucoup que l'on puisse communiquer régulièrement sur nos expériences respectives. Deux Emilie ensemble ça en fait des péripéties (les gens d'Auron ne sont pas prêts de nous oublier) ! Merci aussi bien sûr à Marie, tu as supporté toutes nos histoires de labo lors de nos skypes, soirées et week-ends !

Pour ceux que je n'ai pas encore cités et qui appartiennent à plusieurs des « groupes » ci-dessous, vous avez été

« indispensables » : Benjamin et ses compliments journaliers, ainsi que nos discussions tardives au labo, Simon et sa bonne humeur légendaire, Cédric balèze à Just Dance et en pancakes, Jody le seul garçon en legging de Yoga, également les supers « riders », entre autres Xiao, Manue, Raph,

les yogis du mercredi midi qui m'ont bien souvent réveillée à la fin du cours (entre autres Bénédicte et Jeanne),

les « garçons » de Sophia qui se souviendront très longtemps de certaines musiques : Jules, Clément, Alexis, Corentin, Carlos, Yoan, et tous les autres étudiants de Nice et Sophia avec qui j'ai partagé une pause au labo, une journée

ski ou visite de Nice, une plage, une rando, une bière, un verre, un resto, un ciné ou même simplement un mot dans les couloirs ! Vous avez tous contribué à ma motivation et mon bien-être pendant ces 3 ans. J'ai également une pensée pour les intervenants du Pint of Science qui ont permis le bon déroulement de ce festival, et pour Anthony avec qui j'ai partagé de très bons TPs confinés ! Merci également à Pavel Kuzhir de m'avoir donné cette opportunité d'enseignement, et à tous les gens du Centre des Matériaux d'Evry pour leur aide durant les journées TP ! J'ai un dernier mot pour Alain Ciffréo qui m'a donné ma chance en master P3M, alors que ce n'était pas la voie « directe » après ma licence, c'est également grâce à vous que je suis ici aujourd'hui!

J'aimerais également remercier mes stagiaires Dylan, Margot, Eva et ceux du projet poster des Mines (Laura, Maud, Quentin et Leopold), vous m'avez tous bien aidée avec vos manips ou vos recherches ! Je pense également à mes élèves de cours particuliers qui, depuis des années et surtout ces derniers mois ont été une réelle aération dans ma rédaction, ainsi que les étudiants que j'ai pu côtoyés !

Pour finir ces (longs mais justifiés) remerciements j'ai une pensée sincère et aimante pour ma famille proche, mes amis d'ici et maintenant, surtout d'ailleurs, sans eux rien de tout cela n'aurait été possible. Mon meilleur ami Renaud, que j'ai bien souvent appelé pendant ses heures de sommeil, et qui a été un cobaye hors pair de mes essais culinaires, mon grand frère pour ses conseils et son kit parfait du doctorant, et surtout ma maman. Merci maman, tu peux être fière d'avoir survécu à deux thèses, et surtout de nous avoir amenés, tous les deux, jusque-là ! Merci pour tout, depuis toujours, tu veilles et t'occupes de nous ! Tu es pour une grande part dans cette aventure. J'ai une caresse pour mes monstres poilus, mes boules de réconfort, les meilleurs coussins chauffants, lors de la rédaction, les plus heureux du confinement et du télétravail et des voisins de bureau tendrement collants !

RÉSUMÉ

Ce travail a pour but de fournir une meilleure compréhension du comportement mécanique ainsi que du développement microstructural d'un polymère biosourcé, le PEF. En effet, ce polymère est de plus en plus évoqué pour remplacer un des matériaux les plus utilisés dans l'emballage alimentaire, le PET. Le PEF peut être considéré comme l'analogue biosourcé du PET. La différence entre ces deux matériaux est la présence d'un cycle furanique (composé d'un atome d'oxygène possédant deux doublets non liants) dans le PEF à la place du cycle benzénique. Par rapport au PET, cette spécificité du PEF est responsable d'une température de transition vitreuse ainsi que d'un module élastique plus élevés, d'une vitesse de cristallisation plus lente, d'un cristal moins stable et d'une fusion à plus basse température.

A partir de l'étude de l'étirage du PET amorphe, et de son développement microstructural, l'étirage uniaxial du PEF amorphe a été étudié. En considérant les différences architecturales des chaînes, il apparaît que le PEF et le PET ne peuvent pas être étirés dans les mêmes conditions (vitesse de déformation et température). Pour réaliser des tests mécaniques (étirage uniaxial et biaxial) qui correspondent au PEF, il est nécessaire de définir au préalable la gamme de formage ainsi que des conditions d'étirage adaptées. Dans ce but, un protocole d'étirage spécifique, basé sur la construction et l'utilisation d'une courbe maîtresse à la température de référence propre à chaque matériau, a été défini et appliqué au PEF et au PET. Cette courbe permet de connaître l'état physique initial du matériau en relation avec les couples vitesse de déformation/température. Le contrôle de l'étirage, ainsi que l'utilisation de paramètres d'étirage qui tiennent compte de l'état physique initial du matériau, conduisent à la formation d'un cristal qui va augmenter la stabilité thermique ainsi que la rigidité du matériau. Le comportement mécanique du PEF révèle qu'avec des conditions d'étirage correctes, il se comporte comme le PET. Dans les premières étapes de l'étirage, les deux matériaux présentent une réponse mécanique très similaire. Une différence majeure concernant le moment d'apparition du cristal existe entre le PEF et le PET. En effet, la phase cristalline du PEF doit d'abord se former avant qu'il puisse durcir sous étirage. Jusqu'à la fin de l'étirage, le cristal n'évolue quasiment plus. Au contraire, le PET forme dans un premier temps une mésophase. L'existence du cristal dépend de la déformation finale imposée et des conditions de refroidissement.

La microstructure induite sous étirage a été largement étudiée et comparée à celle présente dans un échantillon cristallisé statiquement. Une grande similitude est notée entre ces deux modes de cristallisation, spécialement au niveau de la définition du cristal. Il apparaît que la microstructure induite sous étirage est plus contrainte que celle obtenue après une cristallisation statique. Ce travail a également mis en évidence que la microstructure formée lors de l'étirage du PEF est relativement similaire et ce, quelles que soient les conditions d'étirage. Pour le PET, le développement microstructural semble être bien plus tributaire des couples vitesse/température utilisés.

MOTS CLÉS

Cristallisation sous étirage, étirage uniaxial et biaxial, polymère biosourcé, analyse microstructurale, PEF, comportement thermomécanique.

ABSTRACT

The aim of this work is to provide a better understanding of the mechanical behaviour as well as of the associated microstructural development of a biobased polymer, named PEF. Indeed, this polymer is more and more evocated to replace one of the polymer used in food packaging, PET. PEF is identified as the biobased counterpart of PET. The difference between these two materials is the presence of a furan ring (composed of an oxygen atom with two non-binding electrons), instead of a benzene one, in PEF. This PEF specificity is responsible of a higher glass transition temperature and elastic modulus, a slower crystallization rate, a lower stability of the crystal and a lower melting temperature in comparison with PET.

Based on the stretching of amorphous PET and on its microstructural development, the stretching of amorphous PEF is investigated. Considering the differences in the chain architecture, it appears that PEF and PET cannot be stretched with the same process parameters (strain rate and temperature). In order to perform efficient PEF uniaxial and biaxial tests, it is necessary to define the forming range and some suitable stretching parameters. In this way, a specific stretching protocol, based on the building and on the reading of a master curve at a reference temperature for each material, has been defined and applied on PEF and PET. This master curve allows to know the initial physical state of the material in relation with the couples strain rate/temperature. The stretching mastering and the use of optimized stretching settings lead to the creation of a crystal that increases the thermal stability as well as the rigidity of the material. The mechanical behaviour of PEF reveals that, after the optimization of the stretching settings, this material acts in a similar way as PET. In the first stages of the stretching, both materials mechanical responses are really close. A major difference exists between PEF and PET concerning the apparition of the crystal upon stretching. Indeed, it is found that PEF must form the crystal to strain harden. Up to the end of the stretching, this crystal does not evolve. On the contrary, PET forms firstly a mesophase. The crystal existence is dependent on the final strain and on the quenching protocol.

The microstructure induced upon stretching has been widely analysed and compared to the microstructure existing when a sample is crystallized in static conditions. A high similarity exists between the two ways of crystallization, especially for the crystal definition. It seems that the microstructure induced during the stretching is more constrained than the one obtained from a static crystallization. It has to be noted that the aliphatic part of the chain is the first one impacted by the stretching. This work has also highlighted that the microstructure induced in PEF under stretching is relatively close whatever the stretching conditions are. Concerning PET, the microstructural development seems to be more dependent on the stretching settings.

KEYWORDS

Strain induced crystallization, uniaxial and biaxial stretching, biobased polymer, microstructural analysis, PEF, thermomechanical behaviour.